Fabrication of Nano-materials Using Vortex Fluidic Devices and Their Biomedical Applications

by

Xuan Luo

Thesis
Submitted to Flinders University
for the degree of

Doctor of Philosophy in Medical Biotechnology
College of Medicine and Public Health
13th March 2019

CONTENTS

LIST OF FIGURES

Microfluidic generation of agarose microgels in encapsulating two types of murine embryonic stem cells (scale 100 µm).[83] (d) A schematic of a droplet-based microfluidic device in generating disk-like Ca-alginate hydrogel beads for cell encapsulation and manipulation; the beads with encapsulated cells can be rolled using a thin needle.[183]

Figure 1.15: (a) Schematic of the staggered herringbone micromixer with sequential regions of asymmetric ridges for the synthesis of PLGA nanoparticles for drug delivery. In vitro N-Acetylcysteine (N-Ac) release profiles from N-Ac loaded PLGA nanoparticles.[206] (b) Schematic of the addition of bFGF or PBAE/DNA nanoparticle to a PEG precursor solution and subsequent microsphere formation in a droplet-based microfluidic device. Fluorescein isothiocyanate-conjugated BSA (green) used to visualise protein encapsulation (scale bar: 200 µm).[208] (c) Synthesis of the combinatory Pt(IV) and Docetaxel loaded PLGA nanoparticles using a flow focusing microfluidic device.[210]

Figure 1.16: (a) Schematic of a microfluidic chip formed by colloidal self-assembly of 310 nm diameter silica particles entrapped in the presence of a 0.5% solution of photopolymerised methacrylates. SEM image of peeled PDMS plate following photopolymerisation.[227] (b) Flowchart for the rapid assembly of the stable photonic crystals into glass microchip channels by evaporation induced assembly and the confocal image of the silica-particle-embedded PC column taken from its centre section.[225] (c) Purification of microalgal protein using an aqueous two phase system intensified by VFD.[228]

Figure 1.17: (a) Schematic of the core-shell hydrogel particle fabrication process while changing the UV intensity and the concentration of PEGDA.[207] (b) Schematic representation of the microfluidic approaches used to prepare efavirenz (EVF)-loaded PLGA nanoparticles.[233] (c) Droplet microfluidics and associated external gelation set-up for fabricating alginate microspheres with immobilised antibodies, which were immobilised on the porous network of the alginate microsphere during the external cross-linking process.[234]

Figure 2.1 Laser-VFD fabrication of carbon dots (CDs) under continuous flow. (a) Schematic of the vortex fluidic device (VFD). (b) Illustration of an unstable dispersion of MWCNTs in aqueous H_2O_2 in a normal syringe. (c) Magnetic-assisted mixing in a syringe for delivering a uniform dispersion of MWCNTs to the base of the rapidly rotating borosilicate glass tube (20 mm O.D. diameter).

Figure 2.2 Continuous flow VFD processing of MWCNTs (0.5 mg mL^{-1}, flow rate of 0.45 mL min^{-1}) under pulsed laser irradiation (1064 nm, 260 mJ) at 45° tilt and different rotational speeds. (a) 5000 rpm. (b) 6500 rpm. (c) 7500 rpm. (d) 8000 rpm. Samples were centrifuged at 1180 × g for 30 min after VFD processing and the supernatant was drop-casted on a silicon wafer for AFM imaging. The average dimension of as received MWCNT is O.D. × I.D. × L equivalent to 10 nm ± 1 nm×4.5nm±0.5nm×3–6µm.An average of ten areas were randomly chosen for all AFM images, with 1–2 representative images presented in this figure (as for all AFM images).

Figure 2.3 Continuous flow VFD processing of MWCNTs (0.5 mg mL^{-1}, flow rate of 0.45 mL min^{-1}, 7500 rpm) at 45° tilt, under pulsed laser irradiation at different laser power. (a) 150 mJ. (b) 260 mJ. (c) 350 mJ. (d) 450 mJ. (e) 670 mJ. Samples were centrifuged before drop-casting on a silicon wafer for AFM imaging.

Figure 2.4 Continuous flow VFD processing of MWCNTs (flow rate of 0.45 mL min^{-1}, 7500 rpm) under pulsed laser irradiation (1064 nm, 450 mJ) at 45° tilt, with different sample concentrations. (a) MWCNTs at 0.5 mg mL^{-1} without laser-VFD (control). (b) MWCNTs processed at 0.5 mg mL^{-1}. (c) 0.25 mg mL^{-1}. (d) 0.1 mg mL^{-1}. (e) 0.1 mg mL^{-1} processed through two cycles with laser-VFD processing. For AFM imaging, as-prepared samples were directly drop-casted on silicon wafers without centrifugation post VFD processing.

Figure 2.5 Raman mapping for CDs processed using two cycles of continuous flow VFD (0.1 mg m^{-1}, flow rate of 0.45 mL min^{-1}, 7500 rpm) under pulsed laser irradiation (1064 nm, 450 mJ) at 45° tilt. (a) AFM images of the mapped area and corresponding zoomed-in images. (b) Optical image and Raman maps of the highlighted area (red square) with the two map images representing the D (1352 cm^{-1}) and G (1594 cm^{-1}) bands of graphitic material. (c) Three representative single spectrum correspond to the three circled spot in b. Scanned area was 20×20 μm^2.

Figure 2.6 CDs fabricated under optimized conditions (two cycles continuous flow, 0.1 mg mL^{-1}, flow rate of 0.45 mL min^{-1}, 7500 rpm, 450 mJ, at 45° tilt). (a) AFM image and height distributions based on >300 individual CDs (inset). (b) SEM image. (c) TEM, selected area electron diffraction pattern (inset) and HRTEM images. (d) XRD results of as received MWCNTs and as-processed CDs.

Figure 2.7 (a) UV-vis spectrum of the CDs. (b) C 1s spectrum of the CDs. (c) FT-IR spectra of the CDs.

Figure 2.8 (a) Contour fluorescence map for excitation and emission of the CDs (from the optimized condition). The black dot represents the maximal fluorescence intensity of the CDs, received at an excitation wavelength of 345 nm and at an emission 450 nm. (b) Fluorescence microscopy excited at 365 nm. (c) PL spectra of the CDs. Two emission peaks at constant wavelength of 435 and 466 nm were for different excitation wavelengths, from 277 to 355 nm. (d) Fluorescence decays of CDs excited at 377 nm. (e) Decaying lifetime of three emissive sites.

Figure 2.9 Schematic of laser-VFD processing for fabricating CDs from MWCNTs. The black dots above and below the ball-and-stick model of the CDs highlight the sample may contain different layers of graphene.

Figure 3.1: (a) Laser beam irradiation of an iron rod placed inside the VFD tube with the device operated in the confined mode. (b) Laser beam irradiation of an iron rod placed inside the VFD tube with the device operated in continuous flow mode. (c) Cartoon of a plasma plume containing iron atoms and ions. (d) Generating iron oxide nanoparticle through diffusion-driven nucleation and aggregation in the presence of a gas and a liquid carrier.

Figure 3.2 (a) Images showing the laser irradiation position with the iron rod placed inside the VFD tube spun at 7500 rpm with the 1064 nm pulsed laser operating at 20, 70, 160, 360 and 560 mJ, from samples 1 to 5 respectively. (b) As prepared sample dispersed in 1 mL water; a stable colloidal suspension was obtained for 360 and 560 mJ. (c) UV-vis spectra. (d) Dynamic light scattering results. (e) Zeta potential data.

Figure 3.3: Characterisation of the as prepared IONPs (laser power 360 mJ for the VFD tube rotated at 7500 rpm for 15 min. in the confined mode for 1 mL water. (a) AFM, TEM

and size distribution plot which represented more than 300 randomly chosen IONPs. (b) XRD diffraction pattern and Raman spectra. (c) FT-IR spectrum.

Figure 3.4 (a) Size of IONPs nanoparticles generated at 360 mJ with the VFD operating in the confined mode containing 1 mL water, for 15 min at different rotational speeds. (b) Particle size estimated using XRD. (c) Raman spectra. (d) XRD of samples conducted under continuous flow mode at 7500 rpm, 0.1 mL/min flow rate (materials exiting and retained inside the tube). (e) Size estimation plot based on TEM for the two samples obtained from continuous flow (materials exiting and retained inside the tube).

Figure 3.5 Representative TEM, HRTEM and SAED (marked indices are planes of magnetite). (a) IONPs existing the VFD operated at a rotational speed of 7500 rpm and a flow rate of 0.1 mL/min. (b) IONPs retained inside the tube during processing at a rotational speed of 7500 rpm and a flow rate of 0.1 mL/min. Both samples showed mixed shapes of spheres and hexagonal prisms. Both samples are single-crystals with individual crystallites highlighted. The FFT patterns were acquired from the HRTEM image.

Figure 3.6 (a) Comparison of magnetic hysteresis curves of the VFD-processed samples (retained and collected). (b) Low-field interval of the magnetization curves of the two samples.

Figure 4.1 Schematic of the vortex fluidic device (VFD) and sample preparation. (a) Confined mode, 45° tilt angle with heating; (b) continuous flow mode; (c) confined mode post VFD-processing for hPEI and PEI$_{800}$.

Figure 4.2 2D Fluorescence maps of VFD processed PEI at 160ºC at different flow rates, and corresponding samples imaged using inverted fluorescence microscopy (EVOS$^{®}$ FL) with three Invitrogen^{TM} EVOS^{TM} light cubes: DAPI (357/44 Ex; 447/60 Em), GFP (470/22 Ex; 510/42 Em) and RFP (531/40 Ex; 593/40 Em) and AFM. (a) PEI$_{800}$ (37 mg/mL, 8600 rpm) 0.1 mL/min; (b) PEI$_{800}$ (37 mg/mL, 8600 rpm) 0.2 mL/min; (c) hPEI (48.6 mg/mL, 8000 rpm) 0.1 mL/min

Figure 4.3 NMR data for nanoparticles derived from PEI$_{800}$ under continuous flow, 0.2 mL/min at 160ºC. (a) ^{13}C NMR spectra. The peaks (a-h) were assigned according to the different combinations of amine nearest neighbours in the structure of PEI.[20] (b) ^{1}H NMR spectra.

Figure 4.4 (a) Optical images of non-treated MCF-7 cells, and cells treated with VFD-processed hPEI and as-received hPEI; (b) Cell viability of MCF-7 cells treated with different concentrations of PEI$_{800}$ and hPEI derivatives for 24 h. Data are presented as mean±SD. Treatment significantly different from the control at $P<0.05$ were presented as * and $P<0.01$ as **; (c) Images of MCF-7 cells treated with VFD processed PEI$_{800}$ (0.2 mL/min) under bright field, GFP (470/22 nm) excitation and the merged image.

Figure 4.5 (a) 2D fluorescence maps for 1 mL of hPEI solution processed in a VFD at 7500 rpm at 160°C (confined mode) for 30 min under different gas environment; (b) the proposed mechanism of the VFD-polymer reaction.

Figure 4.6 2D fluorescence map of VFD processed PEI$_{800}$ (37 mg/mL) at 160ºC under continuous flow, 0.3 mL/min, 8600 rpm. (a) PEI$_{800}$ only; (b) PEI$_{800}$ and citric acid (molar ratio 1:1); (c) PEI$_{800}$ and salicylic acid (molar ratio 1:1); (d) Cell viability of MCF-7cells treated with different concentrations of the three PEI derivatives after 24 h.

Figure 6.2 (a) Purity (A620/A280) of CPC and APC recovered by VFD-ATPS for solutions processed at different rotational speeds (rpm). (b) Yield of CPC and APC recovered by VFD-ATPS for solutions processed at different rotational speeds (rpm). Different uppercase (C-PC) and lowercase (APC) letters indicate significant differences ($p < 0.05$).

Figure 6.3 (a) SDS-PAGE gel, lane 1: molecular weight markers. Lane 2: crude extract. Lane 3: single ATPS-VFD (1′VFD) purified (top phase). Lane 4: multiple ATPS-VFD (4 times or 4′VFD) purified (top phase). Lane 5: 1′VFD (bottom phase). Lane 6: 4′VFD purified (bottom phase). Lane 7: water control. Lane 8: commercial C-PC. A 20 µg portion of overall proteins was loaded in each lane. PEG_{4000} was removed from all samples before running the gel. (b) Percentage of C- PC relative to all proteins in each lane in Figure 3a. Statistical significance is indicated by single ($p < 0.05$) and double ($p < 0.01$) asterisks.

Figure 6.4 Spectroscopic characterization of C-phycocyanin. (a) Absorption and fluorescence spectra of commercial C-PC, 4′ATPS- centrifugation, and 4′ATPS-VFD C-PC. UV−vis/absorbance was conducted at a total protein concentration of 0.5 mg/mL. Fluorescence was conducted at 12.5 µg/mL. (b) FT-IR spectrum of C-PC samples. (c) Circular dichroism spectra of C-PC samples (far- UV) at protein concentration of 0.2 mg/mL.

Figure 7.1 Summary of various materials fabricated using VFD and future directions.

Figure 7.2 (a) *In situ* modification of PEI with VFD (b) *In situ* self-assemly of PEI/DNA coplexes (c) Transfection of MCF-7 cell line with VFD-modified PEI (800Da)/pGFP coplexes compared to the ones form from non-modified PEI (800Da). MCF-7 cells were seeded onto 96 well plate and incubated for 24 h before transfection. PEIs/pGFP coplexes at 15 and 30 w/w ratio pre-incubated for 15 min were added and observed using inverted fluorescence microscope (EVOS$^{®}$ FL) after 24 h. The effect on DNA topology was evaluated using the circular, supercoiled and linearised forms of plasmid GFP (pGFP), which is 5.2 kb on average which is equivalent to 1.716 µm in length.

Figure 7.3 Processing of pGFP with PEI (MW=25kDa) for 10min using **(a)** Benchtop vortex **(b)** VFD at 7500 rpm under confined mode. The concentration of pGFP is 11.2 µg/mL **(c)** Processing of pGFP with PEI (MW=25kDa) using VFD at 5000 rpm for 10 min under confined mode. The concentration of pGFP is 1.12µg/mL. The topographic line profile of two randomly chosen nanoparticles showing a sample height between 2 to 10 nm.

Figure 7.4 Slicing of pGFP in the presence of PEI using VFD at 7500 rpm for 10 min.

Figure 7.5 (a) ZIF-8 prepared by VFD under confine mode at 7500 rpm for 30 min (b) ZIF-8 with BSA by VFD under confined mode at 7500 rpm for 30 min (c) Manipulating the morphology of MOF-5 at different speeds of VFD (d) SEM/EDX mapping of MOF-5 flower (at accelerating voltage of 10 kV).

Figure 7.6 (a) XRD, FTIR and Raman, respectively (b) Encapsulation of C-phycocyanin with ZIF-8 under VFD at 7500 rpm for 20 min. The sample was excited at 532 nm with highest fluorescence intensity presented as the red colour located inside the core part of the nanostructure.

LIST OF ABBREVIATIONS

AFM	Atomic force microscopy
BNP	BSA-based nanoparticles
BSA	Bovine serum albumin
CD	Carbon dot
CD	Circular dichroism
CNT	Carbon nanotube
C-PC	C-phycocyanin
DMEM	Dulbecco Modified Eagle Medium
DWCNT	Double walled carbon nanotube
DNA	Deoxyribonucleic acid
FT-IR	Fourier transform infrared spectroscopy
FWHM	Full width of half maximum
HPLC	High-performance liquid chromatography
HPSEC	High-performance size-exclusion chromatography
HRTEM	High resolution transmission electron microscopy
ID	Inner diameter
IONP	Iron oxide nanoparticle
MOF	Metal organic framework
MW	Molecular weight
MWCNT	Multiwalled carbon nanotube
NMP	N-methyl pyrrolidone
NMR	Nuclear magnetic resonance spectroscopy
Nd:YAG	Neodymium-doped yttrium aluminum garnet
NIR	Near infrared
OD	Outer diameter
1D	One dimensional
PEG	Polyethylene glycol
PEI	Polyethylenimine

PL	Photoluminescence
SAED	Selected area electron diffraction
SWCNT	Single walled carbon nanotube
SEM	Scanning electron microscopy
SANS	Small angle neutron scattering
TEM	Transmission electron microscopy
TGA	Thermo-gravimetric analysis
2D	Two dimensional
UV-Vis	Ultraviolet visible spectroscopy
QD	Quantum dot
VFD	Vortex fluidic device
XPS	X-ray photoelectron spectroscopy
XRD	X-ray powder diffraction

EXECUTIVE SUMMARY

Over the last few decades, there has been a considerable interest in the area of developing various particulate systems with diameters varying from nanometers to micrometers for materials ranging from semicondutors, metals to polymers. These nano and microsized materials could play significant roles in many applications such as biosensors, *in vivo* imaging, cancer theranostics, *in vitro* diagnosis and drug delivery. In each of these fields, the physicochemical properties of particles can have significant influences on their applications and efficacy. An efficient, controllable, scalable and reproducible technique for the synthesis of micro-/nanoparticles with well-defined properties is ideal.

Microfluidic technology provides an alternative strategy for the synthesis of various materials with precise control over size, shape and homogeneity. The focus of my PhD is to create a paradigm shift in nanoscience by employing a novel thin film intensified process - vortex fluidic device (VFD) invented in our laboratory towards well-controlled fabrication and manipulation of nanostructures from various raw materials such as carbon, metal, polymer and protein. Carbon nanodots produced using VFD have a relatively narrow size distribution, between 3 to 13 nm, and have high colloidal stability and are non-toxic up to 200 µg/mL. We have established that this process is also effective in forming superparamagnetic magnetite nanoparticles of spheroidal or hexagonal shapes with a narrow size distribution in a one-step continuous flow process. The VFD could also be applied to manipulate polyethylenimine-based nanoparticles with tunable fluorescence, macroporous bovine serum albumin-based nanospheres or nanopockets and even to be used as a protein purification tool for crude microalgae extracts. This project outcomes present a significant opportunity to explore the potential application of the VFD in generating high-value biomedical materials in a more benign way in filling this gap of research toward many industrial applications.

DECLARATION

I certify that this thesis does not incorporate without acknowledgment any material previously submitted for a degree or diploma in any university; and that to the best of my knowledge and belief it does not contain any material previously published or written by another person except where due reference is made in the text.

Signed.......Xuan Luo....................................

Date.....................November 2018..................................

ACKNOWLEDGEMENTS

This PhD thesis would not have been possible without the cooperation and support of numerous people. Firstly, I would like to express my sincere gratitude and appreciation to my supervisors, Prof. Wei Zhang and Prof. Colin Raston, for their helpful guidance and continuous support throughout this project. Their kind support, both academically and in general life, helped me in all the time of research and writing of this thesis, which will long be remembered with respect. Sincere thanks goes to Raston lab and Flinders Institute for NanoScale Science and Technology (INST), who provided me an opportunity to join the team and gave me access to the laboratory and research facilities. Without the precious support, it would not be possible to conduct this research.

I am also grateful to all of our valued collaborators from INST, including Dr. Chris Gibson and Dr. Jason Gascooke. All of their consistent guidance and invaluable advice contributed to successful and productive research. I would like to thank Dr. Kasturi Vimalanathan for the support, patience and her great guidance in teaching me a lot of techniques about nanotechnology, which accelerated the progress and success of my studies. A significant part of this research would not have been possible without our keen collaborators from a number of local and international universities, most importantly Prof. Jin Zou, Prof. Qin Li and Prof. Rob Lamb.

Moreover, I am particularly grateful to members of Flinders Centre for Marine Bioproducts Development (CMBD) and School of Chemistry and Physical Sciences. In particular, Peng Su and David Vincent for their great help throughout the research; Dr. Hanna Krysinska, who efficiently manage and facilitate all of the work in our laboratory and department; along with Jane Keane, Shirley Sorokin, and Dr. Paul Smith, who all gave me kind support and suggestions. I am thankful to all members of our Centre and Department for their encouragement, friendship, and support during my studies. These contributions will not be forgotten. Also, I am very grateful to people who work in other departments of Flinders University: Dr. Tim Chataway and Nusha Chegeni Farahani from the Proteomics Facility assisted with the SDS-PAGE and LC-MS and Angela Binns, who managed the facility support within Flinders Medical Centre. Ms. Yvette DeGraaf for fluorescence microscopy.

I acknowledge with many thanks the financial support and research funding from the Australian Research Council and Government of South Australia, and Australia Microscopy

& Microanalysis Research Facility (AMMRF) and the Australian National Fabrication Facility (ANFF) for accessing microscopic facilities.

Last but not least, I would like to thank my family members, especially my parents and my husband Xia for truly believing in me and for providing me with great support. Without their support and tremendous encouragement, I certainly could not have reached this far.

DETAILS OF PUBLICATIONS

Journal articles

1. Luo X.; Al-Antaki A. H. M.; Alharbi T. M. D.; Hutchison W. D.; Zou Y.; Zou J.; Sheehan A.; Zhang W,; Raston C. L., Laser ablated vortex fluidic mediated synthesis of superparamagnetic magnetite nanoparticles in water under flow, *ACS Omega* **2018,** *3* (9), 11172-11178.
2. Luo, X.; Al-Antaki, A. H. M.; Harvey, D. P.; Ruan, Y.; He, S.; Zhang, W.; Raston, C. L., Vortex fluidic mediated synthesis of macroporous bovine serum albumin-based microspheres. *ACS Applied Materials & Interfaces* **2018,** *10* (32), 27224-27232.
3. Luo, X.; Al-Antaki, A. H. M.; Vimalanathan, K.; Moffatt, J.; Zheng, K.; Zou, Y.; Zou, J.; Duan, X.; Lamb, R. N.; Wang, S.; Li, Q.; Zhang, W.; Raston, C. L., Laser irradiated vortex fluidic mediated synthesis of luminescent carbon nanodots under continuous flow. *Reaction Chemistry & Engineering* **2018,** *3* (2), 164-170.
4. Luo, X.; Al-Antaki, A. H. M.; Pye, S.; Meech, R.; Zhang, W.; Raston, C. L., High-shear-imparted tunable fluorescence in polyethylenimines. *ChemPhotoChem* **2018,** *2* (4), 343-348.
5. Luo, X.; Smith, P.; Raston, C. L.; Zhang, W., Vortex fluidic device-intensified aqueous two phase extraction of C-phycocyanin from *Spirulina maxima*. *ACS Sustainable Chemistry & Engineering* **2016,** *4* (7), 3905-3911.
6. Luo, X.; Su, P.; Zhang, W., Advances in microalgae-derived phytosterols for functional food and pharmaceutical applications. *Marine Drugs* **2015,** *13* (7), 4231-4254.
7. He, S.; Joseph, N.; Luo, X.; Raston, C., Continuous flow thin film microfluidic mediated nano-encapsulation of fish oil. *LWT* **2019,** *103*, 88-93.
8. Al-Antaki, A. H. M.; Luo, X.; Duan, A.; Lamb, R. N.; Eroglu, E.; Hutchison, W.; Zou, Y. C.; Zou, J.; Raston, C. L., Continuous flow synthesis of phosphate binding h-BN@magnetite hybrid material. *RSC Advances* **2018**, DOI: 10.1039/c8ra08336c.
9. Sitepu, E. K.; Corbin, K.; Luo, X.; Pye, S. J.; Tang, Y.; Leterme, S. C.; Heimann, K.; Raston, C. L.; Zhang, W., Vortex fluidic mediated direct transesterification of wet microalgae biomass to biodiesel. *Bioresource Technology* **2018,** *266*, 488-497.
10. Nguyen, T. T.; Barber, A. R.; Smith, P.; Luo, X.; Zhang, W., Application and optimization of the highly efficient and environmentally-friendly microwave-intensified lactic acid demineralization of deproteinized Rock lobster shells (*Jasus edwardsii*) for chitin production. *Food and Bioproducts Processing* **2017,** *102*, 367-374.

Patent

1. Processing for controlling structure and/or properties of carbon and boron nanomaterials, **2017**.
2. A novel process for fabricating polyethylenimine (PEI)-based fluorescent nanoparticles from PEI with different molecular weights, **2017**.

Conferences

1. Luo, X., Zhang, W., and Raston, C., **2018 '**High-Shear-Imparted Tunable Fluorescence in Polyethylenimines**',** ICONN international conference, Wollongong, Australia.
2. Luo, X., Zhang, W., and Raston, C., **2017** 'Laser irradiated vortex fluidic mediated synthesis of luminescent carbon nanodots under continuous flow', RACI Centenary Congress, Melbourne, Australia.
3. Luo, X., Raston, C. and Zhang, W. **2017**, 'Vortex fluidic device-mediated aqueous two phase extraction of C-phycocyanin from spirulina maxima', BioProcessing Network Conference, Adelaide, Australia.
4. Luo, X., Vimalanathan, K., Meech, R., Raston, C. and Zhang, W. **2016**, 'Preparation of carbon nanotube-phycocyanin conjugate using vortex fluidic device for photo-thermal therapy targeting breast cancer stem cells', NanoCentre Conference 2016, Adelaide, Australia.
5. Luo, X., Raston, C., Smith, P. and Zhang, W. **2016**, 'Vortex fluidic device-mediated aqueous two phase extraction of C-phycocyanin from spirulina maxima',1st Australia New Zealand Marine Biotechnology Society symposium, Adelaide, Australia.

1. INTRODUCTION

Microfluidic processing is continually evolving as a method of choice for manufacturing functional micro- and nano-materials with precise control over size, shapes and homogeneity. Significant advances have been made in the field over the last decade in developing novel microfluidic devices (MD) for exquisite control of material properties and functions. Until now, most MD-related research has focused on three major types, which are single-phase or laminar flow devices, segmented flow devices and droplet-based or two-phase flow devices with non-systematic and non-comprehensive biomedical applications incorporated. In addition, even though recent research starts to combine different types of microchannels in various ways to adapt specific synthesis requirement, issues such as system clogging and actual scaling up potentials exist, which need to be addressed. The first chapter is a systematic and critical review on the rapidly growing literatures on all different categories of MDs and their corresponding applications into fabricating functional materials for biomedical applications, including biomedicine, biosensors, imaging, diseases diagnosis, drug delivery and more. In addition to the conventional MDs, various next generation MDs where mixing is far more efficient are reviewed such as vortex fluidic device (VFD) which has been utilized throughout the thesis towards well-controlled fabrication and manipulation of nanostructures.

This chapter will be submitted for publication.

Author contributions: XL performed the literature research, data summary and analysis, and wrote all the primary contents. PS helped with some data collection and summary. WZ and CR provided advice on the review directions to improve the quality of the manuscript. All the co-authors assisted with the revision of the manuscript prior to inclusion in the thesis and journal submission.

Microfluidic devices in fabricating nano or micro-materials for bio-medical applications

Xuan Luo[1,2], Peng Su[2], Wei Zhang[2*] and Colin L. Raston[1*]

[1] Flinders Institute for NanoScale Science and Technology (INST), College of Science and Engineering, Flinders University, Adelaide, SA 5042, Australia.

[2] Centre for Marine Bioproducts Development, College of Medicine and Public Health, Flinders University, Adelaide, SA 5042, Australia.

1.1 Abstract

Nano or micro-sized particles have been a research focus for several decades, and the advent of microfluidic technologies provides alternative advanced strategies for the synthesis of such materials. This review focuses on recent advances of using different microfluidic devices including continuous laminar flow, segmented flow, droplet-based and other microreactors for the synthesis of nano or micro-sized particles with specific properties for biomedical applications. Different categories of particles fabricated in microfluidic devices are summarised to highlight wide applications of these processing platforms in the development of novel functional materials.

1.2 Introduction

In the last 20 years, many groups have employed microfluidic systems to fabricate particles with diameters from nanometers to micrometers, and materials ranging from semicondutors, metals to polymers. This interest is growing because of potential roles of such materials in many biomedical applications including biomedicine, biosensors, imaging, cancer theranostics and drug delivery.[1] In each of these fields, the physicochemical properties of the particles can be systematically exploited to optimize their efficacy in terms of dispersity, stability, compatibility and fluorescent behavior.[1] Materials prepared using conventional techniques can be grouped into two main categories, top-down and bottom-up approaches. The top-down approach involves mechanical breakdown of large-sized materials into micrometer or nanometer-sized particles using a variety of techniques such as sonication, ball milling, plasma, homogenization and pyrolysis.[2] The bottom-up approach involves the condensation of atoms, monomers or molecular components to assemble particles by polymerization, sol-gel reaction, micro-emulsion, co-precipitation, laser vaporization, and metal evaporation. However, materials prepared from these conventional techniques can agglomerate and become oxidized, and the processing itself can suffer from limited control of the mixing, nucleation and growth in scaling up the syntheses. Indeed, multiple purification steps might be required[3] for optimal homogeneity and reproducibility of the final products.[4,5] Furthermore, fast screening and optimization of the fabrication in conventional batch processing is difficult. There is also a need for alternative synthetic approaches to obtain stable monodisperse nanoparticles (NPs) with more controlled fluid transport and reaction, and with defined morphology.

Over the last few decades, microfluidic systems have attracted much attention due to their ability to allow precise and effective control of reaction conditions (such as mixing and temperature) and fluid transport (such as flow rate and residence time), resulting in precise growth control while minimizing the formation of by-products,[6] even in scale-up processes.[7,8] Other advantages of microfluidic systems include simplicity and flexibility in multi-step reaction processing. Microfluidic devices are designed to manipulate fluids in microchannels or microreactors with dimensions of tens to hundreds of micrometers.[1,9] The miniaturization ensures homogeneous reaction environment and efficient heat and mass transfer associated with the large surface-to-volume ratio, and controlled kinetic parameters within a continuous flow regime.[10,7,11] More importantly, reduction in the consumption of chemicals, particularly with toxic, flammable and potentially explosive properties, guarantees a safer operation with special emphasis on environmental friendliness and green chemistry metrics.[12] These microfluidic devices provide fine control of operation during automating multiple syntheses which allows for fast screening and optimization of the parameters for multi-step synthesis parameters.[13] The aforementioned advantages could potentially overcome the limitations associated with most conventional batch processes.[14] Advanced chemical fabrication has been successfully developed using these devices, including in generating metal, semiconductor, inorganic or polymeric and bio-materials,[10] with different morphologies characteristics, as in nanotubes, nanowires, nanoparticles, core-shell particles, quantum dots, microcapsules and composites (Figure 1.1).

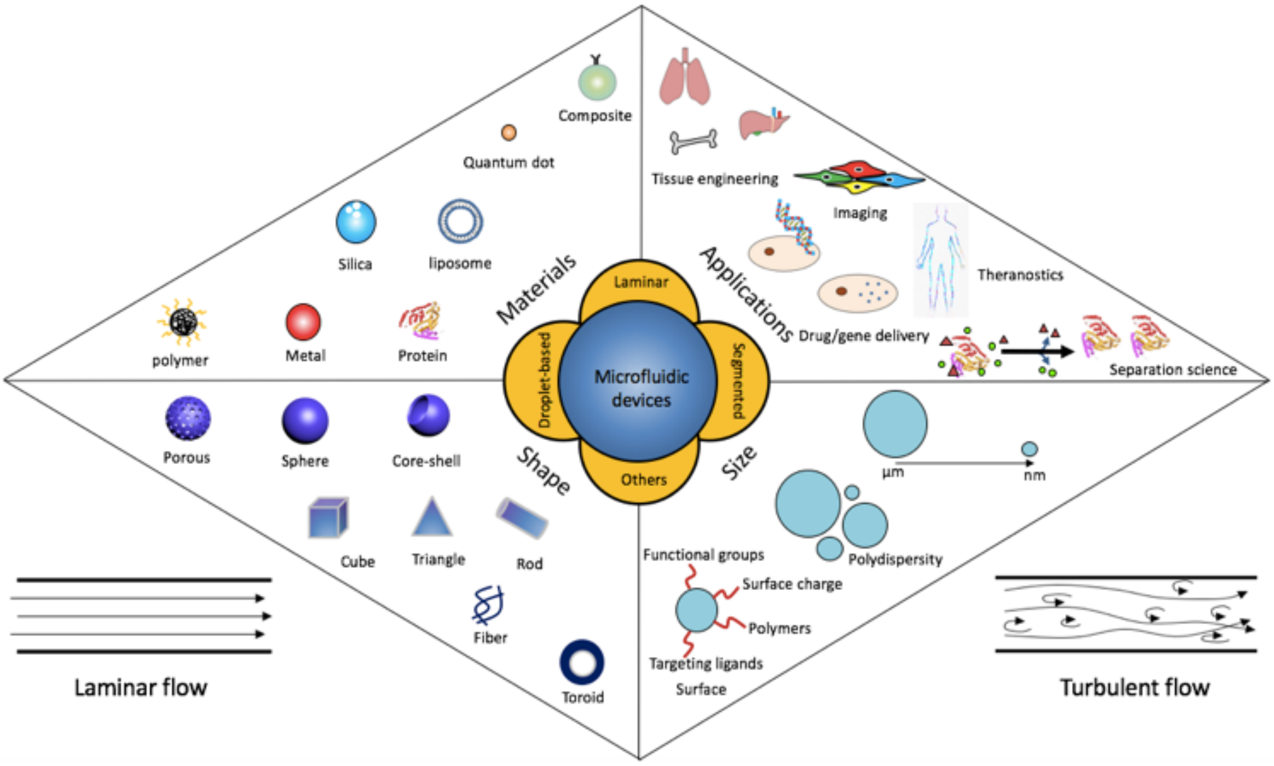

Figure 1.1 *Fabrication of nanoparticles using microfluidic devices and their biomedical applications.*

Microfluidic devices have already been intensively reviewed in the area of single-step reactions, materials synthesis, multi-step reactions, organic materials such as liposome, hydrogels and polymer-based analogues.[15,10,13] Even though micro- or nano-particles have been synthesized through various microfluidic devices, the application of these materials in biomedical applications needs to be further explored. From more than 250 literatures we have been reviewed on fabrication using microfluidic devices, few of them investigated the application in the area of biomedical research. In this review, we contribute to the field in a distinct way, primarily focusing on the research and development of different types of microfluidic devices and biomedical applications of the fabricated nano or micro-sized particles. The review illustrates the versatility of such devices for use in emerging areas of biological engineering, biomedical studies, and diagnostics. The high particle quality required in biomedical applications can supersede the need for large quantities, and the quality standards required for particle synthesis and devices are consequently also raised. We do not discuss the fluid mechanics of liquids nor the fabrication of multiple immiscible phases to form micelles, emulsions, or droplets which have been discussed elsewhere.[16,17] In the first section, an overview of current established microfluidic reactors is provided along with the flow synthesis of various kinds of particles, including metallic and polymeric particles, quantum dots (QDs), silica based nanoparticles, and hybrid composites. The specific applications of the fabricated particles in biomedical applications are also discussed.

1.3 Classification of microfluidic synthesis systems

Microfluidic flow synthesis can be divided into chip based and tubular systems, which can be further classified into nanofluidic, microfluidic and milifluidic systems.[7] Based on the flow type, there are three main categories: (i) continuous laminar or single phase flow devices, (ii) segmented or multiphase based flow devices and (iii) droplet-based flow devices.[10,1] Three main microfluidic devices work under different principles with advantages and disadvantages, and the choice of a device depends on the processing requirements and the nature of the product.

Microfluidic devices are constructed using various materials, depending on the application.[10] Polymer, silicon, glass, stainless steel, metal, plastic[18] have all been used to fabricate microfluidic devices;[1] those made of silicon or glass are advantageous because they can tolerate a broader range of application conditions and have the advantages of low cost.[19] Typically syringe pumps or microfabricated pumps were employed to drive and to control the fluid flow in the microchannels. Reagent solutions are manipulated inside microfluidic devices by either active or passive control.[20] Active control involves applying external forces including electric field, magnetic field, optical force, and heat to control the flow movement in microchannels, which provides more flexibility of the flow pattern. Passive control has the movement of the fluid simply controlled by the channel geometries and or liquid flow rates, which prevents the system complexity and biodegradation arising from the external forces.

1.3.1 Single-phase or laminar flow devices operating under continuous flow

Continuous laminar flow based microfluidic devices are easy to design, manipulate and scale-up, with improved production of uniform nanoparticles.[1,21] Most reports of nanoparticle synthesis in microfluidic devices have discussed a diffusion-based laminar flow synthesis in which continuous streams of fluids flow through microchannels where nucleation and growth of the particles take place.[2] Multiple fluid flows of different compositions and concentrations are pumped into the microfluidic systems through microchannel inlets (Figure 1.2a). In these laminar flow-dominant microfluidic devices, mixing is a key process to control for optimisation of the products. A serpentine micromixer can be employed to enhance the length of the channel, which has been employed for the synthesis of Au nanoparticles in a ceramic microfluidic system.[22] Raw materials can be loaded together, and then flow through a single coiled capillary reactor[23,24,25] (Figure 1.2c) or separately loaded with the flowing liquids mixed using a y-shaped microfluidic device[26,27] (Figure 1.2b). The former set-up is easier to use in making silver,[28,29] gold,[30] and Au-Ag bimetallic[31] nanoparticles with minimal risk of particle attachment and channel clogging. However, it lacks operational flexibility (such as the ratio of premixed reagents) which is required for complex processing.[26] The latter set-up simplifies the operational process by installing multiple inputs and is commonly used in chip-based microfluidic systems,[32] which can be two-in/one-out Y shaped.[33,34] Here the precursors are delivered into separate flows and combined in the mixing chamber or miniature convective mixer[35,36,37,38,27] before they reach the heated reaction section. The presence of mixing was necessary to prevent the formation of clusters over a long period of reaction.[35] Such devices have been used to fabricate cysteine-capped CdS QDs.[34] Laminar flow-based multiple phase co-axial flow-based systems (Figure 1.2d) are widely used in fabricating microfibers for various materials. Poly(dimethylsiloxane) PDMS-based co-axial flow microfluidic devices contain a capillary glass pipette and the sheath and sample flow enables the control of continuous synthesis of microfibers, without clogging.[39] The utility of this approach in tissue engineering application was demonstrated by encapsulating cells and proteins within microfibers, which is discussed further in later sections. Fluid streams flowing in the opposite directions can be combined into laminar flow with sharp and well-defined interfaces.[16] Single phase microfluidic synthesis occurs either in a single-liquid phase or in a multiple-miscible-liquid phase. The reaction is generally preceded by a mixing step that rapidly and uniformly distributes the reactant molecules within the microchannel cross section.

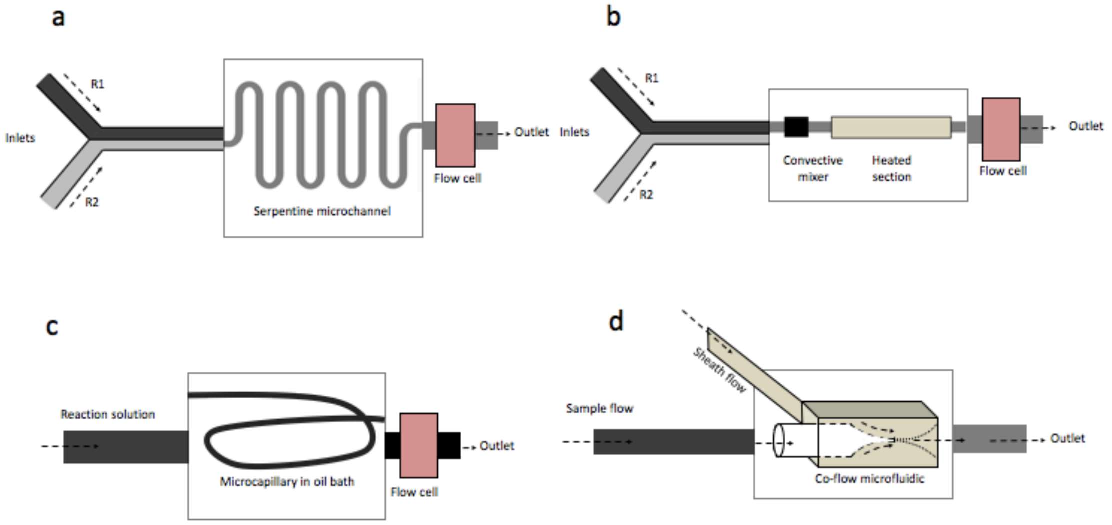

Figure 1.2: *Schematic of continuous laminar flow-based synthesis using (a) a single capillary, (b) a single capillary, immersed in a heated oil-bath, (c) a y-shaped microfluidic device or continuous co-flow microfluidic device made out of coaxially aligned borosilicate glass capillaries, and (d) a co-axial flow-based system.*

Continuous laminar flow microreactors have been widely applied in nanoparticle synthesis, including in fabricating CdSe and CdSe@ZnS core-shell particles.[24,38] Due to the laminar flow of the reaction solution, the system is relatively static, therefore, the mass transfer is not fast and efficient enough such that the particles can grow continuously as in the batch reaction systems. Various strategies have been developed to tackle this problem. Yang *et al*.[36] improved heat and mass transfer and the size uniformity by using a two-temperature approach - high temperature to burst nucleation and low temperature to promote growth. Other than convective micromixers, pneurmatic micromixer[40] are also integrated in different microfluidic devices for improved mixing. In addition, microfluidic devices offer a better approach for surface functionalisation. A surface-capping layer of ZnS or CdS nanoparticles increases the quantum yield (QY) of CdSe QDs,[41] and a one-step integrated thermoplastic-based microfluidic device with multiple geometric microchannels has been used for *in situ* synthesis of ZnSe/ZnS core/shell QDs (Figure 1.3c).[18] For precise fabrication, each section of microchannels have specific roles, (1) mixing of precursor, (2) formation of ZnSe core and (3) coating ZnSe cores with ZnS shells. In addition to *in situ* functionalisation, some studies also report on the precise control of the layer thickness by direct adjustment of the residence time. Varying the residence time can lead to ZnS-layer thickness within 1 nm, which results in high fluorescence QY of above 50%.[24] With precisely controlled residence time, Luan *et al.*[38] utilised a triple-ligand system (trioctylphosphine oxide-oleic acid-oleylamine) to synthesise small sized CdSe@ZnS core-shell structures with QY up to 70% relative to commonly reported *ca.* 10%. Laminar flow-based microfluidic devices are also widely used for size and morphology manipulation. Increasing the reaction temperature from 150 to 300°C offers the control of the shape of CdSe particles, as angular, tripodia, irregular polygon, and spheres, all having unique spectroscopic properties.[42] For improved emitting property qualities, shape and size controls, most recent research focuses on integrating microchannels with different geometries, involving Y-channels, serpentine channels and capillary microchannels.[43,44] Even though many studies have realised the continuous synthesis of CdSe QDs at atmospheric pressure, one difficulty of these procedures is the requirement of solvents that can both dissolve the precursors at ambient conditions and also remain liquid over the entire operating temperature range (25-350°C).[45] Marre *et al.*[45] incorporated supercritical continuous high-pressure (at 5 MPa) and high-temperature microflow for the synthesis of CdSe QDs (Figure 3a). The supercritical phase of hexane at 270°C overcomes some limitations (high-boiling-point, high viscosity and low diffusion), leading to higher super-saturation and narrowing the size distribution of the QDs, with improved reproducibility. In recent few years, research on fabricating semiconducting QDs has focused more on the development of synthesis methods adopting the principles of green chemistry, on-line monitoring and industrial production. Yang *et al.* integrated a laminar flow microfluidic device with a femtosecond laser ablation process,[46,47] for the pH-dependent synthesis of polyethyleimine coated ZnSe QDs micelles (40-80 nm) (Figure 1.3d). Femtosecond laser ablation in liquid has attracted considerable attention since it exhibited great potential in 'green' synthesis of nanomaterials.[47] Toyota *et al.*[48] and Swain *et al.*[49] have developed combinatorial systems using parallel multiple-microreactors with online photospectrometer and computer controlled programmable pumps for rapid CdSe NP synthesis (Figure 1.3b), for higher reproducibility of kinetic control with improved automatic production for industrial scale up. The average time for one reaction, from sample preparation to obtaining the PL spectra, is only 10 min.[49]

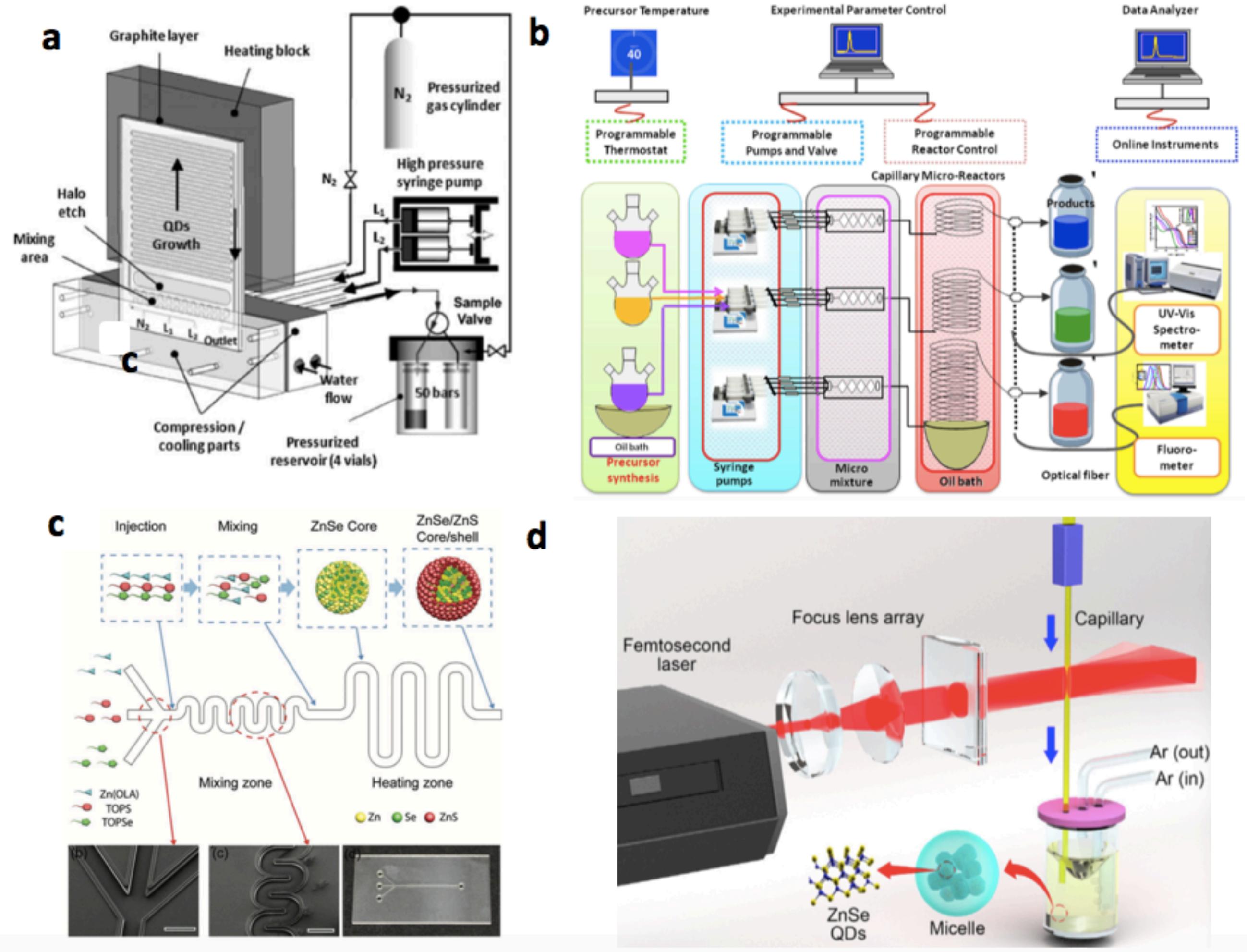

***Figure 1.3**: (a) High-pressure and high temperature microflow synthesis of CdSe QDs.*[45] *(b) Combinatorial synthesis of CdSe nanocrystals for industrial up scaling.*[48] *(c) Schematic illustration of ZnSe/ZnS core/shell nanoparticles involving three major sections for mixing the precursors, formation of the ZnSe core particles and coating with ZnS.*[18] *(d) Schematic diagram for the synthesis of ZnSe QD micelles.*[47]

Apart from semiconducting nanoparticles, laminar continuous flow-based systems have also been used to fabricate Ag,[2,50,51] palladium,[52] Au,[53,54] Fe,[55,56] and polymeric particles.[57,58,59] Carboni *et al.*[2] controlled the synthesis of Ag nanoprisms using $NaBH_4$ (reducing agent), $AgNO_3$, trisodium citrate dehydrate (capping agent) and H_2O_2 (oxidising agent), using a flow focusing microreactor, demonstrating for the first time that the optical properties of triangular shaped silver nanoprisms can be tuned in a microreactor without a seed mediated approach (Figure 1.4a). A more recent study by Wang *et al.*[60] demonstrated the morphology-controlled synthesis of silver nanoparticles (bundles of belts, twisted fibers, clusters, and microspheres) decorated poly(o-phenylenediamine) by simply adjusting the shear rates. As mentioned above, laminar flow-based multiple phase co-axial flow-based systems are widely used in fabricating microfibers. Hwang *et al.*[57] used a phase inversion process to precipitate a stream of poly(lactic-*co*-glycolic acid) PLGA within a microfluidic system for the generation of 3D tissue engineering scaffolds. By adjusting the flow rate of the core solution (PLGA) and sheath solution (glycerol), microfibers were formed with diameters ranging from 20 to 230 µm. Recently, various biopolymers have been extensively studied using this approach because of their excellent biocompatibility and low toxicity in biomedical applications. For example, human hepatocellular carcinoma cell-laden chitosan-alginate fibres were produced using a coaxial flow microfluidic chip, affording higher cell viability and better adhesion efficiency (Figure 1.4b).[61] Apart from nanoprecipitation, particle morphology can also be locked-in via UV-initiated photo-polymerisation.[58] Lewis *et al*.[62] demonstrated the fabrication of hybrid microparticles composed of functionalised tobacco mosaic virus directly embedded in polymeric hydrogels (Figure 1.4d). Microchannels ensure a uniform distribution of UV energy which significantly improves the UV polymerisation efficiency, affording precisely structured hybrid microparticle (~50 µm diameter). The manipulation of the morphology of microfibers can be achieved in a variety of ways, such as in *in situ* formation of CO_2 bubbles, which results in asymmetrically porous polyurethane microfibers or Janus microfibres.[63] Another way to prepare well-defined nanoparticles is through multistep reactions by integrating multiple microfluidic channels, such as demonstrated by Shiba *et al.* in the fabrication of hierarchical hybrid silica/titania-based nanoparticles (Figure 1.4c).[64] This four-stage reaction (titania nucleation, aggregation, silica encapsulation and growth) ensures titania nuclei are pre-formed and utilised as seeds before the sol-gel reaction can occur. The functionalised nanoparticles can be coated onto the surface of a quartz crystal microbalance electrode, showing five times enhanced sensitivity to water vapour compared to a commonly used polymer, PVP.

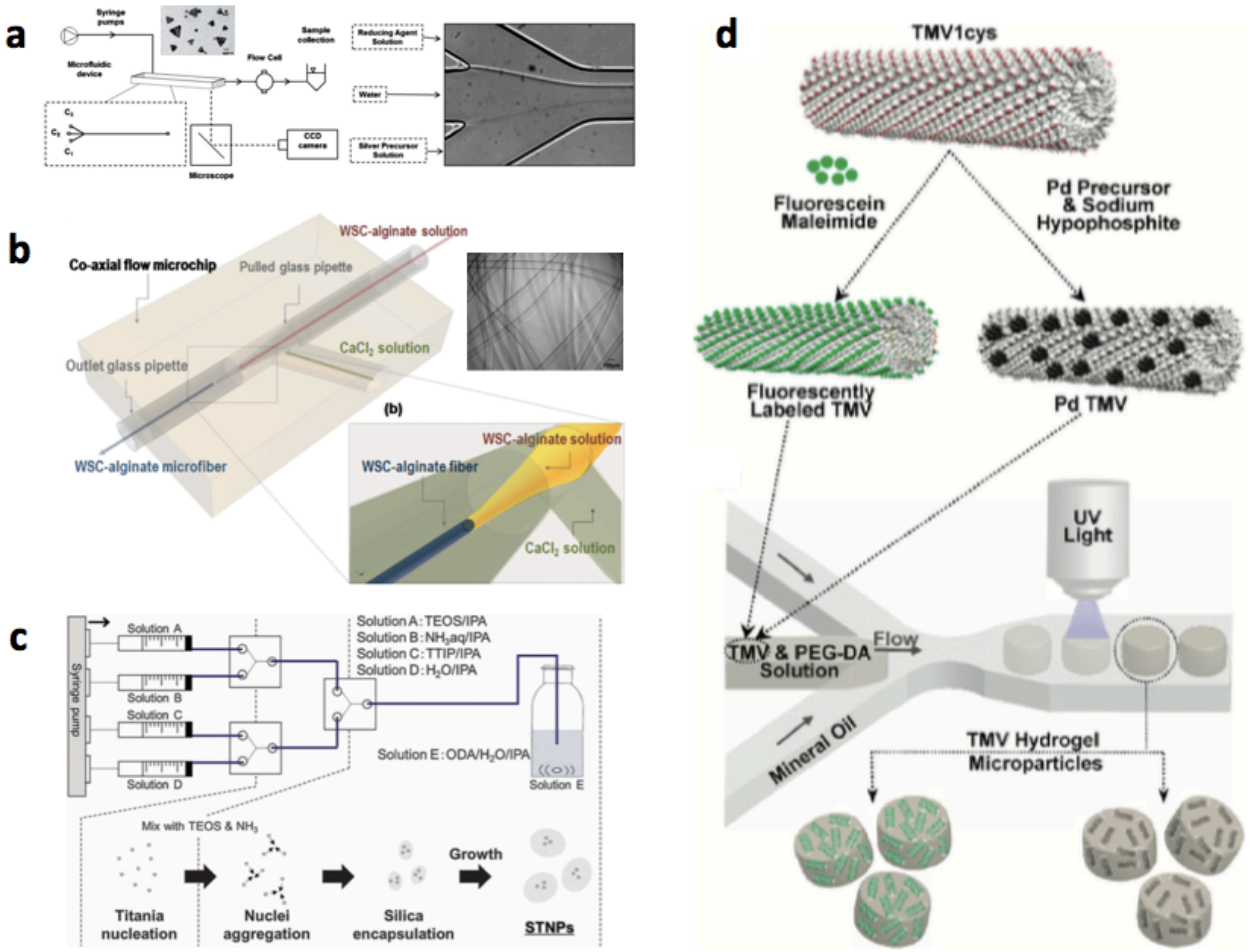

Figure 1.4: *(a) Schematic of a flow focusing device with co-flowing streams for generating silver nanoprism.*[2] *(b) Schematic of a co-axial flow microfluidic device for generating chitosan-alginate microfibres.*[61] *(c) Synthesis of silica-titania hybrid using multistep laminar continuous flow microfluidics.*[64] *(d) Fabrication of microparticles containing fluorescently labelled TMV or palladium-TMV complex using a microfluidic flow-focusing device.*[62]

1.3.2 Segmented flow devices

In single-phase laminar flow, diffusion is the only means of mixing. The inherent problems associated with continuous laminar flow microreactors can be solved to a certain extent using segmented flow microreactors.[14] Here, in a typical design, multiple reagents in liquid phases are introduced into the microchannel through inlets (Figure 1.5). There are two main types of segmented flow microfluidics, liquid-liquid or gas-liquid, which are differentiated on the basis of where the reaction takes place. For liquid-liquid segmented flow, discrete liquid droplets are encapsulated at the nanoliter scale by an immiscible and inert carrier fluid which wets the surface of the microchannels and segments the flow with regular spacing of moving interfaces (Figure 1.5a).[65] The term ‘plug’ is used for the droplet from the dispersed phase in which the reactions occur.[7] In these diffusion-determined mixing systems, particles near the wall spend more time in the reactor than those in the center which results in broad residence time distribution (RTD).[19] Other challenges include difficulties in subsequent addition of reagents into discrete droplets[66] and withdrawing of small aliquots without disturbing the system flow.[19] A gas-liquid segmented microfluidic reactor has a compartmentalized liquid 'slug' separated by discrete gas bubbles (Figure 1.5b), being useful for confining reactions in liquid segments.[7] In these systems, internal circulation within discrete liquid slugs brings material from the wall to the centre of the microchannel, which facilitates convective mixing and efficient mass and heat transfer with narrow RTDs and narrow size distributions.[67] More importantly, inert (N_2), oxidizing (O_2) or reducing (CO, H_2) gases can be introduced, depending on the reaction, leading to different morphologies and crystalline structures in high yield and high reproducibly.[68] Additionally, it is possible to inject additional reactants or withdraw reaction aliquots in a continuous and controllable manner. However, the reaction takes place within the liquid slugs that form the continuous phase in which reagents are exposed to the surface of microchannels. This can result in cross-contamination in the reaction.[69] These problems can be avoided to some extent by increasing the hydrophobicity of the microchannel walls.[70] Extra mixing sections can be added depending on reaction requirements, for example winding channels,[1] which help the mixing process on a sub-millisecond time scale associated with chaotic advection.[71]

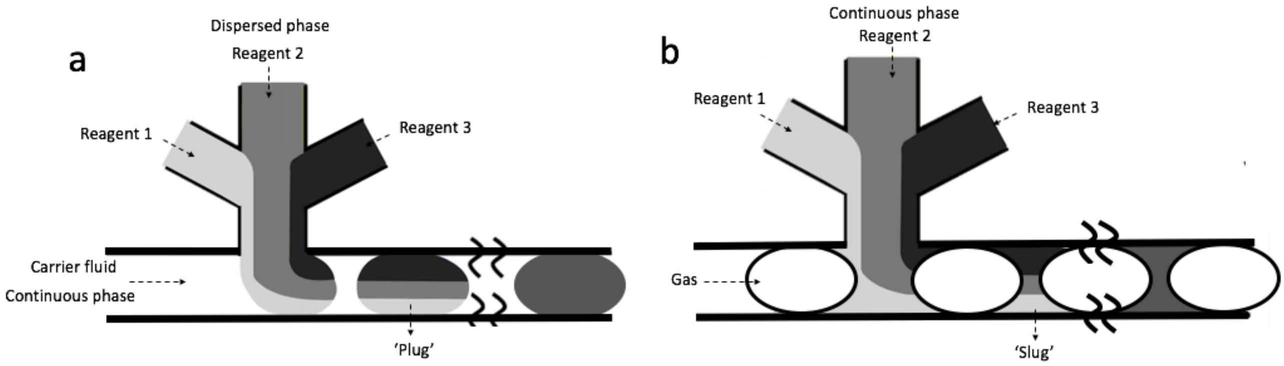

***Figure 1.5**: Segmented flow in microfluidic channels: (a) Discrete liquid plugs encapsulated by an immiscible continuous phase, and (b) liquid slugs with the continuous phase separated by immiscible discrete gas bubbles.*[7]

Variations on flow and shear stress generated by segmented flow systems can lead to significant changes on morphology and crystallinities of the material. These changes can be unique relative to those formed by conventional bulk methods or processing conducted under single phase laminar flow devices. For example, the crystallinities, dimensions and morphologies of polycaprolactone-*block*-poly(ethylene oxide) (PCL-*b*-PEO) nanoparticles change with flow rate in a segmented microfluidic device, but is not observed in a single phase laminar microfluidic device (Figure 1.6a).[72] In general, segmented flow microfluidics have been used for the synthesis of a variety of monodispersed nanoparticles including semiconducting QDs,[19] metal nanocrystals (Pt,[73] Fe,[68] Au,[74] Ag,[75]) and their composites[76] polymer nanoparticles[77,72] and metal organic frameworks (MOFs).[78,79] When performing the synthesis in liquid-liquid segmented microfluidics, Arndt *et al.*[75] accelerated the rate of formation of Ag nanoparticles by a factor of four (30-150 s) compared to batch processing, with diameters ranging from 7 to 120 nm. Clogging of the system can be effectively prevented by using ethylene glycol and hexadecane biphasic segmented system relative to ethylene glycol as a single phase. The continuous synthesis of CdSe QDs at ambient pressure is usually reported using single-phase laminar flow microreactors.[23] However, a requirement of such processing is covering the operating temperature form 25°C to 350°C which significantly limits the choice of solvents, ligands, and precursors that are compatible with continuous flow systems. Furthermore, the solvents that are available typically have high viscous, leading to slow mixing and broad RTD,[45] and as a consequence, broad QD-size distributions. Gas-liquid flow is preferable for performing reactions at elevated temperatures, as most solvents experience increased miscibility with increasing temperature.[67] The application of gas-liquid segmented flow for the continuous synthesis of narrow size distribution CdSe QDs has been developed by Yen *et al.*[67] Here, a silicon-based microreactor was operated with multiple temperature zones (>260°C, <70°C), with enhanced mixing and narrow RTD characteristics of the particles, resulting in significant improvement in reaction yield, size distribution and shorter reaction timescale, in contrast to single-phase devices. Apart from thermal energy input, reactions conducted in gas-liquid segmented flow systems can be facilitated by introducing microwave irradiation. Albuquerque *et al.*[78] synthesized MOF-74(Ni) in a continuous flow microwave-assisted reactor under mild conditions of pressure (~2.5 bar), resulting in high yield, at ~90 g h^{-1} L^{-1} with 96.5% conversion of reagents (Figure 6c). High yields can be achieved in minutes, as opposed to days for traditional batch synthesis, with excellent control over the properties and crystallinity of the material. Ultrafast crystallization was also reported by Paseta *et al.*[79] on fabricating dicarboxylate based MIL-88B type MOFs. The size of the particles can be controlled in the 90 to 900 nm diameter range with relatively narrow crystal size distributions, residence times as short as 20 s, depending on the MOF type and processing conditions. Depending on the reaction, the choice of gas slugs can affect the properties of final product. For example, by varying the composition of the gas segments (H_2, N_2, O_2 or CO), the crystalline phase (magnetite, feroxyhite, goethite), size and shapes (octahedral, nanoflake, platelet, nanosheets, nanobars) of the resulting iron oxide nanoparticles can be accurately tuned.[68] Sebastian *et al.*[73] fabricated Pt nanocubes, Pd nanorods and Pd trigonal and hexagonal nanosheets, using the same gas-liquid segmented microfluidic device, with a change of gas between N_2, O_2, CO leading to a change of morphology (Figure 1.6b). Even though segmented flow microfluidic devices demonstrate better mixing than single phase laminar flow, mixing might still be insufficient for certain reactions, necessitating the use of other mechanical energy such as a ultrasonic bath[68] (Figure 1.6d).

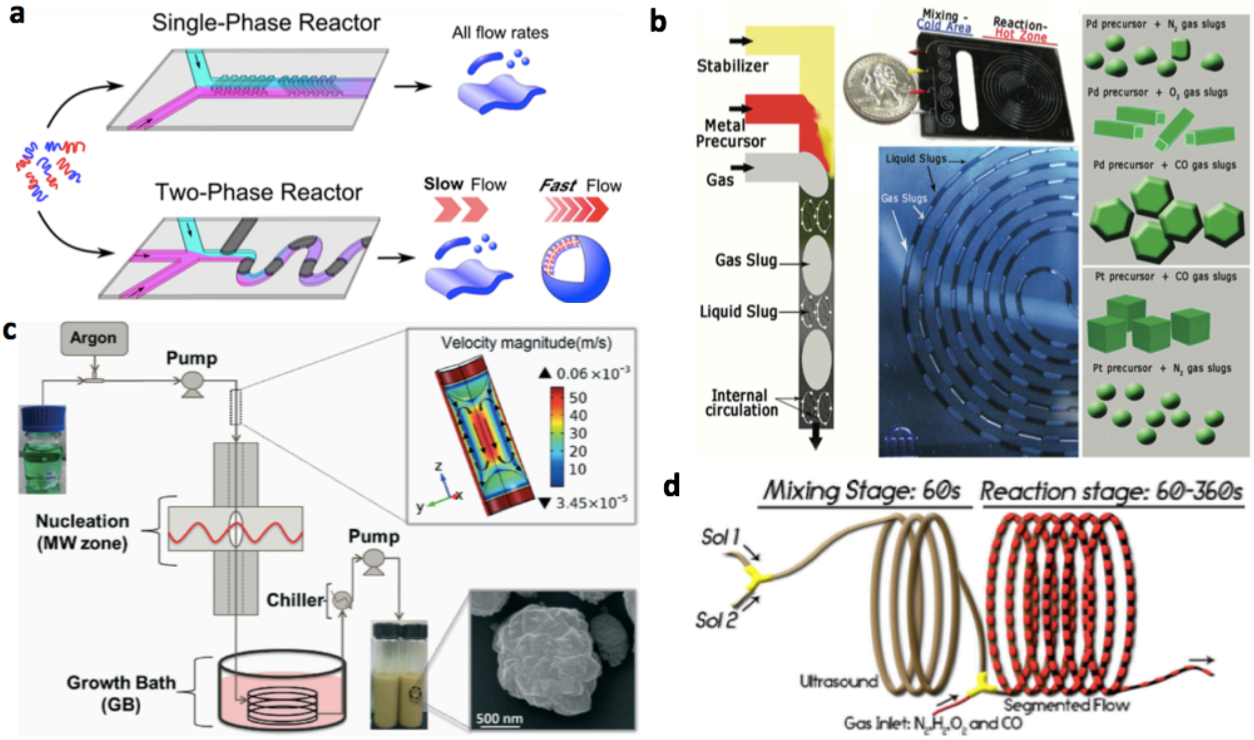

***Figure 1.6**: (a) Schematic of single phase laminar flow and two phase segmented flow synthesis of PCL-b-PEO polymeric nanoparticles[72] (b) Schematic of the gas-liquid segmented flow and internal circulation and the summary of nanomaterials obtained under different gas environment.[73] (c) Schematic of the segmented continuous flow microwave-assisted synthetic reactor for fabricating MOF-74(Ni).[78] (d) Schematic of the gas-liquid segmented microfluidic device to produce magnetic nanoparticles.[68] The mixing stage is irradiated by ultrasound waves, and the reaction stage is where the gas slugs are introduced.*

1.3.3 Droplet-based flow microfluidic systems (two-phase flow devices)

Single-phase microfluidic devices are restricted to slow diffusive reagent mixing, parabolic velocity profiles and broad RTDs, which are detrimental to generating a narrow particle size distribution.[67,14,80] As mentioned above, conducting reactions at elevated temperatures in such devices can address some reproducibility issues.[81] Segmented flow microreactors suffer from physical contact of the reagents and the side microchannels, which can lead to cross-contamination of the product.[1,14] These limitations are addressed in droplet-based microfluidic systems, where there is improved mixing efficiency and better control over the concentration of reagents, which is difficult in laminar flow-dominant microfluidic devices.[65] The majority of microfluidic methods produce droplet diameters ranging from a few micrometers to hundreds of micrometers in a uniform, evenly spaced, continuous stream with the volume ranging from femtolitres to nanolitres.[82] Droplet-based microreactors are one type of multiphase flow microreactor. Figure 1.7 summarises the typical droplet break up events in the generic droplet-based microfluidic geometries, including T-junction, cross-flowing,[83] co-flowing and flow focusing devices.[82] T-junction microfluidic devices were first developed by Thorsen *et al*.[84] in generating reverse micelles varying from monodispersed droplets to helices and ribbons. A T-junction has relatively simple geometries, with the size of the droplet depending on the width of the channel and flow rate.[85] In general, dispersions of the fluid phase (DP) involves injection into a microchannel using a pressure-driven flow (Figure 1.7a). A second immiscible liquid (CP) is driven into a separate microchannel using an independently controlled flow. The two streams meet at a junction, at which the DP extends to form a ‘finger’ or ‘jet’. The geometry of the junction and the shear forces from the cross flow determine the local flow field, which deforms and breaks up the interface. In ‘co-flowing’ geometry, both CP and DP streams flow together with the CP surrounding the DP, which decays into droplets via Rayleigh-Plateau instability.[86] In ‘flow focusing’ geometry, the streams of DP flow in the central channel which is symmetrically pinched by the CP in the outside channels. These are normally focused through a small orifice, which leads to viscous stress action and finally pinch-off of the droplets. CP can be pumped into the device in the same, perpendicular, angled or opposite directions of the DPs (Figure 1.7d).[87] The cross flow capillary device was developed for delivering DP perpendicular to the tube through which the CP flows (Figure 1.7c),[87] with the droplet generated through interfacial polymerisation. The demand on the fabrication and operation of co-flow and flow-focusing devices are higher compared with T-junction geometry, having more complex channel geometries and more fluidic inlets. In addition, flow-focusing geometries allow variation in the effective geometry by adjusting the flow rates of the dispersed and continuous phases, thereby offering flexibility in the droplets size.

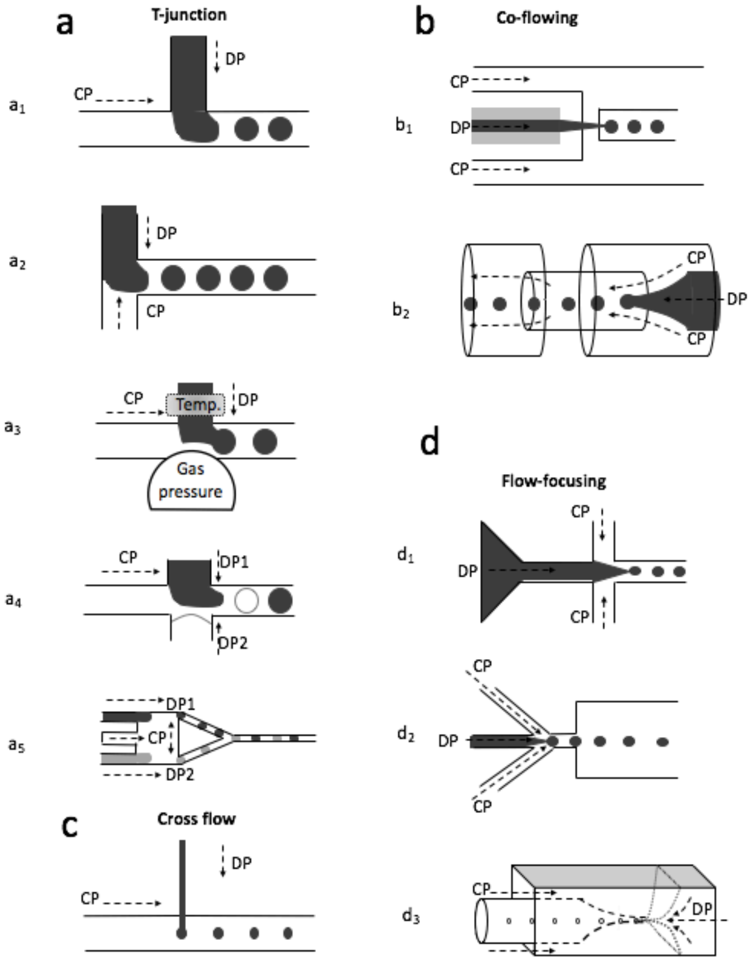

***Figure 1.7**: Schematics of various droplet-based microfluidic devices. (a) T junction: a_1 regular T-junction geometry where the DP is perpendicular into CP; a_2 'Heat on' where the DP and the CP are from opposite sides; a_3 'Active T-junction' which has air pressure or temperature control over the DP; a_4 and a_5 double T-junction for synchronised generation of two types of droplets.[86] (b) Co-flow geometries: b_1 standard co-flow; b_2 axisymmetric co-flow (c) Cross flow geometry[87] (d) Flow-focusing geometry: d_1 and d_2 standard flow-focusing;[88] d_3 co-axial flow focusing.*

Flow-focusing[89] and T-junctions[66] geometries were developed to synthesize semiconductor nanoparticles in droplets and while both methods require sophisticated flow rate control to generate different sized droplets, some T-junctions require a separation stream to prevent mixing of reactants before droplet formation. Combining several geometries, such as integrating a flow-focusing microchannel with T-junction, has also been reported for more complicated reactions, in forming composite materials. For example, size-controllable QD-doped hydrogel microparticles were constructed by shearing sodium alginate solution into microdroplets and *in situ* gelating these droplets into a hydrogel matrix to encapsulate CdSe/ZnS QDs.[90] The application of these QD-encoded microparticles demonstrated the potential practicability in multiplexed biomolecular detection. Thus far, a diversity of other nanoparticles have been prepared using droplet-based microreactors, including polymers,[91,92,93] metal nanocrystals (Pd,[94] Fe,[95] Ag,[96] Au[4]), MOFs,[97,98] and silica.[99] Reactions occur in the micro-droplet and can be used for epitaxial growth of particles with different shapes, including branched gold nanostars.[4] Similar to gas-liquid segmented flow, the capability of shape control conducted in droplet-based microreactors can also arise from the restrictions imposed by the carrier phase. Using air as the carrier phase for the droplets, nano-sized Ag cubes and octahedra with controlled sizes can be continuously generated using droplet microreactors.[96] In addition to forming metallic nanoparticles, these devices also apply to manipulating the morphology of silica particles. Zhao *et al*.[99] synthesised monodispersed hierarchical silica microparticles with raspberry-like surface morphology, from uniform droplets of a mixture of two solutions of a silica sol and $NaHCO_3$ aqueous solution (Figure 1.8c). This process is in a T-junction microchannel and the surface morphology can be easily controlled by adjusting the reaction between HCl and $NaHCO_3$. Other morphologies of silica-based particles are accessible using this type of device, including spheres,[100] rod-like,[101] doughnut-shaped,[102] mesoporous, core-shell and hollowed.[103] The use of microdroplets rather than single-phase continuous flow avoids a critical issue of channel clogging in presence of solid particles such as MOF. HKUST-1, MOF-5, IRMOF-3, UiO-66, Ru_3BTC2 and their composites were efficiently synthesised via solvothermal reactions with substantially faster kinetics relative to conventional batch processing (Figure 1.8b).[97] Moreover, adjusting the hydrophobicity of the microchannels, and the number of coaxially aligned transition capillaries,[104] allows access to droplet or droplet inside another droplet (Figure 1.8a). The complex systems with dispersed droplets containing smaller droplets inside find use in drug delivery, foods, cosmetics and autonomic self-healing materials. A wide range of polymer particles have been synthesised using this system, as solid,[105] crescent[106] and hollow[107] shaped particles. Anisotropic particles have potential as imaging probes for therapy and drug carrier. Monodispersed toroidal particles have been prepared by solidification of droplets of different polymer solutions in a microchannel.[93] More recently, the device has been applied in mass-production nanoliter-sized biphasic Janus droplets, which consist of a biconvex segment of a photocurable monomer and a concaveconvex segment of a non-curable silicone oil containing a surfactant (Figure 1.8d).[108] The prepared biconvex lenses, depending on the processing conditions, exhibited different focusing capability with potential application in miniature optical devices. Droplet-based processing simplifies a lot of reactions that cannot be easily achieved using other types of microfluidic devices, especially in the context of material processing in tissue engineering areas. Using alginate microgels, for example, the droplet formation and the gelation reaction must be separated. Here Ca^{2+} ions are delivered to the alginate without inducing unintended gelation or clogging prior to droplet formation.[109] Droplet-based microreactors require consideration of the geometric design for the generation of droplets, to facilitate scale-up of the process.[14] Several strategies have been developed to increase droplet productions rates, including parallelised droplet production combining up to 96[110] or 128[111] co-flow geometries.

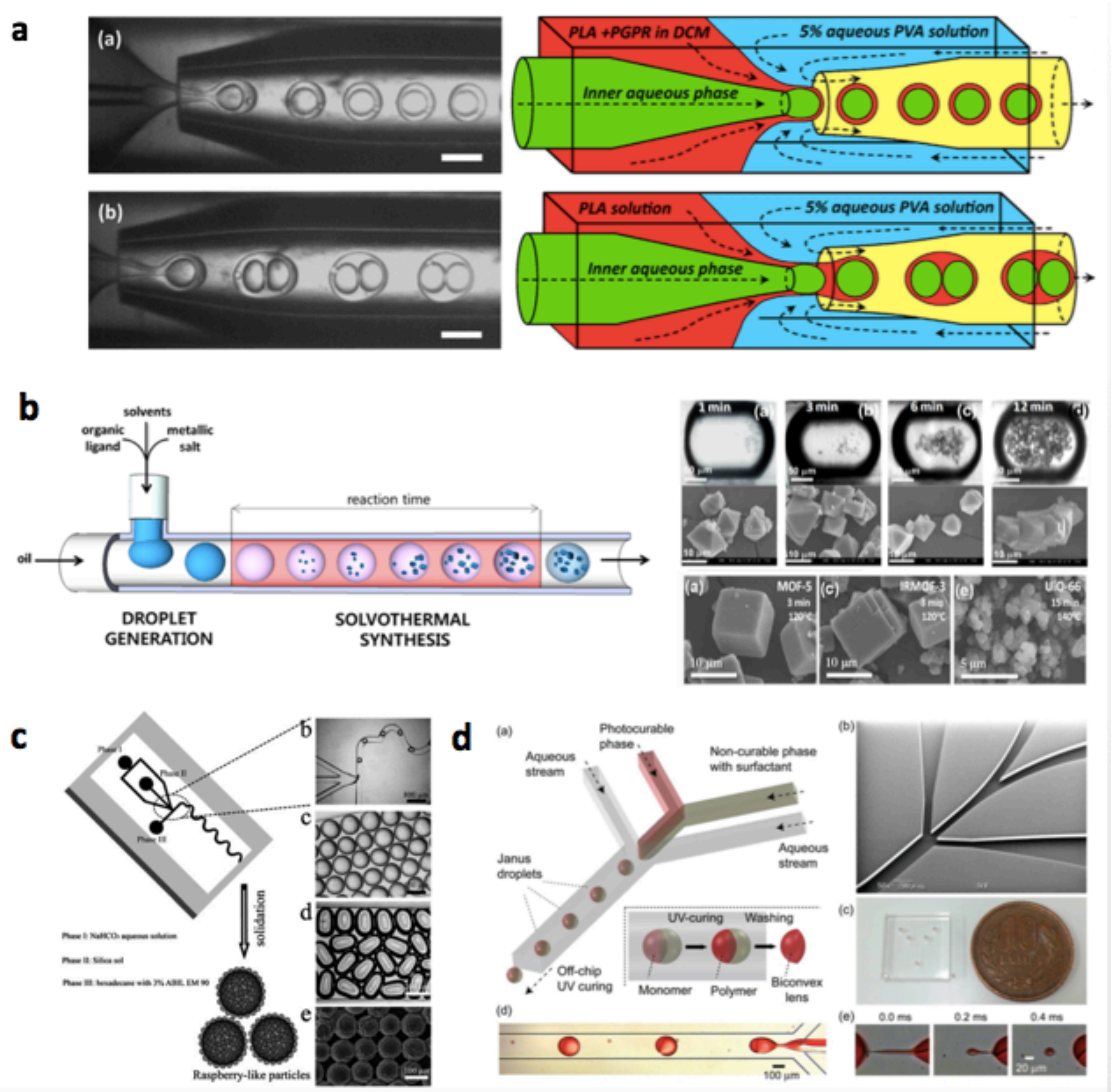

Figure 1.8: *(a) Concurrent/countercurrent flow focusing streams in coaxial assemblies of glass capillaries in generating polylactic acid (PLA) single core microdroplets and dual core microdroplets*[106] *(b) Schematic representation of the synthesis of MOF crystals using a droplet-based microfluidic device*[97] *(c) Droplet-based microfluidic fabrication of raspberry-like silica particles.*[99] *(d) Microfluidic production of polymer Janus and polymerised biconvex particles in a sheath-flow channel.*[108]

1.3.4 Microfluidic-based microreactors

Research on the synthesis of a diversity of micro and nanomaterials in different chip-based microfluidic devices have highlighted the potential of these technologies in the area of material processing. However, there are still some problems and challenges, including constant system clogging, fouling, insufficient premixing and scaling up. The next generation of devices or microreactors are likely to be specific application-directed and will further develop towards more integrated, automated, modular, and multistage microsystems, incorporating real time, andin time processing.

1.3.4.1 Tubular microreactors

Micro-scale reactors or tubular microreactors as an alternative to single phase chip-based microfluidic devices consist of mixcromixers, capillaries or tubes and junctions and have been used in the synthesis of various nanomaterials, including SiO_2,[112,113] quantum dots,[114] CDs,[115] polymer nanoparticles,[116] MOF[117] and metallic nanoparticles.[118] Small tubings (diameter 0.2-1.5 mm) applied in these microreactors results in large surface area-to-volume ratios and also affords a precise control of reaction temperature, residence time and generation of nanoparticles with narrow size distribution as in chip-based systems.[112] One desirable characteristics is their inherent continuous nature and the high potential of scaling up because of tolerating large flow rate differentials.[88] However, the microfabrication techniques required to build or weld such systems are normally expensive and complicated. The stacking of multiple microreactors or modification of a finished microreactor are not always straight forward and economically viable.[112] To solve this issue, research investigated into connecting commercially available ethylene tetrafluoroethylene (ETFE) tubes, and polyether ether ketone (PEEK) connectors for micromixing, which significantly minimises the microfabrication process and increases the replaceability (Figure 1.9a).[113] Tubings could be easily cutted or extended to desirable length to adapt the residence time based on the reaction. Depending on the reaction, other common materials for tubings and connectors are stainless steel, polytetraluoroethylene (PTFE), polydimethylsiloxane (PDMS)[115] and silicone.[118,88] Different from chip-based devices where the reaction is mostly limited by the diffusion control, the set-up flexibility of tubular microreactors allows to include turbulent conditions into the system for a highly efficient micromixing that leads to high supersaturation and kinetically controlled aggregation of hydrophobic compounds.[119] Mejia-Ariza *et al.*[120] used a multi-inlet vortex mixer (MIVM) to form supramolecular gold aggregates, which demonstrated a robust and scable process with high loading capacity relative to laminar flow microfluidic devices (Figure 1.9c). Other type of micromixers reported in tubular microreactors include convective mixer (Figure 1.9e),[121] slit interdigital micromixer,[112] central-collision-type micromixer or K-M mixer (Figure 1.9f).[122,123] All these micromixers share a similar ultimate goal of breaking the fluid flow, shorten the diffusion distance and therefore achiving a better mixing performance. For example, the mixing time of the central-collision-type microreactor at a flow rate of 10 mL/min is 0.3 ms, which is 100-1000 times shorter than a Y-shaped mixer with a millimetre-scale channel.[123] Compared to the one-phase continuous flow synthesis, droplet microreactors effectively eliminates the spread of reagents along the flow tubings, which is similar to chip-based droplet microfluidic devices (Figure 1.9b). Mixing zones as an alternative to micromixing connectors are designed to introduce chaotic advection and recirculation of reagents in order to enhance mixing on droplet basis.[124] Mixing zones could be driven by pressure, electrical, magnetic or thermal fields and have been designed into various shapes and dimensions, which were reviewed by Cai *et al*.[125] Tubular microreactors with micromixer or mixing zones have been applied to synthesize various nanomaterials and have the potential to surpass the mixing performance relative to chip-based devices. They exhibit stable flow pattern over many hours of operation without fouling even for reactions involving solid intermediates.[88] The flexibility of tubing adjustment allows a better thermally activated processes where particle formation only begins when the main capillary passes into a heated oil-bath (Figure 1.9d).

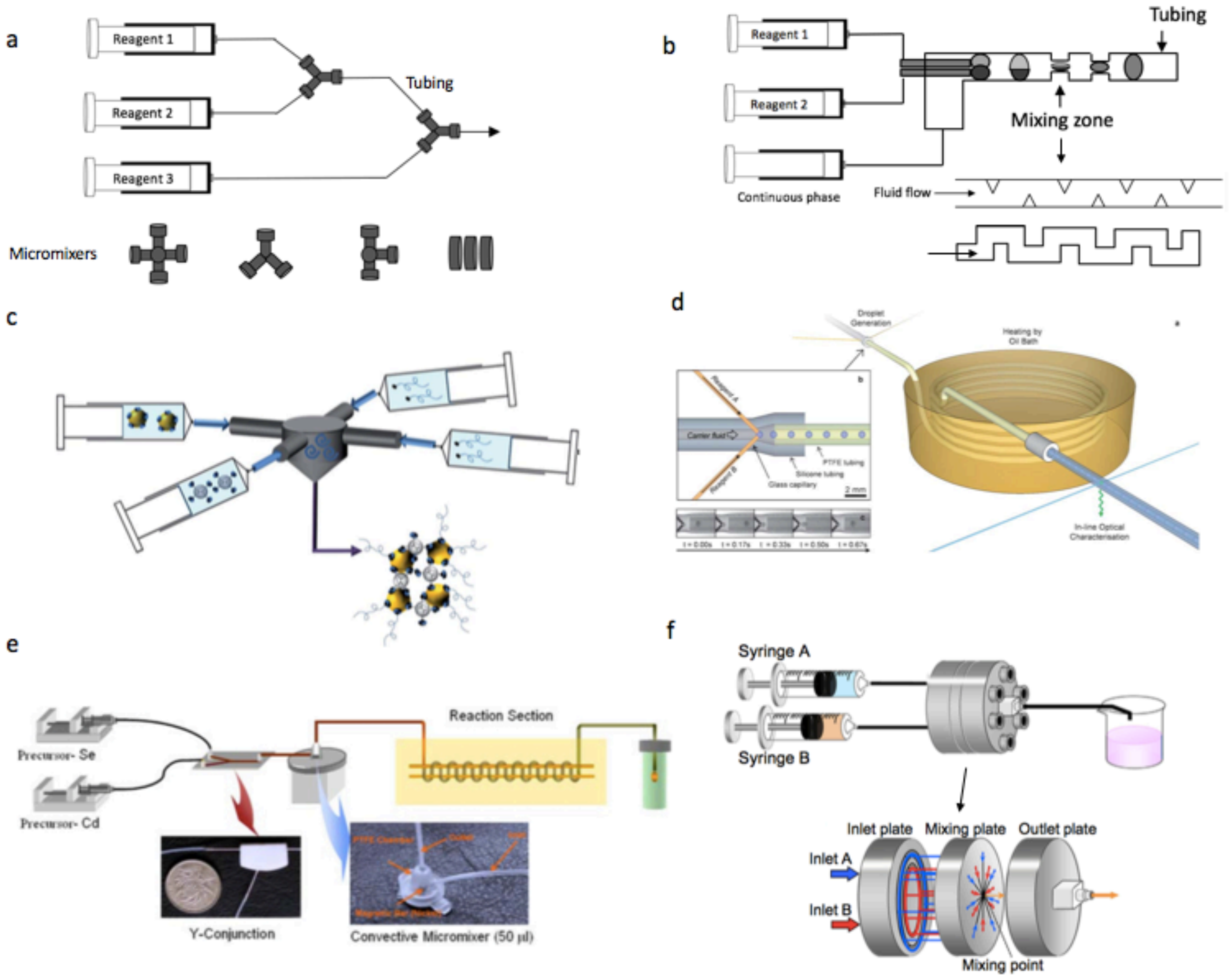

***Figure 1.9**: Schematic diagram of microreactors as an alternative to chip-based microfluidic devices (a) single-phase continuous flow microreactors consist of tubes and micromixing junctions of different shapes. (b) droplet-based continuous flow microreactors with mixing zones integrated. (c) Schematic of the multi-inlet vortex mixer (MIVM) used for the generation of hybrid gold nanoparticle network aggregates[120] (d) Schematic of the synthesis of nanoparticles in a droplet microreactor with heated oil-bath and in-line optical detection for real-time analysis.[88] (e) Schematic of a microreactor with convective micromixer for the synthesis of CdSe nanocrystals[121] (f) Schematic of the central-collision-type microreactor for the synthesis of zeolitic imidazolate frameworks. The fluids from syringes divided into multiple channels after flowing through the inlet plate and then collide at the mixing plate where the merged stream flows out of the reactor through a channel in the outlet plate.[123]*

1.3.4.2 Centrifugal microfluidic devices

Most chip-based microfluidic devices and tubular microreactors are standstill platforms, where the reaction is driven by the patten of fluid flow or thermal-electrical energy input. Another group of microreactors arises which merges the ideal microfluidic processing by wisely applied the kinetic energy of centrifugal forces. The first type of centrifugal microfluidic devices is named centrifugal microfluidic or lab-on-a-disc (LOAD) platforms which have many advantages over other microfluidic systems including simplified fluid transportation, minimal requirement on instrumentation, efficient removal of any disturbing bubbles or residual volumes and inherent density-based sample separation.[126] In general, the disc consists of a loading chamber, normally with various microchannels facing outwards on the disc with an overflow channel at the edge of the disc (Figure 10a). This disc-shaped device enables complete automation of the workflow which relies only on a single rotor.[127] Kim *et al*. achieved high detection sensitivity and high efficiency (30 min) by integrating pathogen detection, DNA extraction, isothermal recombinase polymerase amplification and detection on to a single disc. Current research on the LOAD platforms are not designed for material processing but more for use in the field of diagnostics,[128] handling and analysis of cell or bioparticles,[129] and detection methods,[130] which has been comprehensively reviewed by Gilmore *et al*.[131] and Tang *et al*.[126] Most of the reported microfluidic devices are microchannel based operation under laminar flow, where mixing within channel is limited by either diffusion control, system fouling, clogging or mass production.[2] Another type of centrifugal microreacotrs called spinning disc processing (SDP) using a thin film (25-200 μm) microfluidic continuous flow technology consisting of a rotating disc (adjustable heating and speed) with jet feeds to control the flow of reactants onto the centre of a disc and with reactive or inert gases over the thin film (Figure 10b). SDP utilizes centrifugal fields and causes intense interfering waves while liquids spread outward into thin films. This technology achievies large-scale automated production, with intimate mixing, high mass and heat transfer rate and enhanced surface interactions.[132,133] This processing platform has gradually attracted a lot of interests as viable alternatives to conventional batch processing with two recent reviews on SDP in general[132] and its application on nanocarbon processing.[134] SDP fulfills the need of mass production at reasonable market cost and has been applied to synthesise polymer nanoparticles mostly for drug delivery purpose.[133],[135] The more recently developed thin film microfluidic device (film thickness <200 μm), the vortex fluidic device (VFD), is a more versatile material processing platform for a diverse range of micro and nanomaterials. An important feature of the thin film is high mass and heat transfer with the liquid transitioning into pro-turbulent or turbulent flow, imparting some benefits over conventional microfluidic devices. A standard VFD houses an angled rapidly rotating borosilicate glass tube inclined at 45º relative to the horizontal position, as shown in Figure 10c. The glass tube is usually 20 mm O.D. (17.5 mm I.D., 19.4 cm in length), although the original development of the device was for a 10 mm OD tube. Compared to channel-based microfluidic devices, scaling-up of the processing is easier and is more cost effective, along with avoiding the aforementioned fouling/clogging issue. Typically, VFD processing can be conducted on small sub-milliliter scale as in confined mode where there is a tilt angle dependent shear stress, as well as in the up-scaled under continuous flow mode using a syringe pump (although other metering devices can be used such as peristaltic and gear pumps), with flow rates to be varied from microliters per minute to several milliliters per minute. The advantage of both scaling up and scaling down in this device provides flexibility during process optimization, which minimizes the usage of materials and the generation of waste.

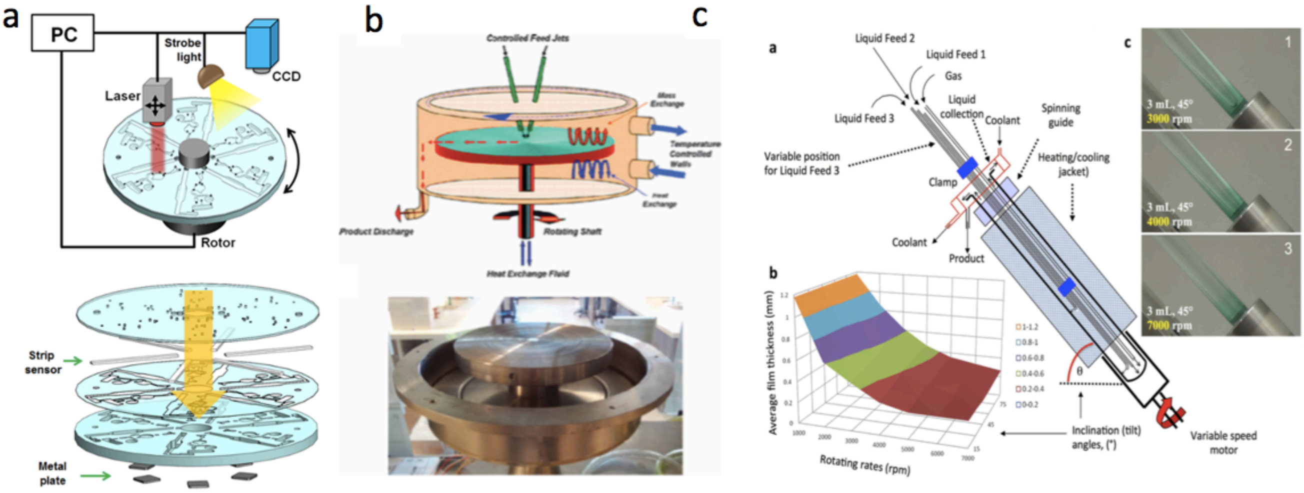

***Figure 1.10**: (a) Schematic illustration of the centrifugal microfluidic device for molecular analysis of food-borne pathogen with integrated three steps of detections on DNA extraction, isothermal recombinase polymerase amplification and detection onto a single disc.*[136] *(b) Schematic view of an spinning disc processing platform and a photograph of a 20 cm diameter SPD.*[132] *(c) Cross sectional illustration of the vortex fluidic device (VFD) and its components. Photographs showing the film of liquid developed for different speeds for the confined mode of operation of the device at a tilt angle of 45^{o}.*[137]

The VFD has a diverse range of applications, including fabricating protein based nanoparticles (Figure 11d),[138] hydrogels for drug delivery,[139] manipulating polymer networks,[140,141] protein folding[142] and accelerating enzymatic reactions.[140] The microfluidic platform has also been used to fabricate and manipulate various nanocarbon material, including decorating *p*-phosphonic acid calix[8]arene functionalised graphene with well-dispersed ultrafine palladium nanoparticles (~2 nm),[143] exfoliating graphite and boron nitride,[144] fabricating single wall carbon nanotube toroids (Figure 11c),[145] decorating carbon nano-onions with platinum or palladium nanoparticles (Figure 11a),[146,147] fabrication carbo dots (~6 nm) from multiwalled carbon nanotube[148] and lateral slicing of carbon nanotubes.[149,150] The VFD is remarkably effective in exfoliating graphite in water and then decorating the multi-layer 2D sheets on the surface of microalgal cells (Figure 11b). Wahid *et al*.[151] reported that these nanobio-hybrid materials are active for waste water treatment, in removing traces of nitrate from liquid effluents, more efficiently than pristine microalgal cells.

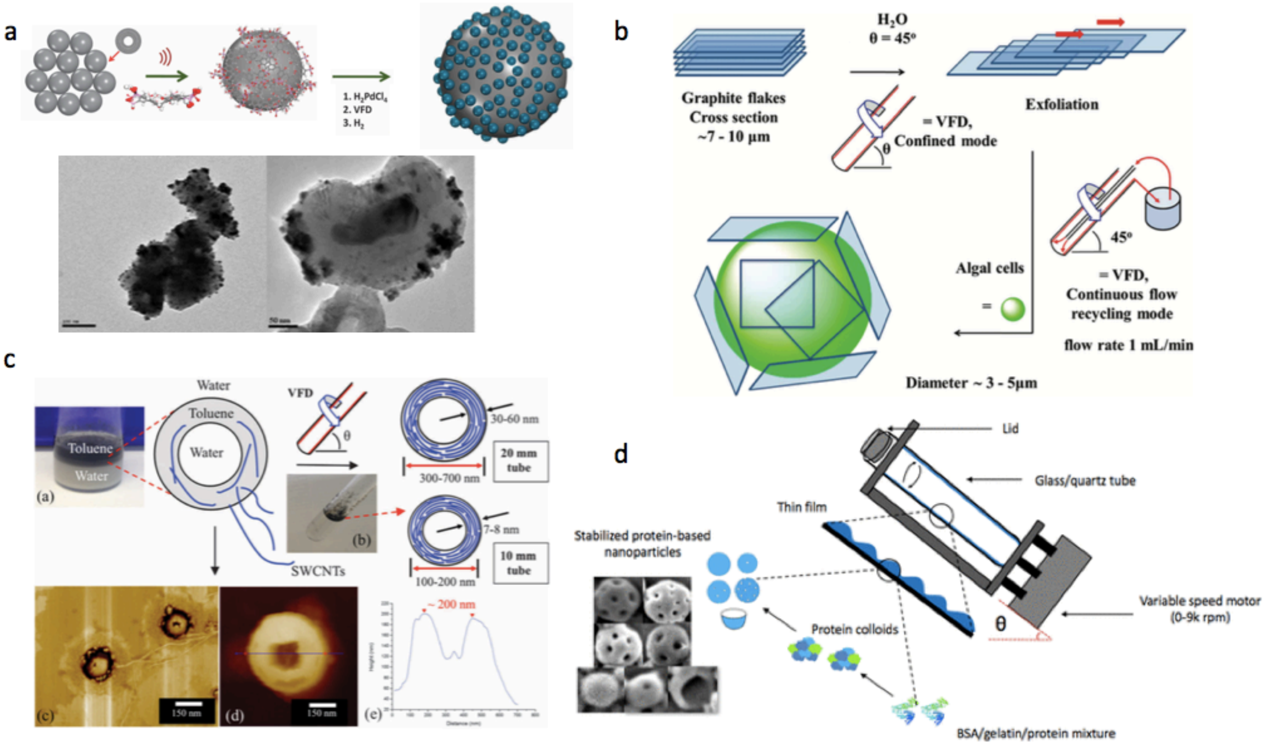

Figure 1.11: *(a) Schematic of decorating carbon nano-onions with Pd nanoparticles using VFD.*[147] *(b) Schematic illustration of the hybridisation process involving exfoliation of graphite flaks into multi-layer graphene sheets followed by hybridisation of these sheets with algal cells using VFD.*[151] *(c) Synthesis of nanorings of single walled carbon nanotubes from VFD processing.*[145] *(d) Fabrication of macroporous bovine serum albumin nanoparticles with controllable diameter and morphology using the VFD.*[138]

1.4 *In situ* monitoring

Real-time monitoring of the flow or the reaction is desirable, which gives continuous and quantitative results on the condition of liquid flow, the phase transition and nucleic growth. Any problems and status of the system such as leakage or blockage or the stage of reaction could be revealed precisely to the users in the first place. Fluorescence spectra of products can be monitored continuously at the end of the reactor using an external capillary flow cell, which allows efficient monitoring over fluorescence peaks and size-dependent synthesis for QDs.[32] An advantage here over a batch reactors is temperature control. For example, a simulation based on heat conduction showed that only 0.4 s was necessary for a 0.2 mm diameter channel to heat a liquid inside from 20 to 300 °C. Such rapid temperature monitoring allows control of the reaction time, especially for short reaction times.**[23]** CdSe nanocrystals of increasing average diameter have been synthesized in a microreactor, by increasing the temperature in 10 °C increments from 180 to 210°C.**[32]** Microfluidic reactors can be used as investigating tools while integrated with sensors and spectroscopy units.**[152]** Direct synthesis of silver nanoprisms in a flow focusing microreactor coupled with UV-Vis-NIR spectrophotometer for real time monitoring (at intervals of 1 min) has been established, noting the correlation of geometry of the nanoprisms with their optical response.**[2]** It demonstrates the capability of the microreactor for the controllable fabrication of nanomaterials, by adjusting the operational parameters of the microfluidic device. The microreactor can be placed on an inverted microscope stage for *in situ* monitoring of the fluidic behavior within the reaction channel, especially if clogging and/or fouling of the channel occurs. This allows testing the robustness of the microreactor system for long time performance.**[2]** Images can be acquired every 15 min by focusing at the bottom wall of the microreactor channel. Yen *et al.* obtained long-time-exposure images for the cooled outlet region of the gas-liquid segmented flow device operating under continuous UV excitation, which allowed real-time monitoring of the quenching effect during the synthesis of QDs.**[19]** The microdroplet-based device reported by Abalde-Cela *et al*.**[4]** was engineered with embedded electrodes, allowing destabilized surface energy for the droplets for a two-step synthesis of Au nanostarts (AuNSTs). In most studies, reaction products can be monitored real-time at ambient temperature in a microflow-cell located downstream of the system, using a spectrometer**[32,26]** to monitor the emission spectra of the emergent particles. Apart from real-time spectroscopic and microscopic monitoring, newmonitoring devices have also been adopted for better monitoring of the reaction process including small-angel netron scattering (SANS),[153] FT-IR,[55] and X-ray absorption (XAS).[154]

1.5 Biomedical applications of microfluidic fabricated materials

1.5.1 Bioimaging and biomolecular detection

New medical imaging contrast agents that permit multiple imaging and therapy applications can lead to more accurate diagnosis and localized treatment of diseased tissue.[155] Solid nanoparticles (5-150 nm in diameter) have emerged as promising imaging and therapy agents. For example, quantum dots (CdS) can be used for optical imaging[156] and gold nanorods for photoacoustic imaging, whereas iron oxide or Gd-loaded nanoparticles can be applied to magnetic resonance imaging. Microfluidic devices have been used for simple, robust and high-throughput generation of protein-lipid coated perfluorobutane microbubbles (about 3 μm) which were incorporated with various silica-coated nanoparticles (CdSe/ZnS QDs, gold nanorods, iron oxide nanoparticles and Gd-loaded mesoporous silica nanoparticles). Nanoparticle-incorporated microbubbles were detected using low-pressure ultrasound, which is applicable for *in vivo* usage.[155] QDs-encoded microparticles can be used in biological and clinical detection. Ji *et al*.[90] fabricated CdSe/ZnS QDs-doped alginate hydrogel microparticles in a droplet-based microfluidic system. These microparticles were further immobilised with goat anti-human IgG and the resulting antibody-immobilised microparticles were used to detect FITC (~520 nm) labelled human IgG in solution with the emergence of a new fluorescence peak. Semiconductor nanoparticles < 10 nm in diameter are gaining considerable interest because of their tuneable optical, electrical properties as well as being less susceptibility to photobleaching.[45,24] Varying the size of semiconductor nanoparticles alters their optical and electrical properties, thus tailoring their applications in emitting devices, optics, electronics sensors, solar cells, biological imaging and diagnostics. Various semiconductor NPs have been fabricated using microfluidic devices, including CdS,[21] CdSe, titania[157] and CdSe-ZnS composites.[22] By far, CdS and CdSe are the most intensely studied in terms of using microfluidics for their fabrication, offering an effective and simple approach to access ultra-small nanoparticles with low polydispersity compared to particles generated using conventional methods.[21] Hong *et al*.[156] demonstrated control in the size and morphology of CdS nanocrystals (spheres, nanorods and multipods, ranging in size from 2.6 to 6.7 nm in diameter) in a millifluidic chip, and used them in *in vitro* bioimaging using RAW264.7 mice macrophage cells (Figure 12b). Tunable photoluminescence is possible by adjusting the molar ratio of the Cd and S precursors, giving rises to shifts in emission peaks under UV irradiation.

Increasing the biocompatibility and targeted labelling of cells is possible by functionalizing the QDs with different ligands including protein, DNA, RNA, peptides and lipids.[158] Hu *et al*.[159] reported the use of a laminar flow microfluidic chip for a one-step synthesis of BSA functionalised CdTe QDs for direct use in targeted cell and tumor imaging. QDs exhibit a significantly higher protein-functionalisation efficiency, photostability and colloidal stability compared to the ones prepared using conventional bench-top methods. Although a diverse range of photoluminescent nanoparticles have been generated for new materials, there is increased concern about their potential environmental impact and human health toxicity.[160]

Accordingly, there has been a switch from heavy metal based QDs, as in CdSe, to carbon dots (CDs) which have excellent luminescent properties and are biocompatible.[161] Even though microfluidic systems offer significant advantages for synthesising nanoparticles, there are limited reports on the synthesis of CDs using them. Pedro *et al*.[160] described the synthesis of 3.3 nm-sized CDs based on the thermal decomposition of ascorbic acid in dimethyl sulfoxide in a microfluidic system comprising a fluidic and a thermal platform operating at 180 to 240°C (Figure 12a). The CDs have pH dependence of their optical properties, over the pH range 2 to 11, and have been used in developing pH fluorescent sensors. Studies on the cytotoxicity and permeability of the CDs on human embryonic kidney cells established that their adsorption on cells has no impact on cellular morphology.[160] Apart from CDs, fluorescence polymers are another biocompatible candidate for cellular imaging.[162] Fluorescent polyethylenimine nanoparticles about 10 nm in diameter, with significantly reduced cytotoxicity against MCF-7 breast cancer cells and being devoid of extended conjugated structures, have been prepared in a VFD microfluidic platform (Figure 12c).[163] Tunability of the fluorescence for these CDs was achieved by varying the flow rate of liquid entering the rapidly rotating glass tube of the VFD, without the need for additional reagents.

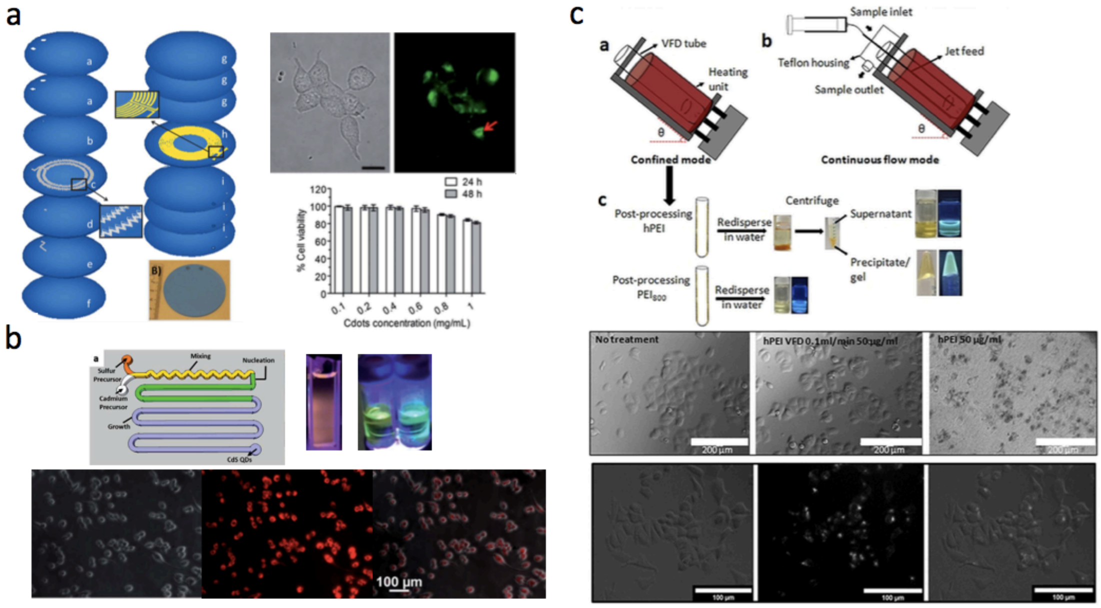

Figure 1.12: *(a) Schematic of different layers that compose the microfluidic system for the synthesis of CDs, which stain membrane edges on HEK293 cells with no evidence for change on cell viability.*[160] *(b) Schematic of the millifluidic chip used in the synthesis of CdS nanocrystals and the as processed sample under UV irradiation. In vitro bioimaging of RAW264.7 macrophage cells with the CdS nanocrystals.*[156] *(c) Schematic of the fabrication of fluorescent polyethylenimine nanoparticles using VFD and the toxicology studies against MCF-7 breast cancer cells.*[163]

1.5.2 Tissue engineering (microfiber) or 3D cell culture

Tissue engineering and regenerative tissue constructs allow generation of artificial bio-tissues for a wide range of diseases. A key aspect of tissue engineering is the development of biocompatible scaffolds that support, stimulate, and direct the attachment, migration, proliferation and differentiation of specific cells.[164] To generate a functional tissue engineering scaffold, biodegradable and biocompatible materials are required. In addition, the physical properties of scaffolds, including porosity, size, shape, spatial distribution, diameter, degree of fibre alignment, surface roughness, elasticity, mechanical strength and the 3D geometry of the scaffold are also critical.[165,63,166] As in 3D morphologies, small pores in the scaffold matrix have been shown to facilitate cell proliferation and the storage of nutrients and chemicals for specific functional roles, by releasing cytokines for controlling cell growth or drugs to prevent infection.[167] Pore dimensions and the overall shape of the scaffolds also affect the degradation rate.[168] For example, microscale fibrous scaffolds are promising material to guide cell growth, proliferation and alignment, which offers reliable mechanical properties.[164] General methods for fibre fabrication include melt spinning,[169] wet spinning,[170] and electrospinning,[171] all of which have problems associated with heating, weak mechanical strength,[172] limited loading of bioactive molecules, and difficulties in controlling the diameter of the fibres.[173]

Microfluidic devices have been developed to generate scaffolds with well-defined physical and architectural features. Microfibers can be generated from different materials including poly(lactic-*co*-glycolic acid) (PLGA),[174,57] chitosan,[175] polyurethane,[63] and alginate,[59] or a mixed composites of the these materials.[61] PLGA is a well-known synthetic polymer that has been approved by the Food and Drug Administration for clinical applications.[57] PLGA microfibers generated by Hwang *et al*.[57] are cylindrical in shape with uniform diameters (20 to 230 μm), having a smooth outer surface and a highly porous interior (Figure 13c), which can be used as a reservoir for cytokines or proteins that promote cell adhesion and growth. L929 fibroblasts cultured for 10 days can cover the PGLA fibres and form a 3D configuration.[57] The diameter of the PLGA microfibers, which can be controlled using microfluidics, is directly related to the mean cellular orientations of the fibroblast L929 cells (Figure 13a).[174] Chitosan is another commonly used material for microfibers and is one of the most suitable scaffold materials for liver tissue due to its similarity to glycosaminoglycans which is natural component of liver extracellular matrix.[175] Microfluidic devices have been used to fabricate pure chitosan microfibers (~1 m long, 70 to 150 μm in diameter) to seed human hepatocarcinoma (HepG2) cells which self-aggregate into spheroid-like structures with over 95% cell viability (Figure 13b).[175] The spheroid-like structure improves the liver function of hepatocytes and enhances hepatic function *in vitro*.[176] Fibrous polyurethane is another scaffold which has been extensively investigated. However, low cellular adhesion to the polymer surface can lead to thrombosis due to the paucity of endothelial cells. Coating the surface with biomaterials can solve this problem, but it is difficult for conventional methods to impart enough surface coverage.[177] Jung *et al*.[63] generated asymmetrically structured or Janus microfibers *in situ* using a one-step photopolymerisation process involving a continuous laminar flow microfluidic device. These Janus microfibers have improved cell adhesion, viability, growth and biocompatibility, even without coating the fibres with peptides or proteins. When the long thread stream of photocurable polyurethane containing oligomer and cross-linker comes into contact with the aqueous continuous phase, radical polymerisation initiation in the presence of CO_2 results in spontaneous generation of an asymmetric porous structure. Nonporous regions improve the mechanical strength of the scaffold, whereas the porous region facilitates cell adhesion and migration. Over 15 days, the maximum distance between fibroblast grown fibres is about 200 μm, and these fibres can be used as an alternative 2D cell culture plate or even a 3D scaffold for tissue engineering.

Diffusion based mass exchange between the polymer and the non-solvent stream generates pores within the microfibers effective in encapsulating proteins and drugs with increased release rates. Cells cultured on the porous microfibers have increased mitochondrial activity as the diameter of the fibres decreases. Despite this, hollow alginate microfibers, produced use a microfluidic chip, have been embedded into hydrogels and emulated vascularised tissue (Figure 13d).[59] Lee *et al*.[61] mixed the alginate with chitosan during the processing which indicates that the HepG2 cells in the composite microfibers are more viable and have better adhesion than pure alginate, which is due to the cross-linking in the chitosan. These aligned cell-loaded fibres have room for cell growth and protein/cytokine incorporation with sustained release, thus mimicking real tissues constructs such as ligament and tendon, heart muscle, spinal cord or neural tissues, and have potential in the area of tissue regeneration. Other biomaterials have also been used including gelatin, Pluronic, hyaluronic acid, silk, collagen and several synthetic polymers,[178] but building the architectures has rarely been explored using microfluidic devices. Gelatin-based fibres are beneficial for creating tissue engineering scaffolds, because gelatin is a natural material, derived from collagen and contains adhesive RGD peptides, with which cells can interact.[178] Microfabrication techniques are worthy of exploration in generating biomimetic microfibers that resemble native extracellular matrix structures, such as those of collagen fibres.

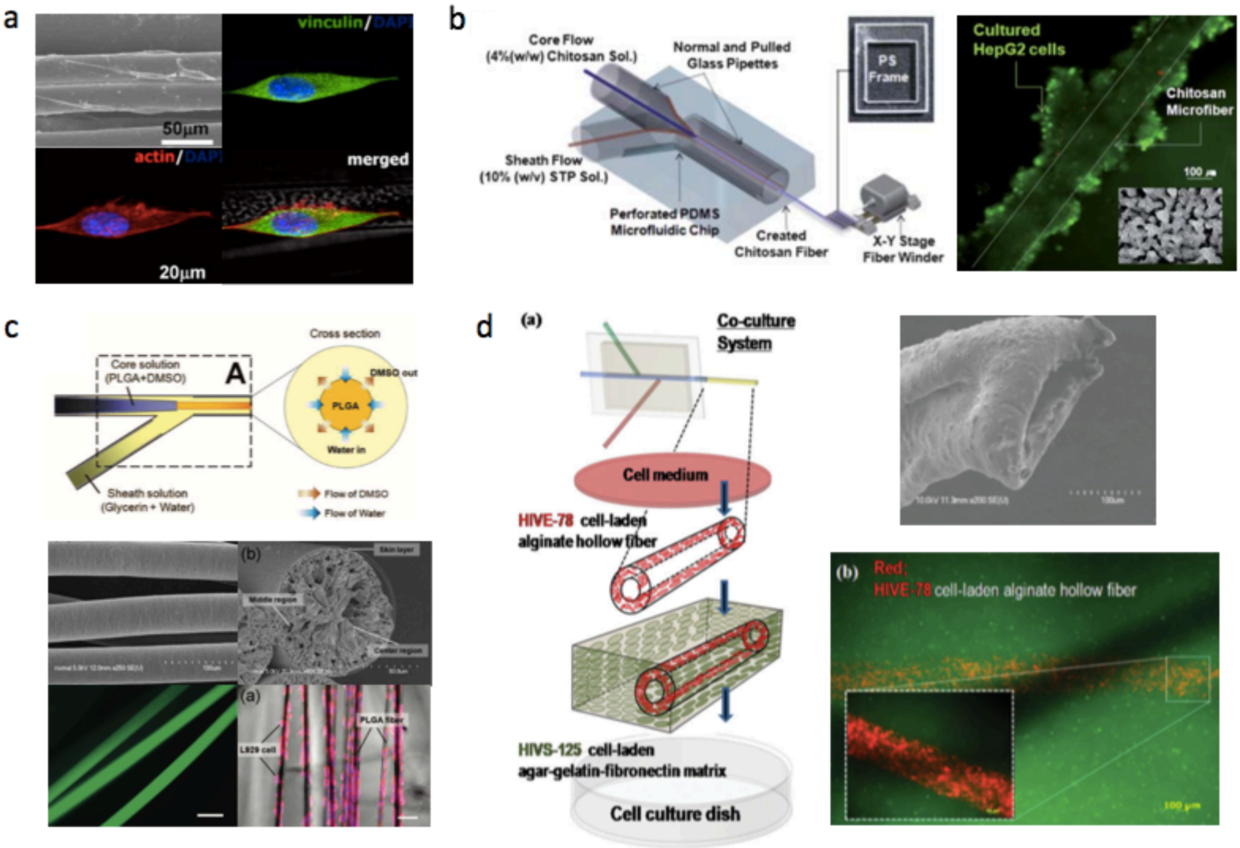

Figure 1.13*: Cellular morphology of mouse L929 fibroblasts on PLGA microfibers with 30 μm diameters.*[174] *(b) Clustered HepG2 cells on chitosan microfibers synthesised using a co-axial microfluidic device.*[175] *(c) Schematic of a microfluidic synthesis of PLGA microfibers and the cross-sectional view; protein incorporation and L929 cell seeded on the PLGA fibres.*[57] *(d) Co-culturing of HIVE-78 and HIVS-125 cells on alginate hollow fibres to emulate vascularised tissue.*[59]

1.5.3 Cell encapsulation

Elasticity of cellular microenvironments strongly influences cell motility,[179] phagocytosis,[180] growth and differentiation.[181] Cells have developed mechanisms to sense the surrounding matrix stiffness by adhering to and pulling upon it, followed by a cytoskeletal cellular response.[182] However, most research on the relationship between matrix stiffness and cell behaviour is conducted for cells seeded on planar substrates, which is not representative enough compared to exposing the cells to a 3D environment or a complex extracellular matrix. Encapsulating cells within natural or synthetic hydrogels with different elasticity enables the investigation of the role of the mechanical properties of 3D environments on cell behaviour. Microbead-shaped encapsulation allows the localisation of cells within a small amount of microenvironment, which offers a relatively simplified system to study cell fate. In addition, encapsulating cells in biocompatible materials has promise for protecting cells against external shear force, reducing the immune response and improving the cell viability, which has significant advantages in cell transplantation.[183] In addition, the encapsulation of cells has been demonstrated as an effective approach to deliver therapeutic agents. Cells encapsulated in porous hydrogels allows effective exchange of nutrients and O_2,[184] and also continuously releasing metabolic products or therapeutic agents to the outside, which can be used as a resource for sustainable drug release for cell-based drug delivery and therapy.[185,186] Although cells can be encapsulated into hydrogel beads using traditional techniques such as emulsion polymerisation and suspension polymerisation,[187] they lack precise control over size and shape of the resulting hydrogel beads that would hinder their performance in the desired applications.

Microfluidic-assisted microencapsulation attracts much interest in biomedical areas and has several advantages. Firstly, it has the capacity to generate 2D cellular microenvironments with precise control over dimensions, and chemical and mechanical properties. Secondly, it is relatively easy to tune the properties of the microenvironments by adjusting the processing parameters such as flow rate or injection ratio. Moreover, the high-throughput technique allows high frequency processing which can be used in generating massive combinatorial libraries.[83] The use of microfluidics combines both the advantages of the synthesis of polymer-based particles and the control of the process of microencapsulation, thus providing a promising route to encapsulating cells in hydrogel particles. Microfluidic-based approaches have been used for the generation of encapsulated cells in droplets or microgels, thereby providing new opportunities for fundamental studies in cell growth and viability,[188] gene expression, and enzymatic activity.[189] Various materials have been applied in such fabrication, including natural materials such as proteins (collage, gelatin, fibrin, elastin-like polypeptides), polysaccharides (alginate,[190,191,183] hyaluronic acid, chitosan, agarose[83]), PEG,[192] and poly(ethylene glycol) diacrylate.[193] The encapsulation of cells in polymer/hydrogel particles with precise control over the number of cells per particle and encapsulation efficiency can be achieved by adjusting the flow rate ratio between continuous and disperse phases, and using high aspect-ratio microchannels.[192] Edd *et al*.[194] demonstrated single-cell microdroplet generation in a flow-focusing geometry by emulsifying concentrated suspensions of HL60 cells immediately after they had traversed a high aspect-ratio rectangular microchannel 27 µm x 52 µm x 6 cm (Figure 14b). Single-cell studies in regards to secretion and uptake of trace biomolecules have much more practical convenience.

Hydrogels are cross-linked hydrophilic polymer networks that can absorb water or other biological components.[190] Alginate, a linear copolymer composed of *β*-D-mannuronic acid and α-L-guluronic acid, can be easily transformed into a gel by binding the guluronic acids with a divalent cation such as Ca^{2+}.[195] Alginate is one of the most popular materials in this regard having high stability (>30 days). It has been used in microfluidic-assisted encapsulation of various biomolecules including proteins, cells and DNA.[190] For example, *in situ* encapsulation of yeast cells expressing green fluorescent protein (GFP) with alginate microbeads has been reported by Choi *et al*,[190] with expression of encoded GFP thereby establishing retaining cell viability during the encapsulation process. Utech *et al*.[109] generated a micron-sized 3D cell culture using a mixture of alginate and a water-soluble calcium-EDTA complex (Figure 14a). The individually encapsulated mesenchymal stem cells within the microbeads had increased cell growth and proliferation. Zhao et al.[196] fabricated magnetic Ca-alginate Janus hydrogel particles through injecting two phases of Na-alginate with one of them containing superparamegentic beads. This allowed the cells and magnetic beads to be separately embedded in two separate hemispheres of one hydrogel particle. Although cells encapsulated in spherical alginate beads facilitates the continuous transport of nutrients and metabolic substances during cell culture, these spherical beads are not available for long-term cell monitoring and biological research due to the rolling of the spherical hydrogel beads and distortion of the images. To improve monitoring of the cell division process, Liu *et al.*[183] used a droplet-based microfluidic device to generate living yeast cells or mammalian cell encapsulated in disk-like Ca-alginate hydrogel beads (Figure 14d). The cell division process can be monitored long-term, without rolling and distortion of the images, by using flat top/bottom surfaces of the disk-like beads. Agarose, a neutral polysaccharide, is another common material for cell encapsulation, which is generally bio-inert, non-adsorptive to proteins, non-adhesive to cells and has readily tuneable mechanical properties.[197] The high-throughput generation of agarose microbeads with tuneable elasticity has been reported by Kumachev *et al.*,[83] for different relative volumetric flow rate ratios of two streams of agarose solutions (Figure 14c). These agarose microbeads with precisely controlled dimensions have been used for encapsulating R1 and YC5-YFP-NEO murine embryonic stem (mES) cells with cell viability of 79.6% and 80%, respectively.

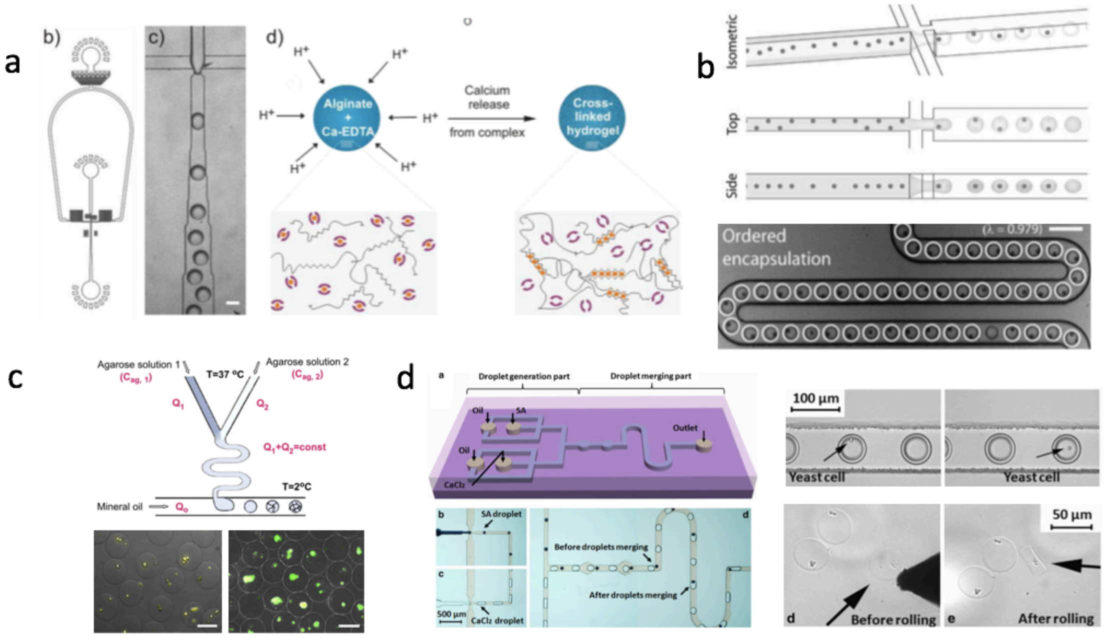

Figure 1.14: *Cell encapsulation with microbeads: (a) Microfluidic flow-focusing generation of homogeneously crosslinked alginate microparticles.*[109] *(b) Ordered cell encapsulation through hydrodynamic interactions. Hydrodynamic interactions allow particles to self-arrange along one side of the microchannel or into a diagonal or alternating pattern.*[194] *(c) Microfluidic generation of agarose microgels in encapsulating two types of murine embryonic stem cells (scale 100 µm).*[83] *(d) A schematic of a droplet-based microfluidic device in generating disk-like Ca-alginate hydrogel beads for cell encapsulation and manipulation; the beads with encapsulated cells can be rolled using a thin needle.*[183]

1.5.4 Biologic delivery and controlled release

Over the last few decades, the application of nanotechnologies in the pharmaceutical field has attracted significant of interests, especially in the field of preventing drug degradation, enhancing cellular uptake and controlling drug release.[198] Conventional approaches to preparing particles for drug delivery purposes typically rely on physical entrapment,[199] increasing affinity of the cargo,[200] covalently linking the biologics to the polymer network,[201] and various solvent-based methods such as interfacial polymerisation, simple or double emulsification-based methods with evaporation or diffusion of polymeric solvent and nanoprecipitation.[202] Among them, bulk mixing such as in the nanoprecipitation method is straightforward and accounts for more than 50% of the nanoparticles reported for drug delivery systems. It allows hydrophilic and hydrophobic compounds to be entrapped.[203] However, the scalability of the nano-encapsulation process, batch-to-batch reproducibility, poor drug entrapment efficiency, size uniformity and quality control, are common issues for some conventional methods.[204] Such methods require extra steps such as filtration or centrifugation to isolate the population of the particles with desired size.[205]

Microfluidics offers a relatively simple and consistent method for overcoming some of these issues, for synthesizing nanoparticles of uniform size, with better releasing profiles, from different materials such as PLGA,[206,207] PEG,[208] polycaprolactone (PCL)[209] and copolymers.[210] Size and morphology of the particles can be controlled by adjusting the input flow rates or the dimensions of the microchannels.[211] Controlled drug release is possible using water-in-oil emulsions, core-shell structures[212] and stimuli-responsive microgels.[213] Increased attention has been given to PLGA based nanoparticles as nanocarriers of small drugs,[214] peptides, proteins,[215] DNA or RNA.[216] PLGA is FDA-approved for human use[217] and is effective in the controlled release of bioactives, which undergo hydrolysis in the body to produce the constituent monomers, lactic acid and glycolic acid with minimal systemic toxicity. However, the lack of robust, reproducible and easily scalable preparation of PLGA nanoparticles has hindered their clinical and commercial uptake.[218] Chiesa *et al*.[206] prepared N-Acetylcysteine-loaded PLGA nanoparticles using a microfluidic device with staggered herringbone micromixing; N-acetylcysteine is a small molecule hydrophilic drug with rapid clearance and unfavourable biodistribution depending on the route of administration. After 60 min incubation, N-acetylcysteine is released from PLGA nanoparticles prepared using the bulk mixing nanoprecipitation method. The rate of release was *ca*. 90% higher than from particles prepared using the microfluidic device, with a prolonged induced *in vitro* release of the drug (Figure 15a). For a more simplified process, paclitaxel-loaded polycaprolactone-*block*-poly(ethylene oxide) (PCL-*b*-PEO) copolymers have been prepared in a segmented gas-liquid microfluidic reactor.[77] The morphology of drug-loaded nanoparticles with various crystallinities, loading efficiency and releasing profile are accessible by simply varying the flow rate and block copolymer composition.

In tissue regeneration and repair, growth factors play an important role in guiding cell fate, and require well-orchestrated dosing and timing.[208] PEG, a hydrophilic bioinert polymer, can be easily tailored to encapsulate and control the release of biologics. Deveza *et al*.[208] used a droplet-based microfluidic device to synthesize PEG-based microspheres for uptake of basic fibroblast growth factors (bFGF) or DNA with well-tuned release kinetics and the encapsulation efficiency of ~80% (Figure 15b). The release rate can be precisely controlled by varying the diameter of the microchannels, from 100 to 200 μm during the processing. Another area of research on drug delivery falls into cancer therapeutics. The development of nanotechnologies for effective delivery of multiple drugs addressed a number of therapeutic challenges including side effects, low therapeutic efficacy and the mechanisms of drug resistance.[210] Using microfluidic devices allows easy definitive delivery of a correct ratio of each drug with minimal batch-to-batch variation. Kollishetti *et al*.[210] established that a blend of PLA-Pt(IV) (polylactide derivative conjugated to a platinum(IV) prodrug) functionalised polymer and carboxyl-terminated poly(D.L-lactic-co-glycolic acid)-block-poly(ethylene glycol) copolymer loaded with hydrophilic Pt(IV) and hydrophobic docetaxel afforded 100 nm diameter nanoparticles in microfluidic channels (Figure 15c). The surface of the nanoparticles was derivatized with A10 aptamers, which binds to the prostate specific membrane antigen on prostate cancer cells where there is controlled release of both drugs over a period of 48 to 72 h. *In vitro* toxicity studies demonstrated superior efficacy of the targeted dual-drug combination nanoparticles over single drug nanoparticle analogues. A more versatile drug delivery system has been reported by Yang *et al*.,[209] on the encapsulation of the anticancer drug tamoxifen, superparamagnetic Fe_3O_4 nanoparticles and CdTe QDs into size controlled PCL microcapsules 270 to 440 μm in diameter using microfluidic emulsification. This composite combines several properties including magnetic targeting, fluorescence imaging and controlled drug release, which enables enhanced biolabelling and targeted drug delivery. Ideal nanoparticle-based therapeutics potentially allow specific targeting of pathologic tissue, thereby minimising or avoiding the side effects of the active therapeutic agents on healthy tissues. To deliver drugs to selected cells, specific interactions between nanoparticles and biological targets must be favoured.[219] Microfluidic processing as a simplified and reproducible processing platform gives a lot of successful examples on tethering targeting ligands include small molecules, oligosaccharides, peptides, proteins, antibodies, and aptamers for more advanced new generation drug delivery system. Future research should also focus on preparing more medically relevant drug-loaded nanoparticles at higher therapeutic loading levels.

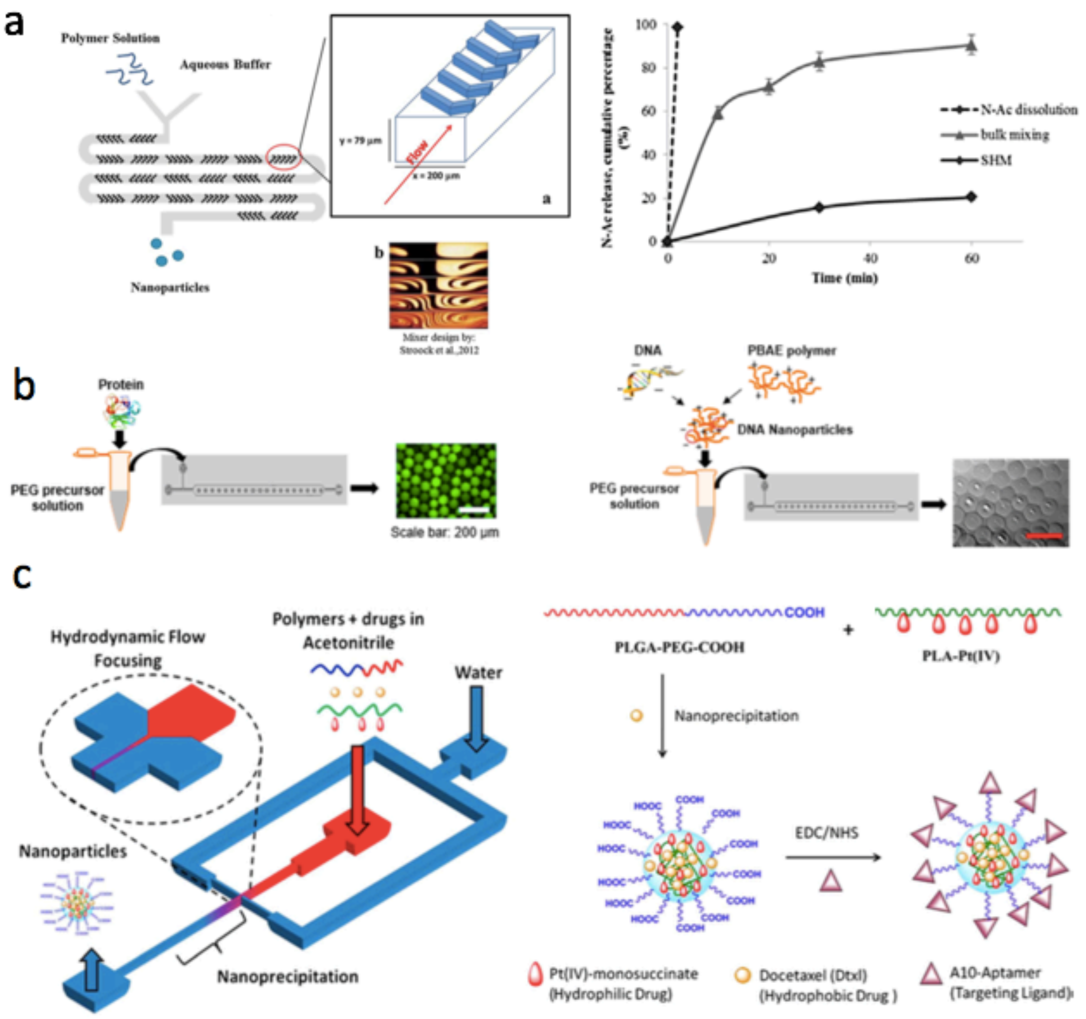

Figure 1.15: *(a) Schematic of the staggered herringbone micromixer with sequential regions of asymmetric ridges for the synthesis of PLGA nanoparticles for drug delivery. In vitro N-Acetylcysteine (N-Ac) release profiles from N-Ac loaded PLGA nanoparticles.*[206] *(b) Schematic of the addition of bFGF or PBAE/DNA nanoparticle to a PEG precursor solution and subsequent microsphere formation in a droplet-based microfluidic device. Fluorescein isothiocyanate-conjugated BSA (green) used to visualise protein encapsulation (scale bar: 200 µm).*[208] *(c) Synthesis of the combinatory Pt(IV) and Docetaxel loaded PLGA nanoparticles using a flow focusing microfluidic device.*[210]

1.5.5 Separation of biological materials

Methods for efficient separation and purification of biomolecules are important in different biomedical research areas, such as diagnostics, chemical biology, proteomics and genomics. By far the most common separation method is sodium dodecyl sulfate polyacrylamide gel electrophoresis (SDS-PAGE). Apart from using randomly structured polyacrylamide gels, micro or nanofabricated nanoporous sieving matrices have been investigated for the size-based separation of biomolecules because of their high rigidity and long-term stability compared to gels. This is because gel needs to be freshly prepared for each analysis and requires time for the separation process. Typical methods for micro/nanofabrication of sieving matrices are complicated and time-consuming, such as electron beam lithography and deep reactive ion etching, and this has hampered their applications. Different materials have been applied in the separation of biomolecules. Separation beds with porous networks, fabricated via colloidal self-assembly (CSA) of nanoparticles, have been used for separating proteins and DNA.[220,221] Attempts have been made to stabilise CSA structures for high performance separation, however, most procedures are complicated,[222] and the formation of cracks in the CSA beds during drying is an issue.[223] Photonic crystals assembled from submicro- or nanoparticles are another type of media for differentiating the size and other properties of DNA,[221] proteins[222] and even small molecules.[224]

Microfluidic devices have been applied in different ways into protein separation. The most common separation method includes packing of stable and crack-free crystals into microchannels.[225] Various materials such as polystyrene and silica particles[223] have been used as the CSA beds confined within microfluidic devices. Gong *et al.*[226] integrated a nanofilm into a 3D microfluidic device, serving as a frit to confine the nanoparticles in the microchannels, which is effective in separating fluorescein and 5-carboxyfluorescein by applying a 125 V/cm potential. Shaabani *et al.*[227] reported a facile method to stabilise CSA silica nanoparticle (310 nm diameter) beds in microchannels for high speed size-based electrophoretic separation of proteins. Silica nanoparticles are entrapped and stabilised within a methacrylate polymer prepared *in situ* through photopolymerisation, with a high degree of order and packing quality (Figure 16a). High electric field (≥ 1800 V/cm) were used for size-based protein separation (length of 13 mm, plate number of > 10^6/m, 200 nm high), providing highly efficient separation performance with resolution of proteins up to 0.6 kDa. However, some of the packing take several days, requiring a number of steps including assembly and immobilisation. Liao *et al.*[225] reported a fast one-step process for packing silica photonic crystals (2 cm in 15 min) into microchannels through evaporation-induced self-assembly and hydrothermal immobilisation, with no evident of formation of cracks (Figure 16b). This is capable of withstanding an electrical field strength up to at 2000 V/cm^{-1} for 5 h and storage in water for 2 months, and is effective for ultra-fast separation of amino acids along a 2.5 mm photonic crystal in 4 s and peptides along a 10 mm one in 12 s. These studies demonstrate the potential to apply stable separation material in different channel-based microfluidic devices in achieving efficient separation in short time. Recently, the thin film VFD microfluidic platform has been used in aqueous two phase separation (ATPS) of microalgal proteins (Figure 16c).[228] VFD-intensified ATPS continuous flow processing has spontaneous phase separation resulting in at least a 9.3 fold increase in phase demixing efficiency, 1.18 fold increase in protein purity and 22% increase in yield compared to batch processing. It is an effective new tool for rapid protein separation.

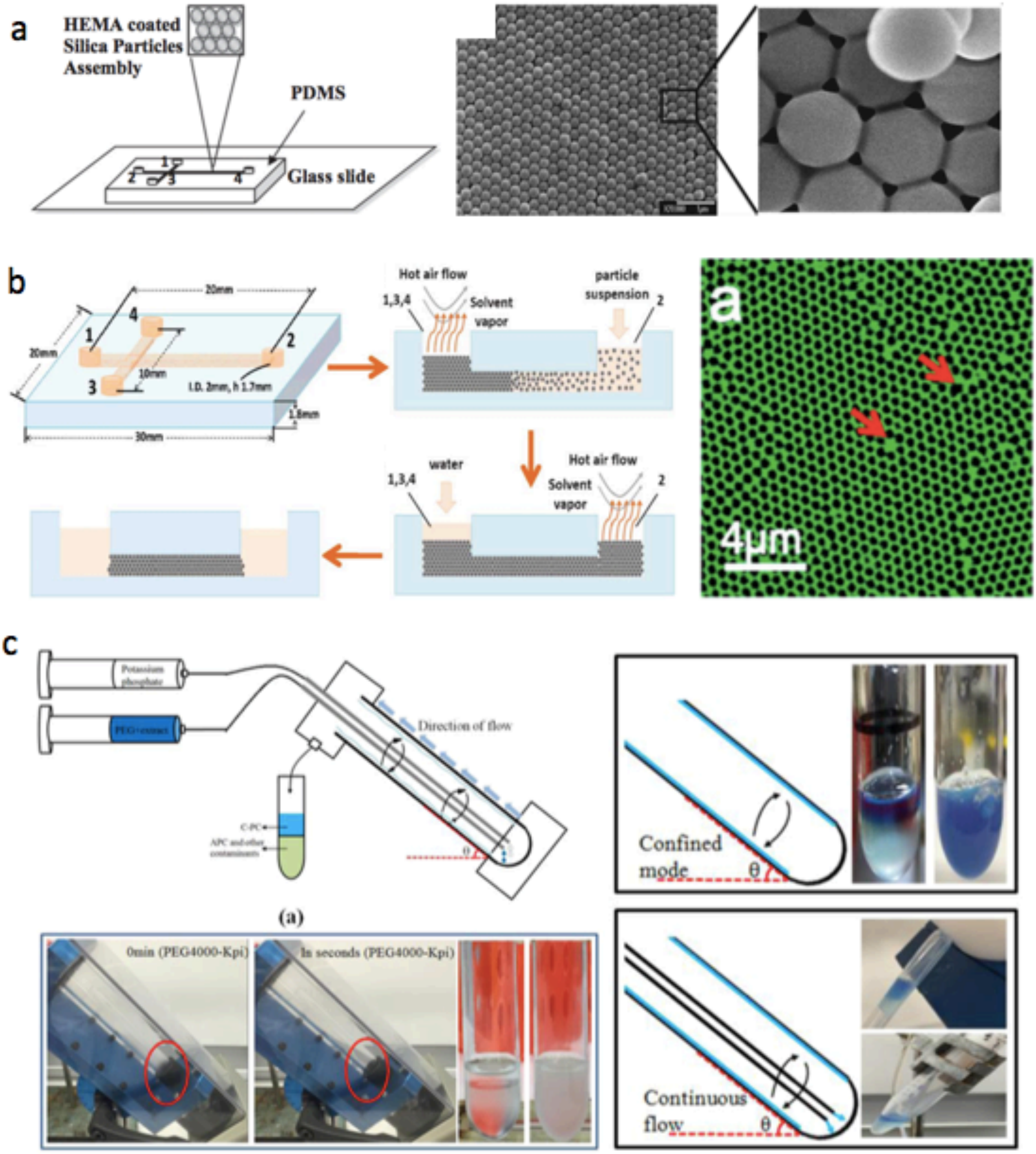

***Figure 1.16**: (a) Schematic of a microfluidic chip formed by colloidal self-assembly of 310 nm diameter silica particles entrapped in the presence of a 0.5% solution of photopolymerised methacrylates. SEM image of peeled PDMS plate following photopolymerisation.[227] (b) Flowchart for the rapid assembly of the stable photonic crystals into glass microchip channels by evaporation induced assembly and the confocal image of the silica-particle-embedded PC column taken from its centre section.[225] (c) Purification of microalgal protein using an aqueous two phase system intensified by VFD.[228]*

1.5.6 Other therapeutics and diagnostics

Other relevant areas of research using microfluidics includes scar therapeutics.[207] Excessive scar formation can be prevented by treatment with some hydrophobic drugs such as corticosteroids and triamcinolone.[229] However, current therapeutic protocols include painful monthly injections to administer high doses of the medication into the scar for prolonged periods.[230] Nevertheless, the recurrence rates are still as high as 50% upon cessation of these injections.[231] The high cost behind these treatment (~200 USD per drug loading process) and undesirable side effects are other disadvantages of such treatment.[232] Core-shell structured hydrogel particles containing corticosteroid-loaded PEGDA/PLGA core/alginate shells, fabricated using droplet-based microfluidics polymerised using UV irradiation, have been developed for effective low cost scar therapeutics.[207] The well-defined core-shell structure has 98% encapsulation of the corticosteroids in the PEGDA core, which is effective for a well-controlled long term release over 30 days in *vivo* with effective therapeutic suppressing of scar formation. Increasing the concentration of the PEGDA from 5 to 20% and the UV light intensity from 40 to 1150 mW/cm^2 results in an increase in the diameter of the core from 21 to 131 µm (Figure 17a). Theranostic fields applying microfluidics also includes HIV therapy.[233] Martins *et al.*[233] developed an efavirenz (EFV, a antiretroviral drug)-loaded PLGA nanoparticles using microfluidics, which targeted the blood brain barrier to treat HIV neuropathology. These particles are 73 nm in diameter, having much higher EVF association efficiency of 80.7% and drug loading efficiency of 10.8% relative to ~133 nm diameter particles formed using the conventional batch method, at 32.7% and 3.2%, respectively (Figure 17b). Other therapeutics include magnetic fluid hyperthermia (MFH), which has attracted interest in anticancer therapies. Magnetic vesicles have outstanding properties for magnetic hyperthermia or magnetic guiding in translational research and nanomedicine. MFH-triggered release gives new hope for the application of MFH to drug delivery systems.[116] Micrometer- and submicrometer-sized functionalised beads are used to capture targets of interest from a biological sample for biological characterisation and disease diagnosis. The main challenge for microbead-based assays is the immobilisation of probe molecules onto the microbead surfaces. Chen *et al.*[234] reported the fabrication of porous alginate microspheres with simultaneous immobilisation of anti-*Mycobacterium tuberculosis* complex IgY and anti-*Escherichia coli* IgG antibodies using a one-step droplet microfluidic device (Figure 17c). These 3D alginate microbead-based immunoassays have equivalent specificity and advantages in regard to size and surface modification and improved access of target analytes compared to enzyme-linked immunosorbent assays (ELISA). The alginate microbead approach involves simpler processing procedures, with lower costs.

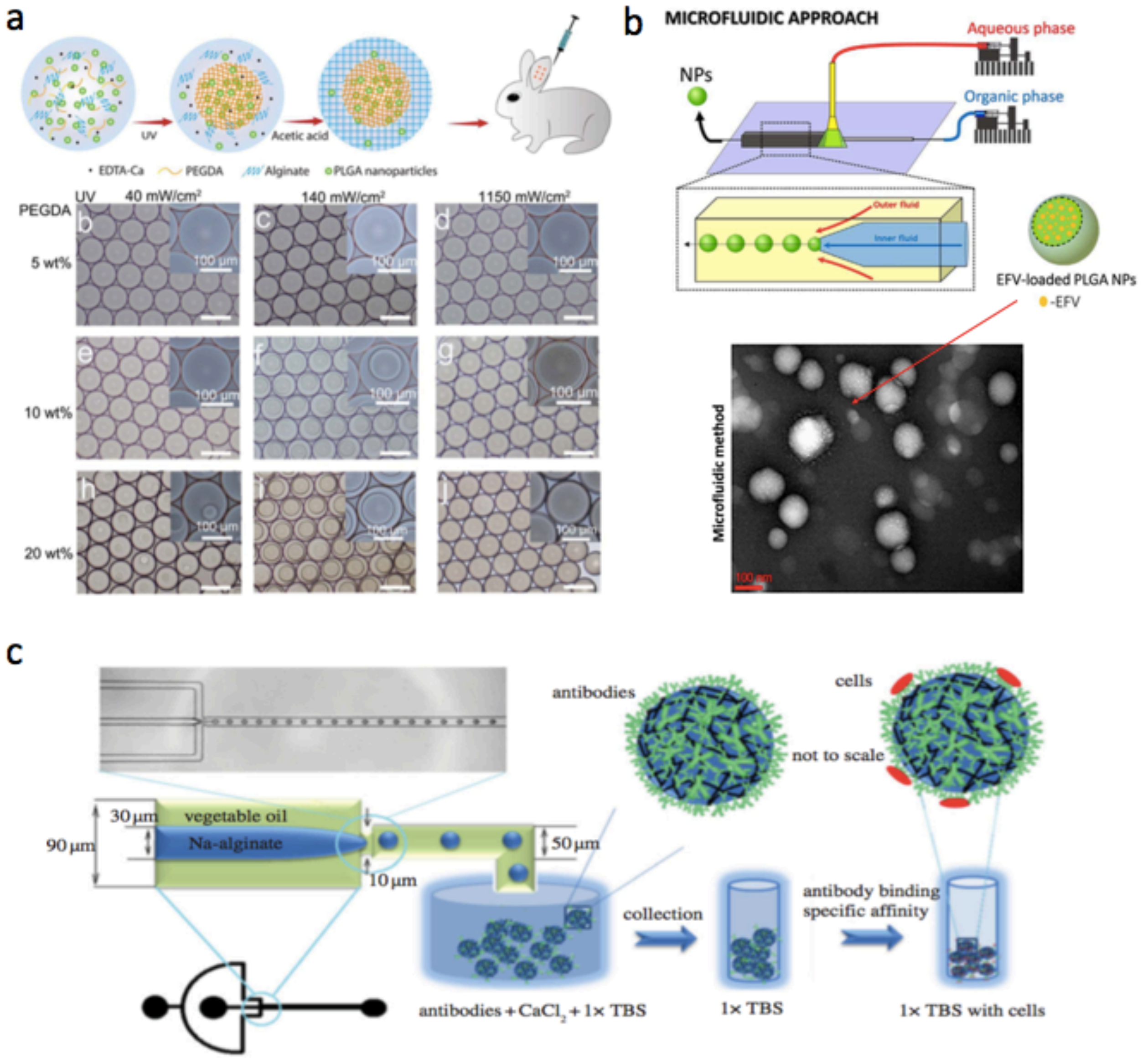

Figure 1.17: *(a) Schematic of the core-shell hydrogel particle fabrication process while changing the UV intensity and the concentration of PEGDA.*[207] *(b) Schematic representation of the microfluidic approaches used to prepare efavirenz (EVF)-loaded PLGA nanoparticles.*[233] *(c) Droplet microfluidics and associated external gelation set-up for fabricating alginate microspheres with immobilised antibodies, which were immobilised on the porous network of the alginate microsphere during the external cross-linking process.*[234]

1.6 Scalability

Microfluidic reactors are of low cost and environment friendly for the fabrication of NPs. They also provide significant advantages for producing nanoparticles on a large scale. A simple calculation established that seventy reactors with a flow rate of 0.25 mL/min can treat 10 L of reaction solution in 10 h, and given the small reactor size, parallel processing for a number of microfluidic devices is realistic. Thus, such devices have potential for industrial processing with well-controlled reactions.[23] A potential limitation to these approaches is that the amount of a reagent that can be held in a syringe is rather limited, and the continuous flow has to be interrupted for the reloading of reagent.[96] Alternatively, a peristaltic pump can continuously drive droplets flow through the tube at a steady flow rate. Continuous flow of droplet microreactors driven by a peristaltic pump are likely to provide a practical solution to the scaled-up production of nanoparticles/nanocrystals with controlled sizes and shapes, and the formation of composites with other materials in developing functional material in a single reactor.[96] However, as the loading volume increases, there is the risk of particle attachment to the channel walls and channel clogging. Clogging can be overcome using a SDP or VFD operated under continuous flow, as a versatile material processing technology for a diverse range of micro and nanomaterials. However, it should be noted that the VFD and other thin film microfluidic platforms, are distinctly different in imparting high shear stress in the liquid, in moving away from diffusion controlled processing (pro-turbulence).[235] This can impart some benefits over conventional microfluidic devices and channel based laminar flow systems.

1.7 Conclusion

Research on the synthesis of a diversity of micro and nanomaterials in different microfluidic reactors highlights the potential of this technology in medical and allied areas, including bioimaging, tissue engineering, bioencapsulation, drug or gene delivery, protein separation and many other theranostics. However, there are still some problems and challenges, including constant system clogging, insufficient premixing and scaling up. The next generation of microreactors are likely to be specific application-directed and will further develop towards more integrated, automated, modular, and multistage microsystems, incorporating real time, and just in time processing. This is for small volume niche applications where a single microfluidic reactor can suffice, or large volumes where parallel processing for relatively inexpensive devices will be adopted.

1.8 Acknowledgement

The authors gratefully acknowledge financial support from the Australia Research Council and the Government of South Australia.

1.9 References

1. Hao, N.; Nie, Y.; Zhang, J. X. J., Microfluidic synthesis of functional inorganic micro-/nanoparticles and applications in biomedical engineering. *International Materials Reviews* **2018**, 63 (8), 461-487.
2. Carboni, M.; Capretto, L.; Carugo, D.; Stulz, E.; Zhang, X., Microfluidics-based continuous flow formation of triangular silver nanoprisms with tuneable surface plasmon resonance. *Journal of Materials Chemistry C* **2013,** *1* (45), 7540-7546.
3. Puntes, V. F.; Krishnan, K. M.; Alivisatos, A. P., Colloidal nanocrystal shape and size control: the case of cobalt. *Science* **2001,** *291* (5511), 2115-2117.
4. Abalde-Cela, S.; Taladriz-Blanco, P.; de Oliveira, M. G.; Abell, C., Droplet microfluidics for the highly controlled synthesis of branched gold nanoparticles. *Sci Rep* **2018,** *8* (1), 2440-2440.
5. Visaveliya, N.; Köhler, J. M., Single-step microfluidic synthesis of various nonspherical polymer nanoparticles via *in situ* assembling: dominating role of polyelectrolytes molecules. *ACS Applied Materials & Interfaces* **2014,** *6* (14), 11254-11264.
6. Baker, S. N.; Baker, G. A., Luminescent carbon nanodots: emergent nanolights. *Angewandte Chemie International Edition* **2010,** *49* (38), 6726-6744.
7. Boken, J.; Soni, S. K.; Kumar, D., Microfluidic Synthesis of Nanoparticles and their Biosensing Applications. *Critical Reviews in Analytical Chemistry* **2016,** *46* (6), 538-561.
8. Karnik, R.; Gu, F.; Basto, P.; Cannizzaro, C.; Dean, L.; Kyei-Manu, W.; Langer, R.; Farokhzad, O. C., Microfluidic platform for controlled synthesis of polymeric nanoparticles. *Nano Letters* **2008,** *8* (9), 2906-2912.
9. Puigmarti-Luis, J., Microfluidic platforms: a mainstream technology for the preparation of crystals. *Chemical Society Reviews* **2014,** *43* (7), 2253-2271.
10. Hung, L.-H.; Lee, A. P., Microfluidic devices for the synthesis of nanoparticles and biomaterials. *Journal of Medical and Biological Engineering* **2007** *27* (1), 1-6.
11. Atencia, J.; Beebe, D. J., Controlled microfluidic interfaces. *Nature* **2004,** *437*, 648.
12. Tu, S. T.; Yu, X.; Luan, W.; Löwe, H., Development of micro chemical, biological and thermal systems in China: A review. *Chemical Engineering Journal* **2010,** *163* (3), 165-179.
13. Hao, N.; Li, L.; Tang, F., Roles of particle size, shape and surface chemistry of mesoporous silica nanomaterials on biological systems. *International Materials Reviews* **2017,** *62* (2), 57-77.
14. Song, Y.; Hormes, J.; Kumar, C. S. S. R., Microfluidic synthesis of nanomaterials. *Small* **2008,** *4* (6), 698-711.
15. McQuade, D. T.; Seeberger, P. H., Applying flow chemistry: methods, materials, and multistep synthesis. *The Journal of Organic Chemistry* **2013,** *78* (13), 6384-6389.
16. Jahn, A.; Reiner, J. E.; Vreeland, W. N.; DeVoe, D. L.; Locascio, L. E.; Gaitan, M., Preparation of nanoparticles by continuous-flow microfluidics. *Journal of Nanoparticle*

Research **2008,** *10* (6), 925-934.

17. Shah, R. K.; Shum, H. C.; Rowat, A. C.; Lee, D.; Agresti, J. J.; Utada, A. S.; Chu, L.-Y.; Kim, J.-W.; Fernandez-Nieves, A.; Martinez, C. J.; Weitz, D. A., Designer emulsions using microfluidics. *Materials Today* **2008,** *11* (4), 18-27.
18. Kwon, B.-H.; Lee, K. G.; Park, T. J.; Kim, H.; Lee, T. J.; Lee, S. J.; Jeon, D. Y., Continuous In Situ Synthesis of ZnSe/ZnS Core/Shell Quantum Dots in a Microfluidic Reaction System and its Application for Light-Emitting Diodes. *Small* **2012,** *8* (21), 3257-3262.
19. Yen, B. K. H.; Günther, A.; Schmidt, M. A.; Jensen, K. F.; Bawendi, M. G., A microfabricated gas–liquid segmented flow reactor for high-temperature synthesis: the case of CdSe quantum dots. *Angewandte Chemie International Edition* **2005,** *44* (34), 5447-5451.
20. Bhushan, B., *Springer handbook of nanotechnology*. Berlin ; New York : Springer-Verlag: Berlin ; New York, 2004.
21. Edel, J. B.; Fortt, R.; deMello, J. C.; deMello, A. J., Microfluidic routes to the controlled production of nanoparticles. *Chemical Communications* **2002,** (10), 1136-1137.
22. Wang, H.; Li, X.; Uehara, M.; Yamaguchi, Y.; Nakamura, H.; Miyazaki, M.; Shimizu, H.; Maeda, H., Continuous synthesis of CdSe-ZnS composite nanoparticles in a microfluidic reactor. *Chemical Communications* **2004,** *7* (1), 48-49.
23. Nakamura, H.; Yamaguchi, Y.; Miyazaki, M.; Maeda, H.; Uehara, M.; Mulvaney, P., Preparation of CdSe nanocrystals in a micro-flow-reactor. *Chemical communications* **2002,** *0* (23), 2844-2845.
24. Wang, H.; Nakamura, H.; Uehara, M.; Yamaguchi, Y.; Miyazaki, M.; Maeda, H., Highly luminescent CdSe/ZnS nanocrystals synthesized using a single-molecular ZnS source in a microfluidic reactor. *Advanced Functional Materials* **2005,** *15* (4), 603-608.
25. Nakamura, H.; Tashiro, A.; Yamaguchi, Y.; Miyazaki, M.; Watari, T.; Shimizu, H.; Maeda, H., Application of a microfluidic reaction system for CdSe nanocrystal preparation: their growth kinetics and photoluminescence analysis. *Lab on a Chip* **2004,** *4* (3), 237-240.
26. Nightingale, A. M.; de Mello, J. C., Controlled synthesis of III–V quantum dots in microfluidic reactors. *ChemPhysChem* **2009,** *10* (15), 2612-2614.
27. Wan, Z.; Yang, H.; Luan, W.; Tu, S.-t.; Zhou, X., Facile synthesis of monodisperse CdS nanocrystals via microreaction. *Nanoscale Research Letters* **2009,** *5* (1), 130-137.
28. He, S. T.; Liu, Y. L.; Maeda, H., Controlled synthesis of colloidal silver nanoparticles in capillary micro-flow reactor. *Journal of Nanoparticle Research* **2008,** *10* (1), 209-215.
29. Lin, X. Z.; Terepka, A. D.; Yang, H., Synthesis of silver nanoparticles in a continuous flow tubular microreactor. *Nano Letters* **2004,** *4* (11), 2227-2232.
30. Jamal, F.; Jean-Sébastien, G.; Maël, P.; Edmond, P.; Christian, R., Gold nanoparticle synthesis in microfluidic systems and immobilisation in microreactors designed for the catalysis of fine organic reactions. *Microsystem Technologies* **2012,** *18* (2), 151-158.
31. Liu, H.; Huang, J.; Sun, D.; Odoom-Wubah, T.; Li, J.; Li, Q., Continuous-flow biosynthesis of Au–Ag bimetallic nanoparticles in a microreactor. *Journal of Nanoparticle Research* **2014,** *16* (11), 2698-2706.
32. Chan, E. M.; Mathies, R. A.; Alivisatos, A. P., Size-controlled growth of CdSe nanocrystals in microfluidic reactors. *Nano Letters* **2003,** *3* (2), 199-201.
33. Krishnadasan, S.; Brown, R. J. C.; deMello, A. J.; deMello, J. C., Intelligent routes to the controlled synthesis of nanoparticles. *Lab on a Chip* **2007,** *7* (11), 1434-1441.

34. Sounart, T. L.; Safier, P. A.; Voigt, J. A.; Hoyt, J.; Tallant, D. R.; Matzke, C. M.; Michalske, T. A., Spatially-resolved analysis of nanoparticle nucleation and growth in a microfluidic reactor. *Lab on a Chip* **2007,** *7* (7), 908-915.

35. Yen, B. K. H.; Stott, N. E.; Jensen, K. F.; Bawendi, M. G., A continuous-flow microcapillary reactor for the preparation of a size series of CdSe nanocrystals. *Advanced Materials* **2003,** *15* (21), 1858-1862.

36. Yang, H. W.; Luan, W. L.; Tu, S. T., Synthesis of nanocrystals via microreaction with temperature gradient: towards separation of nucleation and growth. *Lab Chip* **2008,** *8*, 451-455.

37. Luan, W. L.; Yang, H. W.; Tu, S. T., Open-to-air synthesis of monodisperse CdSe nanocrystals via microfluidic reaction and its kinetics. *Nanotechnology* **2007,** *18* (17), 1-6.

38. Luan, W. L.; Yang, H. W.; Fan, N. N., Synthesis of efficiently green luminescent CdSe/ZnS nanocrystals via microfluidic reaction. *Nanoscale Research Letters* **2008,** *3* (4), 134-139.

39. Kang, E.; Shin, S.-J.; Lee, K. H.; Lee, S.-H., Novel PDMS cylindrical channels that generate coaxial flow, and application to fabrication of microfibers and particles. *Lab on a Chip* **2010,** *10* (14), 1856-1861.

40. Wang, X.; Ma, X.; An, L.; Kong, X.; Xu, Z.; Wang, J., A pneumatic micromixer facilitating fluid mixing at a wide range flow rate for the preparation of quantum dots. *Science China Chemistry* **2013,** *56* (6), 799-805.

41. Talapin, D. V.; Rogach, A. L.; Kornowski, A.; Haase, M.; Weller, H., Highly luminescent monodisperse CdSe and CdSe/ZnS nanocrystals synthesized in a hexadecylamine−trioctylphosphine Oxide−trioctylphospine mixture. *Nano Letters* **2001,** *1* (4), 207-211.

42. Wang, J.; Zhao, H.; Zhu, Y.; Song, Y., Shape-controlled synthesis of CdSe nanocrystals via a programmed microfluidic process. *The Journal of Physical Chemistry C* **2017,** *121* (6), 3567-3572.

43. Tian, Z.-H.; Xu, J.-H.; Wang, Y.-J.; Luo, G.-S., Microfluidic synthesis of monodispersed CdSe quantum dots nanocrystals by using mixed fatty amines as ligands. *Chemical Engineering Journal* **2016,** *285*, 20-26.

44. Tian, Z.-H.; Wang, Y.-J.; Xu, J.-H.; Luo, G.-S., Intensification of nucleation stage for synthesizing high quality CdSe quantum dots by using preheated precursors in microfluidic devices. *Chemical Engineering Journal* **2016,** *302*, 498-502.

45. Marre, S.; Park, J.; Rempel, J.; Guan, J.; Bawendi, M. G.; Jensen, K. F., Supercritical Continuous-Microflow Synthesis of Narrow Size Distribution Quantum Dots. *Advanced Materials* **2008,** *20* (24), 4830-4834.

46. Yang, C.; Feng, G.; Wang, S.; Dai, J.; Zhang, Y.; Zhou, S., Wavelength-tunable photoluminescence of ZnSe quantum dot micelles synthesized by femtosecond laser ablation in microfluidics. *Chemical Physics Letters* **2017,** *684*, 409-413.

47. Yang, C.; Feng, G.; Dai, S.; Wang, S.; Li, G.; Zhang, H.; Zhou, S., Femtosecond pulsed laser ablation in microfluidics for synthesis of photoluminescent ZnSe quantum dots. *Applied Surface Science* **2017,** *414*, 205-211.

48. Toyota, A.; Nakamura, H.; Ozono, H.; Yamashita, K.; Uehara, M.; Maeda, H., Combinatorial synthesis of CdSe nanoparticles using microreactors. *The Journal of Physical Chemistry C* **2010,** *114* (17), 7527-7534.

49. Swain, B.; Hong, M. H.; Kang, L.; Kim, B. S.; Kim, N.-H.; Lee, C. G., Optimization of CdSe nanocrystals synthesis with a microfluidic reactor and development of combinatorial synthesis process for industrial production. *Chemical Engineering Journal* **2017,** *308*, 311-321.
50. Liu, G.; Ma, X.; Sun, X.; Jia, Y.; Wang, T., Controllable synthesis of silver nanoparticles using three-phase flow pulsating mixing microfluidic chip. *Advances in Materials Science and Engineering* **2018,** *2018*, 14.
51. Patil, G. A.; Bari, M. L.; Bhanvase, B. A.; Ganvir, V.; Mishra, S.; Sonawane, S. H., Continuous synthesis of functional silver nanoparticles using microreactor: Effect of surfactant and process parameters. *Chemical Engineering and Processing: Process Intensification* **2012,** *62*, 69-77.
52. Sharada, S.; Suryawanshi, P. L.; Kumar P, R.; Gumfekar, S. P.; Narsaiah, T. B.; Sonawane, S. H., Synthesis of palladium nanoparticles using continuous flow microreactor. *Colloids and Surfaces A: Physicochemical and Engineering Aspects* **2016,** *498*, 297-304.
53. Sugano, K.; Uchida, Y.; Ichihashi, O.; Yamada, H.; Tsuchiya, T.; Tabata, O., Mixing speed-controlled gold nanoparticle synthesis with pulsed mixing microfluidic system. *Microfluidics and Nanofluidics* **2010,** *9* (6), 1165-1174.
54. Singh, A.; Shirolkar, M.; Lalla, N. P.; Khan Malek, C., Room temperature, water-based, microreactor synthesis of gold and silver nanoparticles. *International Journal of Nanotechnology* **2009**; 6 (5-6), 541-551.
55. Shen, X.; Song, Y.; Li, S.; Li, R.; Ji, S.; Li, Q.; Duan, H.; Xu, R.; Yang, W.; Zhao, K.; Rong, R.; Wang, X., Spatiotemporal-resolved nanoparticle synthesis via simple programmed microfluidic processes. *RSC Advances* **2014,** *4* (64), 34179-34188.
56. Lin, S.; Lin, K.; Lu, D.; Liu, Z., Preparation of uniform magnetic iron oxide nanoparticles by co-precipitation in a helical module microchannel reactor. *Journal of Environmental Chemical Engineering* **2017,** *5* (1), 303-309.
57. Hwang, C. M.; Khademhosseini, A.; Park, Y.; Sun, K.; Lee, S.-H., Microfluidic chip-based fabrication of PLGA microfiber scaffolds for tissue engineering. *Langmuir* **2008,** *24* (13), 6845-6851.
58. Hwang, D. K.; Dendukuri, D.; Doyle, P. S., Microfluidic-based synthesis of non-spherical magnetic hydrogel microparticles. *Lab on a Chip* **2008,** *8* (10), 1640-1647.
59. Lee, K. H.; Shin, S. J.; Park, Y.; Lee, S. H., Synthesis of cell-laden alginate hollow fibers using microfluidic chips and microvascularized tissue-engineering applications. *Small* **2009,** *5* (11), 1264-1268.
60. Wang, L.; Ma, S.; Yang, B.; Cao, W.; Han, X., Morphology-controlled synthesis of Ag nanoparticle decorated poly(o-phenylenediamine) using microfluidics and its application for hydrogen peroxide detection. *Chemical Engineering Journal* **2015,** *268*, 102-108.
61. Lee, B. R.; Lee, K. H.; Kang, E.; Kim, D.-S.; Lee, S.-H., Microfluidic wet spinning of chitosan-alginate microfibers and encapsulation of HepG2 cells in fibers. *Biomicrofluidics* **2011,** *5* (2), 022208.
62. Lewis, C. L.; Lin, Y.; Yang, C.; Manocchi, A. K.; Yuet, K. P.; Doyle, P. S.; Yi, H., Microfluidic fabrication of hydrogel microparticles containing functionalized viral nanotemplates. *Langmuir* **2010,** *26* (16), 13436-13441.
63. Jung, J.-H.; Choi, C.-H.; Chung, S.; Chung, Y.-M.; Lee, C.-S., Microfluidic synthesis of a cell adhesive Janus polyurethane microfiber. *Lab on a Chip* **2009,** *9* (17), 2596-2602.

64. Shiba, K.; Sugiyama, T.; Takei, T.; Yoshikawa, G., Controlled growth of silica-titania hybrid functional nanoparticles through a multistep microfluidic approach. *Chemical Communications* **2015,** *51* (87), 15854-15857.
65. Hung, L.-h.; Choi, K. M.; Tseng, W.-y.; Tan, Y.-c.; Shea, K. J.; Lee, A. P., Alternating droplet generation and controlled dynamic droplet fusion in microfluidic device for CdS nanoparticle synthesis. *Lab on a Chip* **2006,** *6* (2), 174-178.
66. Shestopalov, I.; Tice, J. D.; Ismagilov, R. F., Multi-step synthesis of nanoparticles performed on millisecond time scale in a microfluidic droplet-based system. *Lab on a Chip* **2004,** *4* (4), 316-321.
67. Yen, B. K. H.; Günther, A.; Schmidt, M. A.; Jensen, K. F.; Bawendi, M. G., A microfabricated gas–liquid segmented flow reactor for high-temperature synthesis: the case of CdSe quantum dots. *Angewandte Chemie International Edition* **2005,** *44* (34), 5447-5451.
68. Larrea, A.; Sebastian, V.; Ibarra, A.; Arruebo, M.; Santamaria, J., Gas slug microfluidics: a unique tool for ultrafast, highly controlled growth of iron oxide nanostructures. *Chemistry of Materials* **2015,** *27* (12), 4254-4260.
69. Günther, A.; Jhunjhunwala, M.; Thalmann, M.; Schmidt, M. A.; Jensen, K. F., Micromixing of miscible liquids in segmented gas−liquid flow. *Langmuir* **2005,** *21* (4), 1547-1555.
70. Schumacher, J. T.; Grodrian, A.; Kremin, C.; Hoffmann, M.; Metze, J., Hydrophobic coating of microfluidic chips structured by SU-8 polymer for segmented flow operation. *Journal of Micromechanics and Microengineering* **2008,** *18* (5), 1-6.
71. Song, H.; Bringer, M. R.; Tice, J. D.; Gerdts, C. J.; Ismagilov, R. F., Experimental test of scaling of mixing by chaotic advection in droplets moving through microfluidic channels. *Applied physics letters* **2003,** *83* (12), 4664-4666.
72. Xu, Z.; Lu, C.; Riordon, J.; Sinton, D.; Moffitt, M. G., Microfluidic manufacturing of polymeric nanoparticles: comparing flow control of multiscale structure in single-phase staggered herringbone and two-phase reactors. *Langmuir* **2016,** *32* (48), 12781-12789.
73. Sebastian, V.; Smith, C.; F. Jensen, K., *Shape-controlled continuous synthesis of metal nanostructures*. Nanoscale **2016**, *8* (14), 7534-7543.
74. Sebastian Cabeza, V.; Kuhn, S.; Kulkarni, A. A.; Jensen, K. F., Size-controlled flow synthesis of gold nanoparticles using a segmented flow microfluidic platform. *Langmuir* **2012,** *28* (17), 7007-7013.
75. Arndt, D.; Thöming, J.; Bäumer, M., Improving the quality of nanoparticle production by using a new biphasic synthesis in a slug flow microreactor. *Chemical Engineering Journal* **2013,** *228*, 1083-1091.
76. Knauer, A.; Thete, A.; Li, S.; Romanus, H.; Csáki, A.; Fritzsche, W.; Köhler, J. M., Au/Ag/Au double shell nanoparticles with narrow size distribution obtained by continuous micro segmented flow synthesis. *Chemical Engineering Journal* **2011,** *166* (3), 1164-1169.
77. Bains, A.; Moffitt, M. G., Effects of chemical and processing variables on paclitaxel-loaded polymer nanoparticles prepared using microfluidics. *Journal of Colloid and Interface Science* **2017,** *508*, 203-213.
78. Albuquerque, G. H.; Fitzmorris, R. C.; Ahmadi, M.; Wannenmacher, N.; Thallapally, P. K.; McGrail, B. P.; Herman, G. S., Gas-liquid segmented flow microwave-assisted synthesis of MOF-74(Ni) under moderate pressures. *CrystEngComm* **2015,** *17* (29), 5502-5510.
79. Paseta, L.; Seoane, B.; Julve, D.; Sebastián, V.; Téllez, C.; Coronas, J., Accelerating the

controlled synthesis of metal–organic frameworks by a microfluidic approach: a nanoliter continuous reactor. *ACS Applied Materials & Interfaces* **2013,** *5* (19), 9405-9410.

80. Zhao, C.-X.; He, L.; Qiao, S. Z.; Middelberg, A. P. J., Nanoparticle synthesis in microreactors. *Chemical Engineering Science* **2011,** *66* (7), 1463-1479.
81. Demello, J.; Demello, A., Microscale reactors: nanoscale products. *Lab on a chip* **2004,** *4* (2), 11N-15N.
82. Christopher, G. F.; Anna, S. L., Microfluidic methods for generating continuous droplet streams. *Journal of Physics D: Applied Physics* **2007,** *40* (19), R319-R336.
83. Kumachev, A.; Greener, J.; Tumarkin, E.; Eiser, E.; Zandstra, P. W.; Kumacheva, E., High-throughput generation of hydrogel microbeads with varying elasticity for cell encapsulation. *Biomaterials* **2011,** *32* (6), 1477-1483.
84. Thorsen, T.; Roberts, R. W.; Arnold, F. H.; Quake, S. R., Dynamic pattern formation in a vesicle-generating microfluidic device. *Physical Review Letters* **2001,** *86* (18), 4163-4166.
85. Dendukuri, D.; Doyle, P. S., The Synthesis and Assembly of Polymeric Microparticles Using Microfluidics. *Advanced Materials* **2009,** *21* (41), 4071-4086.
86. Seemann, R.; Brinkmann, M.; Pfohl, T.; Herminghaus, S., Droplet based microfluidics. *Reports on Progress in Physics* **2012,** *75* (1), 1-41.
87. Wang, J.-T.; Wang, J.; Han, J.-J., Fabrication of advanced particles and particle-based materials assisted by droplet-based microfluidics. *Small* **2011,** *7* (13), 1728-1754.
88. Nightingale, A. M.; Krishnadasan, S. H.; Berhanu, D.; Niu, X.; Drury, C.; McIntyre, R.; Valsami-Jones, E.; deMello, J. C., A stable droplet reactor for high temperature nanocrystal synthesis. *Lab on a Chip* **2011,** *11* (7), 1221-1227.
89. Chan, E. M.; Alivisatos, A. P.; Mathies, R. A., High-temperature microfluidic synthesis of CdSe nanocrystals in nanoliter droplets. *Journal of the American Chemical Society* **2005**, 127 (40), 13854-13861.
90. Ji, X.-H.; Cheng, W.; Guo, F.; Liu, W.; Guo, S.-S.; He, Z.-K.; Zhao, X.-Z., On-demand preparation of quantum dot-encoded microparticles using a droplet microfluidic system. *Lab on a Chip* **2011,** *11* (15), 2561-2568.
91. Hoang, P. H.; Dien, L. Q., Fast synthesis of an inorganic-organic block copolymer in a droplet-based microreactor. *RSC Advances* **2014,** *4* (16), 8283-8288.
92. Li, J.; Lindley-Start, J.; Porch, A.; Barrow, D., Continuous and scalable polymer capsule processing for inertial fusion energy target shell fabrication using droplet microfluidics. *Scientific Reports* **2017,** *7* (1), 1-10.
93. Wang, B.; Shum, H. C.; Weitz, D. A., Fabrication of monodisperse toroidal particles by polymer Solidification in Microfluidics. *ChemPhysChem* **2009,** *10* (4), 641-645.
94. Kim, Y. H.; Zhang, L.; Yu, T.; Jin, M.; Qin, D.; Xia, Y., Droplet-based microreactors for continuous production of palladium nanocrystals with controlled sizes and shapes. *Small* **2013,** *9* (20), 3462-3467.
95. Kumar, K.; Nightingale, A. M.; Krishnadasan, S. H.; Kamaly, N.; Wylenzinska-Arridge, M.; Zeissler, K.; Branford, W. R.; Ware, E.; deMello, A. J.; deMello, J. C., Direct synthesis of dextran-coated superparamagnetic iron oxide nanoparticles in a capillary-based droplet reactor. *Journal of Materials Chemistry* **2012,** *22* (11), 4704-4708.
96. Zhang, L.; Wang, Y.; Tong, L.; Xia, Y., Seed-mediated synthesis of silver nanocrystals with controlled sizes and shapes in droplet microreactors separated by air. *Langmuir*

2013, *29* (50), 15719-15725.

97. Faustini, M.; Kim, J.; Jeong, G.-Y.; Kim, J. Y.; Moon, H. R.; Ahn, W.-S.; Kim, D.-P., Microfluidic approach toward continuous and ultrafast synthesis of metal–organic framework crystals and hetero structures in confined microdroplets. *Journal of the American Chemical Society* **2013,** *135* (39), 14619-14626.
98. Faustini, M.; Kim, J.; Ahn, W. S.; Kim, D., *Microfluidic synthesis of metal organic frameworks crystals into confined microdroplets*. *16th International Conference on Miniaturized Systems for Chemistry and Life Sciences* **2012**, 1213-1215.
99. Zhao, C.-X.; Middelberg, A. P. J., Microfluidic synthesis of monodisperse hierarchical silica particles with raspberry-like morphology. *RSC Advances* **2013,** *3* (44), 21227-21230.
100. Wacker, J. B.; Lignos, I.; Parashar, V. K.; Gijs, M. A. M., Controlled synthesis of fluorescent silica nanoparticles inside microfluidic droplets. *Lab Chip* **2012,** *12* (17), 3111-3116.
101. Tachibana, M.; Engl, W.; Panizza, P.; Deleuze, H.; Lecommandoux, S.; Ushiki, H.; Backov, R., Combining sol–gel chemistry and millifluidic toward engineering microporous silica ceramic final sizes and shapes: An Integrative Chemistry approach. *Chemical Engineering and Processing: Process Intensification* **2008,** *47* (8), 1317-1322.
102. Fang, A.; Gaillard, C.; Douliez, J.-P., Template-free formation of monodisperse doughnut-shaped silica microparticles by droplet-based microfluidics. *Chemistry of Materials* **2011,** *23* (21), 4660-4662.
103. Li, D.; Guan, Z.; Zhang, W.; Zhou, X.; Zhang, W. Y.; Zhuang, Z.; Wang, X.; Yang, C. J., Synthesis of uniform-size hollow silica microspheres through interfacial polymerization in monodisperse water-in-oil droplets. *ACS Applied Materials & Interfaces* **2010,** *2* (10), 2711-2714.
104. Chu, L. Y.; Utada, A. S.; Shah, R. K.; Kim, J. W.; Weitz, D. A., Controllable monodisperse multiple emulsions. *Angewandte Chemie International Edition* **2007,** *46* (47), 8970-8974.
105. Lan, W.; Li, S.; Xu, J.; Luo, G., Controllable preparation of nanoparticle-coated chitosan microspheres in a co-axial microfluidic device. *Lab on a Chip* **2011,** *11* (4), 652-657.
106. Ekanem, E. E.; Zhang, Z.; Vladisavljević, G. T., Facile microfluidic production of composite polymer core-shell microcapsules and crescent-shaped microparticles. *Journal of Colloid and Interface Science* **2017,** *498*, 387-394.
107. Chen, P. W.; Erb, R. M.; Studart, A. R., Designer polymer-based microcapsules made using microfluidics. *Langmuir* **2012,** *28* (1), 144-152.
108. Nisisako, T.; Suzuki, H.; Hatsuzawa, T., Biconvex polymer microlenses with tunable imaging properties designed by janus droplet microfluidics. *Micromachines* **2015,** *6* (10), 1435-1444.
109. Utech, S.; Prodanovic, R.; Mao, A. S.; Ostafe, R.; Mooney, D. J.; Weitz, D. A., Microfluidic generation of monodisperse, structurally homogeneous alginate microgels for cell encapsulation and 3D cell culture. *Advanced healthcare materials* **2015,** *4* (11), 1628-1633.
110. Zeng, Y.; Novak, R.; Shuga, J.; Smith, M. T.; Mathies, R. A., High-performance single cell genetic analysis using microfluidic emulsion generator arrays. *Analytical Chemistry* **2010,** *82* (8), 3183-3190.
111. Nisisako, T.; Torii, T., Microfluidic large-scale integration on a chip for mass production of monodisperse droplets and particles. *Lab on a Chip* **2008,** *8* (2), 287-293.

112. Gutierrez, L.; Gomez, L.; Irusta, S.; Arruebo, M.; Santamaria, J., Comparative study of the synthesis of silica nanoparticles in micromixer–microreactor and batch reactor systems. *Chemical Engineering Journal* **2011,** *171* (2), 674-683.

113. He, P.; Greenway, G.; Haswell, S. J., Microfluidic synthesis of silica nanoparticles using polyethylenimine polymers. *Chemical Engineering Journal* **2011,** *167* (2), 694-699.

114. Su, Y.-W.; Paul, B. K.; Chang, C.-h., Investigation of CdS nanoparticles formation and deposition by the continuous flow microreactor. *Applied Surface Science* **2018**, DOI.org/10.1016/j.apsusc.2018.02.157.

115. Zhu, L.; Yin, Y.; Wang, C.-F.; Chen, S., Plant leaf-derived fluorescent carbon dots for sensing, patterning and coding. *Journal of Materials Chemistry C* **2013,** *1* (32), 4925-4932.

116. Habault, D.; Dery, A.; Leng, J.; Lecommandoux, S.; Meins, J. F. L.; Sandre, O., Droplet Microfluidics to Prepare Magnetic Polymer Vesicles and to Confine the Heat in Magnetic Hyperthermia. *IEEE Transactions on Magnetics* **2013,** *49* (1), 182-190.

117. Cacho-Bailo, F.; Catalán-Aguirre, S.; Etxeberría-Benavides, M.; Karvan, O.; Sebastian, V.; Téllez, C.; Coronas, J., Metal-organic framework membranes on the inner-side of a polymeric hollow fiber by microfluidic synthesis. *Journal of Membrane Science* **2015,** *476*, 277-285.

118. Xu, L.; Peng, J.; Srinivasakannan, C.; Chen, G.; Shen, A. Q., Synthesis of copper nanocolloids using a continuous flow based microreactor. *Applied Surface Science* **2015,** *355*, 1-6.

119. Liu, Y.; Cheng, C.; Liu, Y.; Prud'homme, R. K.; Fox, R. O., Mixing in a multi-inlet vortex mixer (MIVM) for flash nano-precipitation. *Chemical Engineering Science* **2008,** *63* (11), 2829-2842.

120. Mejia-Ariza, R.; Huskens, J., Formation of hybrid gold nanoparticle network aggregates by specific host–guest interactions in a turbulent flow reactor. *Journal of Materials Chemistry B* **2014,** *2* (2), 210-216.

121. Yang, H.; Fan, N.; Luan, W.; Tu, S.-t., Synthesis of monodisperse nanocrystals via microreaction: open-to-air synthesis with oleylamine as a coligand. *Nanoscale Research Letters* **2009,** *4* (4), 344-352.

122. Ding, S.; Attia, M. F.; Wallyn, J.; Taddei, C.; Serra, C. A.; Anton, N.; Kassem, M.; Schmutz, M.; Er-Rafik, M.; Messaddeq, N.; Collard, A.; Yu, W.; Giordano, M.; Vandamme, T. F., Microfluidic-assisted production of size-controlled superparamagnetic iron oxide nanoparticles-loaded poly(methyl methacrylate) nanohybrids. *Langmuir* **2018,** *34* (5), 1981-1991.

123. Watanabe, S.; Ohsaki, S.; Fukuta, A.; Hanafusa, T.; Takada, K.; Tanaka, H.; Maki, T.; Mae, K.; Miyahara, M. T., Characterization of mixing performance in a microreactor and its application to the synthesis of porous coordination polymer particles. *Advanced Powder Technology* **2017,** *28* (11), 3104-3110.

124. Zhang, L.; Wang, Y.; Tong, L.; Xia, Y., Synthesis of colloidal metal nanocrystals in droplet reactors: the pros and cons of interfacial adsorption. *Nano Letters* **2014,** *14* (7), 4189-4194.

125. Cai, G.; Xue, L.; Zhang, H.; Lin, J., A review on micromixers. *Micromachines* **2017,** *8* (9), 1-27.

126. Tang, M.; Wang, G.; Kong, S.-K.; Ho, H.-P., A review of biomedical centrifugal microfluidic platforms. *Micromachines* **2016,** *7* (2), 1-29.

127. Madou, M.; Zoval, J.; Jia, G.; Kido, H.; Kim, J.; Kim, N., Lab on a CD. *Annual Review of Biomedical Engineering* **2006,** *8* (1), 601-628.

128. Kong, L. X.; Perebikovsky, A.; Moebius, J.; Kulinsky, L.; Madou, M., Lab-on-a-CD: A fully integrated molecular diagnostic system. *Journal of Laboratory Automation* **2015,** *21* (3), 323-355.

129. Burger, R.; Ducrée, J., Handling and analysis of cells and bioparticles on centrifugal microfluidic platforms. *Expert Review of Molecular Diagnostics* **2012,** *12* (4), 407-421.

130. Hwang, H.; Kim, Y.; Cho, J.; Lee, J.-y.; Choi, M.-S.; Cho, Y.-K., Lab-on-a-Disc for simultaneous determination of nutrients in water. *Analytical Chemistry* **2013,** *85* (5), 2954-2960.

131. Gilmore, J.; Islam, M.; Martinez-Duarte, R., Challenges in the use of compact disc-based centrifugal microfluidics for healthcare diagnostics at the extreme point of care. *Micromachines* **2016,** *7* (4), 1-26.

132. Chen, X.; Smith, N. M.; Iyer, K. S.; Raston, C. L., Controlling nanomaterial synthesis, chemical reactions and self assembly in dynamic thin films. *Chemical Society Reviews* **2014,** *43* (5), 1387-1399.

133. Loh, J. W.; Schneider, J.; Carter, M.; Saunders, M.; Lim, L.-Y., Spinning disc processing technology: potential for large-scale manufacture of chitosan nanoparticles. *Journal of Pharmaceutical Sciences* **2010,** *99* (10), 4326-4336.

134. Vimalanathan, K.; Raston, C. L., Dynamic thin films in controlling the fabrication of nanocarbon and its composites. *Advanced Materials Technologies* **2017**, DOI: 10.1002/admt.201600298.

135. Huanbutta, K.; Sriamornsak, P.; Luangtana-anan, M.; Limmatvapirat, S.; Puttipipatkhachorn, S.; Lim, L.-Y.; Terada, K.; Nunthanid, J., Application of multiple stepwise spinning disk processing for the synthesis of poly(methyl acrylates) coated chitosan–diclofenac sodium nanoparticles for colonic drug delivery. *European Journal of Pharmaceutical Sciences* **2013,** *50* (3), 303-311.

136. Kim, T.-H.; Park, J.; Kim, C.-J.; Cho, Y.-K., Fully integrated lab-on-a-disc for nucleic acid analysis of food-borne pathogens. *Analytical Chemistry* **2014,** *86* (8), 3841-3848.

137. Yasmin, L.; Chen, X.; Stubbs, K. A.; Raston, C. L., Optimising a vortex fluidic device for controlling chemical reactivity and selectivity. *Sci. Rep.* **2013,** *3*, 1-6.

138. Luo, X.; Al-Antaki, A. H. M.; Harvey, D. P.; Ruan, Y.; He, S.; Zhang, W.; Raston, C. L., Vortex fluidic mediated synthesis of macroporous bovine serum albumin-based microspheres. *ACS Applied Materials & Interfaces* **2018**, *10* (32), 27224-27232.

139. Tong, C. L.; Boulos, R. A.; Yu, C.; Iyer, K. S.; Raston, C. L., Continuous flow tuning of ordered mesoporous silica under ambient conditions. *RSC Advances* **2013,** *3* (41), 18767-18770.

140. Britton, J.; Meneghini, L. M.; Raston, C. L.; Weiss, G. A., Accelerating enzymatic catalysis using vortex fluidics. *Angewandte Chemie International Edition* **2016,** *55* (38), 11387-11391.

141. Luo, X.; Al-Antaki, A. H. M.; Pye, S.; Meech, R.; Zhang, W.; Raston, C. L., High shear imparted tunable fluorescence in polyethylenimines. *ChemPhotoChem*, **2018**, *2* (4), 343-348.

142. Yuan, T. Z.; Ormonde, C. F. G.; Kudlacek, S. T.; Kunche, S.; Smith, J. N.; Brown, W. A.; Pugliese, K. M.; Olsen, T. J.; Iftikhar, M.; Raston, C. L.; Weiss, G. A., Shear-stress-mediated refolding of proteins from aggregates and inclusion bodies. *ChemBioChem*

2015, *16* (3), 393-396.

143. Chen, X.; Yasin, F. M.; Eggers, P. K.; Boulos, R. A.; Duan, X.; Lamb, R. N.; Iyer, K. S.; Raston, C. L., Non-covalently modified graphene supported ultrafine nanoparticles of palladium for hydrogen gas sensing. *RSC Advances* **2013,** *3* (10), 3213-3217.
144. Chen, X.; Dobson, J. F.; Raston, C. L., Vortex fluidic exfoliation of graphite and boron nitride. *Chemical Communications* **2012,** *48* (31), 3703-3705.
145. Vimalanathan, K.; Chen, X.; Raston, C. L., Shear induced fabrication of intertwined single walled carbon nanotube rings. *Chemical Communications* **2014,** *50* (77), 11295-11298.
146. Goh, Y. A.; Chen, X.; Yasin, F. M.; Eggers, P. K.; Boulos, R. A.; Wang, X.; Chua, H. T.; Raston, C. L., Shear flow assisted decoration of carbon nano-onions with platinum nanoparticles. *Chemical Communications* **2013,** *49* (45), 5171-5173.
147. Yasin, F. M.; Boulos, R. A.; Hong, B. Y.; Cornejo, A.; Iyer, K. S.; Gao, L.; Chua, H. T.; Raston, C. L., Microfluidic size selective growth of palladium nano-particles on carbon nano-onions. *Chemical Communications* **2012,** *48* (81), 10102-10104.
148. Luo, X.; Al-Antaki, A. H. M.; Vimalanathan, K.; Moffatt, J.; Zheng, K.; Zou, Y.; Zou, J.; Duan, X.; Lamb, R. N.; Wang, S.; Li, Q.; Zhang, W.; Raston, C. L., Laser irradiated vortex fluidic mediated synthesis of luminescent carbon nanodots under continuous flow. *Reaction Chemistry & Engineering* **2018**, *3* (2), 164-170.
149. Vimalanathan, K.; Gascooke, J. R.; Suarez-Martinez, I.; Marks, N. A.; Kumari, H.; Garvey, C. J.; Atwood, J. L.; Lawrance, W. D.; Raston, C. L., Fluid dynamic lateral slicing of high tensile strength carbon nanotubes. *Scientific Reports* **2016,** *6*, DOI: 10.1038/srep22865.
150. Alharbi, T.; Vimalanathan, K.; D. Lawrance, W.; Raston, C., Controlled slicing of single walled carbon nanotubes under continuous flow. *Carbon* **2018**, *140*, 428-432.
151. Wahid, M. H.; Eroglu, E.; Chen, X.; Smith, S. M.; Raston, C. L., Functional multi-layer graphene-algae hybrid material formed using vortex fluidics. *Green Chemistry* **2013,** *15* (3), 650-655.
152. Jensen, K. F., Microreaction engineering — is small better? *Chemical Engineering Science* **2001,** *56* (2), 293-303.
153. Udoh, C. E.; Garbin, V.; Cabral, J. T., Microporous polymer particles via phase inversion in microfluidics: impact of nonsolvent quality. *Langmuir* **2016,** *32* (32), 8131-8140.
154. Biswas, S.; Miller Jeffrey, T.; Li, Y.; Nandakumar, K.; Kumar Challa, S. S. R., Developing a millifluidic platform for the synthesis of ultrasmall nanoclusters: ultrasmall copper nanoclusters as a case Study. *Small* **2012,** *8* (5), 688-698.
155. Seo, M.; Gorelikov, I.; Williams, R.; Matsuura, N., Microfluidic assembly of monodisperse, nanoparticle-incorporated perfluorocarbon microbubbles for medical imaging and therapy. *Langmuir* **2010,** *26* (17), 13855-13860.
156. Hong, L.; Cheung, T.-L.; Rao, N.; Ouyang, Q.; Wang, Y.; Zeng, S.; Yang, C.; Cuong, D.; Chong, P. H. J.; Liu, L.; Law, W.-C.; Yong, K.-T., Millifluidic synthesis of cadmium sulfide nanoparticles and their application in bioimaging. *RSC Advances* **2017,** *7* (58), 36819-36832.
157. Wang, H.; Nakamura, H.; Uehara, M.; Miyazaki, M.; Maeda, H., Preparation of titania particles utilizing the insoluble phase interface in a microchannel reactor. *Chemical Communications* **2002,** *0* (14), 1462-1463.
158. Zeng, S.; Baillargeat, D.; Ho, H.-P.; Yong, K.-T., Nanomaterials enhanced surface

plasmon resonance for biological and chemical sensing applications. *Chemical Society Reviews* **2014,** *43* (10), 3426-3452.

159. Hu, S.; Zeng, S.; Zhang, B.; Yang, C.; Song, P.; Hang Danny, T. J.; Lin, G.; Wang, Y.; Anderson, T.; Coquet, P.; Liu, L.; Zhang, X.; Yong, K.-T., Preparation of biofunctionalized quantum dots using microfluidic chips for bioimaging. *Analyst* **2014,** *139* (18), 4681-4690.
160. Pedro, S. G.-d.; Salinas-Castillo, A.; Ariza-Avidad, M.; Lapresta-Fernandez, A.; Sanchez-Gonzalez, C.; Martinez-Cisneros, C. S.; Puyol, M.; Capitan-Vallvey, L. F.; Alonso-Chamarro, J., Microsystem-assisted synthesis of carbon dots with fluorescent and colorimetric properties for pH detection. *Nanoscale* **2014,** *6* (11), 6018-6024.
161. Qu, K.; Wang, J.; Ren, J.; Qu, X., Carbon dots prepared by hydrothermal treatment of dopamine as an effective fluorescent sensing platform for the label-free detection of iron(III) ions and dopamine. *Chemistry – A European Journal* **2013,** *19* (22), 7243-7249.
162. Li, S.; Hu, K.; Cao, W.; Sun, Y.; Sheng, W.; Li, F.; Wu, Y.; Liang, X.-J., pH-responsive biocompatible fluorescent polymer nanoparticles based on phenylboronic acid for intracellular imaging and drug delivery. *Nanoscale* **2014,** *6* (22), 13701-13709.
163. Luo, X.; Al-Antaki, A. H. M.; Pye, S.; Meech, R.; Zhang, W.; Raston, C. L., High shear imparted tunable fluorescence in polyethylenimines. *ChemPhotoChem*, **2018**, *2* (4), 343-348.
164. Neel, E. A. A.; Young, A. M.; Nazhat, S. N.; Knowles, J. C., A facile synthesis route to prepare microtubes from phosphate glass fibres. *Advanced Materials* **2007,** *19* (19), 2856-2862.
165. Khademhosseini, A.; Langer, R.; Borenstein, J.; Vacanti, J. P., Microscale technologies for tissue engineering and biology. *Proceedings of the National Academy of Sciences of the United States of America* **2006,** *103* (8), 2480-2487.
166. Lavik, E.; Langer, R., Tissue engineering: current state and perspectives. *Applied Microbiology and Biotechnology* **2004,** *65* (1), 1-8.
167. Liang, D.; Hsiao, B. S.; Chu, B., Functional Electrospun Nanofibrous Scaffolds for Biomedical Applications. *Advanced drug delivery reviews* **2007,** *59* (14), 1392-1412.
168. Lee, Y. H.; Lee, J. H.; An, I.-G.; Kim, C.; Lee, D. S.; Lee, Y. K.; Nam, J.-D., Electrospun dual-porosity structure and biodegradation morphology of Montmorillonite reinforced PLLA nanocomposite scaffolds. *Biomaterials* **2005,** *26* (16), 3165-3172.
169. Jia, J.; Yao, D.; Wang, Y., Melt spinning of continuous fibers by cold air attenuation I: experimental studies. *Textile Research Journal* **2014,** *84* (6), 593-603.
170. Okuzaki, H.; Harashina, Y.; Yan, H., Highly conductive PEDOT/PSS microfibers fabricated by wet-spinning and dip-treatment in ethylene glycol. *European Polymer Journal* **2009,** *45* (1), 256-261.
171. Kidoaki, S.; Kwon, I. K.; Matsuda, T., Mesoscopic spatial designs of nano- and microfiber meshes for tissue-engineering matrix and scaffold based on newly devised multilayering and mixing electrospinning techniques. *Biomaterials* **2005,** *26* (1), 37-46.
172. Wang, W.; Itoh, S.; Matsuda, A.; Ichinose, S.; Shinomiya, K.; Hata, Y.; Tanaka, J., Influences of mechanical properties and permeability on chitosan nano/microfiber mesh tubes as a scaffold for nerve regeneration. *Journal of Biomedical Materials Research Part A* **2008,** *84A* (2), 557-566.
173. Fridrikh, S. V.; Yu, J. H.; Brenner, M. P.; Rutledge, G. C., Controlling the fiber diameter during electrospinning. *Physical Review Letters* **2003,** *90* (14), 1-4.

174. Hwang, C. M.; Park, Y.; Park, J. Y.; Lee, K.; Sun, K.; Khademhosseini, A.; Lee, S. H., Controlled cellular orientation on PLGA microfibers with defined diameters. *Biomedical Microdevices* **2009,** *11* (4), 739-746.

175. Lee, K. H.; Shin, S. J.; Kim, C.-B.; Kim, J. K.; Cho, Y. W.; Chung, B. G.; Lee, S.-H., Microfluidic synthesis of pure chitosan microfibers for bio-artificial liver chip. *Lab on a Chip* **2010,** *10* (10), 1328-1334.

176. Tsai, W.-B.; Lin, J.-H., Modulation of morphology and functions of human hepatoblastoma cells by nano-grooved substrata. *Acta Biomater* **2009,** *5* (5), 1442-1454.

177. Jozwiak, A. B.; Kielty, C. M.; Black, R. A., Surface functionalization of polyurethane for the immobilization of bioactive moieties on tissue scaffolds. *Journal of Materials Chemistry* **2008,** *18* (19), 2240-2248.

178. Chung, B. G.; Lee, K.-H.; Khademhosseini, A.; Lee, S.-H., Microfluidic fabrication of microengineered hydrogels and their application in tissue engineering. *Lab on a Chip* **2012,** *12* (1), 45-59.

179. Pelham, R. J.; Wang, Y.-l., Cell locomotion and focal adhesions are regulated by substrate flexibility. *Proceedings of the National Academy of Sciences* **1997,** *94* (25), 13661-13665.

180. Coakley, R. J.; Taggart, C.; McElvaney, N. G.; O'Neill, S. J., Cytosolic pH and the inflammatory microenvironment modulate cell death in human neutrophils after phagocytosis. *Blood* **2002,** *100* (9), 3383-3391.

181. Vidane, A. S.; Zomer, H. D.; Oliveira, B. M. M.; Guimarães, C. F.; Fernandes, C. B.; Perecin, F.; Silva, L. A.; Miglino, M. A.; Meirelles, F. V.; Ambrósio, C. E., Reproductive stem cell differentiation: extracellular matrix, tissue microenvironment, and growth factors direct the mesenchymal stem cell lineage commitment. *Reproductive Sciences* **2013,** *20* (10), 1137-1143.

182. Discher, D. E.; Mooney, D. J.; Zandstra, P. W., Growth factors, matrices, and forces combine and control stem cells. *Science* **2009,** *324* (5935), 1673-1677.

183. Liu, K.; Deng, Y.; Zhang, N.; Li, S.; Ding, H.; Guo, F.; Liu, W.; Guo, S.; Zhao, X.-Z., Generation of disk-like hydrogel beads for cell encapsulation and manipulation using a droplet-based microfluidic device. *Microfluidics and Nanofluidics* **2012,** *13* (5), 761-767.

184. Velasco, D.; Tumarkin, E.; Kumacheva, E., Microfluidic encapsulation of cells in polymer microgels. *Small* **2012,** *8* (11), 1633-1642.

185. Hwang, C. M.; Sant, S.; Masaeli, M.; Kachouie, N. N.; Zamanian, B.; Lee, S.-H.; Khademhosseini, A., Fabrication of three-dimensional porous cell-laden hydrogel for tissue engineering. *Biofabrication* **2010,** *2* (3), 035003-035003.

186. Buwalda, S. J.; Vermonden, T.; Hennink, W. E., Hydrogels for therapeutic delivery: current developments and future directions. *Biomacromolecules* **2017,** *18* (2), 316-330.

187. Silva, C. M.; Ribeiro, A. J.; Figueiredo, M.; Ferreira, D.; Veiga, F., Microencapsulation of hemoglobin in chitosan-coated alginate microspheres prepared by emulsification/internal gelation. *The AAPS Journal* **2005,** *7* (4), E903-E913.

188. Clausell-Tormos, J.; Lieber, D.; Baret, J.-C.; El-Harrak, A.; Miller, O. J.; Frenz, L.; Blouwolff, J.; Humphry, K. J.; Köster, S.; Duan, H.; Holtze, C.; Weitz, D. A.; Griffiths, A. D.; Merten, C. A., Droplet-based microfluidic platforms for the encapsulation and screening of mammalian cells and multicellular organisms. *Chemistry & Biology* **2008,** *15* (5), 427-437.

189. Shim, J.-u.; Olguin, L. F.; Whyte, G.; Scott, D.; Babtie, A.; Abell, C.; Huck, W. T. S.;

Hollfelder, F., Simultaneous determination of gene expression and enzymatic activity in individual bacterial cells in microdroplet compartments. *Journal of the American Chemical Society* **2009,** *131* (42), 15251-15256.

190. Choi, C.-H.; Jung, J.-H.; Rhee, Y. W.; Kim, D.-P.; Shim, S.-E.; Lee, C.-S., Generation of monodisperse alginate microbeads and in situ encapsulation of cell in microfluidic device. *Biomedical Microdevices* **2007,** *9* (6), 855-862.
191. Tan, W. H.; Takeuchi, S., Monodisperse alginate hydrogel microbeads for cell encapsulation. *Advanced Materials* **2007,** *19* (18), 2696-2701.
192. Wan, J., Microfluidic-based synthesis of hydrogel particles for cell microencapsulation and cell-based drug delivery. *Polymers* **2012,** *4* (2), 1084-1108.
193. Panda, P.; Ali, S.; Lo, E.; Chung, B. G.; Hatton, T. A.; Khademhosseini, A.; Doyle, P. S., Stop-flow lithography to generate cell-laden microgel particles. *Lab on a Chip* **2008,** *8* (7), 1056-1061.
194. Edd, J. F.; Di Carlo, D.; Humphry, K. J.; Koster, S.; Irimia, D.; Weitz, D. A.; Toner, M., Controlled encapsulation of single-cells into monodisperse picolitre drops. *Lab on a Chip* **2008,** *8* (8), 1262-1264.
195. Silva, C. M.; Ribeiro, A. J.; Figueiredo, I. V.; Gonçalves, A. R.; Veiga, F., Alginate microspheres prepared by internal gelation: Development and effect on insulin stability. *International Journal of Pharmaceutics* **2006,** *311* (1), 1-10.
196. Zhao, L. B.; Pan, L.; Zhang, K.; Guo, S. S.; Liu, W.; Wang, Y.; Chen, Y.; Zhao, X. Z.; Chan, H. L. W., Generation of Janus alginate hydrogel particles with magnetic anisotropy for cell encapsulation. *Lab on a Chip* **2009,** *9* (20), 2981-2986.
197. Agudelo, C. A.; Teramura, Y.; Iwata, H., Cryopreserved agarose-encapsulated Islets As Bioartificial Pancreas: A Feasibility Study. *Transplantation* **2009**; 87 (1), 29-34.
198. Raemdonck, K.; Braeckmans, K.; Demeester, J.; De Smedt, S. C., Merging the best of both worlds: hybrid lipid-enveloped matrix nanocomposites in drug delivery. *Chemical Society Reviews* **2014,** *43* (1), 444-472.
199. Torres-Lugo, M.; Peppas, N. A., Preparation and characterization of P(MAA-g-EG) nanospheres for protein delivery applications. *Journal of Nanoparticle Research* **2002,** *4* (1), 73-81.
200. Oju, J.; Soo Hyun, R.; Ji Hyung, C.; Kim, B.-S., Control of basic fibroblast growth factor release from fibrin gel with heparin and concentrations of fibrinogen and thrombin. *Journal of Controlled Release* **2005,** *105* (3), 249-259.
201. Zisch, A. H.; Lutolf, M. P.; Ehrbar, M.; Raeber, G. P.; Rizzi, S. C.; Davies, N.; Schmokel, H.; Bezuidenhout, D.; Djonov, V.; Zilla, P.; Hubbell, J. A., Cell-demanded release of VEGF from synthetic, biointeractive cell ingrowth matrices for vascularized tissue growth. *The FASEB Journal* **2003,** *17* (15), 2260-2262.
202. Bala, I.; Hariharan, S.; Kumar, M. N. V. R., PLGA nanoparticles in drug delivery: the state of the art. **2004,** *21* (5), 387-422.
203. Colzani, B.; Speranza, G.; Dorati, R.; Conti, B.; Modena, T.; Bruni, G.; Zagato, E.; Vermeulen, L.; Dakwar, G. R.; Braeckmans, K.; Genta, I., Design of smart GE11-PLGA/PEG-PLGA blend nanoparticulate platforms for parenteral administration of hydrophilic macromolecular drugs: synthesis, preparation and in vitro/ex vivo characterization. *International Journal of Pharmaceutics* **2016,** *511* (2), 1112-1123.
204. Desai, N., Challenges in development of nanoparticle-based therapeutics. *The AAPS Journal* **2012,** *14* (2), 282-295.

205. Gaumet, M.; Vargas, A.; Gurny, R.; Delie, F., Nanoparticles for drug delivery: The need for precision in reporting particle size parameters. *European Journal of Pharmaceutics and Biopharmaceutics* **2008,** *69* (1), 1-9.

206. Chiesa, E.; Dorati, R.; Modena, T.; Conti, B.; Genta, I., Multivariate analysis for the optimization of microfluidics-assisted nanoprecipitation method intended for the loading of small hydrophilic drugs into PLGA nanoparticles. *International Journal of Pharmaceutics* **2018,** *536* (1), 165-177.

207. Guo, S.; Kang, G.; Phan, D. T.; Hsu, M. N.; Por, Y. C.; Chen, C. H., Polymerization-induced phase separation formation of structured hydrogel particles via microfluidics for scar therapeutics. *Scientific Reports* **2018,** *8* (1), 2245.

208. Deveza, L.; Ashoken, J.; Castaneda, G.; Tong, X.; Keeney, M.; Han, L.-H.; Yang, F., Microfluidic synthesis of biodegradable polyethylene-glycol microspheres for controlled delivery of proteins and DNA Nanoparticles. *ACS Biomaterials Science & Engineering* **2015,** *1* (3), 157-165.

209. Yang, C. H.; Huang, K. S.; Lin, Y. S.; Lu, K.; Tzeng, C. C.; Wang, E. C.; Lin, C. H.; Hsu, W. Y.; Chang, J. Y., Microfluidic assisted synthesis of multi-functional polycaprolactone microcapsules: incorporation of CdTe quantum dots, Fe_3O_4 superparamagnetic nanoparticles and tamoxifen anticancer drugs. *Lab on a Chip* **2009,** *9* (7), 961-965.

210. Kolishetti, N.; Dhar, S.; Valencia, P. M.; Lin, L. Q.; Karnik, R.; Lippard, S. J.; Langer, R.; Farokhzad, O. C., Engineering of self-assembled nanoparticle platform for precisely controlled combination drug therapy. *Proceedings of the National Academy of Sciences* **2010,** *107* (42), 17939-17944.

211. Xu, Q.; Hashimoto, M.; Dang, T. T.; Hoare, T.; Kohane, D. S.; Whitesides, G. M.; Langer, R.; Anderson, D. G., Preparation of monodisperse biodegradable polymer microparticles using a microfluidic flow-focusing device for controlled drug delivery. *Small* **2009,** *5* (13), 1575-1581.

212. Gong, X.; Peng, S.; Wen, W.; Sheng, P.; Li, W., Design and fabrication of magnetically functionalized core/shell microspheres for smart drug delivery. *Advanced Functional Materials* **2009,** *19* (2), 292-297.

213. Herranz-Blanco, B.; Arriaga, L. R.; Makila, E.; Correia, A.; Shrestha, N.; Mirza, S.; Weitz, D. A.; Salonen, J.; Hirvonen, J.; Santos, H. A., Microfluidic assembly of multistage porous silicon-lipid vesicles for controlled drug release. *Lab on a Chip* **2014,** *14* (6), 1083-1086.

214. Martín-Banderas, L.; Álvarez-Fuentes, J.; Durán-Lobato, M.; Prados, J.; Melguizo, C.; Fernández-Arévalo, M.; Holgado, M. Á., Cannabinoid derivate-loaded PLGA nanocarriers for oral administration: formulation, characterization, and cytotoxicity studies. *International Journal of Nanomedicine* **2012,** *7*, 5793-5806.

215. Colonna, C.; Dorati, R.; Conti, B.; Caliceti, P.; Genta, I., Sub-unit vaccine against S. aureus-mediated infections: Set-up of nano-sized polymeric adjuvant. *International Journal of Pharmaceutics* **2013,** *452* (1), 390-401.

216. Frede, A.; Neuhaus, B.; Klopfleisch, R.; Walker, C.; Buer, J.; Müller, W.; Epple, M.; Westendorf, A. M., Colonic gene silencing using siRNA-loaded calcium phosphate/PLGA nanoparticles ameliorates intestinal inflammation in vivo. *Journal of Controlled Release* **2016,** *222*, 86-96.

217. Makadia, H. K.; Siegel, S. J., Poly lactic-co-glycolic acid (PLGA) as biodegradable controlled drug delivery carrier. *Polymers* **2011,** *3* (3), 1377-1397.

218. Bobo, D.; Robinson, K. J.; Islam, J.; Thurecht, K. J.; Corrie, S. R., Nanoparticle-based

medicines: A review of FDA-approved materials and clinical trials to date. *Pharmaceutical Research* **2016,** *33* (10), 2373-2387.

219. De Crozals, G.; Bonnet, R.; Farre, C.; Chaix, C., Nanoparticles with multiple properties for biomedical applications: A strategic guide. *Nano Today* **2016,** *11* (4), 435-463.

220. Nazemifard, N.; Wang, L.; Ye, W.; Bhattacharjee, S.; Masliyah, J. H.; Harrison, D. J., A systematic evaluation of the role of crystalline order in nanoporous materials on DNA separation. *Lab on a Chip* **2012,** *12* (1), 146-152.

221. Zeng, Y.; Harrison, D. J., Self-assembled colloidal arrays as three-dimensional nanofluidic sieves for separation of biomolecules on microchips. *Analytical Chemistry* **2007,** *79* (6), 2289-2295.

222. Wei, B.; Malkin, D. S.; Wirth, M. J., Plate heights below 50 nm for protein electrochromatography using silica colloidal crystals. *Analytical chemistry* **2010,** *82* (24), 10216-10221.

223. Malekpourkoupaei, A.; Kostiuk, L. W.; Harrison, D. J., Fabrication of binary opal lattices in microfluidic devices. *Chemistry of Materials* **2013,** *25* (19), 3808-3815.

224. Zheng, S.; Ross, E.; Legg, M. A.; Wirth, M. J., High-speed electroseparations inside silica colloidal crystals. *Journal of the American Chemical Society* **2006,** *128* (28), 9016-9017.

225. Liao, T.; Guo, Z.; Li, J.; Liu, M.; Chen, Y., One-step packing of anti-voltage photonic crystals into microfluidic channels for ultra-fast separation of amino acids and peptides. *Lab on a Chip* **2013,** *13* (4), 706-713.

226. Gong, M.; Bohn, P. W.; Sweedler, J. V., Centrifugal sedimentation for selectively packing channels with silica microbeads in three-dimensional micro/nanofluidic devices. *Analytical Chemistry* **2009,** *81* (5), 2022-2026.

227. Shaabani, N.; Jemere, A. B.; Harrison, D. J., Size-based proteins separation using polymer-entrapped colloidal self-assembled nanoparticles on-chip. *Electrophoresis* **2016,** *37* (20), 2602-2609.

228. Luo, X.; Smith, P.; Raston, C. L.; Zhang, W., Vortex fluidic device-intensified aqueous two phase extraction of C-phycocyanin from *Spirulina maxima*. *ACS Sustainable Chemistry & Engineering* **2016,** *4* (7), 3905-3911.

229. Huang, C.; Ogawa, R., Pharmacological treatment for keloids. *Expert Opinion on Pharmacotherapy* **2013,** *14* (15), 2087-2100.

230. Muneuchi, G.; Suzuki, S.; Onodera, M.; Ito, O.; Hata, Y.; Igawa, H. H., Long-term outcome of intralesional injection of triamcinolone acetonide for the treatment of keloid scars in Asian patients. *Scandinavian Journal of Plastic and Reconstructive Surgery and Hand Surgery* **2006,** *40* (2), 111-116.

231. Niessen, F. B.; Spauwen, P. H. M.; Schalkwijk, J.; Kon, M., On the nature of hypertrophic scars and keloids: a review. *Plastic and Reconstructive Surgery* **1999,** *104* (5), 1435-1458.

232. Kadam, R. S.; Tyagi, P.; Edelhauser, H. F.; Kompella, U. B., RETRACTED: Influence of choroidal neovascularization and biodegradable polymeric particle size on transscleral sustained delivery of triamcinolone acetonide. *International Journal of Pharmaceutics* **2012,** *434* (1), 140-147.

233. Martins, C.; Araújo, F.; Gomes, M. J.; Fernandes, C.; Nunes, R.; Li, W.; Santos, H. A.; Borges, F.; Sarmento, B., Using microfluidic platforms to develop CNS-targeted polymeric nanoparticles for HIV therapy. *European Journal of Pharmaceutics and Biopharmaceutics* **2018**, doi.org/10.1016/j.ejpb.2018.01.014.

234. Chen, W.; Kim, J.-H.; Zhang, D.; Lee, K.-H.; Cangelosi, G. A.; Soelberg, S. D.; Furlong, C. E.; Chung, J.-H.; Shen, A. Q., Microfluidic one-step synthesis of alginate microspheres immobilized with antibodies. *Journal of The Royal Society Interface* **2013,** *10* (88), 1-8.

235. Britton, J.; Stubbs, K. A.; Weiss, G. A.; Raston, C. L., Vortex Fluidic Chemical Transformations. *Chemistry – A European Journal* **2017,** *23* (54), 13270-13278.

2. LASER IRRADIATED VORTEX FLUIDIC MEDIATED SYNTHESIS OF LUMINESCENT CARBON NANODOTS UNDER CONTINUOUS FLOW

Several methods have been developed for fabricating carbon nanodots, however most of them involve tedious purification processes, the use of harsh chemicals, difficulties in scaling up and sample inhomogeneity. In recent years, the use of channel based microfluidics has attracted considerable attention in attempting to overcome some of these disadvantages. However, there are still issues in the area of limited scale up potential and system clogging. The vortex fluidic-mediated synthesis of CDs reported in this chapter overcomes the clogging issue as well as enhancing the prospect of product homogeneity under plug flow and uniform irradiation and shear stress. CDs produced using this method have a relatively narrow size distribution, between 3 to 13 nm, and have high colloidal stability and are non-toxic up to 200 µg/mL, as established from a skin fibroblast CRL2076 cytotoxicity study. The CDs exhibit excitation wavelength independent photoluminescence behaviour with two distinctive emission peaks around 420 and 460 nm, being an integration of at least three emissive sites originating from the aromatic core, defects and functional groups. In the context of material processing, this chaper shows one of the examples regarding the application of VFD towards nanocarbon processing where the ideal of green chemistry and the scaling up potential have been emphasized.

This study was orally presented at the RACI Centenary Congress in Melbourne on July 2017, and published in ***RSC Reaction Chemistry and Engineering***, Year 2018, Vol. 3, Issue 2, Pages 164-170, which was also published as the journal inside cover of that issue. The first page of the publication is attached in Appendix 2.1.

Author contributions: **XL** performed all the VFD and tissue culture experiments, most of the characterization experiments and data analysis; wrote all the primary content. **AA**: designed and developed the magnetic mixing syringe used for dispersing MWCNTs in H_2O_2, as indicated in Fig. 1c. **KV** contributed to the project plan and helped with some AFM and Raman. **JM** assisted with some photoluminescence experiments (Fig. 9c, Fig. S6d). **KZ** performed the TEM (Fig. 7c). **YZ** performed the TEM (Fig. S3g; Fig. S10a). **JZ**: supervised the TEM experiments. **XD** performed all the XPS experiments and data analysis. **RL** supervised the XPS experiments. **SW** conducted the PL lifetime measurement (Fig. 9d and e) and interpreted these data. **QL** supervised and planned the PL studies. **WZ** supervised the project and coordinated the toxicology studies. **CR** supervised and coordinated the project and helped on the research directions and plan. All of the co-authors assisted with the revision of the manuscript before and during the publication process.

Laser irradiated vortex fluidic mediated synthesis of luminescent carbon nanodots under continuous flow

Xuan Luo[1,2], Ahmed Hussein Mohammed Al-Antaki[2], Kasturi Vimalanathan[2], Jillian Moffatt,[3] Kun Zheng[4,5], Yichao Zou[6], Jin Zou[4,6], Xiaofei Duan[7], Robert N. Lamb[8], Shujun Wang[9], Qin Li[9], Wei Zhang[1*] and Colin L. Raston[2*]

Graphical abstract

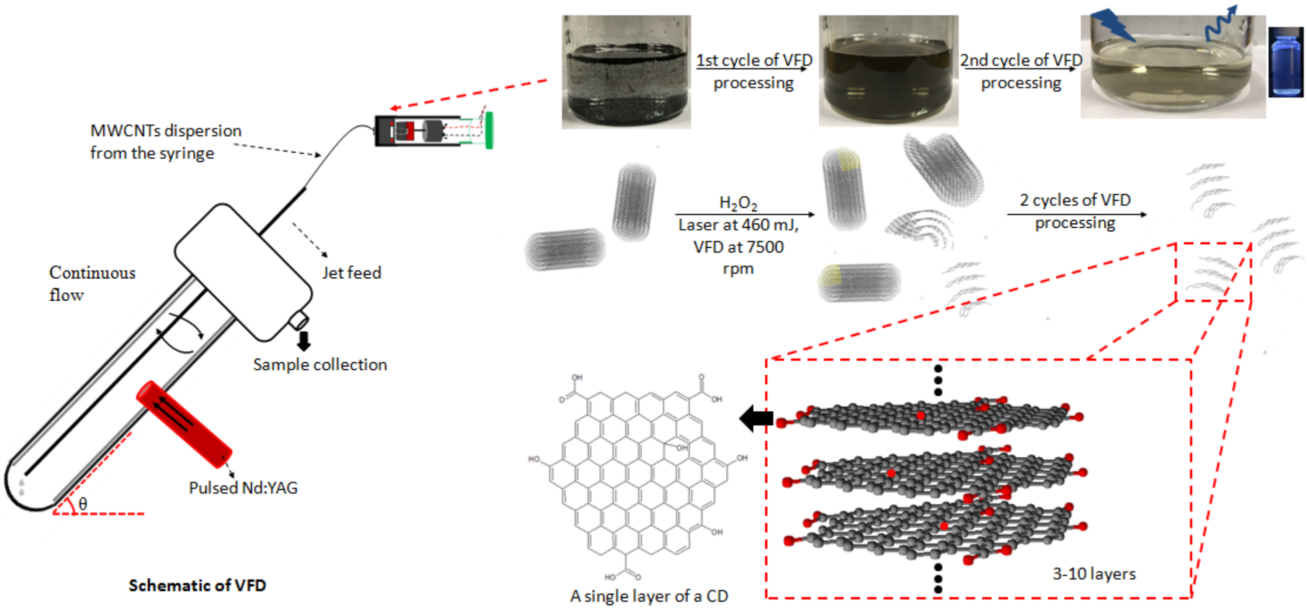

[1] Centre for Marine Bioproducts Development, College of Medicine and Public Health, Flinders University, Adelaide, SA 5042, Australia;

[2] Centre for NanoScale Science and Technology (CNST), College of Science and Engineering, Flinders University, Adelaide, SA 5042, Australia;

[3] Institute for Photonics and Advanced Sensing, and School of Physical Sciences, The University of Adelaide, SA 5005, Australia;

[4] Centre for Microscopy and Microanalysis, The University of Queesland, Brisbane, QLD 4072, Australia; Australian Institute for Bioengineering and Nanotechnology,The University of Queensland, Brisbane, QLD 4072, Australia;

[6] Materials Engineering, The University of Queensland, Brisbane, QLD 4072, Australia;

[7] Trace Analysis for Chemical, Earth and Environmental Sciences (TrACEES), The University of Melbourne, Victoria 3010, Australia;

[8] School of Chemistry, The University of Melbourne, Victoria 3010, Australia;

[9] Environmental Engineering and Queensland Micro and Nanotechnology Centre, Griffith University, Brisbane, QLD 4111, Australia.

2.1 Abstract

Carbon nanodots (CDs) with size dependent fluorescence are synthesized from multi-walled carbon nanotubes (MWCNTs) under continuous flow in a vortex fluidic device (VFD) when irradiated by a pulsed laser with a wavelength of 1064 nm, without subsequent passivation procedures. The CDs have a relatively narrow size distribution averaging ca. 6 nm in diameter, and have low cytotoxicity and high colloidal stability with the highest emission intensity of the solution at 450 nm under a 345 nm excitation wavelength. Further downstream processing on the as-processed CDs revealed tunability of the emission from 450 nm to 325 nm.

2.2 Introduction

Carbon nanodots (CDs) are carbon nanoparticles <10 nm in diameter, consisting of a graphitic structure or amorphous carbon core and carbonaceous surfaces, with rich oxygen-containing groups.[1] CDs exhibit distinct properties, most notably strong quantum confinement and edge effects resulting in exceptional fluorescent characteristics.[2] The unique functional properties and benign chemical composition have rendered CDs a promising new material for a broad range of applications including bioimaging,[3] drug delivery,[4] and optoelectronic devices.[5] Various feedstocks have been used for producing CDs including single walled carbon nanotubes,[6] carbohydrates,[7] polyethylenimine, [8] low molecular weight alcohols,[9] graphite,[10] and carbon soot. [3] In general, the quantum yield of CDs varies dramatically, from 1.32%[11] up to around 43%,[12] depending on the choice of carbon feedstock. A number of methods have been reported to prepare CDs within these dimensions, including chemical ablation, laser ablation,[2] electrochemical carbonisation,[9] arc-discharge pyrolysis,[2] hydrothermal synthesis,[12] and ultrasound and microwave-assisted pyrolysis.[13] Laser ablation is a well-studied technique in synthesizing CDs from various carbon-based targets.[14-16] The significant advantage of this technique over other methods is that the processing is relatively clean, with reduced byproduct formation.[15] However, the potential of synthesizing CDs through laser ablation in liquids is limited by the scalability and gravitational settling of the raw material.[15] Other potential issues using conventional laser ablation processing include controlling the crystallinity of the CDs,[17] relatively long processing times,[15] and the requirement for additional passivation reaction, for example long acid refluxing times.[14,18]

One of the most common methods of fabricating oxygen-containing CDs involves using a mixture of concentrated H_2SO_4 and HNO_3.[19] However, this requires tedious purification procedures to remove the excess acid, and uses toxic and harsh chemicals. The catalytic activity of MWCNTs towards H_2O_2 decomposition (HPD) has been reported in a few studies, and the properties of the nanotubes post processing can be affected.[20] A mixture of H_2O_2 and 1 M HCl or 96 wt% H_2SO_4 has been used for the oxidation and purification of carbon nanotubes (CNTs),[21] with 15% H2O2 alone at 100 °C for 3 hours being effective in removing the end caps and shortening the length of the CNTs with concomitant surface carboxylic group fuctionalization. [22,23] Related to this is the degradation of graphene sheets using H_2O_2, with a time-dependant generation of randomly distributed nanometer- sized holes on the surface of the 2D material.[24] There are no reports on the application of HPD in fabricating CDs in gaining access to particles with uniform morphology nor on laser-assisted continuous production of CDs where there is an emphasis on green chemistry metrics.

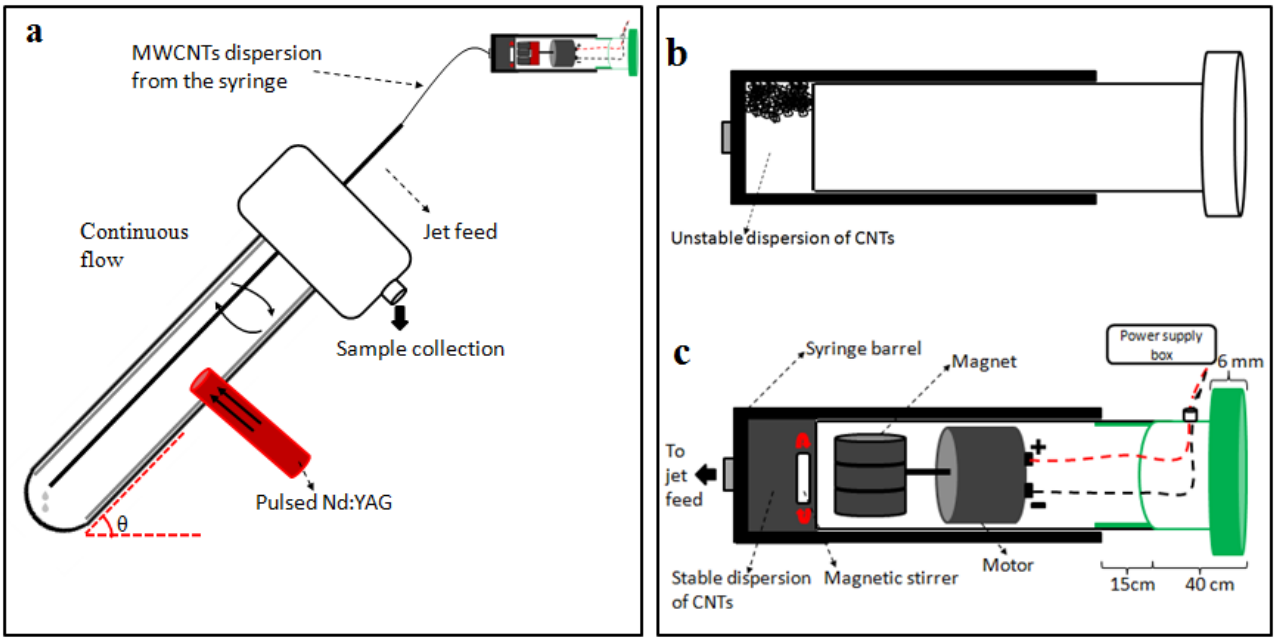

Figure. 2.1 *Laser-VFD fabrication of carbon dots (CDs) under continuous flow. (a) Schematic of the vortex fluidic device (VFD). (b) Illustration of an unstable dispersion of MWCNTs in aqueous* H_2O_2 *in a normal syringe. (c) Magnetic-assisted mixing in a syringe for delivering a uniform dispersion of MWCNTs to the base of the rapidly rotating borosilicate glass tube (20 mm O.D. diameter).*

Given the issues discussed above, we embarked on developing a simple, more environmentally friendly, economical and controllable synthesis of CDs using the recently developed thin film microfluidic vortex fluidic device (VFD) coupled with NIR irradiation using a pulsed laser operating at 1064 nm, under continuous flow (Fig. 1a). The use of VFD mediated synthesis of CDs enhances the prospect of product homogeneity under plug flow and uniform irradiation and high shear stress (mechanoenergy), in overcoming most of the drawbacks of conventional laser ablation processing. In- deed, CDs processed using this rationale approach have better size homogeneity, as evidence by the excitation- wavelength independent fluorescence emission.[11]

The novel top-down reforming of nano-carbon reported herein uses MWCNTs as the feedstock. The controlled reforming of MWCNTs to CDs occurs under continuous flow in the presence of hydrogen peroxide (30% aqueous solution) as the oxidant and solvent, in dynamic thin films in the VFD under laser irradiation at 1064 nm. The unique fluidic dynamic properties of the VFD has been applied in a number of other applications, including lateral slicing of single, double and multi-walled CNTs despite their remarkably high tensile strength,[25] intensified aqueous two phase separation,[26] fabricating fluorescent nanoparticles,[27] exfoliating graphite and boron nitride[28] and fabricating intertwined single walled carbon nanotube rings.[29] The optimum angle of tilt of the rapidly rotating glass tube in the VFD for all of these applications is 45°, and accordingly for the present work this angle was also used, using 20 mm O.D. borosilicate glass tubes, 18 cm in length. In the continuous flow mode, MWCNTs dispersed in solution using an in-house designed magnetic-assisted mixing system (Fig. 1b and c) were delivered via the jet feed to the bottom of the VFD tube and the high shear in the thin film as it whirls up the tube, [25] which improved the scalability of conventional laser ablation processing into effective disintegrating and exfoliating fragmented graphene sheets of the MWCNTs. Aqueous H_2O_2 was the choice of solvent as an inexpensive, green and environmentally-friendly oxidant which produces high concentrations of hydroxyl free radicals under laser irradiation.[30] Fabricated CDs exhibit luminescence with a quantum yield of 2.2%, consistent with derived from similar raw material.[11]

2.3 Materials and methods

MWCNTs (CAS 773840) with dimensions O.D. × I.D. × L equivalent to 10nm±1nm × 4.5nm±0.5nm × 3-6μm were purchased from Sigma Aldrich, as chemical vapor deposition prepared material with an as-received purity ≥98%. 30% H_2O_2 was purchased from Chem-supply (HA 154-2). Magnesium sulphate and Molecular sieves, 4 Å were purchased from Sigma Aldrich. Sample preparation involved the addition of the MWCNTs (10 mg) into a glass beaker containing 100 mL 30% H_2O_2 (0.1 mg mL^{-1}), followed by bath sonication (~3 minutes) to afford a dispersion. The experimental setup mainly followed the previously published work for the VFD-mediated slicing of CNTs.[22] The experiment was carried out in the continuous flow mode at a flow rate of 0.45 mL min^{-1}. Stainless steel jet feeds were used to deliver the MWCNT suspension to the bottom of the rapidly rotating VFD borosilicate glass tube (O.D. 20 mm) inclined 45° relative to the horizontal position, as the so called title angle θ of the device. The tube was simultaneously irradiated using a 5 nanosecond pulsed Q-switch Nd:YAG laser operating at 1064 nm, with an 8 mm diameter laser beam and a repetition rate of 10 Hz (Fig. 1a). The laser beam was directed to the middle of the tube for an optimal processing outcome. To ensure a stable homogeneous dispersion of MWCNTs in the aqueous H_2O_2 during syringe pump delivery of the liquid to the rapidly rotating tube, an in-house designed magnetic-assisted mixing system was developed (Fig. 1c). The magnetic-assisted mixing during the delivery of the liquid to the VFD tube did not contribute to any length or morphological change of the MWCNTs (Fig. S1b†), but it did contribute to some oxidation/functionalisation of the sample.

CDs were characterized using SEM, AFM (Nanoscope 8.10 tapping mode), Raman spectroscopy (WiTec Alpha 300R λ_{exc} = 532 nm and XploRATM Horiba Scientific λ_{exc} = 532 nm), X-ray photoelectron spectroscopy (XPS – Kratos Axis Ultra, Thermo Scientific, UK, with Monochromatic Al Kα X-rays), XRD (Bruker D8 ADVANCE ECO, Co-Kα, λ = 1.78892 Å), infrared microscope (NicoletTM iNTM10, Thermal Scientific), UV-vis spectrophotometer (Varian Cary 50), fluorescence spectrometer (Cary Eclipse, Agilent), Thermo Lumina fluorescence spectrometer and TEM (FEI Tecnai F20 operated at 200 kV). The quantum yield was measured by comparing the integrated fluorescence and absorbance of the sample with anthracene in ethanol as a reference. Photoluminescence measurements were performed using Edinburgh Instruments F980 Spectrofluorimeter, with details of the UV diodes provided in Table S3. All diodes had columnated beams apart from the 355 nm one, which was not directional and emitted light in a cone-shape. The CD sample was mounted on a glass slide and imaged with Olympus AX70 fluorescence microscope.

2.4 Results and Discussion

The optimized VFD operating conditions for fabricating CDs from MWCNTs while irradiated with a pulsed laser are θ 45° and rotational speed 7500 rpm at a flow rate of 0.45 mL min^{-1}. The absence of laser irradiation under the same conditions simply results in debundling of CNTs (Fig. S1a–c). To further decouple the effect of the VFD and the laser irradiation, a pulsed laser at the optimized power of 450 mJ was directed towards the CNTs dispersed in H_2O_2 mixed using a magnetic stirrer in a quartz cuvette rather than in a VFD tube. This resulted in minimal conversion of the CNTs into CDs, with large bundles and aggregates of CNTs still present (Fig. S1d).

In mapping out the optimized conditions for fabricating the CDs, as-processed samples were centrifuged at 1180 × g to remove any aggregates or bundled nanotubes before atomic force microscopy (AFM), following a previously reported procedure.[25] Operating parameters of the VFD and laser were systematically varied under continuous flow, changing one parameter at a time en route to the optimised conditions. For rotational speeds below 6500 rpm at a 45° tilt angle, apart from the presence of large bundles, short length CNTs (about 300 nm) were observed after processing (Fig. 2a and b). At 7500 rpm, a significant amount of CDs formed compared with all other rotational speeds conducted at the same laser power (Fig. 2c), even though large bundles of long CNTs were still persistent. Further increase to 8000 rpm resulted in less amount of CDs being generated. This might be due to material remaining in the VFD tube as a result of increased centrifugal force. These optimal conditions (θ 45°, 7500 rpm) also correspond to the optimal processing condition for lateral slicing of carbon nanotubes using laser-VFD processing.[25] At lower laser powers, ≤260 mJ (Fig. 3a and b), the conversion was ineffective and there was no clear band at the site of laser irradiation of the tube (Fig. S2). The conversion was also ineffective at high laser power (>450 mJ) which might be due to the disturbance of the dynamic thin film. The position of the stainless steel jet feeds delivering solution to the base of the tube needs to avoid direct irradiation by the laser. Otherwise a significant amount of metal oxide nanoparticles are generated, as evidenced by transmission electron microscopy (TEM), Raman spectroscopy and scanning electron microscopy (SEM)/energy dispersive X-ray spectroscopy (EDX) (Fig. S3 and S4). Raman mapping was used to verify the crystalline nature and degree of sp^2 hybridisation of the CDs relative to the MWCNTs. Processing with the laser operating at 532 nm (Fig. S5, Table S1) resulted in less CDs being formed, with poorer sample homogeneity relative to those prepared under the NIR laser (θ 45°, 7500 rpm rotational speed) operating at 1064 nm (Fig. S6).

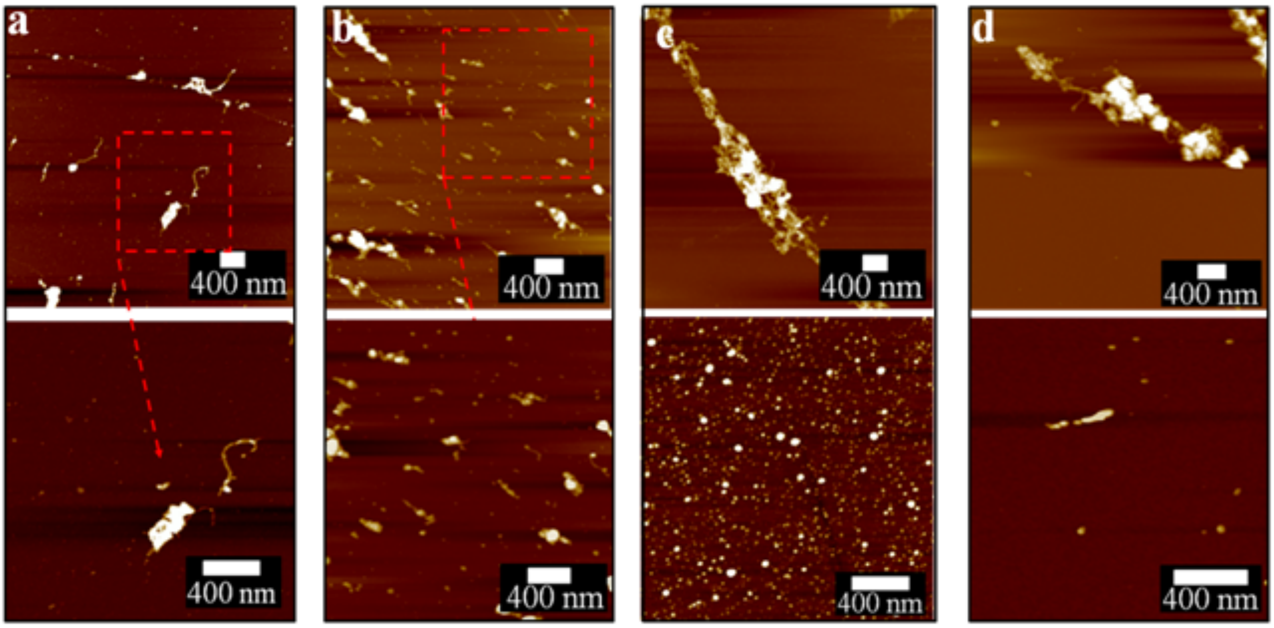

Figure 2.2 *Continuous flow VFD processing of MWCNTs (0.5 mg mL^{-1}, flow rate of 0.45 mL min^{-1}) under pulsed laser irradiation (1064 nm, 260 mJ) at 45° tilt and different rotational speeds. (a) 5000 rpm. (b) 6500 rpm. (c) 7500 rpm. (d) 8000 rpm. Samples were centrifuged at 1180 × g for 30 min after VFD processing and the supernatant was drop-casted on a silicon wafer for AFM imaging. The average dimension of as received MWCNT is O.D. × I.D. × L equivalent to 10 nm ± 1 nm×4.5nm±0.5nm×3–6µm.An average of ten areas were randomly chosen for all AFM images, with 1–2 representative images presented in this figure (as for all AFM figures).*

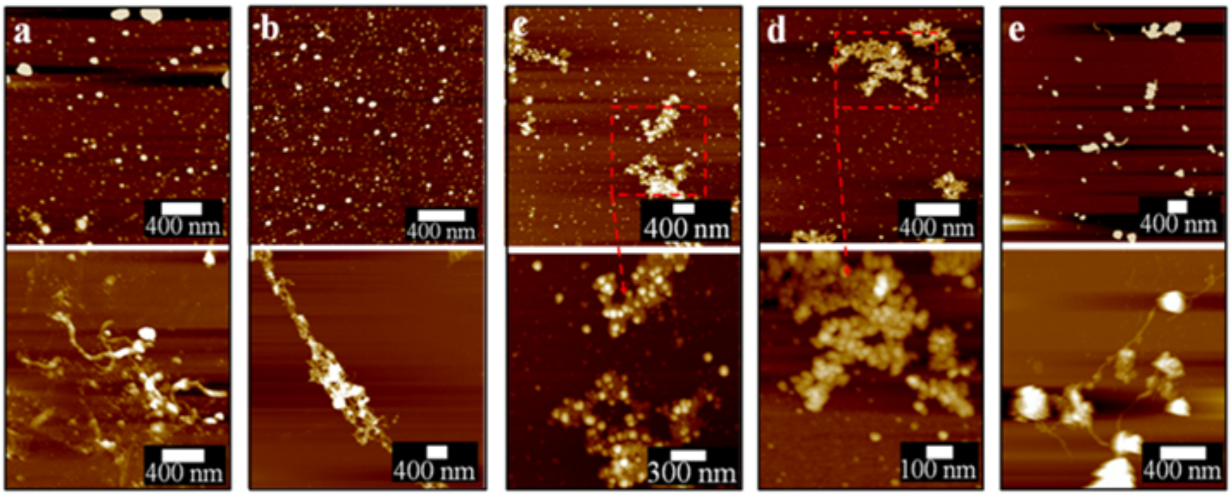

Figure 2.3 *Continuous flow VFD processing of MWCNTs (0.5 mg mL^{-1}, flow rate of 0.45 mL min^{-1}, 7500 rpm) at 45° tilt, under pulsed laser irradiation at different laser power. (a) 150 mJ. (b) 260 mJ. (c) 350 mJ. (d) 450 mJ. (e) 670 mJ. Samples were centrifuged before drop-casting on a silicon wafer for AFM imaging.*

Post-VFD processing, centrifugation improved the sample purity by removing the large bundled MWCNTs but this led to a significant loss of CDs to the pellet. For generating practical quantities of CDs, no centrifugation was applied. The conversion of MWCNTs to CDs could be further improved by lowering the starting material concentration from 0.5 to 0.1 mg mL^{-1} (Fig. 4d). A similar outcome was also reported for slicing of CNTs[25] which was explained by the high concentration of CNTs disturbing the complex fluid dynamics of the thin film in the device. Two sequential continuous NIR laser-VFD cycles of the same sample (θ 45°, 7500 rpm rotational speed, at 450 mJ laser power) further increased the conversion of the MWCNTs nanotubes to CDs (Fig. 4e). This was confirmed using photoluminescence (PL) where the intensity of the second-cycled CDs increased 11.8 times compared with one cycle processed material (Fig. S7), but a reduction of CDs yield revealed when three or more cycles was carried out.

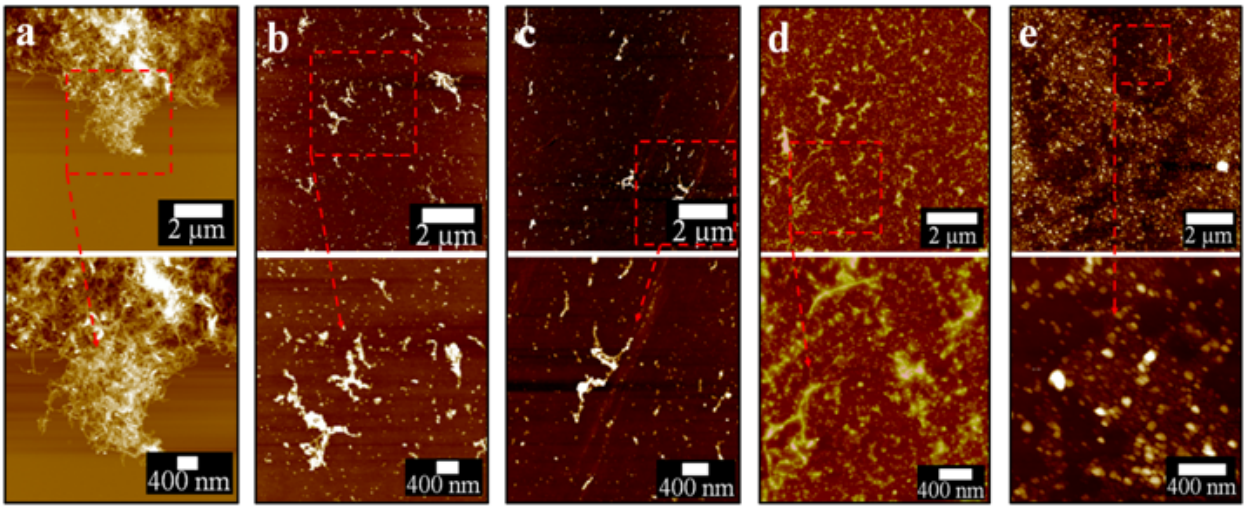

Figure 2.4 *Continuous flow VFD processing of MWCNTs (flow rate of 0.45 mL min^{-1}, 7500 rpm) under pulsed laser irradiation (1064 nm, 450 mJ) at 45° tilt, with different sample concentrations. (a) MWCNTs at 0.5 mg mL^{-1} without laser-VFD (control). (b) MWCNTs processed at 0.5 mg mL^{-1}. (c) 0.25 mg mL^{-1}. (d) 0.1 mg mL^{-1}. (e) 0.1 mg mL^{-1} processed through two cycles with laser-VFD processing. For AFM imaging, as-prepared samples were directly drop-casted on silicon wafers without centrifugation post VFD processing.*

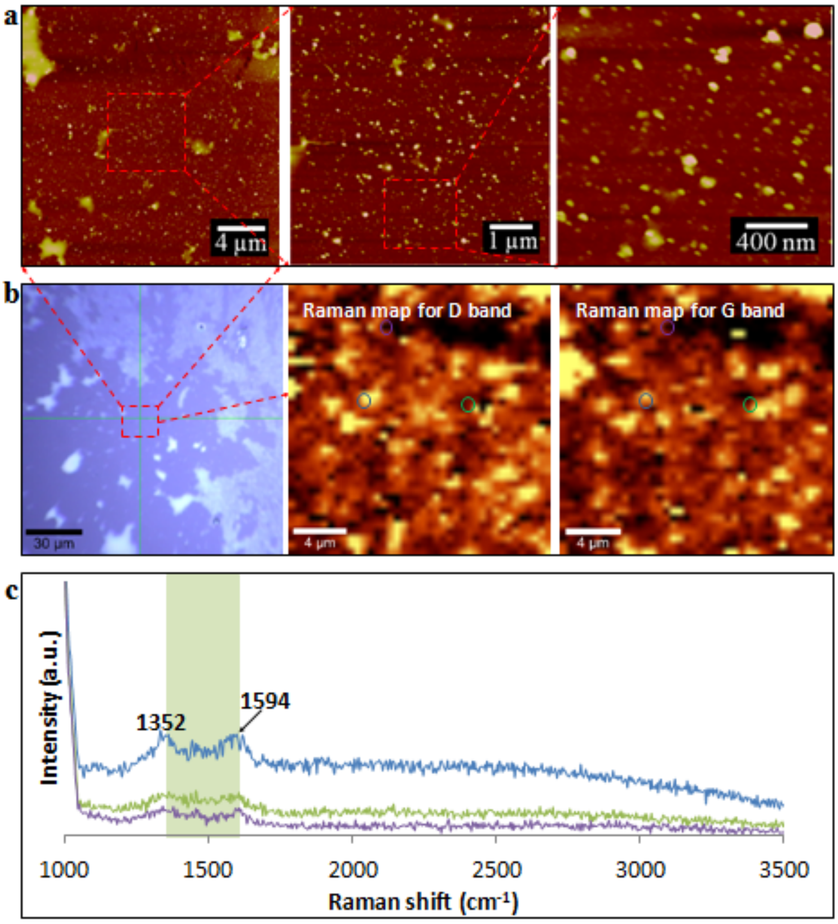

Figure 2.5 *Raman mapping for CDs processed using two cycles of continuous flow VFD (0.1 mg m^{-1}, flow rate of 0.45 mL min^{-1}, 7500 rpm) under pulsed laser irradiation (1064 nm, 450 mJ) at 45° tilt. (a) AFM images of the mapped area and corresponding zoomed-in images. (b) Optical image and Raman maps of the highlighted area (red square) with the two map images representing the D (1352 cm^{-1}) and G (1594 cm^{-1}) bands of graphitic material. (c) Three representative single spectrum correspond to the three circled spot in b. Scanned area was20×20μm^2.*

After two cycles of laser-VFD processing, Raman mapping was conducted over a particle enriched area (AFM confirmed) (Fig. 5a). The two Raman maps correspond to the map for D (1352 cm^{-1}) and the map for G (1594 cm^{-1}) bands (Fig. 5b). As shown, these spherical particles are graphitic with well-matched signals for D and G bands. Single Raman spectrum (Fig. 5c) extracted from three randomly circled areas (Fig. 5b) show a typical graphitic spectrum with the D-band at 1352 cm^{-1} (1346 cm^{-1} for MWCNTs), and the G-band at 1594 cm^{-1} (1586 cm^{-1} for MWCNTs). This blue shift of the G-band to a higher frequency and the disappearance of 2D peak at 2682 cm^{-1} compared to as received MWCNTs (Fig. S1a) is consistent with the surface oxidation of the CD, as reported by Islam et al.[31] for oxidized single layer graphene. The band-width of full width at half maximum (FWHM) significantly increased from 64 cm^{-1} (as received MWCNTs) to 93 cm^{-1} (CDs), which again is consistent with the oxidation state.[32]

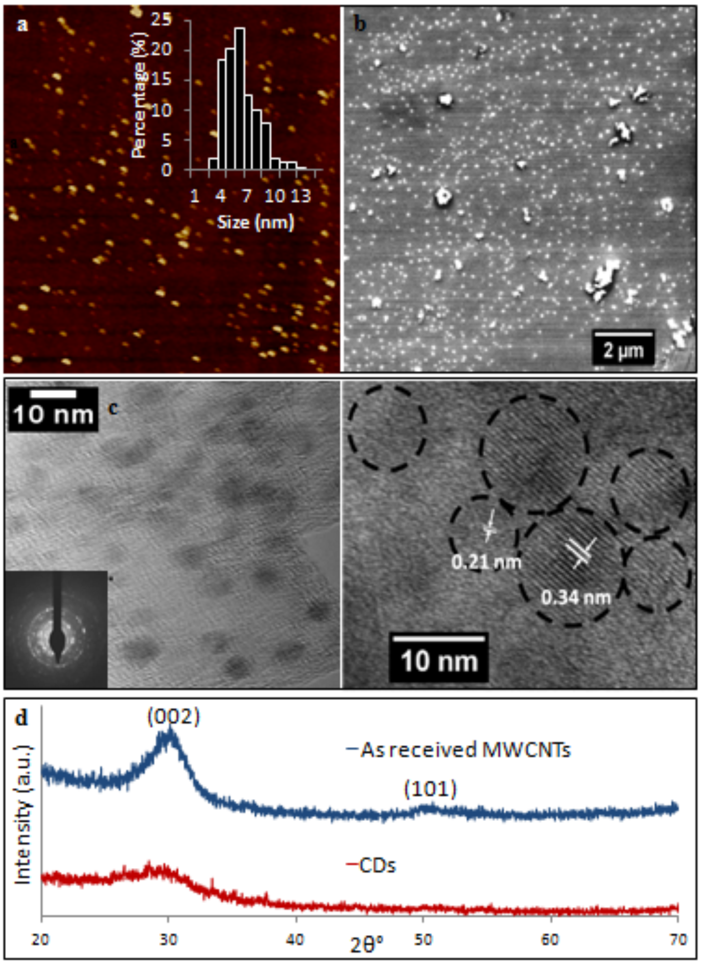

Figure 2.6 *CDs fabricated under optimized conditions (two cycles continuous flow, 0.1 mg mL^{-1}, flow rate of 0.45 mL min^{-1}, 7500 rpm, 450 mJ, at 45° tilt). (a) AFM image and height distributions based on >300 individual CDs (inset). (b) SEM image. (c) TEM, selected area electron diffraction pattern (inset) and HRTEM images. (d) XRD results of as received MWCNTs and as-processed CDs.*

TEM and AFM established that the as-prepared CDs were quasi-spherical and showed an average height ca. 6 nm (from 3 to 13 nm) (Fig. 6). These are formed from fragmentation of 10 nm outer diameter MWCNTs, presumably involving exfoliation and agglomeration of small graphene sheets which have increased surface area and surface energy.[33] High resolution TEM (HRTEM) gave 0.21 nm and 0.34 nm lattice spacings which correspond to the {100} and {002} planes of graphitic carbon.[34] This is in agreement with the spacing calculated from the diffraction pattern taken from the CDs (inset of Fig. 6c). X-ray diffraction (XRD) for the as-received MWCNTs had peaks at 2θ 29.98° and 50.13° (weak) (Fig. 6d) which correspond to (002) and (101) atomic planes respectively for the hexagonal structured graphitic material.[35] XRD of CDs had a broader peak at 2θ 29.04°, and their calculated interlayer d-spacing (d_{002}) is 0.34 nm which is in good agreement with the graphitic interlayer spacing.[36] The broad and weak nature of the peak indicates the presence of some poorly crystalline carbon, which is consistent with the generation of oxygen containing groups during the processing.

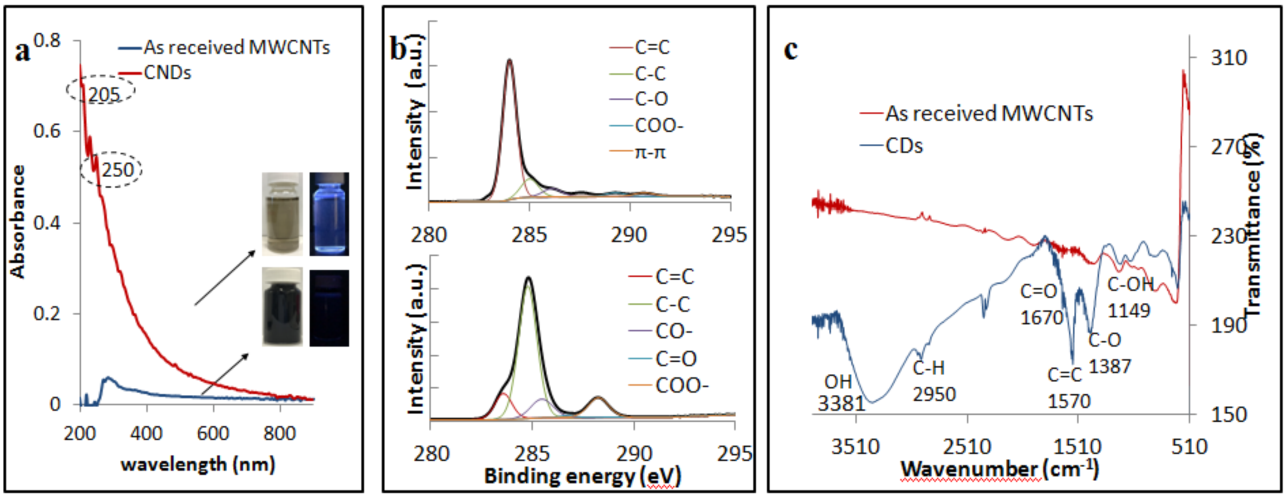

Figure 2.7 *(a) UV-vis spectrum of the CDs. (b) C 1s spectrum of the CDs. (c) FT-IR spectra of the CDs.*

The CDs obtained using the optimal processing conditions had good water solubility and colloidal stability, with little or no change in their optical properties over several weeks, and these are distinctly different from those of as received MWCNTs (Fig. 7a). The CDs had a broad absorption spectrum with a tail extending into the visible region and this is attributed to the π–π* transition of the conjugated C=C bond (205 nm) and n–π* transition of C=O bond (250 nm), which is in good agreement with the findings of Lin et al.[37] XPS established that the oxygen content increased significantly for as received MWCNTs (1.54% oxygen content) of compared to CDs (18.7% oxygen content). The CDs were oxidized (C=C/C–C, 15.5% molar ratio), and deconvolution of the C 1s peak established atomic percentage of different types of C bonds – sp^2 (C=C at 284 eV, 12.2% molar ratio), sp^3 (C–C/C–H at 285.2 eV, 65.0% molar ratio), C–O (285.7 eV, 11.4%), O–C=O (289.4 eV, 10.7% molar ratio) and π–π* interaction (shakeup, 290.9 eV) (Fig. 7b). The sp^3 intensity is much stronger than the sp^2 which confirmed the oxidation of the CDs relative to MWCNTs. FT-IR spectra of the CDs gave characteristic absorption peaks for –OH stretching, 3381 cm^{-1}, and C=O stretching, *ca.* 1670 cm^{-1} (Fig. 7c). These findings agree with the XPS, XRD and HRTEM data. The formation of oxygen-containing functionality on the surface of the CDs during the laser-VFD processing accounts for their water solubility.

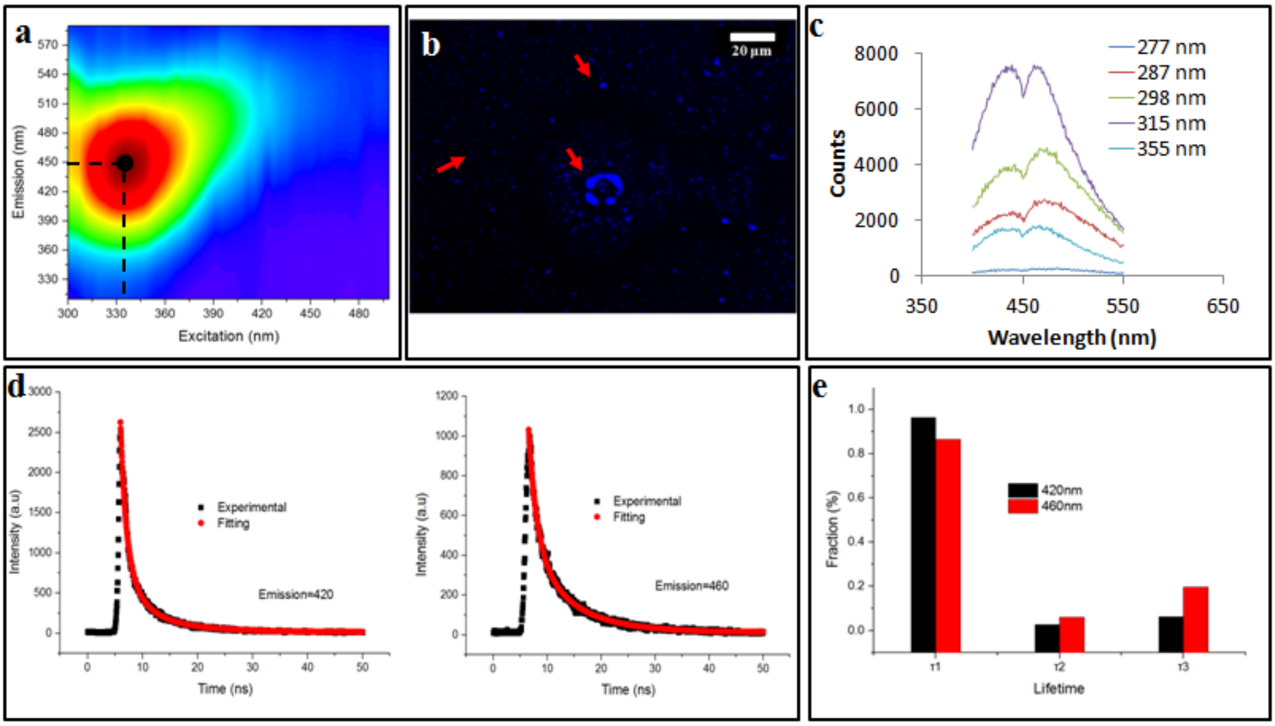

Figure 2.8 *(a) Contour fluorescence map for excitation and emission of the CDs (from the optimized condition). The black dot represents the maximal fluorescence intensity of the CDs, received at an excitation wavelength of 345 nm and at an emission 450 nm. (b) Fluorescence microscopy excited at 365 nm. (c) PL spectra of the CDs. Two emission peaks at constant wavelength of 435 and 466 nm were for different excitation wavelengths, from 277 to 355 nm. (d) Fluorescence decays of CDs excited at 377 nm. (e) Decaying lifetime of three emissive sites.*

The scalability of the process was investigated by processing 50 mg of as received MWCNTs dispersed in 500 mL of H_2O_2. Approximately 40% of starting material was converted to CDs, as deduced from residual material remaining in the syringe and the VFD tube post processing. The yield of dialysed CDs which showed negligible cytotoxicity (Fig. S14) was ca. 10%, based on the total amount of initial MWCNT. 2D-fluorescence maps of the CDs showed maximum excitation wavelength at 345 nm and an emission at 450 nm (blue in the visible region) (Fig. 8a) with the as-received MWCNTs showing no fluorescence. Drop-cast CDs showed UV-excitable (at 365 nm) characteristics under the fluorescence micro- scope (Fig. 8b). Two resolved photoluminescence (PL) emission peaks at 420 and 460 nm (Fig. 8c) which were considered to be constant, meaning the emission is independent of the excitation wavelength (277–355 nm). Such excitation-independent PL emission is attributed to relative size uniformity, as previously noted for graphene quantum dots fabricated using microfluidisation.[11] Fluorescence life- time was analysed for both emission peaks under the excitation of a 377 nm pulsed laser (Fig. 8d). Both decay curves can be well fitted with a 3-component exponential model, which can be understood by the emission being an integration of at least three emissive sites (Fig. 8e). The fastest decay has a lifetime ($\tau 1$) about 1.4 ns, and the intermediate component has a lifetime ($\tau 2$) around 3 ns, while the slowest lifetime ($\tau 3$) is in the range of 8.5 to 9.0 ns. The lifetime results are consistent with a previous report[38] which attributes the PL of CDs as arising from an integration of PL components from three types of emission centres, namely, σ^*–n and π^*–n transitions (emissions from functional groups dominate the blue side, corresponding to $\tau 1$), π^*–π transition (emissions from aromatic core of the CDs, corresponding to τ_2) and π^*-midgap states-π transitions (emission normally on the red side dominated by the midgap states that are created by functional groups and defects, corresponding to τ_3). Since the PL spectrum of CDs shows two distinctive peaks centered at 420 and 460 nm, respectively, PL lifetime analysis was carried out for each emission peak. The percentage of the longer lifetime component ($\tau 3$) of 460 nm emission is more than 13% higher than that of 420 nm emission, which indicates that the origin of 460 nm emission peak arises from stronger association with the surface functional group. Under both acidic (pH = 1) and alkaline conditions (pH = 12), PL of the CDs was quenched (Fig. S15†), with the emissive peak at 460 nm un- der neutral conditions (pH = 7) disappearing when the pH was adjusted either way, acidic or basic. This observation indicates that the emission peak at 460 nm is strongly associated with the surface functional groups, predominantly the $–COO^-$ which is consistent with the XPS results. Either the H^+ or OH^- cause the formation of non-radiative complexes with the surface functional groups of the CDs and lead to static quenching.

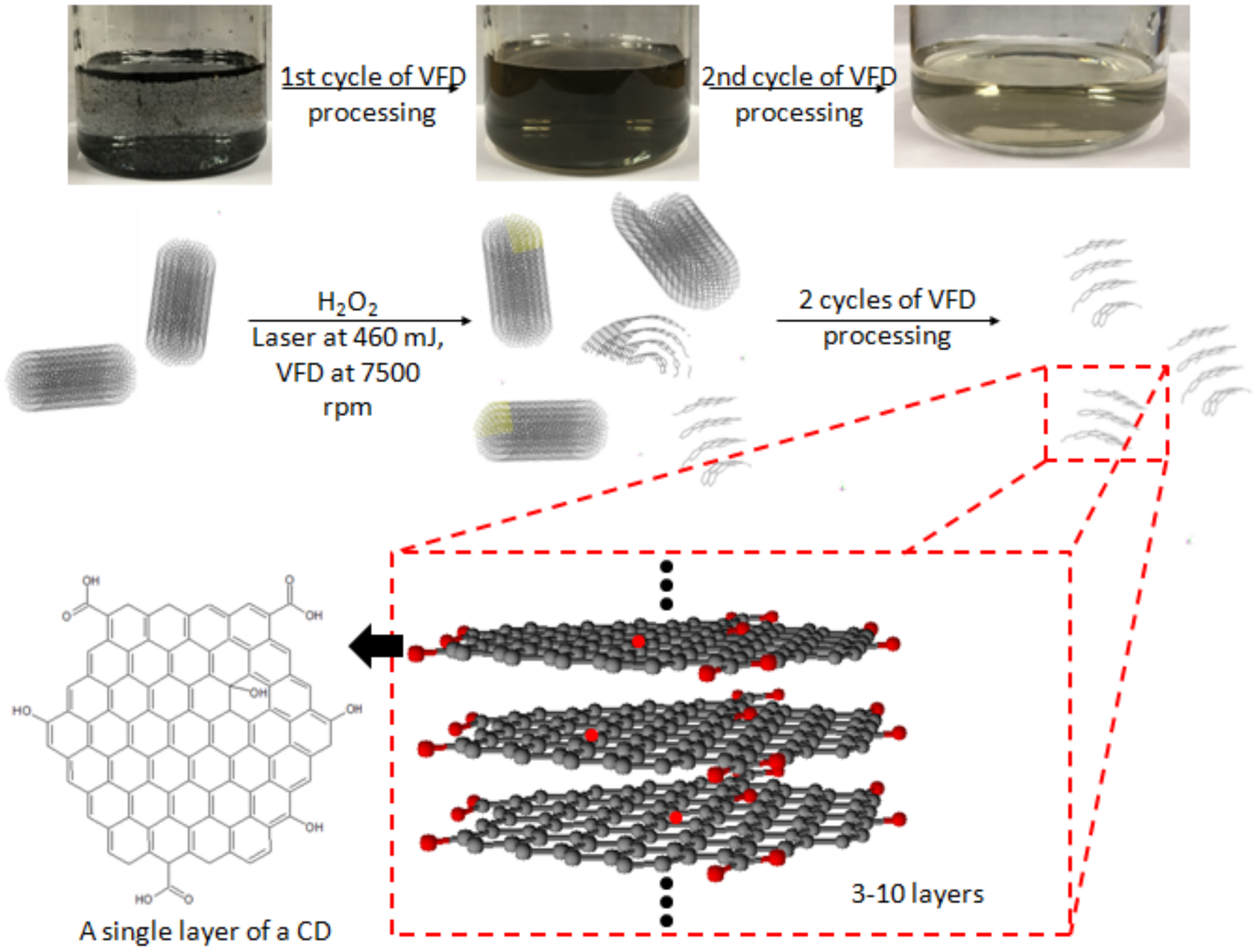

***Figure 2.9** Schematic of laser-VFD processing for fabricating CDs from MWCNTs. The black dots above and below the ball-and-stick model of the CDs highlight the sample may contain different layers of graphene.*

AFM, TEM, Raman, FT-IR, XPS and PL of the CD are consistent with the proposed structure shown in Fig. 9. This corresponds well with what has been proposed in most studies, with CDs having a graphitic core and an oxidized surface. Oxidation of the MWCNTs can occur at the ends of the nanotube or at defect sites on the sidewalls, which includes sp^3- hybridised defects, and vacancies between the nanotube lattice or dangling bonds.[23] The surface functionalisation could be visually evaluated in terms of the solubility changes after the first laser-VFD cycle. Post-VFD processing, uncapped CNTs, nanometer-sized holes, shortened CNTs and disrupted side walls were evident (Fig. S11). These could arise from oxidation of C–C bonds around initial defect sites.24 H_2O_2 may penetrate such defect sites, attacking the underlying C–C bonds causing further sidewall damage facilitated by laser irradiation.[21] Similar effects were also observed with SWCNTs and DWCNTs (Fig. S12). Raman spectroscopy of laser-VFD processed SWCNTs, DWCNTs and MWCNTs all showed significant increase in the I_D/I_G ratio, which is consistent with an increase in functional groups on the sample surface. Over-all, this solvent initiated layer-by-layer degradation in the presence of laser irradiation and mechanical energy input from the VFD are collectively responsible in the fabrication of CDs. Post-VFD processing, further tuning of fluorescence and chemical adoption is achievable (Fig. S16). As-processed CDs (dispersed in H_2O_2) and ethanol (ratio of 1 : 1) were eluted through an adsorption column packed with molecular sieve and magnesium sulphate. Different fluorescence properties were observed. Additionally, CDs dispersed in H_2O_2 and ammonia (25%) (ratio 6 : 1) and heated at 60 °C, as a variation of the method reported by Jiang et al.,[39] resulted in doping of N (1.46% XPS) but there was no change on the PL spectrum (Fig. S13).

2.5 Conclusions

We have developed a simple and relatively benign method using a VFD to produce water soluble CDs with scalability incorporated into the processing. The optimum operating parameters correspond to a sample concentration of 0.1 mg mL^{-1}, rotational speed of 7500 rpm, 0.45 mL min^{-1} flow rate, with a laser power of 450 mJ. The CDs exhibit excitation wavelength independent PL behavior with two distinctive emission peaks around 420 and 460 nm, being an integration of at least three emissive sites originated from the aromatic core, defects and functional groups. CDs are chemically reactive and could be potentially used for further chemical functionalisation. Importantly, VFD processing favours more product homogeneity in the dynamic thin film in the micro-fluidic platform, with product quality independent of the sample volume passing from the VFD. Future experiments will investigate the possibility of tuning the intrinsic fluorescence by controlling the size of CDs which is crucial for red-shifting of the excitation wavelength.[11] This could involve the use of a plasma VFD which is effective in changing the morphology of graphene.[40] Various catalytic peroxidase enzyme such as HRP and lignin peroxidase might be applicable for accelerating the degradation of nanotubes in the presence of H_2O_2.[24] As mentioned, VFD has been applied in nanocarbon proessing such as slicing carbon nanotubes[25] and scrolling graphene sheets, this chapter further extends the laser-mediated-VFD processing towards CD production through an environmently-friendly procedure with practical scaling up potentials. To further explore this frabrication system, in the next chapter, we describe the laser-mediated-VFD processing in metallic nanoparticle processing for the first time.

2.6 Acknowledgement

The authors gratefully acknowledge financial support from the Australian Research Council and the Government of South Australia, and the Australian Microscopy & Microanalysis Research Facility (AMMRF) and the Australian National Fabrication Facility (ANFF) for accessing microscopic facilities and the Edinburgh Instruments Spectrofluorimeter funded by ARC LIEF grant. The authors would also like to thank Dr. Chris Gibson, Mr. Yanting Yin, Dr. Muneer Syed Musthakahmed, Dr Georgios Tsiminis and Prof. Gregory A. Weiss for valuable discussions and help from Dr Jason Gascooke for some laser experiments, Ms. Yvette DeGraaf for fluorescence microscopy, Ms. Ashleigh Clapper for pH- responsive PL experiments and Dr. Faruq Ahmed on tissue culture studies.

2.7 References

1. K. Chua, Z. Sofer, P. Šimek, O. Jankovský, K. Klímová, S. Bakardjieva, Š. Hrdličková Kučková and M. Pumera, ACS Nano, 2015, 9, 2548–2555.
2. Y. Wang and A. Hu, J. Mater. Chem. C, 2014, 2, 6921–6939.
3. S. T. Yang, X. Wang, H. Wang, F. Lu, P. G. Luo, L. Cao, M. J. Meziani, J. H. Liu, Y. Liu, M. Chen, Y. Huang and Y. P. Sun, J. Phys. Chem. C, 2009, 113, 18110–18114.
4. Q. Zeng, D. Shao, X. He, Z. Ren, W. Ji, C. Shan, S. Qu, J. Li, L. Chen and Q. Li, J. Mater. Chem. B, 2016, 4, 5119–5126.
5. X. Li, M. Rui, J. Song, Z. Shen and H. Zeng, Adv. Funct. Mater., 2015, 25, 4929–4947.
6. X. Xu, R. Ray, Y. Gu, H. J. Ploehn, L. Gearheart, K. Raker and W. A. Scrivens, J. Am. Chem. Soc., 2004, 126, 12736–12737.
7. H. Peng and J. Travas-Sejdic, Chem. Mater., 2009, 21, 5563–5565.
8. L. Shen, L. Zhang, M. Chen, X. Chen and J. Wang, Carbon, 2013, 55, 343–349.
9. J.Deng,Q.Lu,N.Mi,H.Li,M.Liu,M.Xu,L.Tan,Q.Xie,Y. Zhang and S. Yao, Chem. – Eur. J., 2014, 20, 4993–4999.
10. Y. Suda, T. Ono, M. Akazawa, Y. Sakai, J. Tsujino and N. Homma, Thin Solid Films, 2002, 415, 15–20.
11. M. Buzaglo, M. Shtein and O. Regev, Chem. Mater., 2016, 28, 21–24.
12. Y. Yang, J. Cui, M. Zheng, C. Hu, S. Tan, Y. Xiao, Q. Yang and Y. Liu, Chem. Commun., 2012, 48, 380–382.
13. X. Zhai, P. Zhang, C. Liu, T. Bai, W. Li, L. Dai and W. Liu, Chem. Commun., 2012, 48, 7955–7957.
14. H. Gonçalves and J. C. G. Esteves da Silva, J. Fluoresc., 2010, 20, 1023–1028.
15. V. Nguyen, L. Yan, J. Si and X. Hou, J. Appl. Phys., 2015, 117, 1–6.
16. D. Tan, S. Zhou, J. Qiu and N. Khusro, J. Photochem. Photobiol., C., 2013, 17, 50–68.
17. D. Reyes, M. Camacho, M. Camacho, M. Mayorga, D. Weathers, G. Salamo, Z. Wang and A. Neogi, Nanoscale Res. Lett., 2016, 11, 1–11.

18. Y. P. Sun, B. Zhou, Y. Lin, W. Wang, K. A. S. Fernando, P. Pathak, M. J. Meziani, B. A. Harruff, X. Wang, H. Wang, P. G. Luo, H. Yang, M. E. Kose, B. Chen, L. M. Veca and S. Y. Xie, J. Am. Chem. Soc., 2006, 128, 7756–7757.
19. S. Zhu, Y. Song, X. Zhao, J. Shao, J. Zhang and B. Yang, Nano Res., 2015, 8, 355–381.
20. K. Voitko, A. Tóth, E. Demianenko, G. Dobos, B. Berke, O. Bakalinska, A. Grebenyuk, E. Tombácz, V. Kuts, Y. Tarasenko, M. Kartel and K. László, J. Colloid Interface Sci., 2015, 437, 283–290.
21. Y. Wang, H. Shan, R. H. Hauge, M. Pasquali and R. E. Smalley, J. Phys. Chem. B, 2007, 111, 1249–1252.
22. R. Marega, G. Accorsi, M. Meneghetti, A. Parisini, M. Prato and D. Bonifazi, Carbon, 2009, 47, 675–682.
23. B. Czech, P. Oleszczuk and A. Wiącek, Environ. Pollut., 2015, 200, 161–167.
24. W. Xing, G. Lalwani, I. Rusakova and B. Sitharaman, Part. Part. Syst. Charact., 2014, 31, 745–750.
25. K. Vimalanathan, J. R. Gascooke, I. Suarez-Martinez, N. A. Marks, H. Kumari, C. J. Garvey, J. L. Atwood, W. D. Lawrance and C. L. Raston, Sci. Rep., 2016, 6, 22865.
26. X. Luo, P. Smith, C. L. Raston and W. Zhang, ACS Sustainable Chem. Eng., 2016, 4, 3905–3911.
27. X. Luo, A. H. M. Al-Antaki, S. Pye, R. Meech, W. Zhang and C. L. Raston, ChemPhotoChem, DOI: 10.1002/cptc.201700206.
28. X. Chen, J. F. Dobson and C. L. Raston, Chem. Commun., 2012, 48, 3703–3705.
29. K. Vimalanathan, X. Chen and C. L. Raston, Chem. Commun., 2014, 50, 11295–11298.
30. M. Kashima-Tanaka, Y. Tsujimoto, K. Kawamoto, N. Senda, K. Ito and M. Yamazaki, J. Endod., 2003, 29, 141–143.
31. A. E. Islam, S. S. Kim, R. Rao, Y. Ngo, J. Jiang, P. Nikolaev, R. Naik, R. Pachter, J. Boeckl and B. Maruyama, RSC Adv., 2016, 6, 42545–42553.
32. C. Brolly, J. Parnell and S. Bowden, Planet. Space Sci., 2016, 121, 53–59.
33. E. Vahabzadeh and M. J. Torkamany, J. Cluster Sci., 2014, 25, 959–968.
34. J. Cheng, C.-F. Wang, Y. Zhang, S. Yang and S. Chen, RSC Adv., 2016, 6, 37189–37194.
35. R. Thangaraj and A. S. Kumar, Anal. Methods, 2012, 4, 2162–2171.
36. B. De and N. Karak, RSC Adv., 2013, 3, 8286–8290.
37. L. Lin and S. Zhang, Chem. Commun., 2012, 48, 10177–10179.
38. S. Wang, I. S. Cole, D. Zhao and Q. Li, Nanoscale, 2016, 8, 7449–7458.
39. D. Jiang, Y. Chen, N. Li, W. Li, Z. Wang, J. Zhu, H. Zhang, B. Liu and S. Xu, PLoS One, 2016, 10, 1–15.
40. D. B. Jones, X. Chen, A. Sibley, J. S. Quinton, C. J. Shearer, C. T. Gibson and C. L. Raston, Chem. Commun., 2016, 52, 10755–10758.

Appendix: Journal inside cover of the published article, the article's first page and the first page of the published supplementary information

Volume 3 | Number 2 | April 2018 | Pages 121–228

Reaction Chemistry & Engineering

Linking fundamental chemistry and engineering to create scalable, efficient processes

rsc.li/reaction-engineering

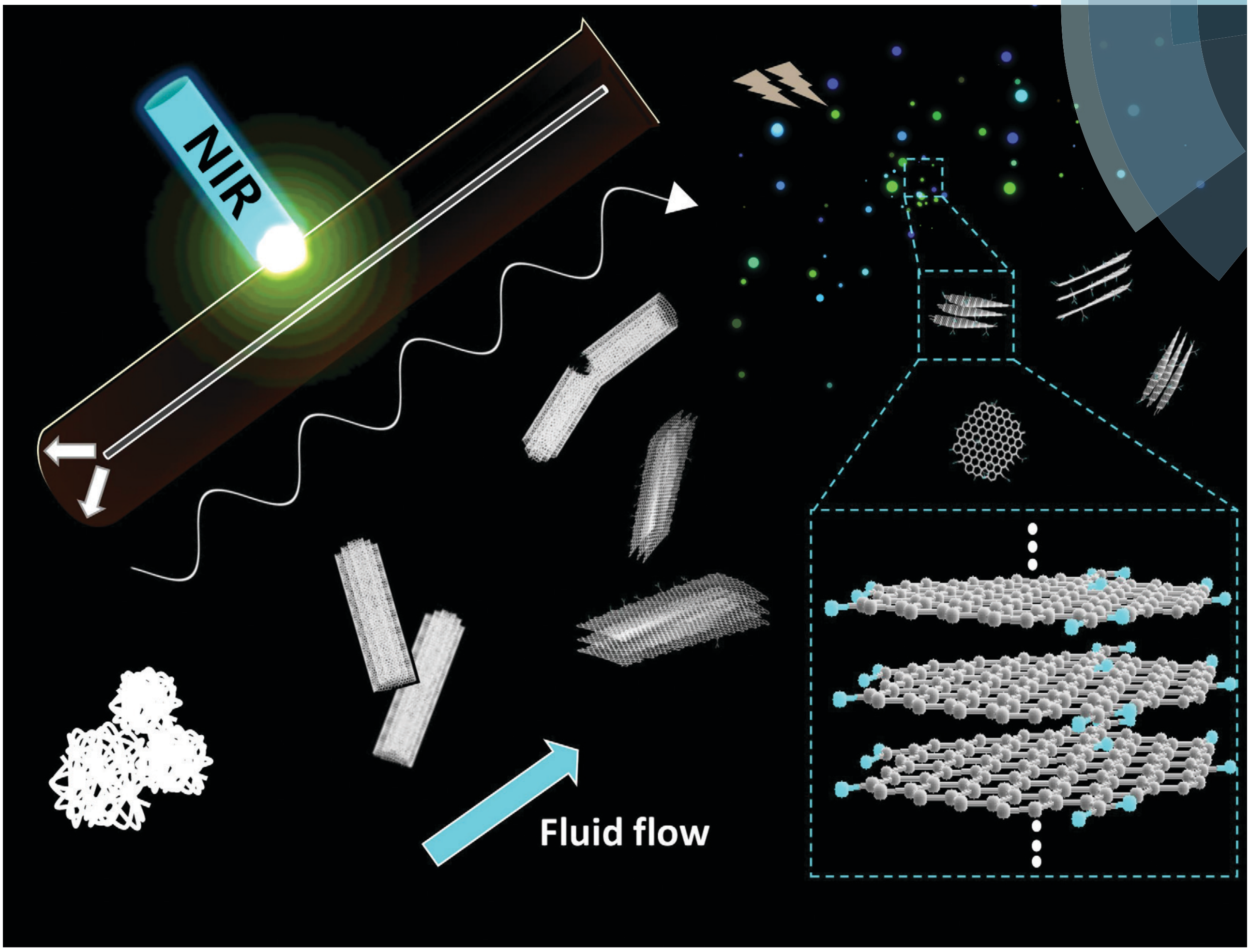

ISSN 2058-9883

ROYAL SOCIETY OF CHEMISTRY

PAPER

Wei Zhang, Colin L. Raston *et al.*

Laser irradiated vortex fluidic mediated synthesis of luminescent carbon nanodots under continuous flow

Reaction
Chemistry &
Engineering

PAPER

Check for updates

Cite this: *React. Chem. Eng.*, 2018, **3**, 164

Laser irradiated vortex fluidic mediated synthesis of luminescent carbon nanodots under continuous flow†

Xuan Luo,[ab] Ahmed Hussein Mohammed Al-Antaki,[b] Kasturi Vimalanathan,[b] Jillian Moffatt,[c] Kun Zheng,[de] Yichao Zou,[f] Jin Zou,[df] Xiaofei Duan,[g] Robert N. Lamb,[h] Shujun Wang,[i] Qin Li,[i] Wei Zhang*[a] and Colin L. Raston*[b]

Received 30th November 2017,
Accepted 15th January 2018

DOI: 10.1039/c7re00197e

rsc.li/reaction-engineering

Carbon nanodots (CDs) with size dependent fluorescence are synthesized from multi-walled carbon nanotubes (MWCNTs) under continuous flow in a vortex fluidic device (VFD) when irradiated by a pulsed laser with a wavelength of 1064 nm, without subsequent passivation procedures. The CDs have a relatively narrow size distribution averaging *ca.* 6 nm in diameter, and have low cytotoxicity and high colloidal stability with the highest emission intensity of the solution at 450 nm under a 345 nm excitation wavelength. Further downstream processing on the as-processed CDs revealed tunability of the emission from 450 nm to 325 nm.

Introduction

Carbon nanodots (CDs) are carbon nanoparticles <10 nm in diameter, consisting of a graphitic structure or amorphous carbon core and carbonaceous surfaces, with rich oxygen-containing groups.[1] CDs exhibit distinct properties, most notably strong quantum confinement and edge effects resulting in exceptional fluorescent characteristics.[2] The unique functional properties and benign chemical composition have rendered CDs a promising new material for a broad range of applications including bioimaging,[3] drug delivery,[4] and optoelectronic devices.[5] Various feedstocks have been used for producing CDs including single walled carbon nanotubes,[6] carbohydrates,[7] polyethylenimine,[8] low molecular weight alcohols,[9] graphite,[10] and carbon soot.[3] In general, the quantum yield of CDs varies dramatically, from 1.32% (ref. 11) up to around 43%,[12] depending on the choice of carbon feedstock. A number of methods have been reported to prepare CDs within these dimensions, including chemical ablation, laser ablation,[2] electrochemical carbonisation,[9] arc-discharge pyrolysis,[2] hydrothermal synthesis,[12] and ultrasound and microwave-assisted pyrolysis.[13] Laser ablation is a well-studied technique in synthesizing CDs from various carbon-based targets.[14–16] The significant advantage of this technique over other methods is that the processing is relatively clean, with reduced byproduct formation.[15] However, the potential of synthesizing CDs through laser ablation in liquids is limited by the scalability and gravitational settling of the raw material.[15] Other potential issues using conventional laser ablation processing include controlling the crystallinity of the CDs,[17] relatively long processing times,[15] and the requirement for additional passivation reaction, for example long acid refluxing times.[14,18]

One of the most common methods of fabricating oxygen-containing CDs involves using a mixture of concentrated H_2SO_4 and HNO_3.[19] However, this requires tedious purification procedures to remove the excess acid, and uses toxic and harsh chemicals. The catalytic activity of MWCNTs towards H_2O_2 decomposition (HPD) has been reported in a few studies, and the properties of the nanotubes post processing can be affected.[20] A mixture of H_2O_2 and 1 M HCl or 96 wt% H_2SO_4 has been used for the oxidation and purification of carbon nanotubes (CNTs),[21] with 15% H_2O_2 alone at 100 °C for 3 hours being effective in removing the end caps and shortening the length of the CNTs with concomitant surface

---

[a] *Centre for Marine Bioproducts Development, College of Medicine and Public Health, Flinders University, Adelaide, SA 5042, Australia. E-mail: wei.zhang@flinders.edu.au*
[b] *Centre for NanoScale Science and Technology (CNST), College of Science and Engineering, Flinders University, Adelaide, SA 5042, Australia. E-mail: colin.raston@flinders.edu.au*
[c] *Institute for Photonics and Advanced Sensing, and School of Physical Sciences, The University of Adelaide, SA 5005, Australia*
[d] *Centre for Microscopy and Microanalysis, The University of Queensland, Brisbane, QLD 4072, Australia*
[e] *Australian Institute for Bioengineering and Nanotechnology, The University of Queensland, Brisbane, QLD 4072, Australia*
[f] *Materials Engineering, The University of Queensland, Brisbane, QLD 4072, Australia*
[g] *Trace Analysis for Chemical, Earth and Environmental Sciences (TrACEES), The University of Melbourne, Victoria 3010, Australia*
[h] *School of Chemistry, The University of Melbourne, Victoria 3010, Australia*
[i] *Environmental Engineering and Queensland Micro and Nanotechnology Centre, Griffith University, Brisbane, QLD 4111, Australia*

† Electronic supplementary information (ESI) available. See DOI: 10.1039/c7re00197e

This journal is © The Royal Society of Chemistry 2018

Electronic Supplementary Material (ESI) for Reaction Chemistry & Engineering.
This journal is © The Royal Society of Chemistry 2018

Supporting Information

Laser irradiated vortex fluidic mediated synthesis of luminescent carbon nanodots under continuous flow

Xuan Luo[1,2], Ahmed Hussein Mohammed Al-Antaki[2], Kasturi Vimalanathan[2], Jillian Moffatt,[3] Kun Zheng[4,5], Yichao Zou[6], Jin Zou[4,6], Xiaofei Duan[7], Robert N. Lamb[8], Shujun Wang[9], Qin Li[9], Wei Zhang[1*] and Colin L. Raston[2*]

[1] Centre for Marine Bioproducts Development, College of Medicine and Public Health, Flinders University, Adelaide, SA 5042, Australia;

[2] Centre for NanoScale Science and Technology (CNST), College of Science and Engineering, Flinders University, Adelaide, SA 5042, Australia;

[3] Institute for Photonics and Advanced Sensing, and School of Physical Sciences, The University of Adelaide, SA 5005, Australia;

[4] Centre for Microscopy and Microanalysis, The University of Queensland, Brisbane, QLD 4072, Australia;

[5] Australian Institute for Bioengineering and Nanotechnology,The University of Queensland, Brisbane, QLD 4072, Australia;

[6] Materials Engineering, The University of Queensland, Brisbane, QLD 4072, Australia;

[7] Trace Analysis for Chemical, Earth and Environmental Sciences (TrACEES), The University of Melbourne, Victoria 3010, Australia;

[8] School of Chemistry, The University of Melbourne, Victoria 3010, Australia;

[9] Environmental Engineering and Queensland Micro and Nanotechnology Centre, Griffith University, Brisbane, QLD 4111, Australia.

Corresponding Authors

*C. Raston. Tel.: +61 8 82017958. Fax: +61 8 8201290. E-mail: colin.raston@flinders.edu.au

*W. Zhang. Tel.: +61 8 72218557. Fax: +61 8 72218555. E-mail: wei.zhang@flinders.edu.au

3. IN SITU METAL LASER ABLATION SYNTHESIS OF SUPERPARAMAGNETIC MAGNETITE NANOPARTICLES IN WATER UNDER FLOW

Magnetite is one of the most intensively studied iron oxide nanoparticles (IONPs), and can be prepared using a number of different methods. The existing methods have different disadvantages relating to shape/size control, stability, scalability, mono-dispersity and production cost. Among them, the co-precipitation method is relatively simple and fast, and has potential for scaling up, however it generates nanoparticles with a wide particle size distribution and a waste stream incorporating toxic chemicals. Pulsed laser ablation, which can be a simple, surfactant and counter-ion free technique, has been used to prepare magnetic nanoparticles with a narrow size distribution. However, selectively forming only one iron oxide phase, precisely controlling the collapse of plume and scaling up are major challenges for conventional laser processing techniques. Laser ablation of an iron target in the gas-phase can circumvent some of the above drawbacks in liquid ablation processing, using air as the oxidant. In this chapter, we have established that the VFD is effective in forming superparamagnetic magnetite nanoparticles of spheroidal or hexagonal shapes with a narrow size distribution, as a one-step continuous flow process at ambient pressure, using i*n situ* laser ablation form a pulsed laser operating in the NIR. This time, the laser is extended to an ablation function which minimizes the generation of waste by avoiding the need for any chemicals/surfactants; and avoids time consuming purification steps by reducing any negative impact of the processing on the environment.

This study was published in ***ACS Omega***, Year 2018, Vol. 3, Issue 9, Pages 11172-11178. The first page of the publication is attached in Appendix 3.1.

Author contributions: **XL** performed all the VFD and tissue culture experiments, most characterization experiments and data analysis; wrote all the primary content. **AA** help on some VFD experiments, the use of heating jacket and assisted with the O_2 experiments. **SP** performed the NMR and assisted with data analysis. **RM** supervised the tissue culture experiments. **WZ** and **CR** supervised and coordinated the project and helped on the research directions and plan, and the final revision of the manuscript. All of the co-authors assisted with the revision of the manuscript before and during the publication process.

Laser ablated vortex fluidic mediated synthesis of superparamagnetic magnetite nanoparticles in water under flow

Xuan Luo,[a,b] *Ahmed H. M. Al-Antaki,*[a] *Thaar M. D. Alharbi,*[a] *Wayne D. Hutchison,*[c] *Yi-chao Zou,*[d] *Jin Zou,*[d] *Antony Sheehan,*[e] *Wei Zhang**[b] *and Colin L. Raston**[a]

a. Flinders Institute for NanoScale Science and Technology (CNST), College of Science and Engineering, Flinders University, Adelaide, SA 5042, Australia

b. Centre for Marine Bioproducts Development, College of Medicine and Public Health, Flinders University, Adelaide, SA 5042, Australia

c. School of PEMS, University of New South Wales, ADFA campus, Canberra BC, ACT 2610, Australia

d. Materials Engineering and Centre for Microscopy and Microanalysis, The University of Queensland, Brisbane, QLD 4072, Australia

e. TGR Biosciences Pty Ltd, 31 Dalgleish St, Thebarton, Adelaide, SA 5031, Australia

Graphical abstract

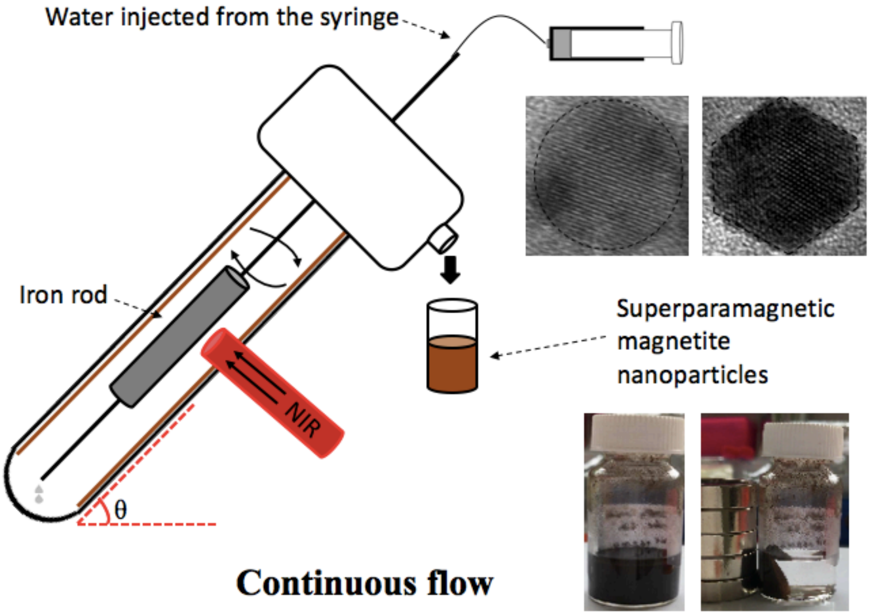

Corresponding Author

*C. Raston. Tel.: +61 8 82017958. Fax: +61 8 8201290. E-mail:
colin.raston@flinders.edu.au

*W. Zhang. Tel.: +61 8 72218557. Fax: +61 8 72218555. E-mail:
wei.zhang@flinders.edu.au

3.1 Abstract

Selective formation of only one iron oxide phase is a major challenge in conventional laser ablation process, as is scaling up the process. Herein, superparamagnetic single-phase magnetite nanoparticles of hexagonal and spheroidal-shape, with an average size *ca*. 15 nm, are generated by laser ablation of bulk iron metal at 1064 nm in a vortex fluidic device (VFD). This is a one-step continuous flow process, in air at ambient pressure, with *in situ* uptake of the nanoparticles in the dynamic thin film of water in the VFD. The process minimizes the generation of waste, in avoiding the need for any chemicals or surfactants, and avoids time consuming purification steps, in reducing any negative impact of the processing on the environment.

KEYWORDS: Laser ablation, iron oxide nanoparticles, superparamagnetism.

3.2 Introduction

The synthesis and availability of iron oxide nanoparticles (IONPs) is of general interest in many fields of research and in a number of applications. Some common phases of IONPs include α-Fe_2O_3 (hematite), Fe_3O_4 (magnetite), γ-Fe_2O_3 (maghemite), α-Fe (ferrite), Fe_3C (iron carbide) and FeO (wustite). For magnetite, smaller than 20 nm have superparamagnetic properties, and are known as superparamagnetic IONPs.[1,2] This property relates to the large magnetic moment resulting from the coupling of the atomic spins within the nanosized magnetite nanoparticles.[3] Magnetite is one of the most intensively studied IONPs, which can be prepared using a number of different methods, including co-precipitation,[1] sol-gel,[4] micro emulsion,[5] ultrasonic spray pyrolysis[6] and microwave plasma.[7] They have different advantages and disadvantages relating to shape/size control, stability, scalability, mono-dispersity and production cost. Among them, the co-precipitation method is relatively simple and fast, and has potential for scaling up, however it generates nanoparticles with a wide particle size distribution[1] and can generate a waste stream incorporating toxic chemicals.[8]

Pulsed laser ablation, which can be a simple and surfactant and counter-ion free technique[9], has been used to prepare magnetic nanoparticles with a narrow size distribution.[2] IONPs can be generated by laser ablation of bulk iron in either the gas or liquid phase,[10] the latter being the most studied,[11] with Nd:YAG laser processing at 1064 nm affording nanoparticles with enhanced magnetic properties.[2] Water is the preferred solvent in terms of applications and environmental considerations, with the use of organic solvents generating amorphous carbon and iron carbide from its breakdown.[8,11,12] However, selectively forming only one iron oxide phase in water is a major challenge in laser processing.[2,9,12] Also noteworthy is that after each laser pulse, the time taken for collapse of the plume is crucial in controlling the nucleation and growth of the IONPs;[2] longer times equate to longer growth times, affording mainly larger particles during the ablation in the liquid. On the other hand, laser ablation of an iron target in the gas-phase can circumvent some of the above drawbacks for liquid ablation processing, using air as the oxidant.[13] Also noteworthy is that the generation of nanoparticles from ablation in the gas-phase is preferred due to increased yield relative to ablation in the liquid-phase.[13] Maghemite has been generated by laser ablation in a mixture of nitrogen and oxygen at atmospheric pressure,[12] albeit with a broad size distribution of the particles, 5 to 90 nm in diameter. Laser ablation processing in the gas phase requires a more sophisticated setup with a specially-designed ablation chamber and particle collector relative to liquid phase ablation.[13,14]

We were motivated to integrate laser ablation in both gas- and liquid-phases using the versatile vortex fluidic device (VFD) in association with a Nd:YAG pulsed laser, in developing a scalable process for preparing magnetite in water with control over the size of particles, and without requiring chemical additives. The VFD is a thin film microfluidic platform that is effective in high yield and controllable organic and material synthesis, in harnessing the intense micro-mixing and high heat and mass transfer in the dynamic film.[15] Nd:YAG pulsed laser-assisted VFD processing has been used for fabricating graphene oxide scrolls from graphene oxides[16] and lateral slicing of high tensile strength carbon nanotubes[17] noting that in the absence of the laser, the mechano-energy in the film is effective in forming compact single walled carbon nanotube toroids or rings.[18] The VFD is also effective in enhancing chemical reactivity and selectivity,[19] intensifying multi-phase separation,[20] enhancing enzymatic reactions,[21] and in many more applications.[22] In the present study, the VFD was operated at 45 degree tilt angle for the rapidly rotating borosilicate glass tube (O.D. 20 mm, I.D. 17.5 mm), which is the optimal angle for a number of processes.[17-22] VFD processing can be conducted on small sub-millilitre scales, in the so called confined mode where there is tilt angle dependent shear stress, as well as up-scaled under continuous flow, Figure 1. Polyvinyl pyrrolidine (PVP) coated superparamagnetic magnetite nanoparticles with a mean diameter of <10 nm have been previously fabricated using a co-precipitation method under continuous flow using a VFD with a 10 mm O.D. glass tube in an ammonia/nitrogen atmosphere.[23] Herein we have established that the VFD with a 20 mm O.D. glass tube with higher volume capacity and safer laser ablation distance is effective in forming superparamagnetic magnetite nanoparticles with a narrow size distribution, as a one-step continuous flow process at ambient pressure. The process is devoid of any gas flow which simplifies the set-up and minimizes the generation of waste, while avoiding the need for any chemicals/surfactants, as well as time consuming purification steps, in reducing any negative impact of the processing on the environment.

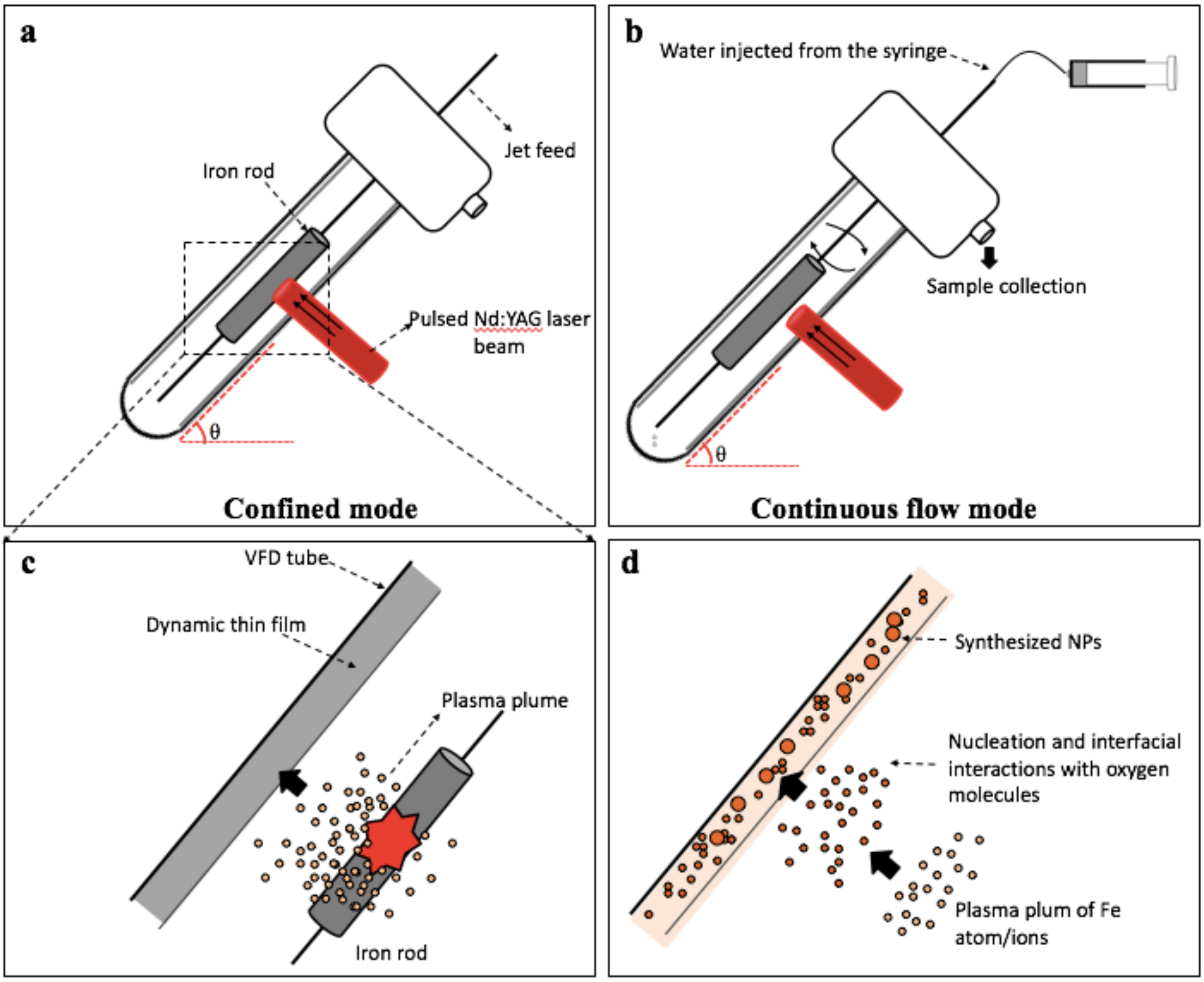

***Figure 3.1** (a) Laser beam irradiation of an iron rod placed inside the VFD tube with the device operated in the confined mode. (b) Laser beam irradiation of an iron rod placed inside the VFD tube with the device operated in continuous flow mode. (c) Cartoon of a plasma plume containing iron atoms and ions. (d) Generating iron oxide nanoparticle through diffusion-driven nucleation and aggregation in the presence of a gas and a liquid carrier.*

3.3 Materials and methods

The experiments were carried out under both the confined mode and continuous flow mode of operation of the VFD, as indicated in Figure 1. In a typical confined mode experiment, 15 minute processing time was carried out in a rapidly rotating tube at θ 45° tilt with a simultaneously 5 nanosecond pulsed laser at 1064 nm (pulsed Q-switch Nd:YAG laser) with a 8 mm diameter laser beam irradiating a high purity (>99.998%) iron rod 5 mm in diameter which was immobilized on a stainless steel jet feed (Figure 1a). In continuous flow, experiments were conducted under the same conditions as described in the confine mode, except that stainless steel jet feeds were used for both immobilizing the iron rod and delivering liquid into the rapidly rotating tube (Figure 1b). Optimizing the flow rate of water involved studying 0.1, 0.5 and 1.0 mL/min flow rates, using a syringe pump. Under both processing conditions, the laser beam was positioned perpendicular to the target surface, with the formation of hot and high pressure plasma plumes containing iron atoms and ions expanding in all directions (Figure 1c and d). The laser beam was focused about 7.5 mm away from the thin film surface with the expanding plumes restrained within the VFD tube.

As prepared samples were dried in the open air as per previous studies[2] and were characterized by UV-vis spectrophotometer (Varian Cary 50) in the 200-1000 nm range in a quartz cell and X-ray diffraction (Bruker D8 ADVANCE ECO, Co-Kα, λ=1.79 Å) with radiation generated at 35 kV and 28 mA and a grazing incidence angle (3 °) in the 2θ range of 20° to 80°. The lattice parameter calculations were obtained using the EVA software. The average crystallite size was estimated using Debye-Scherrer equation. Particle sizes/morphology and crystalline structures were observed using dynamic light scattering (DLS) (Malvern Instrument, UK), scanning electron microscopy (SEM), transmission electron microscopy (TEM), and atomic force microscopy (AFM). TEM was conducted on a FEI TECNAI F20 microscope operated at 200 kV. Raman spectroscopy was performed with an excitation wavelength of 532 nm for an integration time of 30 s to differentiate the presence of magnetite and maghemite. As processed materials were investigated using Raman spectroscopy after drop-casting one drop of the colloidal material on a glass substrate. Magnetic measurements were carried out using a Quantum Design PPMS with ACMS option at room temperature (295 K) by saturating the sample in a field of up to 15,000 Oe.

3.4 Results and discussion

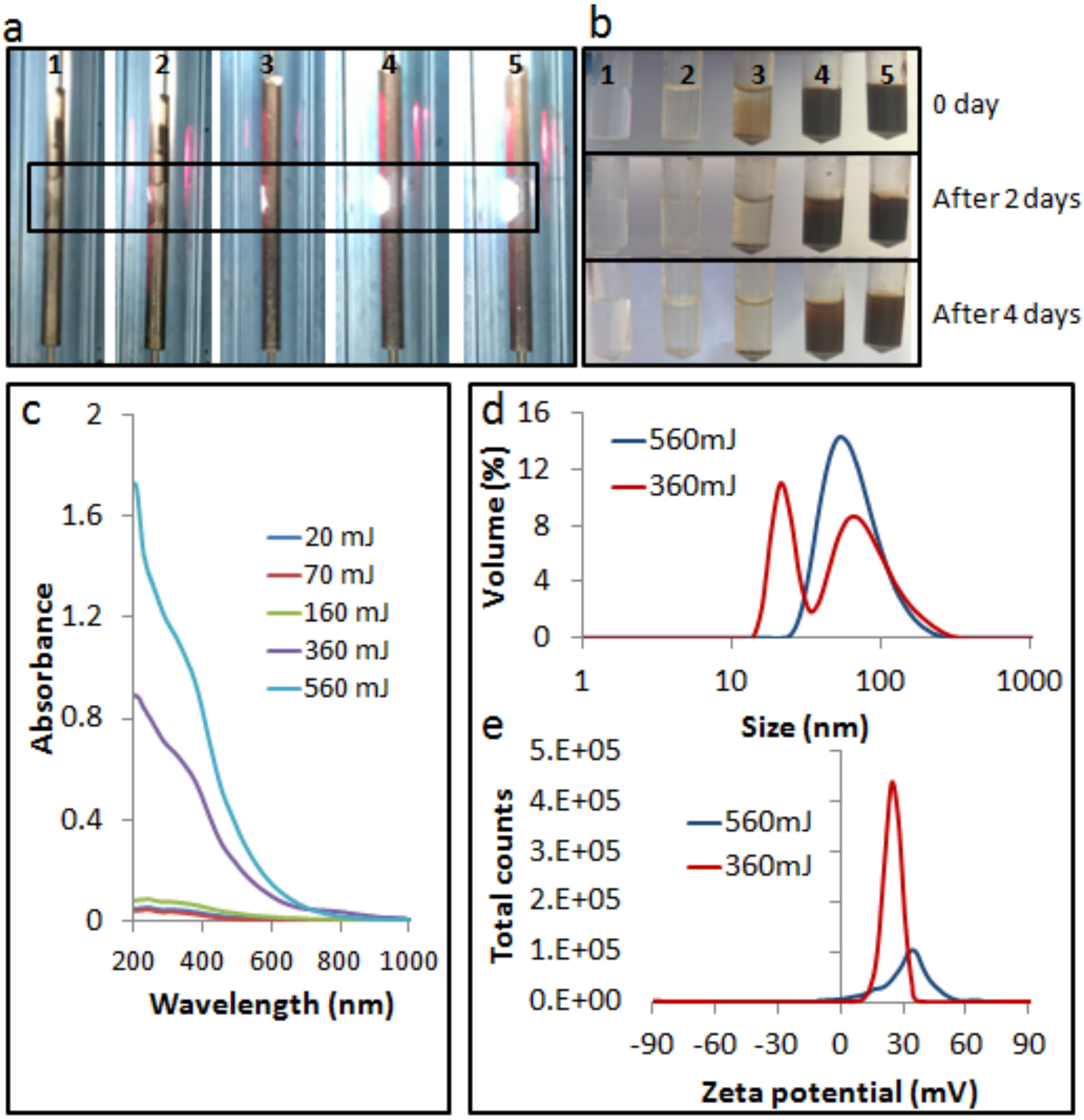

Figure 3.2 *(a) Images showing the laser irradiation position with the iron rod placed inside the VFD tube spun at 7500 rpm with the 1064 nm pulsed laser operating at 20, 70, 160, 360 and 560 mJ, from samples 1 to 5 respectively. (b) As prepared sample dispersed in 1 mL water; a stable colloidal suspension was obtained for 360 and 560 mJ. (c) UV-vis spectra. (d) Dynamic light scattering results. (e) Zeta potential data.*

All the optimization experiments were initially conducted with the VFD operated in the confined mode with 1 mL water. The laser power was optimized first by conducting the experiment for 15 min at different laser powers, 20, 70, 160, 360 and 560 mJ, Figure 2a. Brown suspensions, as an indicator of the formation of iron oxide particles, were only obtained for experiments conducted at high laser power, at 360 and 560mJ. The suspensions have good colloidal stability for days, Figure 2b, in agreement with the zeta-potential about +30 mV, Figure 2e. Post VFD processing, the pH of the as processed IONPs became slightly acidic relative to the MilliQ water, affording positively charged particles.[24] As prepared IONPs are not coated, and are likely to agglomerate in water (Figure 2d) in reducing their large surface area to volume ratio, as reported by Demirer *et al.*.[1] Iron-based nanoparticles lack sharp UV-vis spectrum absorption bands[8] but can be characterized by an absorption threshold for wavelengths lower than 400 nm (Figure 2c), typically representing different iron oxide phases of hematite, magnetite and iron carbide.[8,25] The concentration of the as prepared samples could be indirectly estimated using UV-vis spectroscopy with high absorbance associated with higher yield, as established by Fazio *et al.*[25] Figure 2c indicated that processing at 360 and 560 mJ generated the highest quantities of IONPs compared to other conditions. However, the borosilicate glass tube VFD deteriorated with the risk of fracture using a laser power of 560 mJ, and accordingly the lower power of 360 mJ was used.

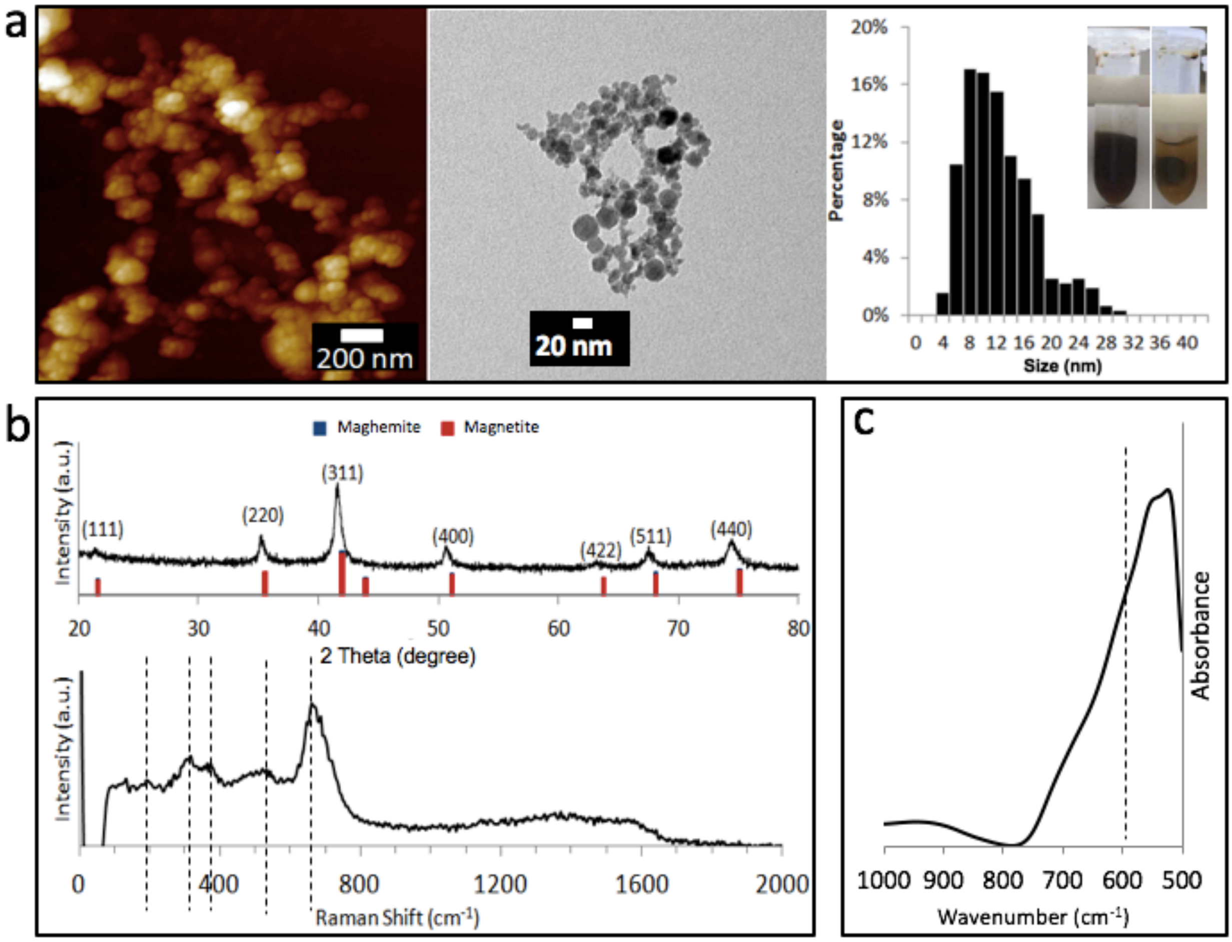

Figure 3.3 *Characterisation of the as prepared IONPs (laser power 360 mJ for the VFD tube rotated at 7500 rpm for 15 min. in the confined mode for 1 mL water. (a) AFM, TEM and size distribution plot which represented more than 300 randomly chosen IONPs. (b) XRD diffraction pattern and Raman spectra. (c) FT-IR spectrum.*

AFM, TEM and XRD analyses were carried out on the samples ablated at 360 mJ, in establishing their composition and morphology. AFM revealed large aggregates of small spherical nanoparticles, Figure 3a, in accordance with TEM images that gave an estimated average particle of 12 nm, with a relatively narrow size distribution. XRD established that the material is either magnetite (COD 1011032) or maghemite (COD 9006316), with a crystallite size of *ca.* 14.2 nm, using the Debye-Scherrer equation, Figure 3b. The variation of the size estimation by XRD from TEM could be due to the presence of strain in the crystals that can lead to overestimation of particle diameters.[26] Raman spectroscopy can be used to differentiate between magnetite and maghemite.[27] The magnetite crystal belongs to the cubic space group *Fd*3*m*, having five Raman-active bands, A_{1g}, E_g and three T_{2g}, and four infrared active bands T_{1u}.[28] The most intense band for magnetite (A_{1g} mode) was observed at 662 cm^{-1} (Figure 3b). Three smaller bands were observed at 192 (T_{2g}), 313 (E_g) and 526 (T_{2g}) cm^{-1} representing the phonon frequencies of magnetite. Two weak peaks between 1380 to 1600 cm^{-1} possibly correspond to graphitic material.[28] The yellow colour of the solution after the migration of the samples to a magnet (Figure 3a) can be ascribed to the presence of residual nanomagnetic amorphous carbon in solution as described by Amendola *et al*.[8] Second-order Raman spectra are effective for determining the crystallinity of the carbon, [29] but the absence of such in this case (Figure S1 and S2) does not rule out the presence of amorphous carbon[30] that could arise from traces of storage solvent from the iron rod and fixation of carbon dioxide in the air. FTIR spectroscopy gave a band at 550 cm^{-1} corresponding to magnetite (Figure 3c), whereas maghemite having an analogous band at 600 cm^{-1}.[28,31] The black colour of the samples is also consistent with magnetite being the dominant phase.[32]

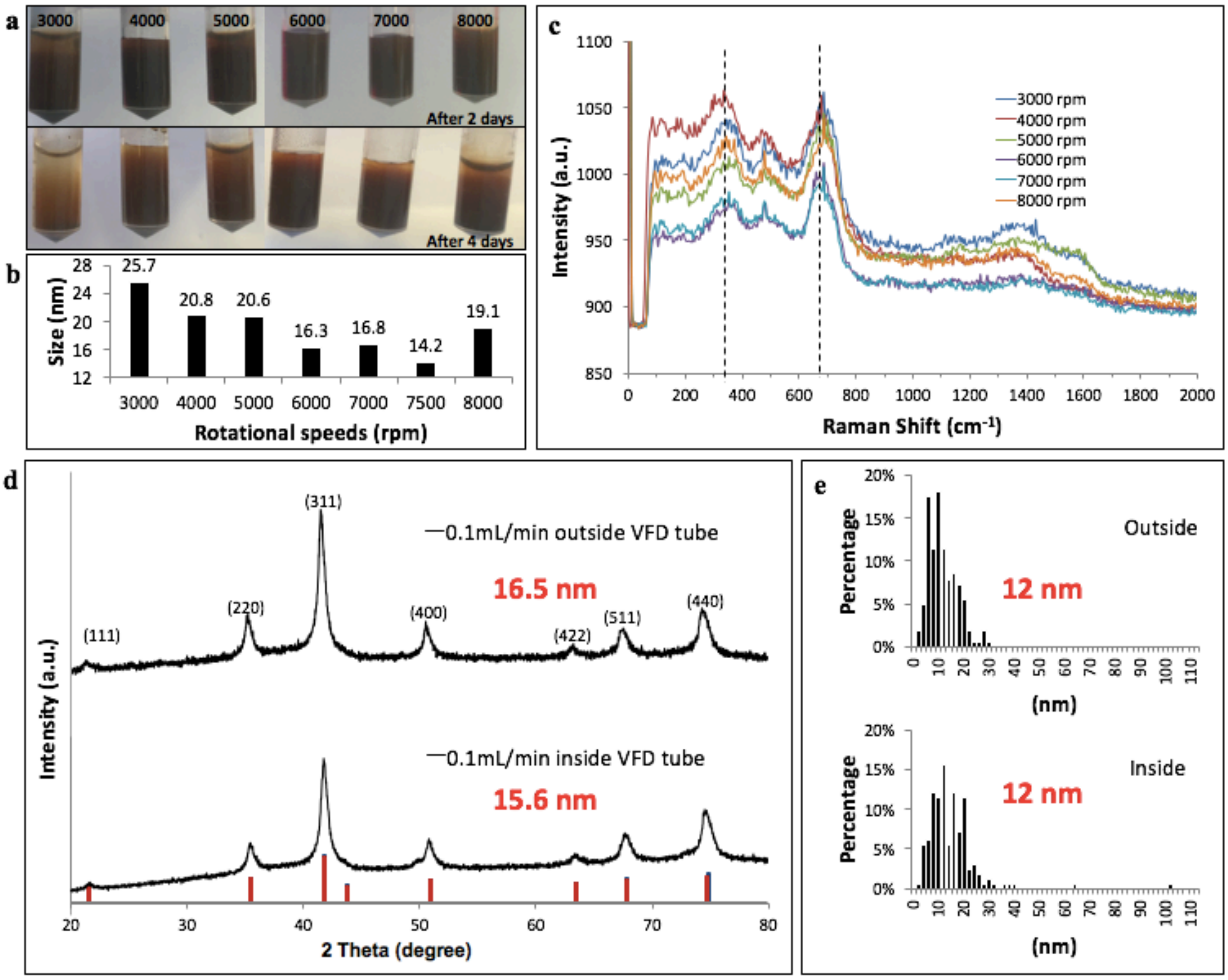

Figure 3.4 *(a) Size of IONPs nanoparticles generated at 360 mJ with the VFD operating in the confined mode containing 1 mL water, for 15 min at different rotational speeds. (b) Particle size estimated using XRD. (c) Raman spectra. (d) XRD of samples conducted under continuous flow mode at 7500 rpm, 0.1 mL/min flow rate (materials exiting and retained inside the tube). (e) Size estimation plot based on TEM for the two samples obtained from continuous flow (materials exiting and retained inside the tube).*

Rotational speed of the VFD tube controls the size of the nanoparticle (Figure 4a-b), with the smallest size obtained at 7500 rpm, 360 mJ laser power, for 15 min in the confined mode, for 1 mL of water in the tube. The particles were rapidly formed during the laser ablation process with the shear presumably preventing the growth and coalescence of nanoparticles. XRD of these samples indicate the presence of magnetite or maghemite for all rotational speeds (Figure S3). The weak Raman peak contribution at 720 cm^{-1} might arise from a small quantity of maghemite[28] at some rotational speeds (Figure 4c). Raman spectra were recorded using a significantly low laser power in order to avoid the transition of magnetite to maghemite or hematite as a result of local radiation.[24,33] A well-defined FT-IR band at 550 cm^{-1}

corresponding to magnetite was observed for all these samples (Figure S4). To scale up the process, a continuous flow mode was used in which a syringe pump delivered water to the base of the VFD tube through a stainless-steel jet feed. Flow rates were varied at 0.1, 0.5 and 1 mL/min, and the average size of particles derived from XRD data, was 15.4±1.1, 19.6±1.0 and 20.3±0.2 nm, respectively (Figure S5). A flow rate of 0.1 mL/min gave similar results (15.4±1.1 nm), comparable to results for the confined mode, for 15 min processing time (14.2 nm). Thus, the processing time in the VFD is critical for controlling the nucleation and growth of the particles. In continuous flow mode, the solution laden IONPs whirl up the rotating tube, exiting through a Teflon housing unit. This ensures more uniform processing during the laser irradiation, affording a more monodispersed size distribution.[11] Post-processing at 0.1 mL/min, deep brown fine particles were distributed along the VFD tube (Figure S6) and were retrieved by dispersing them into fresh water. The yield of the product under continuous flow was estimated to be about 42 μg and 83 μg per minute of samples exiting the VFD (outside) and adhering to the inside of the VFD tube (inside), respectively. The IONPs were recovered by placing a magnet next to the wall of the vial containing the colloidal solution. Characterization using XRD on 0.1 mL/min sample (both inside and outside) confirmed the presence of magnetite (Figure 4d) with an average particle size of around 12 nm (Figure 4e1), with no evidence for the presence of other materials, including carbon.

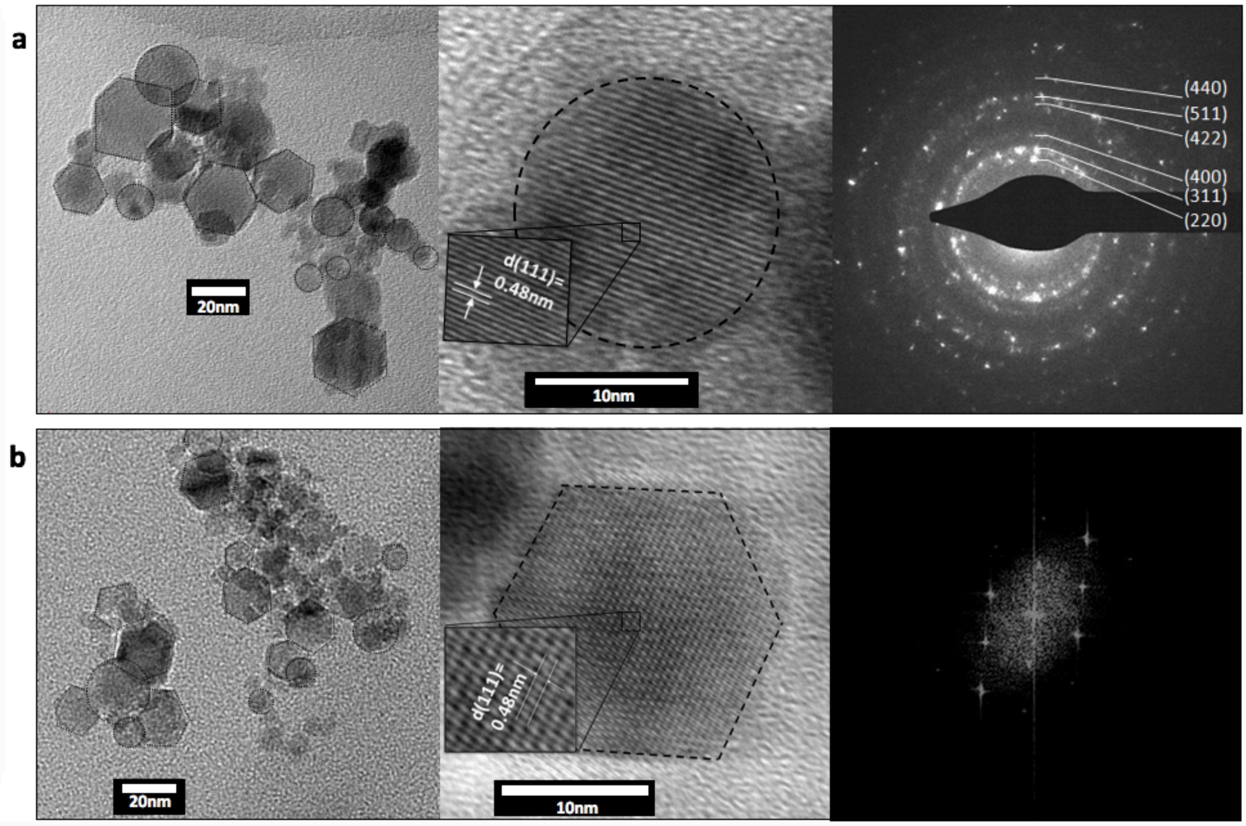

Figure 3.5 *Representative TEM, HRTEM and SAED (marked indices are planes of magnetite). (a) IONPs existing the VFD operated at a rotational speed of 7500 rpm and a flow rate of 0.1 mL/min. (b) IONPs retained inside the tube during processing at a rotational speed of 7500 rpm and a flow rate of 0.1 mL/min. Both samples showed mixed shapes of spheres and hexagonal prisms. Both samples are single-crystals with individual crystallites highlighted. The FFT patterns were acquired from the HRTEM image.*

HRTEM and SAED showed that the IONPs both exiting the tube under flow and retained inside the tube are single crystals, and showed two shapes of spheres and hexagonal prisms (Figure 5).[8] Magnetite nanohexagons are usually obtained using chemical synthesis from iron acetylacetonate under high temperatures up to 290ºC for extended time. However, the average particle size for such hexagons is about 85 nm or up to a hundred nm,[32,34] whereas in our case they are between 15 to 20 nm (Figure 5b). The generation of hexagonal particles at smaller and narrow size range using laser ablation, further highlights the significance of our findings, and the versatility of the VFD.

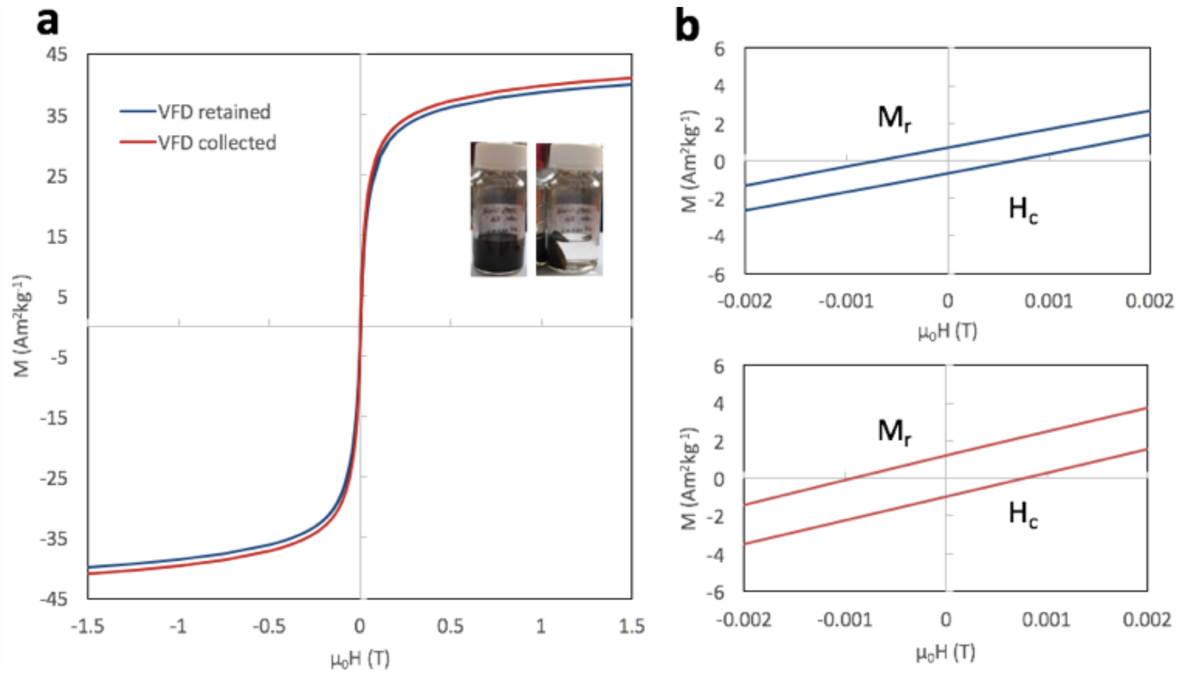

Figure 3.6 *(a) Comparison of magnetic hysteresis curves of the VFD-processed samples (retained and collected). (b) Low-field interval of the magnetization curves of the two samples.*

Both samples exhibit superparamagnetic characteristics with the highest saturation magnetization (M_s) value of about 41 Am^2kg^{-1} at room temperature (Figure 6a-b),[6] which is consistent with the average particle size of about 12 nm in both samples. The slight decrease in M_s for the sample (retained) can be attributed to the slightly disordered surface and reduced crystallinity,[12,28] which could be due to the longer exposure to the laser beam. The low-field interval of both magnetization curves reveals the negligibility of the hysteresis which again implies the superparamagnetism.[35] Apart from generating single phase crystals, laser ablated IONPs prepared using the VFD have higher saturation magnetization than those prepared using conventional laser ablation processing in water. For example, the M_s of IONPs prepared by Vahabzadeh *et al.*[2] in water were 14.8-22.5 emu/g with H_c of 11.5-22 Oe, which were not considered as superparamagnetic. Maneeratanasarn *et al.*[36] reported the generation of amorphous α-Fe_2O_3 nanoparticles with a low saturation magnetization of only 1.315 emu/g using laser ablation in water. The superparamagnetic IONPs prepared using the VFD resulted from precise control of the oxidative states, particle size and morphology during the process.

The plasma plume that is a mixture of atoms, ions and radicals, is generated in air and reacts immediately,[37] with particles colliding with each other[12] and then with uptake in the dynamic thin film in the VFD. In the presence of a gas- or liquid-phase in a conventional sense, diffusion-driven nucleation and aggregation processes play an important role in the generation and size control of the particles.[2] However, this is not readily adjustable. Experiments conducted without any liquid in the VFD showed a significantly larger particle size of about 20.7 nm compared to 14.2 nm when formed in the presence of water (Table S1). To decouple the effect of oxygen, the reaction was conducted under N_2 gas (Figure S7), but this resulted in negligible formation of iron oxide. Thus, the presence of oxygen is essential for the reaction. Liu *et al.*[38] reported that rapid quenching of species generated at high temperature using laser ablation generates pure iron oxide species. In this context, the rapid heat dissipation from the VFD may be important in determining the nature of the iron oxide species generated during the processing.

3.5 Conclusions

In summary a novel highly selective method has been developed for preparing single-phase superparamagnetic magnetite nanoparticles directly by laser ablation of a metal iron in the presence of both gas- and liquid- phases. The nanoparticles obtained under different conditions showed spherical or hexagonal shapes, with relative uniform average diameters of around 15 nm. Compared with conventionally processes, this method can selectively control phase composition, and size and shape of the particles in establishing a new application for VFD. Future experiments will investigate the fabrication of protective coatings on the particle surface to stabilise the structure and further improve the magnetism. Apart from previously described laser-mediated nanocarbon proessing, this chapter further extends the application towards laser ablation. The processing is environmentally friendly without the addition of harsh chemicals. The use of iron rod as a continual source for magnetite nanoparticles is particularly attractive as it could be easily scaled up and ready to be used for further applications. Except carbon or metallic based nanoparticles, polymer based nanoparticles have also been intensively explored in biomedical research. The next chapter will discuss, for the first time, the production of such materials using VFD and the application of it in cellular imaging.

3.6 Acknowledgement

The authors gratefully acknowledge financial support from the Australia Research Council and the Government of South Australia, also the expertise, equipment and support provided by the Australian Microscopy and Microanalysis Research Facility (AMMRF), and the Australian National Fabrication Facility (ANFF) at the South Australian nodes of the AMMRF and ANFF under the National Collaborative Research Infrastructure Strategy.

3.7 References

(1) Demirer, G. S.; Okur, A. C.; Kizilel, S. Synthesis and Design of Biologically Inspired Biocompatible Iron Oxide Nanoparticles for Biomedical Applications. *J. Mater. Chem. B* **2015,** *3*, 7831-7849.

(2) Vahabzadeh, E.; Torkamany, M. J. Iron Oxide Nanocrystals Synthesis by Laser Ablation in Water: Effect of Laser Wavelength. *J. Clust. Sci.* **2014,** *25*, 959-968.

(3) Majewski, P.; Thierry, B. Functionalized Magnetite Nanoparticles—Synthesis, Properties, and Bio-applications. *Crit. Rev. Solid State Mater. Sci.* **2007,** *32*, 203-215.

(4) Liu, B.; Wang, D.; Huang, W.; Yao, A.; Kamitakahara, M.; Ioku, K. Preparation of Magnetite Nanoparticles Coated with Silica via a Sol-gel Approach. *J. Ceram. Soc. Jpn.* **2007,** *115*, 877-881.

(5) Chin, A. B.; Yaacob, I. I. Synthesis and Characterization of Magnetic Iron Oxide Nanoparticles via w/o Microemulsion and Massart's Procedure. *J. Mater. Process. Technol*. **2007,** *191*, 235-237.

(6) Thorek, D. L.; Chen, A. K.; Czupryna, J.; Tsourkas, A. Superparamagnetic Iron Oxide Nanoparticle Probes for Molecular Imaging. *Ann. Biomed. Eng*. **2006,** *34*, 23-38.

(7) Li, S. Z.; Hong, Y. C.; Uhm, H. S.; Li, Z. K. Synthesis of Nanocrystalline Iron Oxide Particles by Microwave Plasma Jet at Atmospheric Pressure. *Jpn. J. Appl. Phys*. **2004,** *43*, 7714-7717.

(8) Amendola, V.; Riello, P.; Meneghetti, M. Magnetic Nanoparticles of Iron Carbide, Iron Oxide, Iron@Iron Oxide, and Metal Iron Synthesized by Laser Ablation in Organic Solvents. *J. Phys. Chem. C* **2011,** *115*, 5140-5146.

(9) Dadashi, S.; Poursalehi, R.; Delavari, H. Structural and Optical Properties of Pure Iron and Iron Oxide Nanoparticles Prepared via Pulsed Nd:YAG Laser Ablation in Liquid. *Proced. Mater. Sci*. **2015,** *11*, 722-726.

(10) Barcikowski, S.; Hahn, A.; Kabashin, A. V.; Chichkov, B. N. Properties of Nanoparticles Generated during Femtosecond Laser Machining in Air and Water. *Appl. Phys. A* **2007,** *87*, 47-55.

(11) Franzel, L.; Bertino, M. F.; Huba, Z. J.; Carpenter, E. E. Synthesis of Magnetic Nanoparticles by Pulsed Laser Ablation. *Appl. Surf. Sci*. **2012,** *261*, 332-336.

(12) Maneeratanasarn, P.; Khai, T. V.; Kim, S. Y.; Choi, B. G.; Shim, K. B. Synthesis of Phase-controlled Iron Oxide Nanoparticles by Pulsed Laser Ablation in Different Liquid Media. *Phys. Status Solidi* **2013,** *210*, 563-569.

(13) Dudoitis, V.; Ulevičius, V.; Račiukaitis, G.; Špirkauskaitė, N.; Plauškaitė, K. Generation of Metal Nanoparticles by Laser Ablation. *Lith. J. Phys.,* **2011,** *51*, 248-259.

(14) Hahn, A.; Barcikowski, S.; Chichkov, B. Influences on Nanoparticle Production during Pulsed Laser Ablation. *J. Laser Micro Nanoen.,* **2008**, *3*, 73-77.

(15) Britton, J.; Stubbs, K. A.; Weiss, G. A.; Raston, C. L. Vortex Fluidic Chemical Transformations. *Chem. Eur. J.* **2017,** *23*, 13270-13278.

(16) Alharbi, T. M. D.; Harvey, D.; Alsulami, I. K.; Dehbari, N.; Duan, X.; Lamb, R. N.; Lawrance, W. D.; Raston, C. L. Shear Stress Mediated Scrolling of Graphene Oxide. *Carbon* **2018,** *137*, 419-424.

(17) Vimalanathan, K.; Gascooke, J. R.; Suarez-Martinez, I.; Marks, N. A.; Kumari, H.; Garvey, C. J.; Atwood, J. L.; Lawrance, W. D.; Raston, C. L. Fluid Dynamic Lateral Slicing of High Tensile Strength Carbon Nanotubes. *Sci. Rep.* **2016,** *6*, 22865.

(18) Vimalanathan, K.; Chen, X.; Raston, C. L. Shear Induced Fabrication of Intertwined Single Walled Carbon Nanotube Rings. *Chem. Comm.* **2014,** *50*, 11295-11298.

(19) Yasmin, L.; Chen, X.; Stubbs, K. A.; Raston, C. L. Optimising a Vortex Fluidic Device for Controlling Chemical Reactivity and Selectivity. *Sci. Rep.* **2013,** *3*, 1-6.

(20) Luo, X.; Smith, P.; Raston, C. L.; Zhang, W. Vortex Fluidic Device-Intensified Aqueous Two Phase Extraction of C-Phycocyanin from Spirulina maxima. *ACS Sustain. Chem. Eng.* **2016,** *4*, 3905-3911.

(21) Britton, J.; Meneghini, L. M.; Raston, C. L.; Weiss, G. A. Accelerating Enzymatic Catalysis Using Vortex Fluidics. *Angew. Chem. Int. Ed.* **2016,** *55*, 11387-11391.

(22) Yuan, T. Z.; Ormonde, C. F. G.; Kudlacek, S. T.; Kunche, S.; Smith, J. N.; Brown, W. A.; Pugliese, K. M.; Olsen, T. J.; Iftikhar, M.; Raston, C. L.; Weiss, G. A. Shear-Stress-Mediated Refolding of Proteins from Aggregates and Inclusion Bodies. *ChemBioChem* **2015,** *16*, 393-396.

(23) D'Alonzo, N. J.; Eggers, P. K.; Raston, C. L. Vortex Fluidics Synthesis of Polymer Coated Superparamagnetic Magnetite Nanoparticles. *New J. Chem.* **2017**, *41*, 552-558.

(24) Ji, Y. Ions Removal by Iron Nanoparticles: A Study on Solid–water Interface with Zeta Potential. *Colloid. Surface. A.* **2014**, *444*, 1-8.

(25) Fazio, E.; Santoro, M.; Lentini, G.; Franco, D.; Guglielmino, S. P. P.; Neri, F. Iron Oxide Nanoparticles Prepared by Laser Ablation: Synthesis, Structural Properties and Antimicrobial Activity. *Colloids Surf. A* **2016,** *490*, 98-103.

(26) Kumar, P. A.; Ray, S.; Chakraverty, S.; Sarma, D. D. Magnetoresistance and Electroresistance Effects in Fe_3O_4 Nanoparticle System. *J. Exp. Nanosci*. **2014,** *9*, 391-397.

(27) Bersani, D.; Lottici, P.; Montenero, A. Micro-Raman Investigation of Iron Oxide Films and Powders Produced by Sol–gel Syntheses. *J. Raman spectrosc.* **1999,** *30*, 355-360.

(28) Chourpa, I.; Douziech-Eyrolles, L.; Ngaboni-Okassa, L.; Fouquenet, J.-F.; Cohen-Jonathan, S.; Souce, M.; Marchais, H.; Dubois, P. Molecular Composition of Iron Oxide Nanoparticles, Precursors for Magnetic Drug Targeting, as Characterized by Confocal Raman Microspectroscopy. *Analyst* **2005,** *130*, 1395-1403.

(29) Lee, Y. J. The Second Order Raman Spectroscopy in Carbon Crystallinity. *J. Nucl. Mater.* **2004**, *325*, 174-179.

(30) Marton, M.; Vojs, M.; Zdravecká, E.; Himmerlich, M.; Haensel, T.; Krischok, S.; Kotlár. M.; Michniak, P.; Veselý, M.; Redhammer, R. Raman Spectroscopy of Amorphous Carbon Prepared by Pulsed Arc Discharge in Various Gas Mixtures. *J. Spectrosc.* **2013**, *2013*, 6.

(31) Amendola, V.; Riello, P.; Polizzi, S.; Fiameni, S.; Innocenti, C.; Sangregorio, C.; Meneghetti, M. Magnetic Iron Oxide Nanoparticles with Tunable Size and Free Surface Obtained via a "Green" Approach Based on Laser Irradiation in Water. *J. Mater. Chem.* **2011,** *21*, 18665-18673.

(32) Shebanova, O. N.; Lazor, P. Raman Study of Magnetite (Fe_3O_4): Laser-Induced Thermal Effects and Oxidation. *J. Raman Spectrosc.* **2003**, *34*, 845-852.

(33) Eom, Y.; Abbas, M.; Noh, H.; Kim, C. Morphology-controlled Synthesis of Highly Crystalline Fe_3O_4 and $CoFe_2O_4$ Nanoparticles using a Facile Thermal Decomposition Method. *RSC Adv.* **2016,** *6*, 15861-15867.

(34) Wang, H.; Shrestha, T. B.; Basel, M. T.; Pyle, M.; Toledo, Y.; Konecny, A.; Thapa, P.; Ikenberry, M.; Hohn, K. L.; Chikan, V.; Troyer, D. L.; Bossmann, S. H. Hexagonal Magnetite Nanoprisms: Preparation, Characterization and Cellular Uptake. *J. Mater. Chem. B* **2015,** *3*, 4647-4653.

(35) Atefeh, J.; Mojtaba, S.; Saber Farjami, S.; Zahra, H.; Ahmad Bitarafan, R.; Komail, B.; Ali, N. Synthesis and Characterization of Bombesin-superparamagnetic Iron Oxide Nanoparticles as a Targeted Contrast Agent for Imaging of Breast Cancer using MRI. *Nanotechnol.* **2015,** *26*, 075101.

(36) Maneeratanasarn, P.; Khai, T. V.; Kim, S. Y.; Choi, B. G.; Shim, K. B. Synthesis of Phase-controlled Iron Oxide Nanoparticles by Pulsed Laser Ablation in Different Liquid Media. *Phys. status solidi A* **2013**, *210*, 563-569.

(37) Salik, M.; Hanif, M.; Wang, J.; Zhang, X. Plasma Properties of Nano-second Laser Ablated Iron Target in Air. *Int. J. Phys. Sci*. **2013,** *8*, 1738-1745.

(38) Liu, P.; Cai, W.; Zeng, H. Fabrication and Size-Dependent Optical Properties of FeO Nanoparticles Induced by Laser Ablation in a Liquid Medium. *J. Phys. Chem. C* **2008,** *112*, 3261-3266.

Appendix: The article's first page and the first page of the published supplementary information

This is an open access article published under an ACS AuthorChoice License, which permits copying and redistribution of the article or any adaptations for non-commercial purposes.

ACS OMEGA
Article
Cite This: ACS Omega 2018, 3, 11172−11178
http://pubs.acs.org/journal/acsodf

Downloaded via 203.63.75.205 on October 14, 2018 at 03:54:22 (UTC).
See https://pubs.acs.org/sharingguidelines for options on how to legitimately share published articles.

Laser-Ablated Vortex Fluidic-Mediated Synthesis of Superparamagnetic Magnetite Nanoparticles in Water Under Flow

Xuan Luo,[†,‡] Ahmed H. M. Al-Antaki,[†] Thaar M. D. Alharbi,[†] Wayne D. Hutchison,[§] Yi-chao Zou,[∥] Jin Zou,[∥] Antony Sheehan,[⊥] Wei Zhang,*[,‡] and Colin L. Raston*[,†]

[†]Flinders Institute for NanoScale Science and Technology, College of Science and Engineering, and [‡]Centre for Marine Bioproducts Development, College of Medicine and Public Health, Flinders University, Adelaide, South Australia 5042, Australia

[§]School of PEMS, University of New South Wales, ADFA campus, Canberra BC, Australian Capital Territory 2610, Australia

[∥]Materials Engineering and Centre for Microscopy and Microanalysis, The University of Queensland, Brisbane, Queensland 4072, Australia

[⊥]TGR Biosciences Pty Ltd, 31 Dalgleish Street, Thebarton, Adelaide, South Australia 5031, Australia

Supporting Information

ABSTRACT: Selective formation of only one iron oxide phase is a major challenge in conventional laser ablation process, as is scaling up the process. Herein, superparamagnetic single-phase magnetite nanoparticles of hexagonal and spheroidal-shape, with an average size of ca. 15 nm, are generated by laser ablation of bulk iron metal at 1064 nm in a vortex fluidic device (VFD). This is a one-step continuous flow process, in air at ambient pressure, with in situ uptake of the nanoparticles in the dynamic thin film of water in the VFD. The process minimizes the generation of waste by avoiding the need for any chemicals or surfactants and avoids time-consuming purification steps in reducing any negative impact of the processing on the environment.

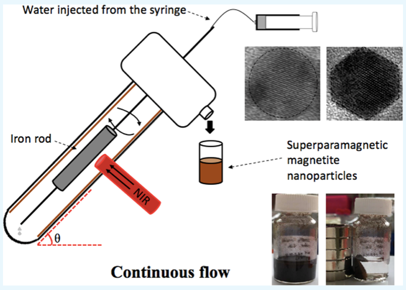

INTRODUCTION

The synthesis and availability of iron oxide nanoparticles (IONPs) are of general interest in many fields of research and in a number of applications. Some common phases of IONPs include α-Fe_2O_3 (hematite), Fe_3O_4 (magnetite), γ-Fe_2O_3 (maghemite), α-Fe (ferrite), Fe_3C (iron carbide), and FeO (wustite). For magnetite, IONPs smaller than 20 nm have superparamagnetic properties and are known as superparamagnetic IONPs.[1,2] This property relates to the large magnetic moment resulting from the coupling of the atomic spins within the nanosized magnetite nanoparticles.[3] Magnetite is one of the most intensively studied IONPs, which can be prepared using a number of different methods, including coprecipitation,[1] sol−gel,[4] microemulsion,[5] ultrasonic spray pyrolysis,[6] and microwave plasma.[7] They have different advantages and disadvantages relating to shape/size control, stability, scalability, monodispersity, and production cost. Among them, the coprecipitation method is relatively simple and fast and has potential for scaling up; however, it generates nanoparticles with a wide particle size distribution[1] and can generate a waste stream incorporating toxic chemicals.[8]

Pulsed laser ablation, which can be a simple and surfactant and counter-ion-free technique,[9] has been used to prepare magnetic nanoparticles with a narrow size distribution.[2] IONPs can be generated by laser ablation of bulk iron in either the gas or liquid phase,[10] the latter being the most studied,[11] with Nd:YAG laser processing at 1064 nm affording nanoparticles with enhanced magnetic properties.[2] Water is the preferred solvent in terms of applications and environmental considerations, with the use of organic solvents generating amorphous carbon and iron carbide from its breakdown.[8,11,12] However, selectively forming only one iron oxide phase in water is a major challenge in laser processing.[2,9,12] Also, noteworthy is that after each laser pulse, the time taken for collapse of the plume is crucial in controlling the nucleation and growth of the IONPs;[2] longer times equate to longer growth times, affording mainly larger particles during the ablation in the liquid. On the other hand, laser ablation of an iron target in the gas phase can circumvent some of the above drawbacks for liquid ablation processing, using air as the oxidant.[13] Also, noteworthy is that the generation of nanoparticles from ablation in the gas phase is preferred because of increased yield relative to ablation in the liquid phase.[13] Maghemite has been generated by laser ablation in a mixture of nitrogen and oxygen under atmospheric pressure,[12] albeit with a broad size distribution of the particles, 5 to 90 nm in diameter. Laser ablation processing in the gas phase requires a more sophisticated setup with a specially designed ablation

Received: July 11, 2018
Accepted: August 31, 2018
Published: September 14, 2018

Supporting Information

Laser ablated vortex fluidic mediated synthesis of superparamagnetic magnetite nanoparticles in water under flow

Xuan Luo,[a,b] *Ahmed H. M. Al-Antaki,*[a] *Thaar M. D. Alharbi,*[a] *Wayne D. Hutchison,*[c] *Yi-Chao Zou,*[d] *Jin Zou,*[d] *Antony Sheehan,*[e] *Wei Zhang**[b] *and Colin L. Raston**[a]

[a] *Flinders Institute for NanoScale Science and Technology, College of Science and Engineering, Flinders University, Adelaide, SA 5042, Australia*
[b] *Centre for Marine Bioproducts Development, College of Medicine and Public Health, Flinders University, Adelaide, SA 5042, Australia*
[c] *School of PEMS, University of New South Wales, ADFA campus, Canberra BC, ACT 2610, Australia*
[d] *Materials Engineering, The University of Queensland, Brisbane, QLD 4072, Australia*
[e] *TGR Biosciences Pty Ltd, 31 Dalgleish St, Thebarton, Adelaide, SA 5031, Australia*

Corresponding Authors

*C. Raston. Tel.: +61 8 82017958. Fax: +61 8 8201290. E-mail:

colin.raston@flinders.edu.au

*W. Zhang. Tel.: +61 8 72218557. Fax: +61 8 72218555. E-mail:

wei.zhang@flinders.edu.au

4. HIGH-SHEAR-IMPARTED TUNABLE FLUORESCENCE IN POLYETHYLENIMINES

Published methods for fabricating fluorescent polymer nanoparticles typically involve purification processes, the use of harsh chemicals, difficulties in scaling up, the use of high energy input and long processing times, with limited sample homogeneity. In addition, the tunability of the fluorescence of the nanoparticles is rarely addressed. Polyethylenimine (PEI) is a water-soluble cationic polyelectrolyte which contains a large number of amino groups in a 3D network structure and has been widely used for producing fluorescent nanoparticles.

Following previous chapters' theme on nanoparticles fabrication, this chapter continually discussed the generation of polymer based nanoparticles using the VFD under shear stress and high termperature facilitated oxidation in air. Nanoparticles with low toxicity and good photostability were rapidly prepared in a VFD. The optimum quantum yield is higher than that of most published PEI-based nanoparticles devoid of auxiliary moieties. Chemical-adoption of amide functional groups triggers enhanced fluorescence intensity and auto-fluorescence over a wide excitation range, and the resulting nanoparticles showed significantly reduced cytotoxicity against MCF7 cell line compared to as received materials. The biocompatibility of these fluorescent nanoparticles facilitated their application in imaging live cells, with the overall study contributing to an understanding of fluorescence arising from amino-containing materials and the development of new functional fluorescent nanoparticles.

This study was orally presented at the ICONN international conference in Wollongong in January 2018, and published in ***ChemPubSoc Europe ChemPhotoChem***, Year 2018, Vol. 2, Issue 4, Pages 343-348, which was also published as the journal front cover of that issue. The first page of the publication is attached in Appendix 2.1.

Author contributions: **XL** performed all the VFD and tissue culture experiments, most characterization experiments and data analysis; wrote all the primary content. **AA** help on some VFD experiments, the use of heating jacket and assisted with the O_2 experiments. **SP** performed the NMR and assisted with data analysis. **RM** supervised the tissue culture experiments. **WZ** and **CR** supervised and coordinated the project and helped on the research directions and plan, and the final revision of the manuscript. All of the co-authors assisted with the revision of the manuscript before and during the publication process.

High-shear-imparted tunable fluorescence in polyethylenimines

Xuan Luo,[1, 2], Ahmed Hussein Mohammed Al-Antaki,[1] Scott Pye,[1] Robyn Meech,[3] Wei Zhang*[2] and Colin L. Raston*[1]

[1] Centre for NanoScale Science and Technology (CNST), College of Science and Engineering, Flinders University, Adelaide, SA 5042, Australia;

[2] Centre for Marine Bioproducts Development, College of Medicine and Public Health, Flinders University, Adelaide, SA 5042, Australia;

[3] Clinical Pharmacology, College of Medicine and Public Health, Flinders University, Adelaide, SA 5042, Australia.

Graphical abstract

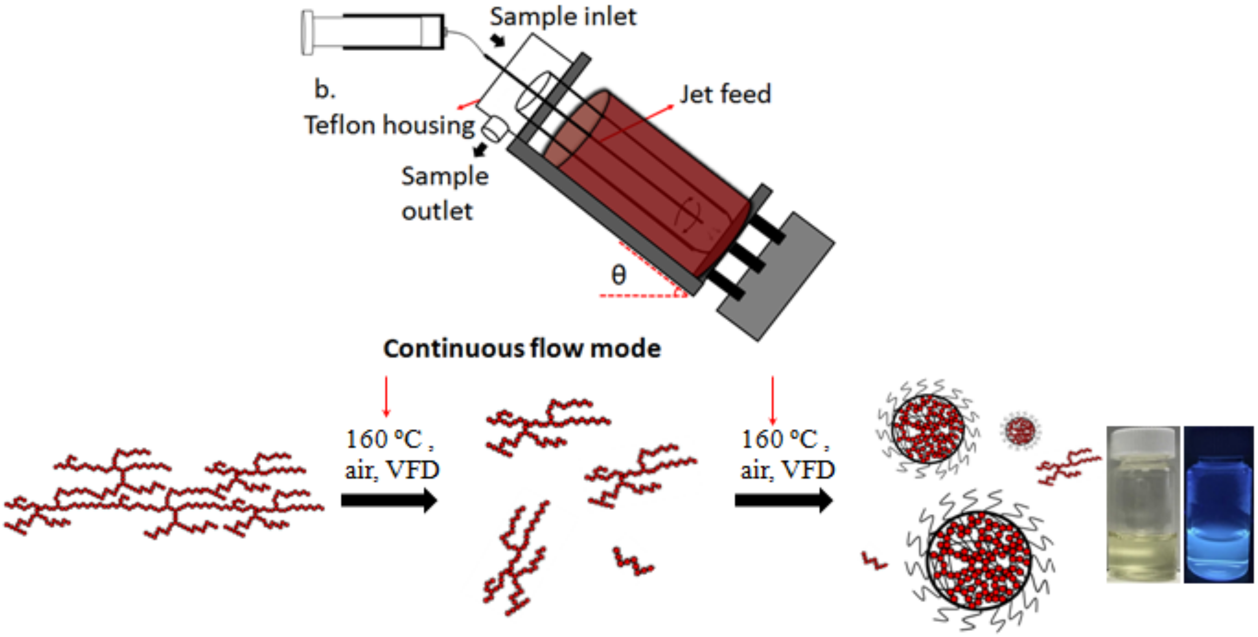

4.1 Abstract

In general, fluorescent polyethylenimine (PEI) nanoparticles absorb primarily UV light, with the fluorophores typically having extended conjugated structures. In this work, PEI nanoparticles of circa 10 nm in diameter, devoid of such structural features and with tunable fluorescence, were generated in a microfluidic platform. Tunability of the fluorescence was achieved by varying the flow rate of liquid entering the rapidly rotating tube in a vortex fluidic device (VFD), without the need for additional reagents. Chemical incorporation of amide functional groups triggered enhanced fluorescence intensity and auto-fluorescence over a wide range, and the resulting nanoparticles showed significantly reduced cytotoxicity compared to as-received polymers.

Keywords: cellular imaging, cytotoxicity, fluorescence, nanoparticles, polyethylenimine

4.2 Introduction

Fluorescent nanoparticles derived from amino-containing dendritic polymers have been used for biological imaging and biosensors[1-3] where the fluorophores are usually extended conjugated chemical structures.[4] Even though simple oxidation, acidification or methylation can further enhance the intrinsic fluorescence,[5] the mechanism of fluorescence from these dendritic polymers is not well understood. Some propose that the origin of fluorescence arises from oxygen-doped interior tertiary amine[6] and interior urea-doped with peripheral amino groups.[7] These fluorescent polymers can contain Schiff base moieties,[5] tertiary amine or carbonyl groups in an dendrimer interior with terminal groups such as monohydroxyl,[8] air[6] or hydrogen peroxide[9] oxidized amines, amine-rich nanoclusters,[5] and carbamato anion.[2] The nature of the dendritic structure and macromolecular backbone can also significantly influence the fluorescence properties.[1,5]

Polyethylenimine (PEI) is a water-soluble cationic polyelectrolyte which contains a large number of amino groups, and has been used to prepare various fluorescent materials.[10] The fluorescence of PEI is unexpected given the absence of chromophores.[5] Refluxing 25 kDa PEI in nitric acid at 120ºC for 12 h affords photoluminescent nanoparticles (λ_{ex} = 360 nm, λ_{em} = 450 nm) bearing amide linkages (NHCO).[11] Hyper-branched PEI (hPEI)-based fluorescent particles have been prepared at high temperature (200ºC)[12] or via microwave irradiation.[13] Adding formaldehyde at 90ºC results in fluorescent polymeric nanoparticles (λ_{ex}=365nm, λ_{em}=508nm) or gels (λ_{ex}=350nm, λ_{em}=476nm). Similarly, adding salicylaldehyde imparts fluorescence (λ_{ex} = 370 nm, λ_{em} = 495 nm)[14] which arises from the formation of Schiff base moieties.[3,5] Hydrothermal treatment of hPEI with aldehydes at 95ºC generates fluorescent polymer nanoparticles,[3] depending on the pH which can complicate the processing. The carbamate anion is another moiety responsible for fluorescence (λ_{ex} = 364 nm, λ_{em} = 470 nm), formed by reacting PEI with CO_2.[2] Based on our knowledge, tunability of fluorescence has never been ad- dressed on PEI-based nanoparticles with mostly reported optimum excitation in the UV region, as described above. Furthermore, there is a lack of knowledge on the relationship between molecular weight of PEI, particle surface functionality and the emission property. Other limitations include the need for time-consuming dialysis to remove unreacted reagents in the fabrication process.[5]

Liu et al.[5] reported that ideal fluorescent polymer nanoparticles should be autofluorescent without doping an external fluorochrome. We are motivated by this idea to fabricate fluorescence-tunable PEI-based nanoparticles from PEI devoid of extended conjugates or precursors, under high shear in a continuous-flow thin-film vortex fluidic device (VFD; Figure 4.1). This thin film microfluidic platform has diverse applications,[15] including the entanglement of 3D gel networks,[16] intensifying multi-phase separation,[17] enhancing enzymatic reactions[18] and fabricating hydrogels.[19] This study extends the applications of VFD into fabricating tunable fluorescence nanoparticles based on branched PEI and hPEI. Modifying low and high molecular weight PEI under continuous flow in the VFD, as immediately scalable processes, has the potential to avoid the use of precursors typically required for PEI-based fluorescence with tunability addressed by only varying the processing conditions. The use of a VFD also lends itself to decoupling the effect of the gas environment and heating on imparting fluorescence into PEI.

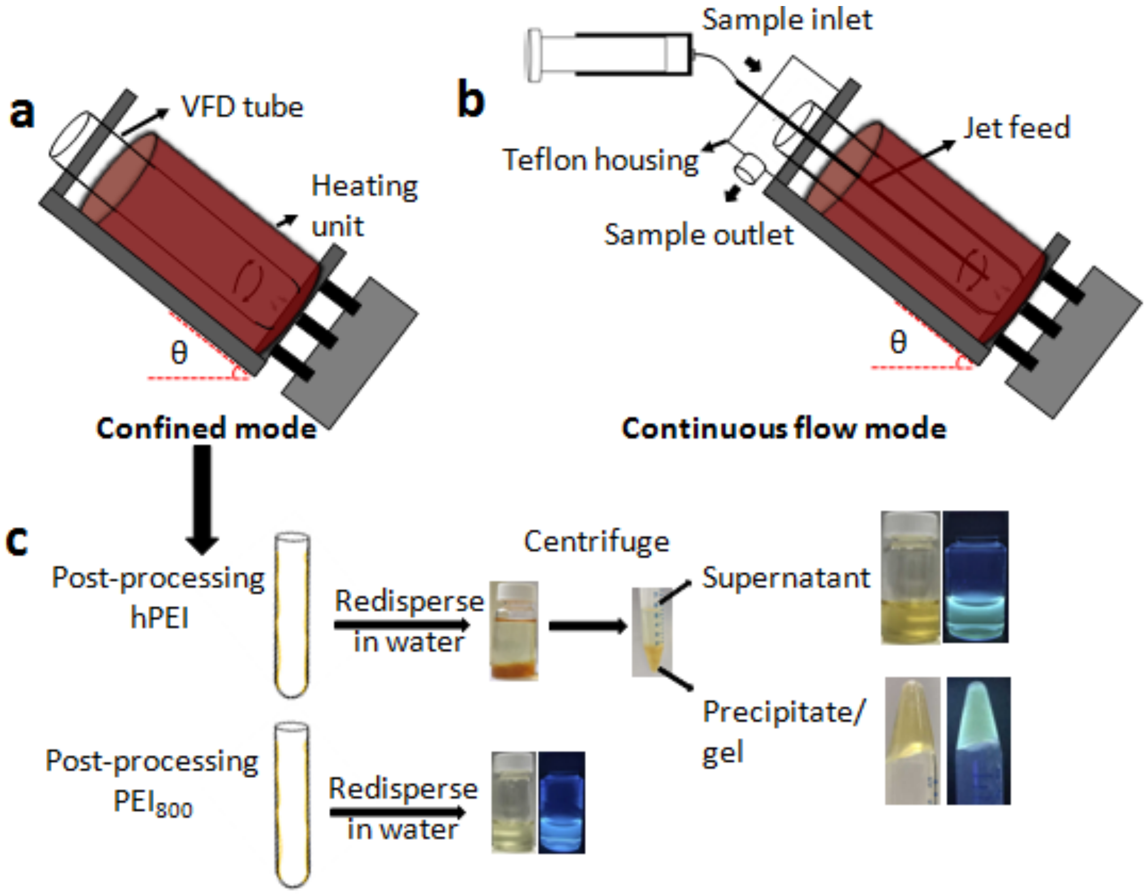

Figure 4.1 *Schematic of the vortex fluidic device (VFD) and sample preparation. (a) Confined mode, 45° tilt angle with heating; (b) continuous flow mode; (c) confined mode post VFD-processing for hPEI and* PEI_{800}.

4.3 Materials and methods

hPEI (CAS 9002-98-6) of 750 kDa, PEI_{800} (CAS 25987-06-8), deuterium oxide (D_2O), citric acid and salicylic acid were purchased from Sigma-Aldrich. Quinine sulphate (CAS 207671-44-1) and fluorescein (C.I. 45350) were chosen as reference for quantum yield measurement. All chemicals were of analytical grade and used as received without further purification or treatment. For a typical confined mode experiment, 1 mL of the sample at certain concentration was processed using a VFD, systematically exploring the operating parameters of the device, including sample concentration, processing time, temperature and rotational speed.

Experiments conducted in the open air, as summarised in Figure 4.1 a; the VFD borosilicate glass tube (O.D. 20 mm) was placed at 45° tilt angle and spun at a defined rotational speed. For thermal treatment, a heating unit was placed over the VFD tube. Post-VFD processing of PEI_{800}, 1 mL of MilliQ water was added to dissolve the product for characterisation. However, for hPEI, the product did not fully dissolved in water, and here 6 mL of MilliQ water was added and the aqueous phase (centrifugation at 1180 × g for 30 min) was used for characterisation (Figure 4.1 c). Optimisation was conducted initially under confined mode, in varying the temperature, reaction time, sample concentration and rotational speed. While decoupling the impact of reaction gases, a specific gas flow (either air, O_2, CO_2 and N_2) was introduced into the tube via a stainless steel jet feed held by a Teflon housing unit. At least 15 min was allowed for the system to equilibrate with the gas before starting the reaction. Continuous flow mode of VFD was carried out by linking the system with a syringe pump, varying the flow rate from 0.1 to 0.3 mL/min for optimizing the conditions for scalable processing (Figure 4.1 b). Precipitates were not formed in the continuous flow processed samples. Therefore, centrifugation was not conducted and samples collected from the Teflon housing unit were directly used for further studies. Each experiment was set to run for 1 h to investigate the potential of scalability of the process.

Absorption and fluorescence spectra measurements were recorded in a quartz cuvette (1 cm path length) on a UV-vis spectrophotometer (Cary Eclipse, Agilent) and a fluorescence spectrometer (Cary Eclipse, Agilent), respectively. Scanning electron microscope (SEM), atomic force microscopy (AFM – Nanoscope 8.10 tapping mode), 2D fluorescence maps were generated from excitation wavelength of 200 nm with 15 nm step-wise increments until

600 nm (Cary Eclipse, Agilent fluorescence spectrometer). Emission spectra were continuously collected from 250 nm to 800 nm for each corresponding excitation wavelength. The quantum yield was measured by comparing the integrated fluorescence intensity (excited at 325 nm) of the nanoparticles prepared from hPEI 0.1 mL/min and PEI_{800} 0.1 mL/min with that of quinine sulphate in 0.1 M H_2SO_4 (Φ_R=54.6%).[1] As for nanoparticles prepared from PEI_{800} 0.2 mL/min, the quantum yield was determined by comparing to fluorescein (Φ_R=95%).[1] The mean zeta potential ζ was investigated using a Nano Zetasizer (Malvern). Isoelectric points were determined from ζ potential titrations. All spectra were normalised using Origin 9.0 and presented as 2D contour plots. Fourier transform infrared (FT-IR) spectra were recorded on a Perkin Elmer Frontier instrument. ^{1}H and ^{13}C NMR spectra were collected on a 600 MHz Bruker advance spectrometer with a freeze-dried product dissolved in D_2O. All chemical shifts are presented in ppm using residual solvent as the internal standard. SEC was performed on UFLC (Shimadzu, $UFLC_{XR}$) with sequential two columns, GPC/SEC column PL aquagel-OH Mixed-H 8μm 300 x 7.5 mm (6kDa-10 MDa) and GPC/SEC column PL aquagel-OH 30 8μm 300 x 7.5 mm (0.1- 60 kDa). The columns and detector (refractive index) were equilibrated with the mobile phase until a flat baseline is achieved. Dextran standards (CAS 9004-54-0) have molecular weights of 1, 5, 25, 80, 270, 670 and 1100 kDa. Mobile phase is 0.1 M sodium nitrate (CAS 7631-99-4) at a flow rate of 1 mL/min. Standards and samples were all dissolved in water at concentrations of 10 mg/mL and 50 μL was injected for each condition.

The cytotoxicity of the samples was evaluated by MTT assay. Breast cancer MCF-7 cells were cultured in Dulbecco's Modified Eagle's Medium (DMEM) supplemented with 10% fetal bovine serum, 1% penicillin, and 1% streptomycin under a constant temperature of 37ºC, 95% air and 5% CO_2 humidified conditions. The cells were harvested from the cultures by trypsin/EDTA solution and were resuspended in fresh complete medium before plating. 1×10^5 cells were seeded in a 96 well plate and cultured for 24 h. After the medium was removed, cells were treated with PEIs at different concentrations of 0, 12.5, 25, 50, 100 and 200 μg/mL for a further 24 h at 37ºC. Then the medium was removed and the cells were washed thoroughly with phosphate buffer saline (PBS) three times. Thereafter, the cells were treated with 0.5 mg/mL MTT followed by 37ºC incubation for 4 h whereupon 80 μL of 20% (w/v) sodium dodecyl sulfate (SDS) in 0.02 M HCl was added to each well to dissolve the formazan crystals formed. The plates were kept in the dark at room temperature for 17 h. The absorbance of the formazan product was measured at 570 nm with a reference wavelength of 630 nm on an µQuant Automatic Spectrophotometer (Bio-TEK instruments). Cells cultured in the medium without treatment were taken as the controls. The morphology of the cells was investigated using an inverted fluorescence microscopy (EVOS® FL) under bright field, with a scale bar added using image J software. One day before imaging, MCF-7 cells were plated on tissue culture plate and incubated in fresh media at 37ºC, 5% CO_2 humidified conditions. The cells were then incubated with the PEI derivatives dissolved in the DMEM medium for 24 hr whereupon the medium was removed and the cells washed with PBS for three times. The cells were kept in PBS as previously reported by Fan et al.[3] for performing optical imaging under inverted fluorescent microscopy (EVOS® FL) equipped with three Invitrogen™ EVOS™ light cubes, DAPI (357/44 Ex; 447/60 Em), GFP (470/22 Ex; 510/42 Em) and RFP (531/40 Ex; 593/40 Em).

4.4 Result and Discussion

PEI nanoparticles with tunable fluorescence, low toxicity and good photo-stability were rapidly prepared in a VFD in the absence of auxiliary reagents. Quantum yields (QY) range from 3.7 % to 7.4 %, depending on the molecular weight of the PEI and the flow rate. A strong fluorescence emission is present for the VFD-processed low MW PEI (λ_{ex} = 447 nm, λ_{em} = 500 nm or λ_{ex} =325 nm, λ_{em} =400 nm), as well as for hPEI (λ_{ex} = 325 nm, λ_{em} = 400 nm) where there is the formation of Schiff base, carbamate, hydroxyl and formamide moieties. The biocompatibility of these fluorescent nanoparticles facilitated their application in live cell imaging, with the overall study contributing to an understanding of fluorescence arising from amino-containing materials and the development of new functional fluorescent nanoparticles on demand.

Process optimization was initially in air using the VFD in the confined mode (1 mL of solution), for decoupling the effects of varying the PEI_{800} concentration, processing time, rotational speed and reaction temperature (see Figure S1 in the Supporting Information). One parameter was varied at a time for optimizing the fluorescence intensity. The VFD-processed PEI_{800} resulted in *ca.* 9 fold enhancement in fluorescence intensity compared to the oven processed samples under the same conditions (Figure S1). As for PEI_{800}, VFD processed hPEI (MW 750 kDa) resulted in *ca.* 7 fold enhancement in fluorescence (Figure S2).

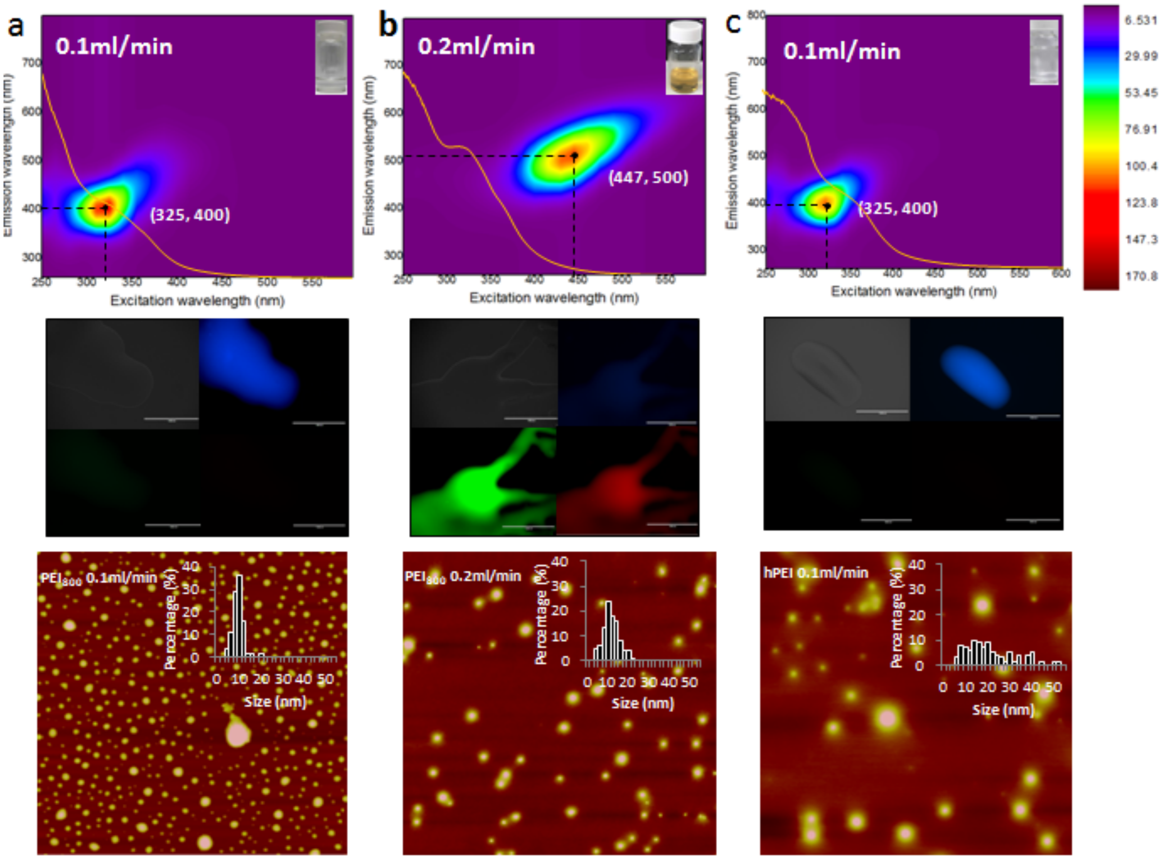

Figure 4.2 *2D Fluorescence maps of VFD processed PEI at 160ºC at different flow rates, and corresponding samples imaged using inverted fluorescence microscopy (EVOS® FL) with three Invitrogen™ EVOS™ light cubes: DAPI (357/44 Ex; 447/60 Em), GFP (470/22 Ex; 510/42 Em) and RFP (531/40 Ex; 593/40 Em) and AFM. (a) PEI$_{800}$ (37 mg/mL, 8600 rpm) 0.1 mL/min; (b) PEI$_{800}$ (37 mg/mL, 8600 rpm) 0.2 mL/min; (c) hPEI (48.6 mg/mL, 8000 rpm) 0.1 mL/min.*

Continuous VFD flow processing of PEI_{800} was conducted initially under the optimized confined mode conditions, for 0.1 and 0.2 mL min^{-1} flow rates (Figure 4.2 a,b). The optimum excitation and emission wavelength of processed PEI_{800} could be tuned by varying the flow rate with the optimal outcomes at 0.1 mL min^{-1} (λ_{ex} = 325 nm, λ_{em} = 400 nm) and 0.2 mL min^{-1} (λ_{ex} = 447 nm, λ_{em} = 500 nm). 2D fluorescence maps showed a more focused signal region indicating relatively higher sample homogeneity and fluorescence intensity (1.7 fold) relative to samples prepared using the confined mode of operation of the VFD (Figure S1). The florescence is in good agreement with observations under fluorescence microscopy (Figure 4.2), showing multicolor fluorescence under specific excitation wavelength.

UV/Vis absorption spectra revealed new absorption bands of the processed samples relative to as-received material (non- emissive, Figure S4), at circa λ = 310 nm and 350 nm, depending on the flow rate (Figure 4.2) which possibly arise from π–π^* transitions.[11] Another new absorption band at *ca.* λ = 369 nm can be assigned to $n \rightarrow \pi^*$ and $n \leftarrow \pi^*$ transitions for C=N moieties.[3] The QY for PEI_{800} 0.1 mL min^{-1} and hPEI 0.1 mL min^{-1} was 3.7 and 7.0%, respectively based on quinine sulfate as a standard, and 7.4 % for PEI_{800} 0.2 mL min^{-1} based on fluorescein as a standard (Table S1). The optimum QY is higher than published PEI-based carbon nanoparticles devoid of auxiliary moieties (2 %)[11] and salicylaldehyde-functionalized PEI polymer nanoparticles (4.6%).[14] AFM of the continuous flow processed PEI_{800} (0.1 mL min^{-1}) revealed the formation of monodispersed and spherical nanoparticles (Figure 4.2) with a narrow size distribution centered at 10 nm, which is consistent with SEM data (Figure S6). PEI-based nanoparticles are generated under continuous flow, regardless of the molecular weight of the PEI.

Amide linkages (CONH),[11] Schiff bases (C=N),[3,5] and carbamate anions[2] are the most commonly reported chromophore for PEI-based fluorescent nanoparticles. Most dendritic polymers such as PEI lack fluorescence-emitting moieties,[5] and we speculated that new functional groups or fluorescent chromophores were generated during the processing. Post-VFD there is a new sharp peak at 1656 cm^{-1} (Figure S10) which is assigned to the formation of amide linkages[3,11] or Schiff base moieties,[5] which have been previously reported for PEI-based nanoparticles. The N-H peak at 1577 cm^{-1} had reduced intensity post-processing which is consistent with chemical grafting onto the surface of the nanoparticles.[13] Abundant amines can introduce defects on the nanoparticle surface via the passivation process, introducing the so-called excitation energy traps.[11] In addition, the presence of the broad peak around 3292 cm^{-1} and the new peak at 1388 cm^{-1} correspond to O-H functional groups in the polymer.[3] The new peak at 1163 cm^{-1} is consistent with C-O vibrations.[5] Comparing the two processing conditions of 0.1 and 0.2 mL min^{-1}, the peaks at 3353 cm^{-1} (assigned to N-H stretching vibrations), 2944, 2822 and 1456 cm^{-1} (assigned to CH$_2$ stretching vibrations) are less significant for 0.1 mL min^{-1} prepared samples compared to 0.2 mL min^{-1}. The new peak at 1388 cm^{-1} corresponding to -OH is much more intense for 0.1 mL min^{-1} prepared samples than 0.2 mL min^{-1}. Collectively, these are consistent with the processing conditions at 0.1 mL min^{-1} resulting in higher degradation of the polymer structure and higher incorporation of the -OH functionality than the processing conditions for 0.2 mL min^{-1}, especially given the longer residence time for the lower flow rate of 0.1 mL min^{-1}.

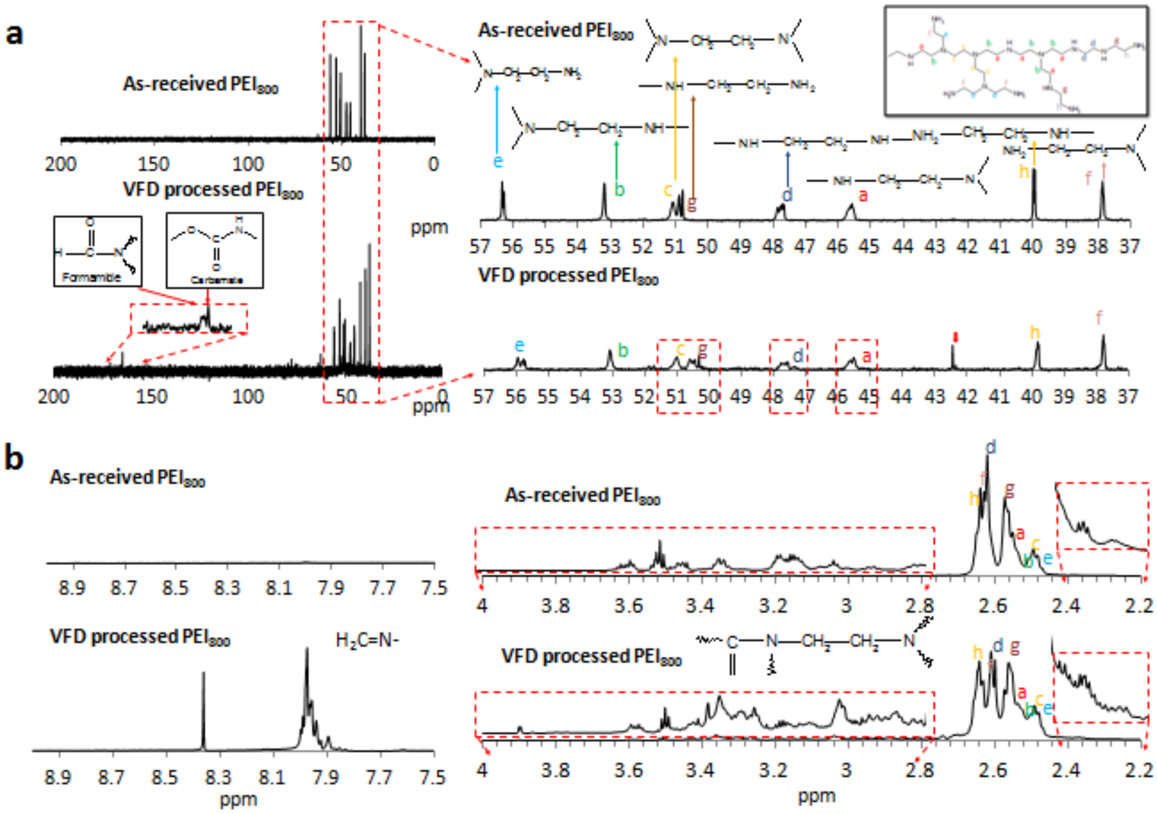

***Figure 4.3** NMR data for nanoparticles derived from PEI_{800} under continuous flow, 0.2 mL/min at 160ºC. (a) ^{13}C NMR spectra. The peaks (a-h) were assigned according to the different combinations of amine nearest neighbours in the structure of PEI.[20] (b) ^{1}H NMR spectra.*

NMR spectroscopy for the as-received PEI shows primary, secondary and tertiary amine groups with 8 unique ^{13}C NMR resonance signals (Figure 4.3).[21] VFD processing results in new ^{13}C NMR signals between δ = 160–175 ppm which could be assigned to the formation of Schiff base, carbamate[22] and formamide (-CH=O).[20] The new signal at δ = 42.5 ppm can be assigned to oligomers formed on degradation of PEI_{800}.[21] These signals were more significant for 0.1 mL min^{-1} than 0.2 mL min^{-1} flow rates (Figure S14). A number of new signals were evident in the region δ = 2.5–4 ppm which can be assigned to the protons for $N\text{-}CH_2\text{-}N$, CH_2OH and $CH_2\text{-}O\text{-}$.[5,20] The signals at δ = 8 ppm are assigned to Schiff base moieties[5] and the new singlet at 8.4 ppm is assigned to -CONH-,[3] which is consistent with the FT-IR spectra (Figure S10). Other signals in the region of δ = 7.7–8.5 ppm can be assigned to formamide.[20] Comparing the two processing conditions of 0.1 and 0.2 mL min^{-1}, the longer retention time from 0.1 mL min^{-1} results in more destructive effect on the amine groups of PEI (Figure S14 c and S15 c), which is consistent with the FT-IR results. The differences on the polymer degradation level and the ratios of different functional groups could be one of the main reasons for the different fluorescent behavior for material prepared under these two conditions.

The VFD-processed PEI nanoparticles have pH-insensitive fluorescent features (Figure S11), with only slight changes (0.6 fold reduction) arising from varying the pH from 3 to 12. This is in contrast to a significant decrease by more than 3 fold in other reported PEI functionalized nanoparticles.[12] This reduced pH-sensitivity could be due to the formation of OH functionality on the surface of the polymer particles, as for pH insensitive fluorescence in nanoparticles derived from polyethylene glycol.[11] Surface charge analysis showed a clear downward trend in fluorescence when the pH increases (Figure S11), due to deprotonation of the amine moieties.[23] At acidic pH, as-received PEI_{800} and hPEI have more positive zeta potential values compared with the VFD processed materials, as expected with a net loss of amine groups and an increase in hydroxyl group post-processing. This was confirmed by a net decrease of isoelectric points (IEP), where the total charge of the diffusion layer around the particles equals zero (Figure S11). The reduction in IEP is consistent with loss of some surface NH_2 groups post-processing rendering the surface less basic.[24]

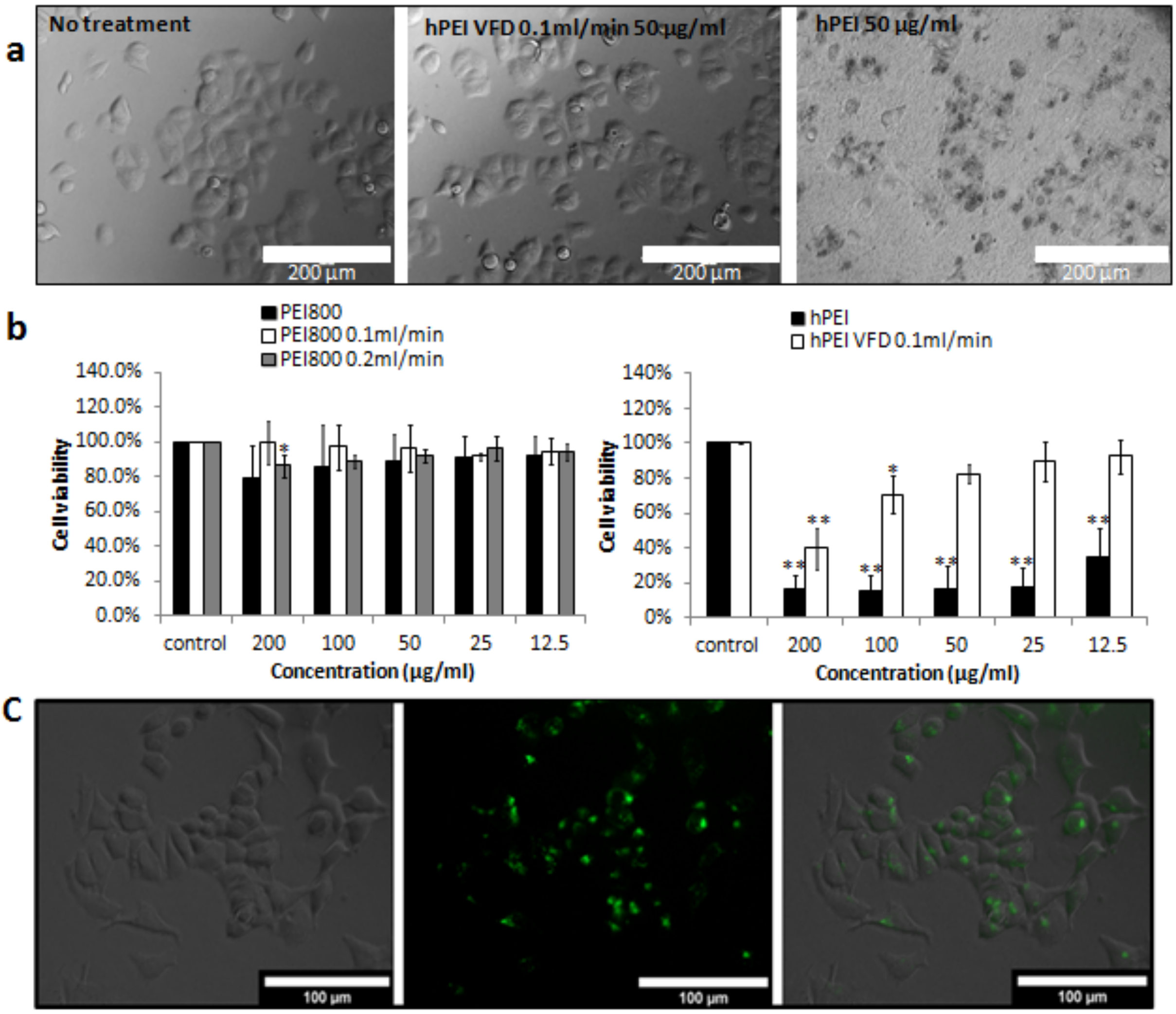

Figure 4.4 *(a) Optical images of non-treated MCF-7 cells, and cells treated with VFD-processed hPEI and as-received hPEI; (b) Cell viability of MCF-7 cells treated with different concentrations of* PEI_{800} *and hPEI derivatives for 24 h. Data are presented as mean±SD. Treatment significantly different from the control at* $P<0.05$ *were presented as * and* $P<0.01$ *as **; (c) Images of MCF-7 cells treated with VFD processed* PEI_{800} *(0.2 mL/min) under bright field, GFP (470/22 nm) excitation and the merged image.*

Cytotoxicity of PEI is size-dependent with higher toxicity observed for higher molecular weight polymer.[25] This is attributed to high positive charge which can cause cell membrane damage.[13] MTT on hPEI nanoparticles revealed that post-

VFD processing, hPEI showed significantly reduced ($p < 0.01$) cytotoxicity on MCF-7 cells (Figure 4.4 b). This is consistent with a significant reduction in surface amine groups in hPEI post-processing, in accordance with the above zeta potential results. Reduced cytotoxicity of processed hPEI can result from the formation of amide and carbamate moieties, facilitating the in situ degradation of the polymer into low molecular weight fragments in a cellular environment.[25] After 24 hour treatment with VFD processed PEI_{800} (at 0.2 mL min^{-1}), the images clearly show the distribution of fluorescent material in the cytoplasm (Figure 4.4 c). Cellular uptake of the nanoparticles could be due to the positively charged surface which leads to strong electrostatic interaction with the negatively charged cell membrane followed up by particle wrapping and cellular uptake.[26] The overall reduction in cytotoxicity arises from a combined effect of reduced polymer size, decreased net positive charge on the nanoparticle surface and the new functional moieties.

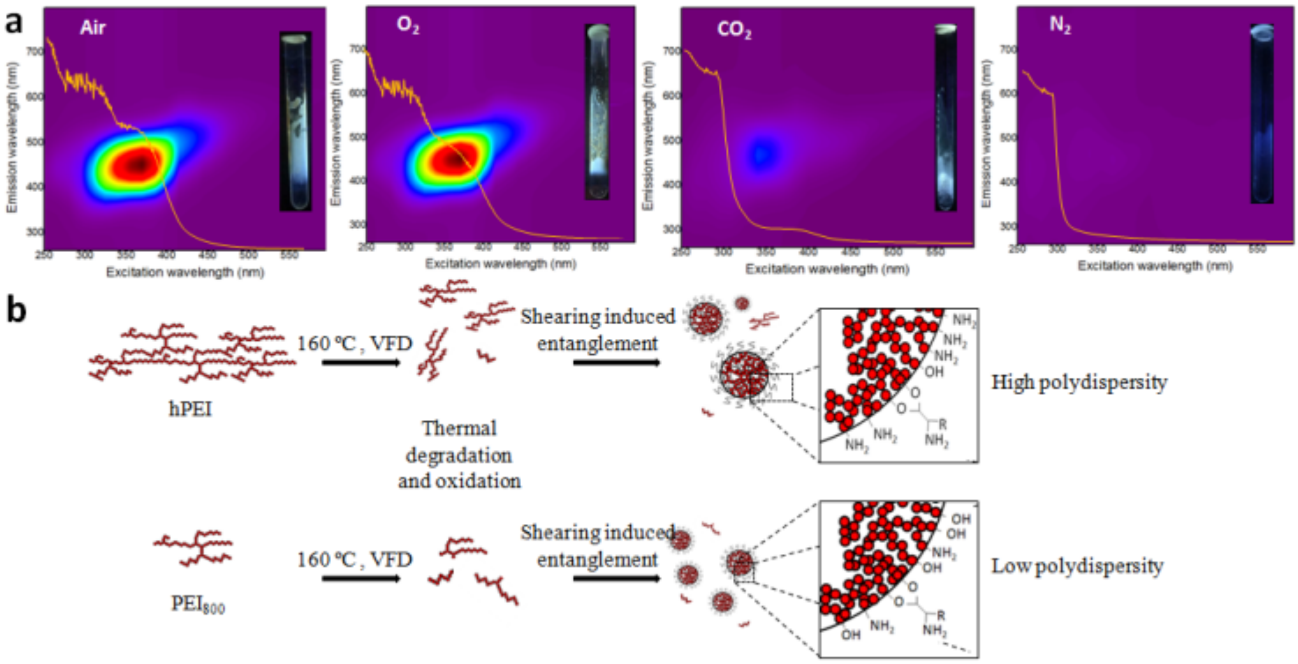

Figure 4.5 *(a) 2D fluorescence maps for 1 mL of hPEI solution processed in a VFD at 7500 rpm at 160°C (confined mode) for 30 min under different gas environment; (b) the proposed mechanism of the VFD-polymer reaction.*

The reaction mechanism could include several possibilities as shown in Figure 5. Given that the degradation is oxidative, some derivatives are presumably amides.[20] Another pathway could involve chain scission of an initially formed hydroperoxide. The resulting aldehydes and carboxylates could be PEI oligomers with oxidized end groups. The result from size exclusion chromatography (Figure S11c) on VFD-processed PEI_{800} at 0.2 mL min^{-1} flow rate revealed the presence of smaller and larger sized polymers in the final product relative to as received PEI_{800}. This is consistent with oxidative chain degradation and oxidative coupling of some “sliced” PEI chains. The slightly basic nature of as-prepared PEI is consistent with the presence of primary amine groups, which could survive oxidation. Others probably result from oxidation of a portion of the primary amine and also from chain cleavage by hydrolysis.[27] Cleavage from shear stress in the thin film in the VFD is also possible.[28]

In decoupling the effect of the gas above the dynamic thin film in the VFD, hPEI was processed at 160ºC in a flow of air, O_2, CO_2 and N_2, respectively (Figure 4.5 a). As shown, the fluorescence intensity was about 6 fold higher after processing in air or O_2 compared to that of CO_2, and no fluorescence for material processed under an atmosphere of pure N_2. The proposed mechanism of formation of fluorescent nanoparticles is summarized in Figure 4.5 b. This is based on (i) the above discussion where the generation of newly-formed fluorescent derivatives is mainly due to the oxidative degradation and chain scission of PEI, and (ii) VFD-mediated oxidative coupling of degraded or existing polymers into nanoparticles. Our previous studies established that the shear stress generated in a VFD is effective in completely disrupting fluorous bis-urea derived gels at room temperature.[16] In addition, the shear stress could result in compacting and intertwining single walled carbon nanotubes into nanoring structures.[29] In the present study, the dual effect from mechanical thin film shear and high temperature facilitates oxidation triggered polymer degradation and coupling into nanoparticles, independent of the sample molecular weight. The intrinsic fluorescence originates from the formation of newly formed functional groups arising mainly through oxidation.

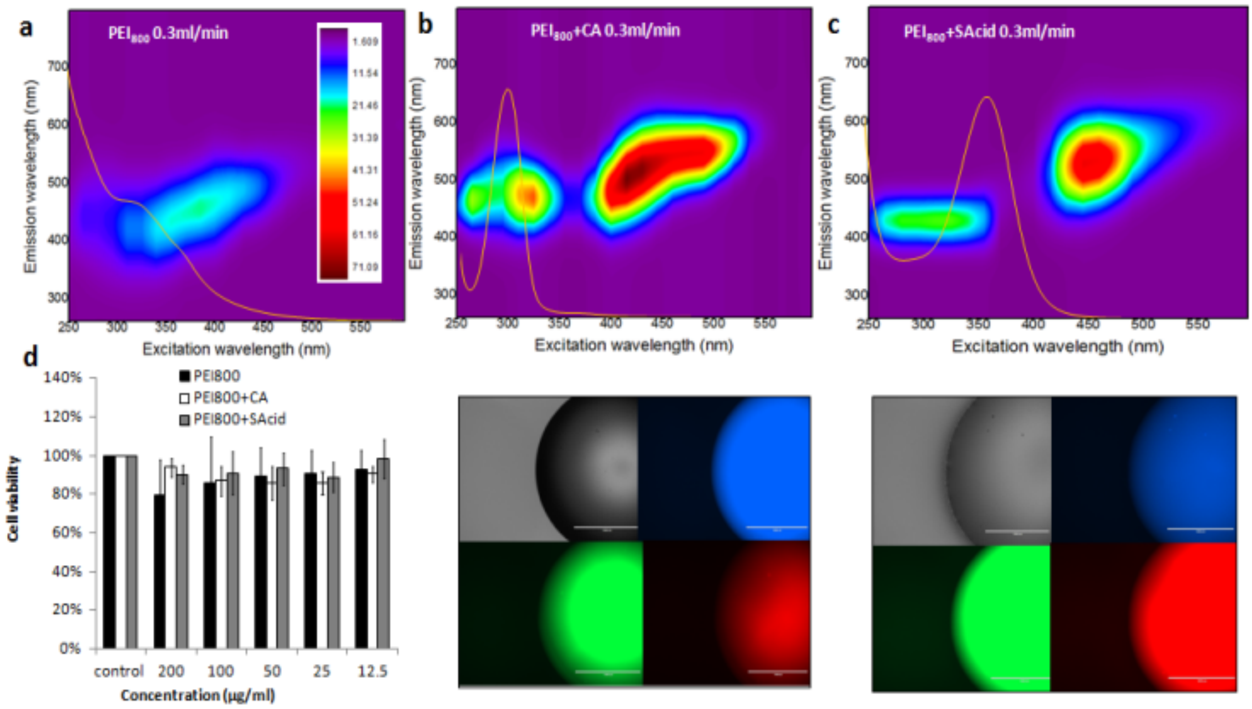

Figure 4.6 *2D fluorescence map of VFD processed PEI_{800} (37 mg/mL) at 160ºC under continuous flow, 0.3 mL/min, 8600 rpm. (a) PEI_{800} only; (b) PEI_{800} and citric acid (molar ratio 1:1); (c) PEI_{800} and salicylic acid (molar ratio 1:1); (d) Cell viability of MCF-7cells treated with different concentrations of the three PEI derivatives after 24 h.*

To further explore the origin of the fluorescence, we hypothesized that by changing the functional group (in this case amide moieties), would allow further tuning of the fluorescence. Citric acid (CA, a tri-carboxylic acid) and salicylic acid (o-hydroxybenzoic acid) were separately added during VFD processing of PEI_{800} (160ºC, 0.3mLmin^{-1}) and this resulted in strong auto-fluorescence, significantly different to the fluorescence from processing PEI_{800} alone under the same conditions (Figure 4.6). Distinctly different UV-visible absorption bands were also observed. An upfield shift of CA (methylene groups) and a downfield shift and broadening of PEI characteristic signals were evident in the ^{1}H NMR spectra, relative to as-received PEI (Figure S12). These results are consistent with the formation of ammonium groups,[30] arising from protonation of N-H in the PEI by carboxylic acid derivatives.[31] ^{13}C NMR showed characteristic resonance signals for the carboxylic acid (176 and 173 ppm) with an upfield shift with respect to VFD-processed sample (182 and 179 ppm), in accordance with the previous published PEI/CA complex.[30] A similar result was also found for processed PEI in the presence of salicylic acid (Figure S13). Thus enhanced fluorescence intensity and manipulation of the nature of the fluorescence is possible by varying the functional groups. Cytotoxicity test against MCF-7 cell lines showed negligible effect on cell viability.

4.5 Conclusion

In conclusion, we report a tunable, efficient and continuous flow process to prepare fluorescent PEI-based nanoparticles with a controlled average diameter of *ca.* 10 nm. High-temperature and high-shear mechanoenergy in VFD in air results in polymer degradation, chain scission and reorganization of the fragmented chains into self-passivated nanoparticles. The fluorescence of these nanoparticles could be readily tuned by varying the flow rate of the liquid entering the rapidly rotating tube without the need for auxiliary reagents. Chemical incorporation of amide groups triggers enhanced fluorescence intensity and auto-fluorescence over a wide excitation range. Importantly, the VFD-processed nanoparticles show significantly reduced cytotoxicity compared to as-received materials and have potential for medical applications.

4.6 Acknowledgements

The authors gratefully acknowledge support from the Australia Research Council and the Government of South Australia, and the Australian Microscopy and Microanalysis Research Facility (AMMRF), and the Australian National Fabrication Facility (ANFF) for access to characterization facilities. The authors would also like to thank Ms Yvette DeGraaf for florescence microscopy and valuable discussions.

4.7 References

[1] D. Wang, T. Imae, J. Am. Chem. Soc. 2004, 126, 13204–13205.

[2] X. Pan, G. Wang, C. L. Lay, B. H. Tan, C. He, Y. Liu, Sci. Rep. 2013, 3, 2763.

[3] Y. Ling, F. Qu, Q. Zhou, T. Li, Z. F. Gao, J. L. Lei, N. B. Li, H. Q. Luo, Anal. Chem. 2015, 87, 8679–8686.

[4] Y. Chen, L. Zhou, Y. Pang, W. Huang, F. Qiu, X. Jiang, X. Zhu, D. Yan, Q. Chen, Bioconjugate Chem. 2011, 22, 1162–1170.

[5] S. G. Liu, N. Li, Y. Ling, B. H. Kang, S. Geng, N. B. Li, H. Q. Luo, Langmuir

2016, 32, 1881 – 1889.

[6] C.C.Chu,T.Imae,Macromol.RapidCommun.2009,30,89–93.

[7] R. B. Restani, P. I. Morgado, M. P. Ribeiro, I. J. Correia, A. Aguiar-Ricardo, V.D.B. Bonifµcio, Angew. Chem. Int. Ed. 2012, 51, 5162–5165; Angew. Chem. 2012, 124, 5252–5255.

[8] D. C. Wu, Y. Liu, C. B. He, S. H. Goh, Macromolecules 2005, 38, 9906 – 9909.

[9] S.Y. Lin, T.H. Wu, Y.C. Jao, C.P. Liu, H.Y. Lin, L.W. Lo, C.S. Yang, Chem. Eur. J. 2011, 17, 7158–7161.

[10] L. Pastor-Pÿrez, Y. Chen, Z. Shen, A. Lahoz, S. E. Stiriba, Macromol. Rapid Commun. 2007, 28, 1404–1409.

[11] L. Shen, L. Zhang, M. Chen, X. Chen, J. Wang, Carbon 2013, 55, 343– 349.

[12] Y. Dong, R. Wang, G. Li, C. Chen, Y. Chi, G. Chen, Anal. Chem. 2012, 84, 6220 – 6224.

[13] C. Liu, P. Zhang, X. Zhai, F. Tian, W. Li, J. Yang, Y. Liu, H. Wang, W. Wang, W. Liu, Biomaterials 2012, 33, 3604–3613.

[14] S.G. Liu, T. Liu, N. Li, S. Geng, J.L. Lei, N.B. Li, H.Q. Luo, J. Phys. Chem. C 2017, 121, 6874–6883.

[15] L. Yasmin, X. Chen, K. A. Stubbs, C. L. Raston, Sci. Rep. 2013, 3, 2282.

[16] H. Kumari, S. R. Kline, S. R. Kennedy, C. Garvey, C. L. Raston, J. L. Atwood, J. W. Steed, Chem. Commun. 2016, 52, 4513 – 4516.

[17] X. Luo, P. Smith, C. L. Raston, W. Zhang, ACS Sustainable Chem. Eng. 2016, 4, 3905–3911.

[18] J. Britton, L. M. Meneghini, C. L. Raston, G. A. Weiss, Angew. Chem. Int. Ed. 2016, 55, 11387–11391; Angew. Chem. 2016, 128, 11559–11563.

[19] C. L. Tong, U. H. Stroeher, M. H. Brown, C. L. Raston, RSC Adv. 2015, 5, 7953 – 7958.

[20] S. A. Idris, O. A. Mkhatresh, F. Heatley, Polym. Int. 2006, 55, 1040 – 1048.

[21] D. R. Holycross, M. Chai, Macromolecules 2013, 46, 6891 – 6897.

[22] P. V. Kortunov, M. Siskin, M. Paccagnini, H. Thomann, Energy Fuels 2016, 30, 1223–1236.

[23] M. Bloemen, W. Brullot, T. T. Luong, N. Geukens, A. Gils, T. Verbiest, J. Nanopart. Res. 2012, 14, 1100.

[24] K. H. Park, C. H. Lee, S. K. Ryu, X. Yang, Carbon Lett. 2007, 8, 321 – 325.

[25] M. L. Forrest, J. T. Koerber, D. W. Pack, Bioconjugate Chem. 2003, 14, 934 – 940.

[26] T. Xia, M. Kovochich, M. Liong, H. Meng, S. Kabehie, J. I. Zink, A. E. Nel, ACS Nano 2009, 3, 3273–3286.

[27] H. C. Haas, N. W. Schuler, R. L. Macdonald, J. Polym. Sci. A 1972, 10, 3143 – 3158.

[28] K. Vimalanathan, J. R. Gascooke, I. Suarez-Martinez, N. A. Marks, H. Kumari, C. J. Garvey, J. L. Atwood, W. D. Lawrance, C. L. Raston, Sci.Rep. 2016, 6, 22865.

[29] K. Vimalanathan, X. Chen, C. L. Raston, Chem. Commun. 2014, 50, 11295 – 11298.

[30] M. D. Giron-Gonzalez, R. Salto-Gonzalez, F. J. Lopez-Jaramillo, A. Salinas-Castillo, A. B. Jodar-Reyes, M. Ortega-MuÇoz, F. Hernandez-Mateo, F. Santoyo-Gonzalez, Bioconjugate Chem. 2016, 27, 549–561.

[31] P. F. Cao, L. H. Rong, A. de Leon, Z. Su, R. C. Advincula, Macromolecules 2015, 48, 6801–6809.

Appendix: Journal front cover of the published article, the article's first page and the first page of published supplementary information.

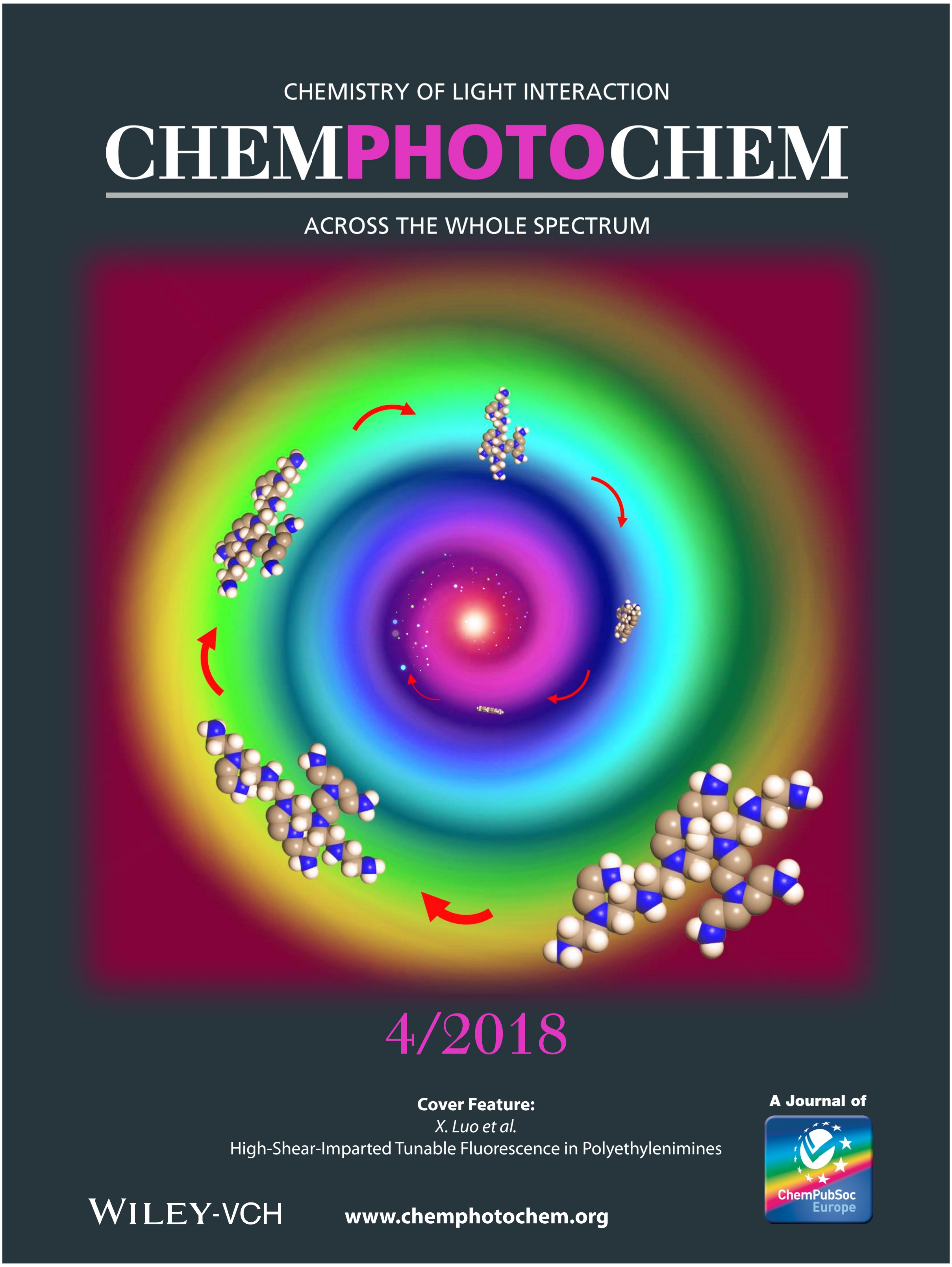

CHEMISTRY OF LIGHT INTERACTION

CHEMPHOTOCHEM

ACROSS THE WHOLE SPECTRUM

4/2018

Cover Feature:
X. Luo et al.
High-Shear-Imparted Tunable Fluorescence in Polyethylenimines

A Journal of
ChemPubSoc Europe

WILEY-VCH

www.chemphotochem.org

ChemPubSoc Europe
DOI: 10.1002/cptc.201700206
CHEMPHOTOCHEM
Communications

High-Shear-Imparted Tunable Fluorescence in Polyethylenimines

Xuan Luo,[a, b] Ahmed Hussein Mohammed Al-Antaki,[a] Scott Pye,[a] Robyn Meech,[c] Wei Zhang,*[b] and Colin L. Raston*[a]

In general, fluorescent polyethylenimine (PEI) nanoparticles absorb primarily UV light, with the fluorophores typically having extended conjugated structures. In this work, PEI nanoparticles of circa 10 nm in diameter, devoid of such structural features and with tunable fluorescence, were generated in a microfluidic platform. Tunability of the fluorescence was achieved by varying the flow rate of liquid entering the rapidly rotating tube in a vortex fluidic device (VFD), without the need for additional reagents. Chemical incorporation of amide functional groups triggered enhanced fluorescence intensity and auto-fluorescence over a wide range, and the resulting nanoparticles showed significantly reduced cytotoxicity compared to as-received polymers.

Fluorescent nanoparticles derived from amino-containing dendritic polymers have been used for biological imaging and biosensors[1–3] where the fluorophores are usually extended conjugated chemical structures.[4] Even though simple oxidation, acidification or methylation can further enhance the intrinsic fluorescence,[5] the mechanism of fluorescence from these dendritic polymers is not well understood. Some propose that the origin of fluorescence arises from oxygen-doped interior tertiary amine[6] and interior urea-doped with peripheral amino groups.[7] These fluorescent polymers can contain Schiff base moieties,[5] tertiary amine or carbonyl groups in an dendrimer interior with terminal groups such as monohydroxyl,[8] air[6] or hydrogen peroxide[9] oxidized amines, amine-rich nanoclusters,[5] and carbamato anion.[2] The nature of the dendritic structure and macromolecular backbone can also significantly influence the fluorescence properties.[1,5]

Polyethylenimine (PEI) is a water-soluble cationic polyelectrolyte which contains a large number of amino groups, and has been used to prepare various fluorescent materials.[10] The fluorescence of PEI is unexpected given the absence of chromophores.[5] Refluxing 25 kDa PEI in nitric acid at 120 °C for 12 h affords photoluminescent nanoparticles ($\lambda_{ex}=360$ nm, $\lambda_{em}=450$ nm) bearing amide linkages (NHCO).[11] Hyperbranched PEI (hPEI)-based fluorescent particles have been prepared at high temperature (200 °C)[12] or via microwave irradiation.[13] Adding formaldehyde at 90 °C results in fluorescent polymeric nanoparticles ($\lambda_{ex}=365$ nm, $\lambda_{em}=508$ nm) or gels ($\lambda_{ex}=350$ nm, $\lambda_{em}=476$ nm). Similarly, adding salicylaldehyde imparts fluorescence ($\lambda_{ex}=370$ nm, $\lambda_{em}=495$ nm)[14] which arises from the formation of Schiff base moieties.[3,5] Hydrothermal treatment of hPEI with aldehydes at 95 °C generates fluorescent polymer nanoparticles,[3] depending on the pH which can complicate the processing. The carbamate anion is another moiety responsible for fluorescence ($\lambda_{ex}=364$ nm, $\lambda_{em}=470$ nm), formed by reacting PEI with CO_2.[2] Based on our knowledge, tunability of fluorescence has never been addressed on PEI-based nanoparticles with mostly reported optimum excitation in the UV region, as described above. Furthermore, there is a lack of knowledge on the relationship between molecular weight of PEI, particle surface functionality and the emission property. Other limitations include the need for time-consuming dialysis to remove unreacted reagents in the fabrication process.[5]

Liu et al.[5] reported that ideal fluorescent polymer nanoparticles should be autofluorescent without doping an external fluorochrome. We are motivated by this idea to fabricate fluorescence-tunable PEI-based nanoparticles from PEI devoid of extended conjugates or precursors, under high shear in a continuous-flow thin-film vortex fluidic device (VFD; Figure 1). This thin film microfluidic platform has diverse applications,[15] including the entanglement of 3D gel networks,[16] intensifying multi-phase separation,[17] enhancing enzymatic reactions[18] and fabricating hydrogels.[19] This study extends the applications of VFD into fabricating tunable fluorescence nanoparticles based on branched PEI and hPEI. Modifying low and high molecular weight PEI under continuous flow in the VFD, as immediately scalable processes, has the potential to avoid the use of precursors typically required for PEI-based fluorescence with tunability addressed by only varying the processing conditions. The use of a VFD also lends itself to decoupling the

---

[a] X. Luo, A. H. M. Al-Antaki, S. Pye, Prof. C. L. Raston
Flinders Centre for NanoScale Science and Technology (CNST)
College of Science and Engineering
Flinders University
Bedford Park, Adelaide, 5042 (Australia)
E-mail: colin.raston@flinders.edu.au

[b] X. Luo, Prof. W. Zhang
Flinders Centre for Marine Bioproducts Development
College of Medicine and Public Health
Flinders University
Bedford Park, Adelaide, 5042 (Australia)
E-mail: wei.zhang@flinders.edu.au

[c] Dr. R. Meech
Clinical Pharmacology, College of Medicine and Public Health
Flinders University
Adelaide, SA 5042 (Australia)

Supporting Information and the ORCID identification number(s) for the author(s) of this article can be found under: https://doi.org/10.1002/cptc.201700206.

© 2018 Wiley-VCH Verlag GmbH & Co. KGaA, Weinheim

CHEMISTRY OF LIGHT INTERACTION
CHEMPHOTOCHEM
ACROSS THE WHOLE SPECTRUM

Supporting Information

High-Shear-Imparted Tunable Fluorescence in Polyethylenimines

Xuan Luo,[a, b] Ahmed Hussein Mohammed Al-Antaki,[a] Scott Pye,[a] Robyn Meech,[c] Wei Zhang,*[b] and Colin L. Raston*[a]

cptc_201700206_sm_miscellaneous_information.pdf

5 VORTEX FLUIDIC MEDIATED SYNTHESIS OF MACROPOROUS BOVINE SERUM ALBUMIN-BASED MICROSPHERES

Continuing from previous chapters, this chapter shows another example of VFD facilitated nanoparticle fabrication. Different from metallic materials discussed previously, nanoparticles derived from bovine serum albumin (BNPs) are more biodegradable, biocompatible, and have advantages over synthetic polymers in medical applications. Biocompatible BNPs have potential in drug delivery applications with a capacity for incorporating drugs within the particle matrix for enhanced endocytic uptake. However, most of the cross-linking processes applied in the desolvation of BNPs have long processing times and none of those reported particles appear to be devoid of pores connecting the outer surface with the core of the particles. The shear stress in the VFD can mediate the fabrication of BNPs with tuneable size and shape, while at the same time controlling the crosslinking chemistry. Herein we report a rapid novel and highly efficient process for the synthesis of homogeneous spheroidal BNPs with inbuilt porosity. Macroporous BNPs are readily generated in high homogeneity, and remarkable as spheroidal particles with randomly localised pores on their surface. These BNPs particles have a strong intrinsic fluorescence emission at 555 nm when excited at 532 nm, and have high absorption efficiency of Rhodamine B compared to non-optimised particles with smooth surfaces devoid of any pores. Further reduction of the size of BNPs is effective by incorporating c-phycocyanin protein into the system during processing in the VFD, as well as controlling their shape, from spheres to pockets, as established by systematically exploring the parameter space of the microfluidic platform. This chapter shows a great example of VFD induced micro- and nano-materials with precise control over size, shapes and homogeneity. Different from conventionally developed MD systems, VFD effectively overcomes one of the biggest problems such as system clogging.

This study was published in ***ACS Applied Materials & Interfaces***, Year 2018, Vol. 10, Issue 32, Pages 27224-27232. The first page of the publication is attached in Appendix 5.1.

Author contributions: **XL** performed all the VFD and most characterization experiments; wrote all the primary content. **AA** assisted with VFD scaled up experiments. **DH** performed the STA analysis. **YR** and **SH** assisted with confocal mapping. **WZ** and **CR** supervised and coordinated the project and helped on the research directions and plan, and the final revision of the manuscript. All of the co-authors assisted with the revision of the manuscript before and during the publication process.

Vortex fluidic mediated synthesis of macroporous bovine serum albumin-based microspheres

Xuan Luo[1,2], Ahmed Hussein Mohammed Al-Antaki[1], David P. Harvey[1], Yinlan Ruan,[3] Shan He,[4] Wei Zhang*[2] and Colin L. Raston*[1]

[1]*Flinders Centre for NanoScale Science and Technology (CNST), College of Science and Engineering, Flinders University, Adelaide, SA 5042;* [2]*Flinders Centre for Marine Bioproducts Development, College of Medicine and Public Health, Flinders University, Adelaide, SA 5042;* [3]*Institute of Photonics and Advanced Sensing, School of Physical Sciences, Adelaide University;* [4]*Department of Food Science and Engineering, School of Chemistry Chemical Engineering, Guangzhou University, 510006 (China)*

Graphical abstract

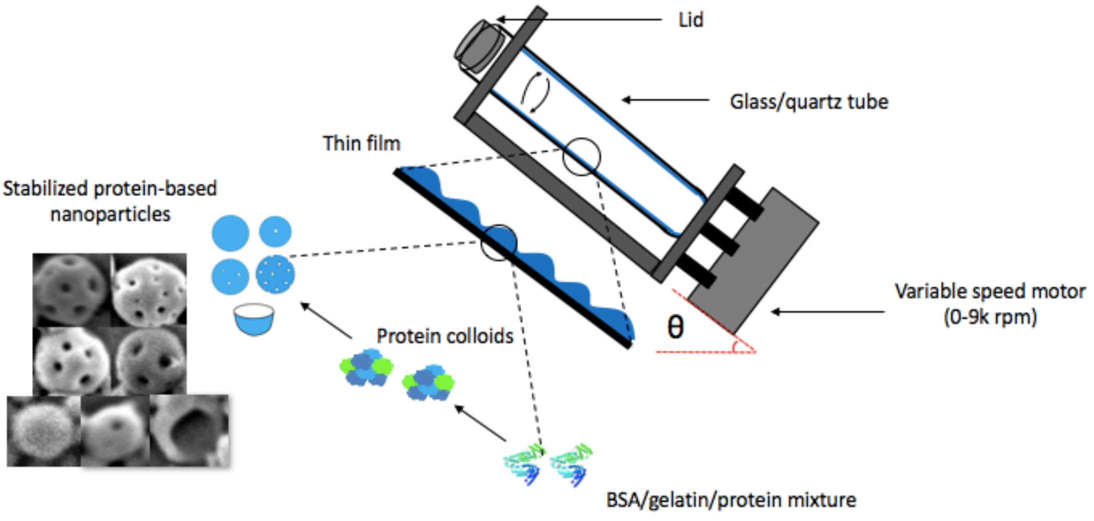

5.1 Abstract

Macroporous bovine serum albumin (BSA) nanoparticles with controllable diameter were readily fabricated in a rapidly rotating angled glass tube in a vortex fluidic device (VFD). Systematically varying the rotational speed and the ratio of BSA, ethanol and glutaraldehyde led to conditions for generating *ca.* 600 nm diameter macroporous particles that have intrinsic fluorescence emission at 520 nm when excited at 490 nm. The presence of the macropores increased the absorption efficiency of Rhodamine B with potential applications for drug delivery purpose, compared to BSA nanoparticles having surfaces devoid of pores. Further control over the size of BSA nanoparticles occurred in the presence of c-phycocyanin protein during the VFD processing, along with control of their shape, from spheres to pockets, as established in exploring the parameter space of the microfluidic device.

Keywords: bovine serum albumin, macroporous, nanoparticle, fluorescence, microfluidics

5.2 Introduction

Nanoparticles derived from bovine serum albumin (BSA nanoparticles or BNPs) are biodegradable, biocompatible,[1] non-toxic and non-immunogenic,[2] and have advantages over synthetic polymers in medical applications such as drug delivery.[3] Given the defined primary structure of protein and its high content of charged amino acid moieties such as lysine,[4] BNPs offer scope for surface modification in terms of covalent drug attachment[5,6] and electrostatic adsorption of positively charged or negatively charged molecules either internally and/or on their surfaces.[4] Protein-based nanoparticles can be prepared by freeze drying,[7] supercritical fluid processing,[8] spray-drying,[9] de-solvation,[5] and enzymatic cross-linking.[10] De-solvation is considered a robust reproducible method,[4] consisting of drop-wise addition of ethanol to an aqueous solution of albumin followed by continuous stirring until it becomes turbid. The turbidity arises from the diminished water solubility of denaturated BSA in ethanol, with disruption of the protein tertiary structures.[11,12] BNPs are generated by fixation with glutaraldehyde where the amino residues in lysine and arginine residues in guanidine side chains of albumin are cross linked by condensation with the aldehyde.[4]

Biocompatible BNPs have potential in drug delivery applications with a capacity for incorporating drugs within the particle matrix for their enhanced endocytic uptake.[13,14]

The use of nano-scaled materials for drug delivery and diagnostics is at the forefront of medicine, with the encapsulation of drugs into NPs significantly improving their release profile in cells or tissues.[3] For instance, BNPs has been used for local delivery of Rhodamine B (RhB) into the inner ear with potential applications in the field of treating inner ear disorders.[15] However, most of the cross-linking processes applied in the desolvation of BNPs have long processing times. Intrinsically fluorescent BNPs with emission at 535 nm after being excited at 495 nm[12] have been reported, but their preparation requires 18 hours processing time. In other studies, the cross-linking process under batch stirring of the suspension takes 24 hours or more.[14-16] As to drug loading experiments, Doxorubicin has been separately loaded over an additional 2 hours of stirring.[16] Even though this process can be facilitated by repeated homogenization,[2] the overall energy efficiency of the processing is predictably low and the homogenisation could significantly change the surface zeta potential, affect the *in vitro* release rate and reduce the loading quantity of hydrophobic drugs.[17] A number of studies have been reported on controlling the size of BNPs by varying the concentration of BSA or ethanol, but the particles appear to be devoid of pores connecting the outer surface with the core of the particles.

Porous submicron particles (macropores > 50 nm, mesopores 2-50 nm and micropores < 2 nm)[18] are attractive materials for low dielectric fillers, adsorbents, drug delivery systems, catalyst carriers and optics. Most of these porous structures have been obtained through the polymerization of styrene.[19] For example, Okubo *et al*. reported on the fabrication of 1.77 micron-sized poly(methyl methacrylate)/polystyrene composite particles having 50-150 nm sized dents on their surface, using a seeded dispersion polymerization method in the presence of decalin.[20] Porous polystyrene particles and poly(styrene-divinylbenzene) microparticles have been fabricated through multistep swelling and polymerization of styrene.[21-23] Most of these fabrication processes require multiple steps, pressure adjustment (20-245 kPa) and heating (80-120 °C), which represent energy and cost penalties.[24] More importantly, the use of these particles can be unpleasant on safety and environmental grounds.[25] Given that albumin itself has been successfully administered in medical applications such as aerosol inhalation,[24] the fabrication of porous BNPs through vortex fluidic device (VFD) processing has the potential to overcome some of the issues discussed above. We hypothesised that the shear stress in the VFD can mediate the fabrication of BNPs with tuneable size, while at the same time controlling the crosslinking chemistry.

Herein we report a rapid novel and highly efficient process for the synthesis of homogeneous spheroidal BNPs with inbuilt porosity in a VFD which houses an angled rapidly rotating borosilicate glass tube (20 mm O.D., 17.5 mm I.D., 19.4 cm in length, or 20 mm O.D., 17.1 mm I.D., 39 cm in length, both inclined at 45º relative to the horizontal position), as shown in Figure 5.1. This thin film microfluidic platform has a number of diverse applications including the fabrication of various nano-carbon materials,[26-27] intensified aqueous two phase separation for protein purification,[28] fabricating hydrogels for drug delivery,[29] manipulating polymer networks,[30-31] exfoliating graphite and boron nitride,[32] protein folding[33] and accelerating enzymatic reactions.[30] By precisely varying the speed of the glass tube and ratio between BSA, ethanol and glutaraldehyde, macroporous BNPs were readily generated in high homogeneity, and remarkably as spheroidal particles with randomly localised pores on their surface. These BNPs particles have a strong intrinsic fluorescence emission at 520 nm when excited at 490 nm, and have high absorption efficiency of Rhodamine B compared to non-optimised particles with smooth surfaces devoid of any pores. Further reduction of the size of BNPs was effective by incorporating c-phycocyanin protein into the system during processing in the VFD, as well as controlling their shape, from spheres to pockets, as established by systematically exploring the parameter space of the microfluidic platform.

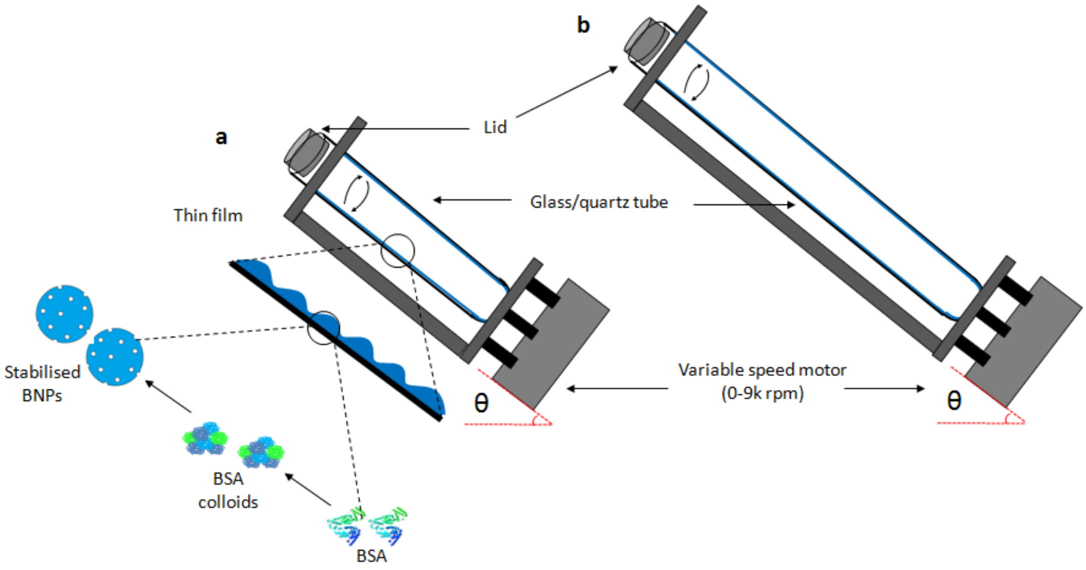

Figure 5.1 *Schematic of (a) the standard vortex fluidic device (VFD) (20 mm O.D. 17.5 mm I.D., length 19.4 cm) operated under the confined mode at a tilt angle of 45° and the preparation of BNPs from BSA, ethanol and glutaraldehyde, and (b) a long tube VFD (O. D. 20 mm, I.D. 17.1 mm, length 39 cm) operated under confined mode at a tilt angle of 45°.*

5.3 Materials and Methods

BSA, ethanol and glutaraldehyde were obtained from Sigma-Aldrich as analytical grade. C-phycocyanin was obtained from Fuqing King Dnarmsa Spirulina Co., Ltd. The fabrication process for macroporous BNPs using the VFD involved adding specific volumes of ethanol solution to a specified volume of BSA using the de-solvation method at 1 mg/mL at room temperature.[15] For the standard VFD (20 mm O.D., 17.5 mm I.D., length 19.4 cm), volume combinations for BSA (1 mg/mL), ethanol and glutaraldehyde were 300 µL, 900 µL and 15 µL, respectively. Then, 1 mL of a combined solution was quickly transferred to the VFD and the glass tube spun at 6k rpm for 1 min. For the VFD housing a long glass tube (20 mm O.D. 17.1 mm I.D., length 39 cm), volume combinations for BSA (1 mg/mL), ethanol and glutaraldehyde were 2400 µL, 7200 µL and 120 µL, respectively. Then 8 mL of the combined solutions was quickly transferred to the long tube which was spun at 6k rpm for 1 min. Addition of ethanol resulted in the spontaneous formation of an opalescent suspension. Depending on the optimisation, various amount of glutaraldehyde (%, v/v) was added to the colloidal suspension during processing in the VFD to induce cross linking. Post VFD processing (1 min), samples were recovered by centrifugation at 11800 × g for 15 min and washed with the same volume of Milli Q water three times to remove excess reactants.

The morphology of the BNPs was determined using scanning electron microscopy (SEM) and atomic force microscopy (AFM). For SEM, a drop of diluted suspension was deposited on a silicon wafer, and the air-dried sample was coated with 5 nm platinum before imaging. The particle size (dynamic light scattering (DLS)) and zeta potential were performed using a Malvern particle size analyser (Malvern Zetasizer). A rotary evaporator (Buchi, Switzerland) was operated at 40 °C and pressure of 35 mbar to remove solvents. Fluorescence spectroscopy measurements were performed using an inverted fluorescence microscope under bright field as a EVOS® FL equipped with three Invitrogen™ EVOS™ light cubes, DAPI (357/44 Ex; 447/60 Em), GFP (470/22 Ex; 510/42 Em) and RFP (531/40 Ex; 593/40 Em. Brunauer-Emett-Teller (BET, Micromeritics TriStar II) was used to measure the porosity of the BNPs. The elemental and chemical composition was evaluated using Fourier transform infrared spectroscopy analysis (FTIR, PerkinElmer, in the range of 550-4000 cm^{-1}). To analyse the effectiveness of the removal of glutaraldehyde and its effect on sample stability, simultaneous thermal analysis (STA) was performed using a PerkinElmer STA 8000. The sample was heated from 30 to 100 °C at a rate of 2 °C min^{-1}. The sample was held for 2 minute at 100 °C and then heated from 100 to 900 °C at a rate of 5 °C min^{-1}. Far-UV CD spectra were acquired for three accumulations between 195 and 260 nm with a resolution of 0.1 nm, bandwidth of 1 nm, signal averaging time of 1 s, and a path length of 1 mm. The raw data in milli-degrees was converted to mean residue ellipticity $[\theta]_{MRE}$ (deg cm^2 $dmol^{-1}$) using a mean residue weight of 115 as described in Patil *et al.*[34] The scanning confocal microscopy with 532 nm excitation wavelength was used to map and evaluate emission properties of individual nanoparticles. A large-molecule adsorption analysis was measured as described in Nandiyanto *et al.*[35] Beer's law was adopted and the data were normalized to a red wavelength (554 nm) based on UV-vis spectrometry. The fluorescence spectroscopy of BNP-RhB was determined at an excitation wavelength of 550 nm and an emission wavelength of 580 nm as in Yu *et al*.[15] To investigate the effect of the macroporous structure on the ability of materials adsorbing RhB, the as-prepared BNPs of different morphologies were freeze-dried and re-dispersed into 0.01 M pH 7.4 PBS buffer solution. In addition, RhB was dissolved in the same buffer solution to a concentration of 2 mg/mL. Both suspensions were well dispersed and mixed in a volume ratio of 1:1 using vigorous mixing. Thereupon the sample was immediately studied in a UV-vis spectrophotometer, then continuously measured for several hours, up to one day. After thorough washing with water, the supernatants were collected and analysed for any residual RhB that was evaluated by measuring the absorbance at 554 nm after suitable dilution. Each sample was performed in triplicate. The drug loading capacity and encapsulation efficiency were calculated as follows: [15]

$$Drug\ loading\ (w/w\%) = \frac{\text{Amount of RhB in BNPs}}{\text{Amount of BNPs}} \times 100\%\ (1)$$

$$Encapsulation\ efficiency\ (w/w\%) = \frac{\text{Amount of RhB in BNPs}}{\text{Initially added RhB}} \times 100\%\ (2)$$

5.4 Results and Discussion

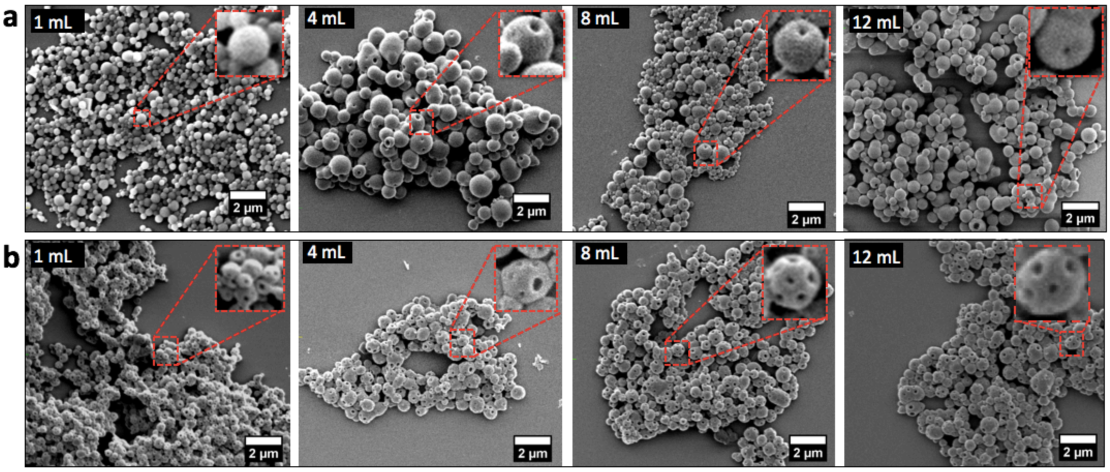

Figure 5.2 *Fabricating BNPs using different volumes in the standard VFD (1 mL of solution) and a long tube VFD (>1 mL), at a tilt angle of 45°; (a) volume ratio for BSA (1 mg/mL), ethanol and glutaraldehyde 400 μL, 800 μL and 10 μL, respectively, (b)*

volume ratio for BSA (1 mg/mL), ethanol and glutaraldehyde, 300 µL, 900 µL and 15 µL, respectively. All experiments were conducted in a VFD with the glass tube rotating at 6k rpm for 1 min.

One processing parameter was varied at a time (processing time, concentration, rotational speed) *en route* to optimizing the conditions for generating a particular particle size, shape and homogeneity. Fabricating BNPs in a VFD was efficient with fully developed spheroidal BNPs formed after only 1 min processing time under confined mode, with the tube rotating at 7.5k rpm (Figure S1); no noticeable changes were observed using longer processing times. Poly-dispersity of BNPs could be significantly reduced by lowering the BSA concentration from 10 mg/mL to 1 mg/mL (Figure S2) and by adjusting the rotational speeds to 6k rpm (Figure S3). Further optimization involved varying the ratio of BSA to ethanol (Figure S4) and the concentration of glutaraldehyde (Figure S5 and S6). Previous studies have intensively investigated the de-solvation process under conventional stirring conditions.[5] Briefly, the particle size and the number of free amino groups depend on the amount of ethanol and glutaraldehyde, respectively. An increase in ethanol leads to an increase in particle size whereas an increase in the glutaraldehyde concentration leads to a reduction in the amount of free amino groups.[5-6] However, under VFD processing, porous BNPs were observed when the BSA (1 mg/mL) to ethanol ratio was reduced from 1:2 (Figure 5.2 a, 1mL) to 1:3 (Figure 5.2 b, 1mL). This has been identified as a critical ratio for preparing such porous structures (Figure S4 and S5). Control experiments used the same materials and processed them using bench-top vortexing for 1 min (no VFD processing). This resulted in the formation of a mixture of porous and non-porous BNPs (with rugged surface) together with large and irregular shaped particles (Figure S7).

The surface of the optimised BNPs have pores that extend into the core of the particles, rather than being simply indentations on their surfaces. Rotary evaporator of BNPs at 35 mbar and 40 °C to remove the solvent did not affect the overall morphology of the BNPs (Figure S8). In contrast, particles devoid of the pores, with smooth surfaces, were fragmented under the same conditions, which implies balancing of the pressure difference through the pores. To investigate the effect of sample volume on the processing, a modified VFD was used, housing a longer tube (O.D. 20 mm, I.D. 17.1 mm, length 39 cm) (Figure 5.2 b). As the overall volume of liquid in this tube increased, above 4 mL, an increase in particle size was observed, *ca.* 500 to 600 nm in diameter (Figure 5.2).

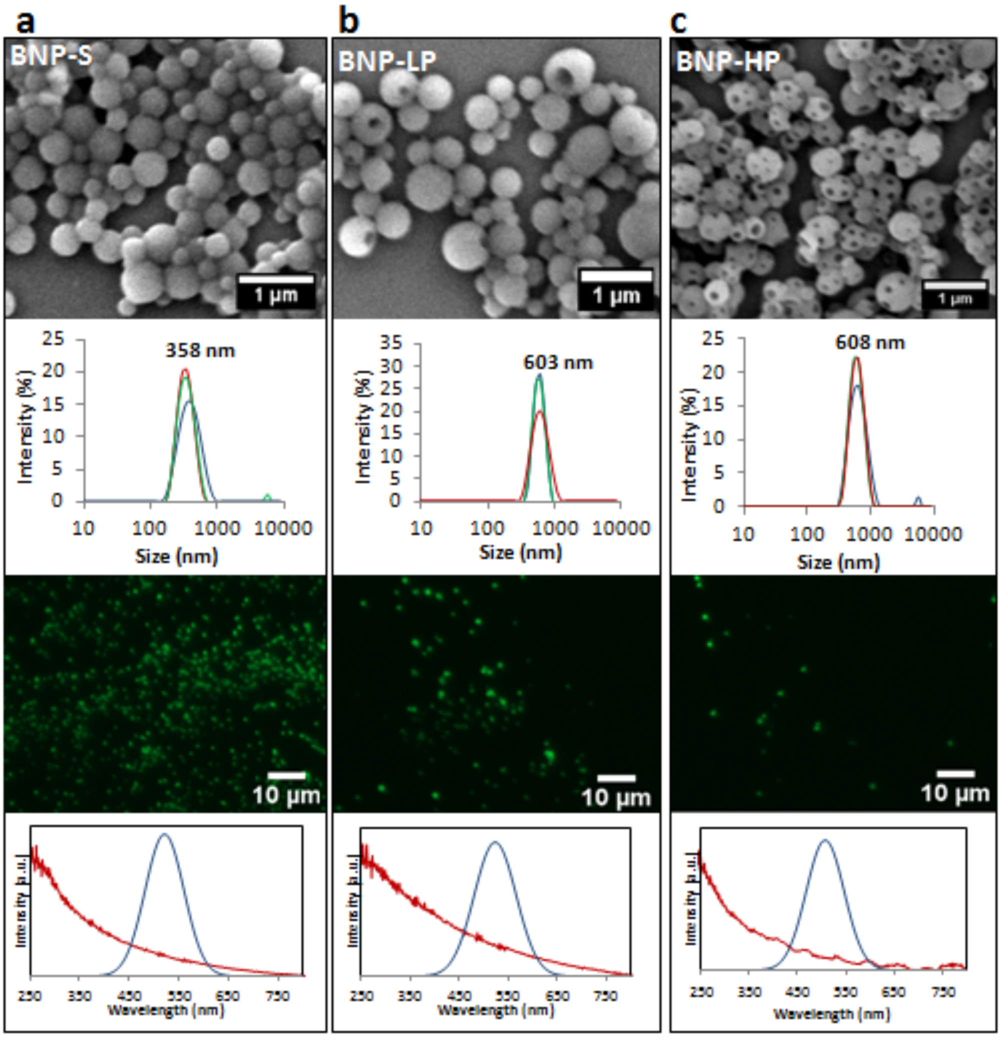

Figure 5.3 *Characterisation of BNPs using SEM, DLS, fluorescence microscopy, UV-vis and fluorescence spectroscopy from top to the bottom, respectively: (a) BNPs with smooth surface, designated as BNP-S. (b) BNPs with some pores, designated as BNP-LP. (c) BNPs with highly porous surfaces, designated as BNP-HP. Blue: fluorescence emission under excitation wavelength of 490 nm. Red: Absorption.*

Further optimization established three BNPs with different surface morphologies, (i) spheroidal particles devoid of pores (achieved at 500 µL, 800 µL and 10 µL for BSA, ethanol and glutaraldehyde, respectively) referred to as 'BNP-S', (ii) spheroidal particles with some pores (achieved at 400 µL, 800 µL and 10 µL) referred to as 'BNP-LP', and (iii) highly porous spheroidal particles (achieved at 300 µL, 900 µL and 15 µL), referred to as 'BNP-HP' (Figure 5.3). Processing conditions for all three types of particles were at 6k rpm for 1 min under confined operation mode of the VFD, for a total volume of 12 mL. SEM images of BNPs showed spheroidal particles with some level of agglomerations. The size of these spheroidal particles was determined using DLS, and they varied in diameter from 358 to about 600 nm, depending on the ratio of the solvent used in their fabrication. We note that such uniformity (Figure S9) and aqueous stability (Figure S13) cannot be achieved in a controlled manner using conventional benchtop vortex mixing, but rather it requires VFD.

As-received BSA is excitable at 280 nm with the emission wavelength at 350 nm, which shows no fluorescence in the visible range (Figure S10). The native fluorescence of proteins normally originates from the primary amino acid sequence containing aromatic groups such as phenylalanine, tryptophan, tyrosine.[36] Owing to the flexible structure, the π electrons in the native proteins are mainly localized, resulting in a rigid and large energy gap for electron transitions in the UV region.[12] However, BNPs in the present study showed a significant shift in both excitation and emission peaks with a single discernible emission at 520 nm when excited at 490 nm, regardless of the shape of the particles (Figure S11). De-solvation can alter parts of the chemical structure of the native amino acid sequence to form large chromophores, as reported by Yang *et al.*[12] For example, the post-translational modification of the tripeptide sequence Ser^{65}Tyr^{66}Gly^{67} to 4-(p-hydroxybenzylidene)-imidazolidin-5-one results in the fluorophore of green fluorescent protein (GFP).[36] Re-organisation of the denatured proteins into a more rigid structure through chemical cross-linking of glutaraldehyde, as in the present study, can induce overlap or reformation of chromophore groups along the amino acid sequence, thereby altering the electronic energy gap for visible wavelength fluorescence emission.[12] Fluorescent microscopy with EVOS^{TM} light cubes GFP (470/22 Ex; 510/42 Em) revealed bright and homogenous green fluorescence of these BNPs, which is in good agreement with the spectroscopic analysis.

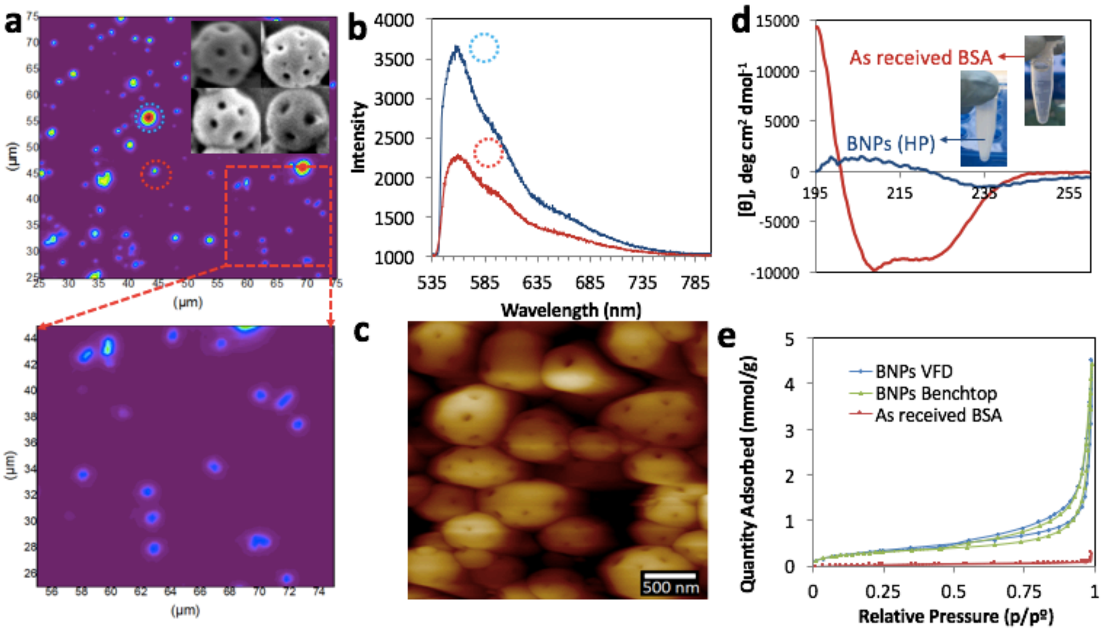

Figure 5.4 *Characterisation of BNPs with macropores using (a) Confocal mapping. (b) Emission wavelength for single macroporous BNPs highlighted in coloured circles in (a) with samples excited with a 532 nm wavelength laser. (c) AFM images. (d) Circular dichroism of as received BSA and macroporous BNP-HPs prepared using a VFD. (e) Nitrogen adsorption analysis of porous BNPs.*

The ability to generate porous BNPs is without precedent, and we therefore carried out further studies to fully reveal the morphology, surface functionalisation, surface area, phase composition and stability of these structures. BNP-HP showed randomly distributed macropores (50-100 nm) in the spheroidal particles (Figure 5.4 a inset), with some of the particles approximating to icosahedral symmetry with a pore centred on each pentagonal face and a few others with button-like distribution and different pore sizes. Confocal mapping was conducted on the macroporous BNPs, which allowed direct measurement of single particle emission at about 555 nm after being excited at 532 nm (Figure 5.4 a and b). This newly revealed emission spectrum might indicate the denaturation of as-received BSA and the formation of new chromophores. To confirm this, circular dichroism (CD) was used which clearly established that the

BSA has undergone significant structural changes during processing in the VFD. The BSA contains predominantly α-helices as secondary structural elements, giving two negative bands at 208 and 220 nm in the CD spectra (Figure 5.4 d and S12). The conformation of the BNPs is thought to differ from the native conformation of BSA in aqueous solutions. Post VFD processing, BNPs form an emulsion, with two major peaks around 207 and 235 nm in the CD spectra, which might indicate denaturation of the α-helical structure into *β* sheets, as reported by Zelasko-Leon *et al*. for BSA modified gold nanorods.[37] Hydrogen bonding interactions can bring together antiparallel peptide strands in the neighbouring BSA molecules, which produce *β* sheet structures, thereby perturbing the CD spectra. These results highlight a modification of BSA secondary structure of α-helices during the processing in the VFD, which is in agreement with the re-organisation of proteins to form new chromophores.[38,39] Pores on the surface of the submicron spheroidal particles were typically randomly arranged (Figure 5.4 c). The average pore sizes were around 70 to 100 nm based on AFM, which is consistent with SEM. The N_2 adsorption isotherm confirmed that the porous BNPs exhibited characteristics of a type II curve for macroporous structures. The specific surface area (S_{BET}) of the macroporous BNPs prepared in VFD was 28 m^2/g, which was very similar to the ones prepared from bench-top vortexing of 25 m^2/g but significantly different from the curves of as received BSA. This is consistent with the absence of pores connecting the outer and inner surfaces of the hollow particles.[35]

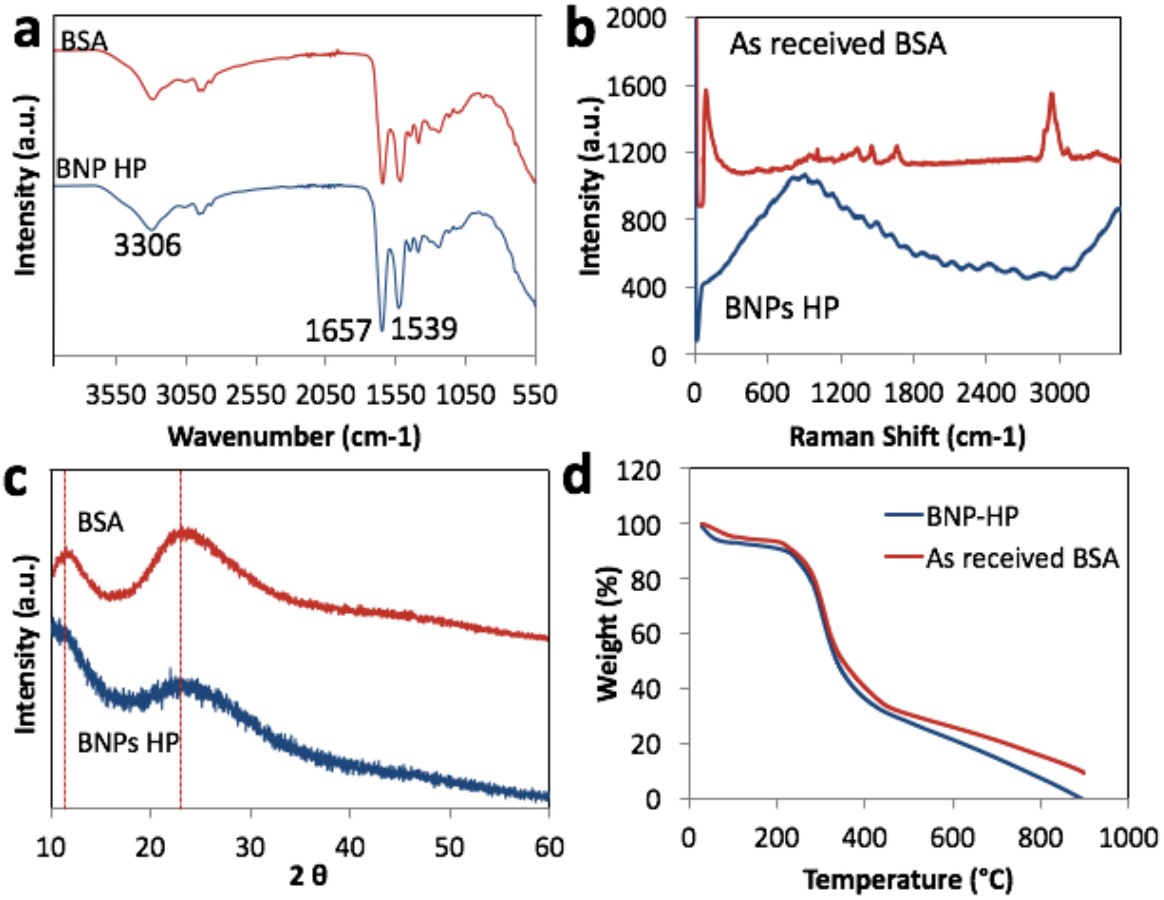

Figure 5.5 *Characterisations of macroporous BNPs prepared in a VFD using (a) FTIR, (b) Raman, (c) XRD, and (d) STA.*

FTIR absorption peaks in the macroporous BNPs at 3306 cm^{-1}, 1657 cm^{-1} and 1539 cm^{-1}, correspond to O-H stretching, amide I band (mainly C=O stretching vibrations) and amide II band (mainly N-H and C-N), respectively.[40] The absence of a Raman signature could arise from sample fluorescence under laser irradiation at 532 nm (Figure 5.5 b). XRD highlights the amorphous nature of both as received BSA and macroporous BNPs, with slight difference at 2θ = 12° (Figure 5.5 c). Stable amorphous forms are advantageous in having higher rates of dissolution which is expected to enhance drug release and subsequent absorption and bioavailability.[41] STA analysis of both macroporous BNPs and as received BSA showed no significant difference (Figure 5.5 d). Both samples started to degrade at about 250 °C and this was followed by an abrupt weight loss at about 300 °C, which could be due to the loss of small molecules such as carbon dioxide and ammonia.[42] A slight weight loss difference between the two was observed from 350 to 550 °C and the difference slowly became larger beyond 500 °C. This could be due to the reduced crystalline nature[42] of the macroporous BNPs relative to as received BSA, as indicated in the XRD.

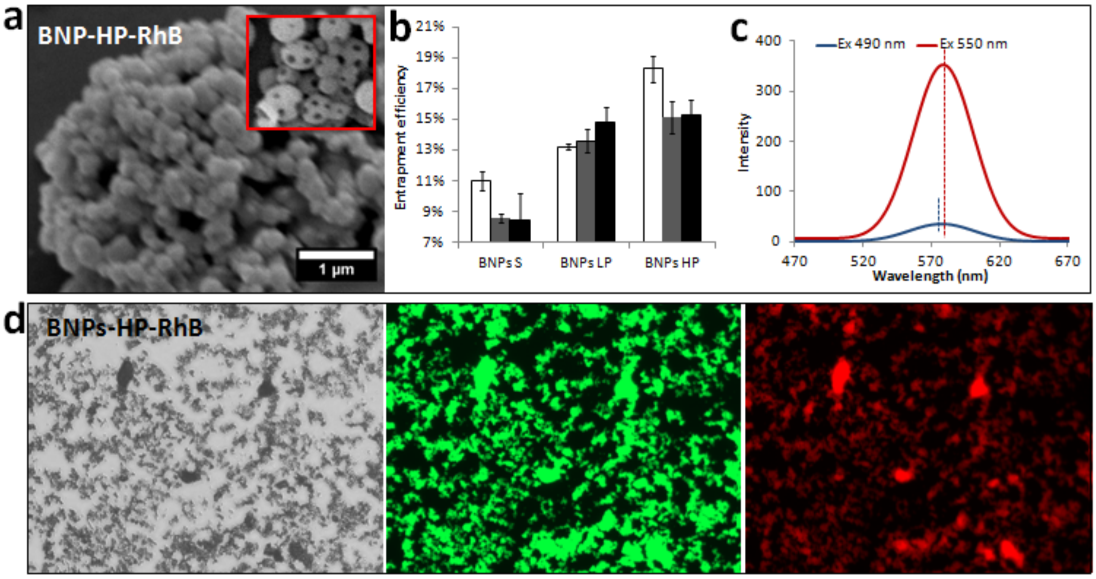

Figure 5.6 *(a) Macroporous BNPs pre- (inset) and post- loaded with RhB. (b) Entrapment efficiency of RhB by BNPs with different morphologies at time points of 4 h (white), 8 h (grey) and 24 h (black). (c) Fluorescence spectroscopy of RhB loaded macroporous BNPs. (d) Fluorescence microscopy of macroporous BNPs-RhB under Invitrogen^{TM} EVOS^{TM} light cubes for bright field, GFP (470/22 Ex; 510/42 Em) and RFP (531/40 Ex; 593/40 Em), respectively.*

The macroporous BNPs had zeta potential values of -32.1 at pH 7.66, which is significantly higher than those previously reported by Yu *et al* of -15.4.[15] Typically, an electro-stable suspension has a net ζ potential value of above 30 mV.[40] The results suggest that the BNPs remain stable under physiological conditions. The potential difference demonstrated that the positively charged RhB could have an interaction with the negatively charged BSA, and promote the attachment of RhB to the BNPs. Therefore, the drug loading capacity and encapsulation efficiency of BNPs were also evaluated. The concentration of RhB decreased gradually over time because of the adsorption of RhB by the BNPs, with the amount of RhB adsorbed varying with different morphologies. BNP-HPs exhibited the highest loading capacity, with BNP-LP having intermediate capacity and BNP-Ss the lowest, and this applied to all time-dependent studies (Figure 5.6 b). This result confirmed that the BNPs with a smooth surface had a lower tendency to adsorb large molecules than did the macroporous BNPs. This is consistent with the work of Nandiyanto *et al*.,[35] reporting high adsorption efficiency of RhB by silica particles with a porous structure. RhB is 1.44 nm × 1.09 nm × 0.64 nm and can penetrate a pore diameter > 1.5 nm.[43] In the present study, in the absence of pores, adsorption will occur only on the outer surface of the particles, and thus lower amounts of RhB are loaded. Fluorescence spectroscopy afforded characteristics peaks of RhB (ex. 550 nm) and BNPs (ex. 490 nm), with significant enhancement of fluorescence intensity for macroporous BNP-RhB compared to BNPs with other surface morphologies (Figure 5.6 c and S16). The morphology and structure of RhB-loaded macroporous BNPs with 'filled pores' also showed significant changes compared with those of non-loaded macroporous BNPs (Figure 5.6 a). Fluorescence microscopy established an increase in signal intensity at this wavelength for RhB-loaded macroporous BNPs. Smaller differences were observed with other BNP morphologies after the loading process with RhB (Figure S17). After an intensive washing process, 84% of RhB was released from BNP-S-RhB, 51% from BNP-LP-RhB and 62% from BNP-HP-RhB. Further release of RhB conducted at 37°C for 72 h after an intensive washing step was similar for all three shapes (Figure S18).

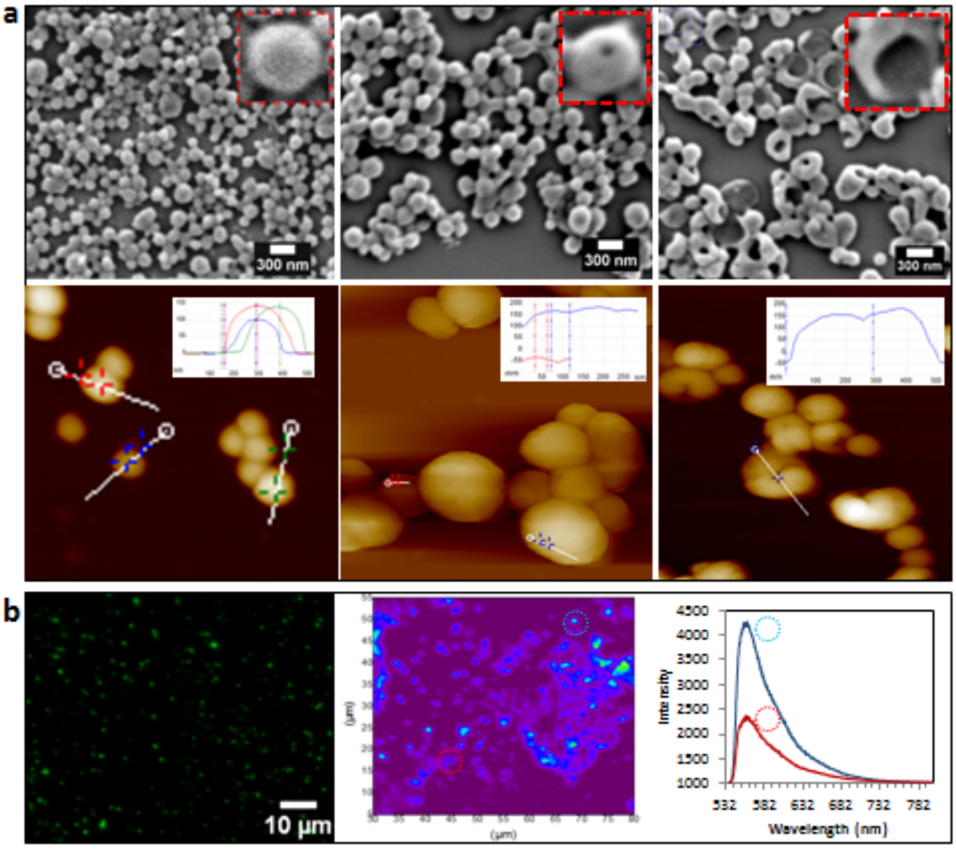

Figure 5.7 *(a) Characterization of BNP/CPC using SEM, revealing smooth surfaces, less porous surface and pocket-like morphology, from left to right. (b) Characterization of nano-pocket BNP/CPC using fluorescence microscopy, confocal mapping and corresponding measurements on single particle emission after excitation at 532 nm.*

Finally, we explored the applicability of this process for other proteins. Replacing BSA by gelatin also resulted in porous nanoparticles under the same processing conditions used for fabricating BNP-HP (Figure S24). We note that controlling the size of BNPs has been intensively studied over the last decade but only with respect to varying the concentrations of BSA, ethanol and the cross-linking agent.[12] We now find that the size of the BNP particles can be readily reduced by incorporating another type of fluorescent protein named C-phycocyanin (C-PC) (ex. 620 nm, em. 650 nm) into the processing of BSA. The α (162 residues) and β (172 residues) subunits of C-PC form a heterodimer αβ monomer, which contains three phycocyanobilin, the chromophore, with one in the α subunits and two in the β subunits,[44] and three of the monomers can oligomerise to form disc-shaped trimers $(\alpha\beta)_3$. Figure 5.7 a illustrates the shape and size of the newly obtained BNPs (as BNP/CPC) using the same experimental conditions for BSA alone, as in Figure 5.3, with the only difference being adding C-PC. A distinct difference in the composite protein particle is a dramatic reduction in size from *ca*. 358 nm to *ca*. 150 nm in diameter. In addition, instead of forming pores on the surface, pocket-like structures were produced (Figure 5.7 a). Further characterization of single pocket-like structure established that BNP/CPC had the same excitation and emission spectrum as the BNPs, with single discernible emission at 555 nm when excited at 532 nm (Figure 5.7 b). BNP/CPC showed no signature fluorescence of C-PC after excitation at 620 nm, which could arise from distortion of the 3D structures during the de-solvation process. Overall, this process for generating protein-based nanostructures has potential for fabricating protein composites for a variety of different proteins and combinations thereof.

5.5 Conclusion

Spheroidal macroporous BSA-based nanoparticles with controllable particle diameter are effectively prepared using the relatively new VFD thin film microfluidic processing platform, in the confined mode of operation. Rapidly rotating glass tubes of different length established that using a longer tube facilitates scaling up of the process by 8 to 12 times relative to the standard VFD. Importantly the macroporous particles can be fabricated with a narrow size distribution *ca*. 608 nm in diameter with high homogeneity. We have also established that the process is effective for gelatin in generating porous particles, and that introducing another protein with BSA, phycocyanin, allows control of the particles morphology, affording smaller particles and particles with nano-sized pockets. This processing methodology is therefore likely to be applicable to other proteins and mixtures of proteins. Future studies will focus on controlling the release rate by further controlling the pore sizes, along with testing other proteins to be incorporated into the composite material.

5.6 Acknowledgements

The authors gratefully acknowledge financial support from the Australia Research Council (DP170100452) and the Government of South Australia, and the Australian Microscopy and Microanalysis Research Facility (AMMRF), the Australian National Fabrication Facility (ANFF) and the Flinders Microscope for access to characterization facilities.

5.7 Reference

(1) Deshapriya, I. K.; Stromer, B. S.; Pattammattel, A.; Kim, C. S.; Iglesias-Bartolome, R.; Gonzalez-Fajardo, L.; Patel, V.; Gutkind, J. S.; Lu, X.; Kumar, C. V. Fluorescent, Bioactive Protein Nanoparticles (Prodots) for Rapid, Improved Cellular Uptake. *Bioconjugate Chem.* **2015,** *26*, 396-404.

(2) Kim, T. H.; Jiang, H. H.; Youn, Y. S.; Park, C. W.; Tak, K. K.; Lee, S.; Kim, H.; Jon, S.; Chen, X.; Lee, K. C. Preparation and Characterization of Water-soluble Albumin-bound Curcumin Nanoparticles with Improved Antitumor Activity. *Int. J. Pharm.* **2011,** *403*, 285-291.

(3) Bronze-Uhle, E. S.; Costa, B. C.; Ximenes, V. F.; Lisboa-Filho, P. N. Synthetic Nanoparticles of Bovine Serum Albumin with Entrapped Salicylic Acid. *Nanotechnol. Sci. Appl.* **2017,** *10*, 11-21.

(4) Elzoghby, A. O.; Samy, W. M.; Elgindy, N. A. Albumin-based Nanoparticles as Potential Controlled Release Drug Delivery Systems. *J. Control. Release* **2012,** *157*, 168-182.

(5) Weber, C.; Coester, C.; Kreuter, J.; Langer, K. Desolvation Process and Surface Characterisation of Protein Nanoparticles. *Int. J. Pharm.* **2000,** *194*, 91-102.

(6) Weber, C.; Kreuter, J.; Langer, K. Desolvation Process and Surface Characteristics of HSA-nanoparticles. *Int. J. Pharm.* **2000,** *196*, 197-200.

(7) Costantino, H. R.; Firouzabadian, L.; Hogeland, K.; Wu, C.; Beganski, C.; Carrasquillo, K. G.; Córdova, M.; Griebenow, K.; Zale, S. E.; Tracy, M. A. Protein Spray-Freeze Drying. Effect of Atomization Conditions on Particle Size and Stability. *Pharm. Res.* **2000,** *17*, 1374-1382.

(8) Muhrer, G.; Mazzotti, M. Precipitation of Lysozyme Nanoparticles from Dimethyl Sulfoxide Using Carbon Dioxide as Antisolvent. *Biotechnol. Progr.* **2003,** *19*, 549-556.

(9) Lee, S. H.; Heng, D.; Ng, W. K.; Chan, H. K.; Tan, R. B. H. Nano Spray Drying: A Novel Method for Preparing Protein Nanoparticles for Protein Therapy. *Int. J. Pharm.* **2011,** *403*, 192-200.

(10) Aimi, M.; Nemori, R.; Miyashita, Y.; Yokoyama, H. Enzymatically Crosslinked Protein Nanoparticles. Google Patents, 2007, US20090004278A1.

(11) Langer, K.; Balthasar, S.; Vogel, V.; Dinauer, N.; von Briesen, H.; Schubert, D. Optimization of the Preparation Process for Human Serum Albumin (HSA)

Nanoparticles. *Int. J. Pharm.* **2003,** *257*, 169-180.

(12) Yang, Q.; Ye, Z.; Zhong, M.; Chen, B.; Chen, J.; Zeng, R.; Wei, L.; Li, H. W.; Xiao, L. Self-Assembled Fluorescent Bovine Serum Albumin Nanoprobes for Ratiometric pH Measurement inside Living Cells. *ACS Appl. Mater. Inter.* **2016,** *8*, 9629-9634.

(13) Abbasi, S.; Paul, A.; Shao, W.; Prakash, S. Cationic Albumin Nanoparticles for Enhanced Drug Delivery to Treat Breast Cancer: Preparation and *In Vitro* Assessment. *J. Drug Deliv.* **2012,** *2012*, 1-8.

(14) Jithan, A. V.; Madhavi, K.; Madhavi, M.; Prabhakar, K. Preparation and Characterization of Albumin Nanoparticles Encapsulating Curcumin Intended for the Treatment of Breast Cancer. *Int. J. Pharm. Invest.* **2011,** *1*, 119-125.

(15) Yu, Z.; Yu, M.; Zhang, Z.; Hong, G.; Xiong, Q. Bovine Serum Albumin Nanoparticles as Controlled Release Carrier for Local Drug Delivery to the Inner ear. *Nanoscale Res. Letters* **2014,** *9*, 343-343.

(16) Dreis, S.; Rothweiler, F.; Michaelis, M.; Cinatl, J.; Kreuter, J.; Langer, K. Preparation, Characterisation and Maintenance of Drug Efficacy of Doxorubicin-loaded Human Serum Albumin (HSA) Nanoparticles. *Int. J. Pharm.* **2007,** *341*, 207-214.

(17) Mistry, P.; Mohapatra, S.; Dash, A. Effect of High-pressure Homogenization and Stabilizers on the Physicochemical Properties of Curcumin-loaded Glycerol Monooleate/chitosan Nanostructures. *Nanomedicine* **2012,** *7*, 1863-1876.

(18) Zdravkov, B. D.; Čermák, J. J.; Šefara, M.; Janků, J. Pore Classification in the Characterization of Porous Materials: A perspective. *Cent. Eur. J. Chem.* **2007,** *5*, 385-395.

(19) Keita, K.; Keita, I.; Shozo, I.; Takahiro, N. Shape Control of Self-organized Porous Silica Submicron Particles and their Strength Evaluation. *JPN. J. Appl. Phys.* **2016,** *55*, 06GP121-06GP126.

(20) Okubo, M.; Takekoh, R.; Suzuki, A. Preparation of Micron-sized, Monodisperse Poly(methyl methacrylate)/polystyrene Composite Particles having a Large Number of Dents on their Surfaces by Seeded Dispersion Polymerization in the Presence of Decalin. *Colloid Polym. Sci.,* **2002,** *280*, 1057-1061.

(21) Griffiths, P. C.; Wellappili, C.; Hemsley, A. R.; Stephens, R. Ultra-porous Hollow Particles. *Colloid Polym. Sci.* **2004,** *282*, 1155-1159.

(22) Kao, C. Y.; Lo, T. C.; Lee, W. C. Influence of Polyvinylpyrrolidone on the Hydrophobic Properties of Partially Porous Poly(styrene–divinylbenzene) Particles for Biological Applications. *J. Appl. Polym. Sci.* **2003,** *87*, 1818-1824.

(23) Unsal, E.; Irmak, T.; Durusoy, E.; Tuncel, M.; Tuncel, A. Monodisperse Porous Polymer Particles with Polyionic Ligands for Ion Exchange Separation of Proteins. *Anal. Chim. Acta* **2006,** *570*, 240-248.

(24) Iskandar, F.; Nandiyanto, A. B. D.; Widiyastuti, W.; Young, L. S.; Okuyama, K.; Gradon, L. Production of Morphology-controllable Porous Hyaluronic Acid Particles using a Spray-drying Method. *Acta Biomater.* **2009,** *5*, 1027-1034.

(25) Pitt, J. A.; Kozal, J. S.; Jayasundara, N.; Massarsky, A.; Trevisan, R.; Geitner,

N.; Wiesner, M.; Levin, E. D.; Di Giulio, R. T. Uptake, Tissue Distribution, and Toxicity of Polystyrene Nanoparticles in Developing Zebrafish (*Danio rerio*). *Aquat. Toxicol.* **2018,** *194*, 185-194.

(26) Vimalanathan, K.; Gascooke, J. R.; Suarez-Martinez, I.; Marks, N. A.; Kumari, H.; Garvey, C. J.; Atwood, J. L.; Lawrance, W. D.; Raston, C. L. Fluid Dynamic Lateral Slicing of High Tensile Strength Carbon Nanotubes. *Sci. Rep.* **2016,** *6*, 1-7.

(27) Luo, X.; Al-Antaki, A. H. M.; Vimalanathan, K.; Moffatt, J.; Zheng, K.; Zou, Y.; Zou, J.; Duan, X.; Lamb, R. N.; Wang, S.; Li, Q.; Zhang, W.; Raston, C. L. Laser Irradiated Vortex Fluidic Mediated Synthesis of Luminescent Carbon Nanodots under Continuous Flow. *React. Chem. Eng.* **2018**, *3*, 164-170.

(28) Luo, X.; Smith, P.; Raston, C. L.; Zhang, W. Vortex Fluidic Device-Intensified Aqueous Two Phase Extraction of C-Phycocyanin from *Spirulina maxima*. *ACS Sustain. Chem. Eng.* **2016,** *4*, 3905-3911.

(29) Tong, C. L.; Boulos, R. A.; Yu, C.; Iyer, K. S.; Raston, C. L. Continuous Flow Tuning of Ordered Mesoporous Silica under Ambient Conditions. *RSC Adv.* **2013,** *3*, 18767-18770.

(30) Britton, J.; Meneghini, L. M.; Raston, C. L.; Weiss, G. A. Accelerating Enzymatic Catalysis Using Vortex Fluidics. *Angew. Chem. Int. Edit.* **2016,** *55*, 11387-11391.

(31) Luo, X.; Al-Antaki, A. H. M.; Pye, S.; Meech, R.; Zhang, W.; Raston, C. L. High-shear-imparted Tunable Fluorescence in Polyethylenimines. *ChemPhotoChem*, **2018**, *2*, 343-348.

(32) Chen, X.; Dobson, J. F.; Raston, C. L. Vortex Fluidic Exfoliation of Graphite and Boron Nitride. *Chem. Comm.* **2012,** *48*, 3703-3705.

(33) Yuan, T. Z.; Ormonde, C. F. G.; Kudlacek, S. T.; Kunche, S.; Smith, J. N.; Brown, W. A.; Pugliese, K. M.; Olsen, T. J.; Iftikhar, M.; Raston, C. L.; Weiss, G. A. Shear-Stress-Mediated Refolding of Proteins from Aggregates and Inclusion Bodies. *ChemBioChem* **2015,** *16*, 393-396.

(34) Patil, G.; Chethana, S.; Sridevi, A. S.; Raghavarao, K. S. M. S. Method to Obtain C-phycocyanin of High Purity. *J. Chromatogr. A* **2006,** *1127*, 76-81.

(35) Nandiyanto, A. B. D.; Akane, Y.; Ogi, T.; Okuyama, K. Mesopore-Free Hollow Silica Particles with Controllable Diameter and Shell Thickness via Additive-Free Synthesis. *Langmuir* **2012,** *28*, 8616-8624.

(36) Tsien, R. Y. The Green Fluorescent Protein. *Annu. Rev. Biochem.* **1998,** *67*, 509-544.

(37) Zelasko-Leon, D. C.; Fuentes, C. M.; Messersmith, P. B. MUC1-Targeted Cancer Cell Photothermal Ablation Using Bioinspired Gold Nanorods. *PLOS ONE* **2015,** *10*, 1-20.

(38) Hosseinkhani, S.; Ranjbar, B.; Naderi-Manesh, H.; Nemat-Gorgani, M. Chemical Modification of Glucose Oxidase: Possible Formation of Molten Globule-like Intermediate Structure. *FEBS Lett.* **2004,** *561*, 213-216.

(39) Heim, R.; Tsien, R. Y. Engineering Green Fluorescent Protein for Improved Brightness, Longer Wavelengths and Fluorescence Resonance Energy Transfer.

Curr. Biol. **1996,** *6*, 178-182.

(40) Lam, P. L.; Kok, S. H. L.; Gambari, R.; Kok, T. W.; Leung, H. Y.; Choi, K. L.; Wong, C. S.; Hau, D. K. P.; Wong, W. Y.; Lam, K. H.; Bian, Z. X.; Lee, K. K. H.; Chui, C. H. Evaluation of Berberine/bovine Serum Albumin Nanoparticles for Liver Fibrosis Therapy. *Green Chem.* **2015,** *17*, 1640-1646.

(41) Boateng, J. S.; Areago, D. Composite Sodium Alginate and Chitosan Based Wafers for Buccal Delivery of Macromolecules. *J. Anal. Pharm. Chem.* **2014,** *1*, 1-7.

(42) Singh, P.; Singh, H.; Castro-Aceituno, V.; Ahn, S.; Kim, Y. J.; Yang, D. C. Bovine Serum Albumin as a Nanocarrier for the Efficient Delivery of Ginsenoside Compound K: Preparation, Physicochemical Characterizations and *in vitro* Biological Studies. *RSC Adv.* **2017,** *7*, 15397-15407.

(43) Nandiyanto, A. B. D.; Kim, S.-G.; Iskandar, F.; Okuyama, K. Synthesis of Spherical Mesoporous Silica Nanoparticles with Nanometer-size Controllable pores and Outer Diameters. *Micropor. Mesopor. Mat.* **2009,** *120*, 447-453.

(44) Romay, C.; Gonzalez, R.; Ledon, N.; Remirez, D.; Rimbau, V. C-phycocyanin: a Biliprotein with Antioxidant, Anti-inflammatory and Neuroprotective effects. *Curr. Protein Pept. Sci.* **2003,** *4*, 207-216.

Appendix: the first page of published article and the first page of the published supplementary information

Downloaded via FLINDERS UNIV on September 9, 2018 at 08:32:12 (UTC).
See https://pubs.acs.org/sharingguidelines for options on how to legitimately share published articles.

ACS APPLIED MATERIALS & INTERFACES
Research Article
Cite This: ACS Appl. Mater. Interfaces 2018, 10, 27224−27232
www.acsami.org

Vortex Fluidic Mediated Synthesis of Macroporous Bovine Serum Albumin-Based Microspheres

Xuan Luo,[†,‡] Ahmed Hussein Mohammed Al-Antaki,[†] David P. Harvey,[†] Yinlan Ruan,[§] Shan He,[‖] Wei Zhang,[*,‡] and Colin L. Raston[*,†]

[†]Flinders Institute for NanoScale Science and Technology (CNST), College of Science and Engineering, and [‡]Flinders Centre for Marine Bioproducts Development, College of Medicine and Public Health, Flinders University, Adelaide, South Australia 5042, Australia

[§]ARC Centre of Excellence for Nanoscale BioPhotonics, Institute of Photonics and Advanced Sensing, Adelaide University, Adelaide, South Australia 5005, Australia

[‖]Department of Food Science and Engineering, School of Chemistry Chemical Engineering, Guangzhou University, Guangzhou 510006, China

Supporting Information

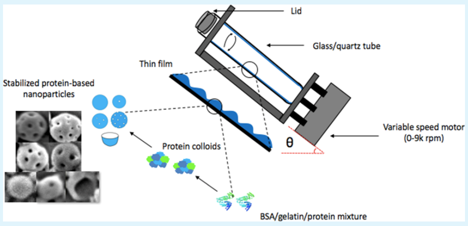

ABSTRACT: Macroporous bovine serum albumin (BSA) nanoparticles with controllable diameter were readily fabricated in a rapidly rotating angled glass tube in a vortex fluidic device (VFD). Systematically varying the rotational speed and the ratio of BSA, ethanol, and glutaraldehyde led to conditions for generating ca. 600 nm diameter macroporous particles that have intrinsic fluorescence emission at 520 nm when excited at 490 nm. The presence of the macropores increased the absorption efficiency of rhodamine B with potential applications for drug delivery purpose, compared with BSA nanoparticles having surfaces devoid of pores. Further control over the size of BSA nanoparticles occurred in the presence of C-phycocyanin protein during the VFD processing, along with control of their shape, from spheres to pockets, as established in exploring the parameter space of the microfluidic device.

KEYWORDS: *bovine serum albumin, macroporous, nanoparticle, fluorescence, microfluidics*

1. INTRODUCTION

Nanoparticles derived from bovine serum albumin (BSA nanoparticles or BNPs) are biodegradable, biocompatible,[1] nontoxic, and nonimmunogenic[2] and have advantages over synthetic polymers in medical applications such as drug delivery.[3] Given the defined primary structure of protein and its high content of charged amino acid moieties such as lysine,[4] BNPs offer scope for surface modification in terms of covalent drug attachment[5,6] and electrostatic adsorption of positively charged or negatively charged molecules either internally and/or on their surfaces.[4] Protein-based NPs can be prepared by freeze-drying,[7] supercritical fluid processing,[8] spray-drying,[9] de-solvation,[5] and enzymatic cross-linking.[10] De-solvation is considered a robust reproducible method,[4] consisting of dropwise addition of ethanol to an aqueous solution of albumin followed by continuous stirring until it becomes turbid. The turbidity arises from the diminished water solubility of denaturated BSA in ethanol, with disruption of the protein tertiary structures.[11,12] BNPs are generated by fixation with glutaraldehyde where the amino residues in lysine and arginine residues in guanidine side chains of albumin are cross-linked by condensation with the aldehyde.[4]

Biocompatible BNPs have potential in drug delivery applications with a capacity for incorporating drugs within the particle matrix for their enhanced endocytic uptake.[13,14] The use of nanoscaled materials for drug delivery and diagnostics is at the forefront of medicine, with the encapsulation of drugs into NPs significantly improving their release profile in cells or tissues.[3] For instance, BNPs have been used for local delivery of rhodamine B (RhB) into the inner ear with potential applications in the field of treating inner ear disorders.[15] However, most of the cross-linking processes applied in the desolvation of BNPs have long processing times. Intrinsically, fluorescent BNPs with emission at 535 nm after being excited at 495 nm[12] have been reported but their preparation requires 18 h processing time. In other studies, the cross-linking process under batch stirring of the suspension takes 24 h or more.[14−16] As to drug loading experiments, doxorubicin has been separately loaded over an additional 2 h of stirring.[16] Even though this process can be facilitated by

Received: June 5, 2018
Accepted: July 20, 2018
Published: July 20, 2018

ACS Publications © 2018 American Chemical Society

DOI: 10.1021/acsami.8b09316
ACS Appl. Mater. Interfaces 2018, 10, 27224−27232

Supporting information

Vortex fluidic mediated synthesis of macroporous bovine serum albumin-based microspheres

Xuan Luo[1,2], Ahmed Hussein Mohammed Al-Antaki[1], David P. Harvey[1], Yinlan Ruan[3], Shan He[4], Wei Zhang[2], Colin L. Raston[1*]*

[1]Flinders Institute for NanoScale Science and Technology (CNST), College of Science and Engineering, Flinders University, Adelaide, SA 5042; [2]Flinders Centre for Marine Bioproducts Development, College of Medicine and Public Health, Flinders University, Adelaide, SA 5042; [3]ARC Centre of Excellence for Nanoscale BioPhotonics, Institute of Photonics and Advanced Sensing, Adelaide University, Adelaide, South Australia 5005, Australia; [4]Department of Food Science and Engineering, School of Chemistry Chemical Engineering, Guangzhou University, 510006 (China)

Corresponding Authors

*Z. Wei. Tel.: +61 8 72218557. Fax: +61 8 72218555. E-mail: wei.zhang@flinders.edu.au

*R. Colin. Tel.: +61 8 82017958. Fax: +61 8 8201290. E-mail: colin.raston@flinders.edu.au

6 VORTEX FLUIDIC DEVICE-INTENSIFIED AQUEOUS TWO PHASE EXTRACTION OF C-PHYCOCYANIN FROM *SPIRULINA MAXIMA*

Most protein purification methods involve the use of chromatographic techniques and such methods can suffer from high cost, low efficiency, low recovery rates and difficulties in scaling up. The use of aqueous two phase systems (ATPS) has attracted considerable attention in attempting to overcome some of these disadvantages. However, one of the obstacles to the application of ATPS is slow demixing rates for the phase separation. Apart from gravity and centrifugation-facilitated phase separation, demixing efficiency can be improved using external electric, magnetic, acoustic and microwave fields. However, a heating free, energy efficient and technically simplified method for protein recovery from ATPS is required. To this end, we further explored the biomedical application of VFD on protein separation. This chapter is an extension in the use of shear stress to intensify ATPS for C-pphycocyanin (C-PC) purification. We show that efficient purification of C-PC derived from microalgae *Spirulina maxima* by VFD-intensified ATPS as an example with spontaneous and instant demixing and phase separation post-VFD-ATPS extraction, demonstrated the potential of using VFD as a new phase demixing technology in protein purification. This novel process results in a 1.18 fold increase in purity of C-PC with a 22% increase in yield compared to conventional ATPS methods. Multi-stage counter current distribution (CCD) using VFD-ATPS followed by a removal of PEG and salt led to a 6 fold increase in C-PC purity compared to crude extract, from 0.5 to 3.0. Overall, this work establishes the utility of using a novel VFD-intensified ATPS process for protein purification and its potential as an effective new tool for rapid processing of biologically active and intact proteins.

This study was orally presented at the BioProcessing Network Conference in Adelaide on October 2017 and 1st Australia New Zealand Marine Biotechnology Society Symposium in Adelaide on April 2016, and published in ***ACS Sustainable Chemistry & Engineering***, Year 2016, Vol. 4, Issue 7, Pages 3905-3911. The first page of the publication is attached in Appendix 6.1.

Author contributions: **XL** performed all the VFD and characterization experiments; wrote all the primary content. **PS** guided some of the research direction. **WZ** and **CR** supervised and coordinated the project and helped on the research directions and plan, and the final revision of the manuscript. All of the co-authors assisted with the revision of the manuscript before and during the publication process.

Vortex Fluidic Device-Intensified Aqueous Two Phase Extraction of C-Phycocyanin from *Spirulina maxima*

Xuan Luo[1,2], Paul Smith[4], Colin L. Raston[3*] and Wei Zhang[1,2*]

Graphical abstract

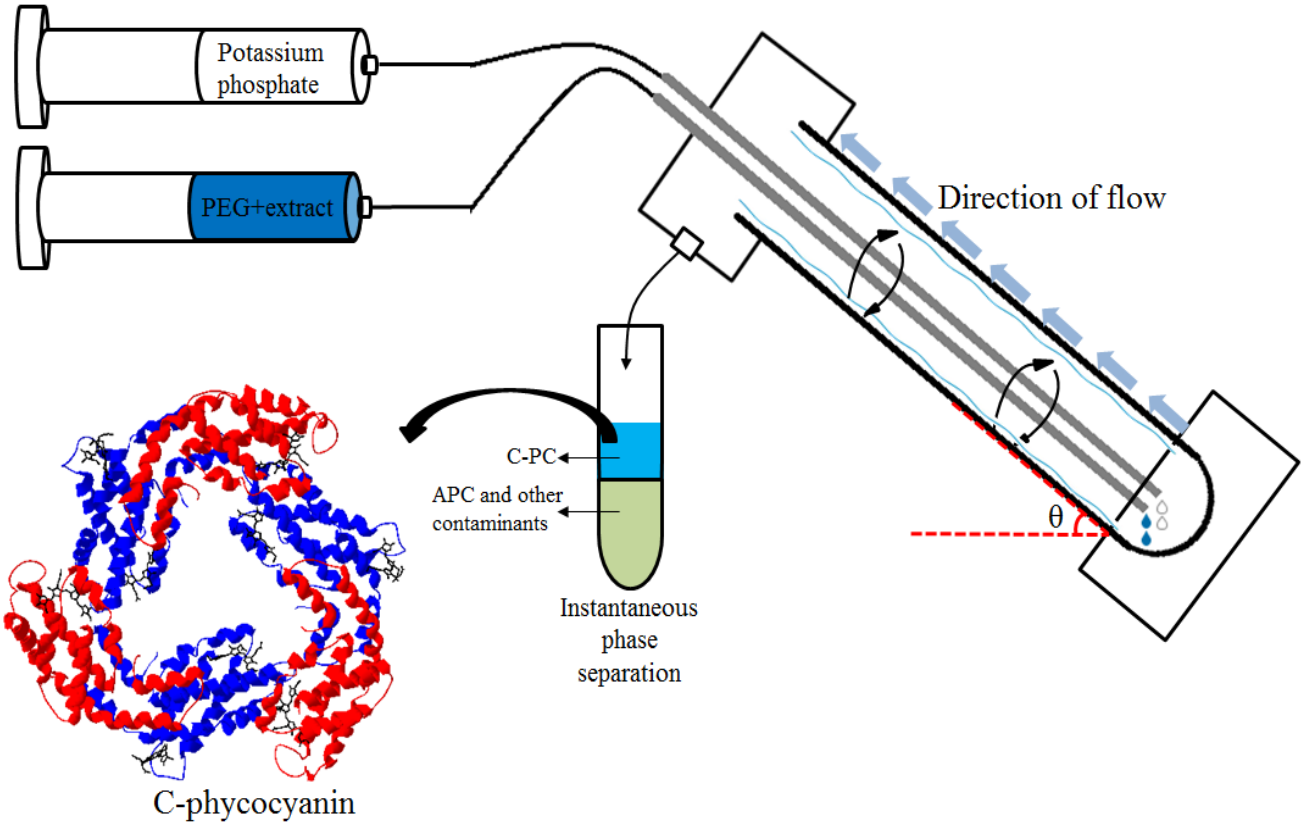

[1]Centre for Marine Bioproducts Development, Flinders University, Adelaide, South Australia 5042, Australia

[2]Department of Medical Biotechnology, School of Medicine, Flinders University, Adelaide, South Australia 5042, Australia

[3]Centre for NanoScale Science and Technology, School of Chemistry and Physical Sciences, Flinders University, Adelaide, South Australia 5042, Australia

[4]The Australian Wine Research Institute, Hartley Grove, Urrbrae, South Australia 5064, Australia

6.1 Abstract

A vortex fluidic device (VFD) is effective for downstream processing of C-phycocyanin (C-PC) from blue-green microalga *Spirulina maxima* using an aqueous two phase system (ATPS): polyethylene glycol (PEG) and aqueous potassium phosphate. The VFD-intensified ATPS continuous flow processing (VFD-ATPS) has spontaneous phase separation of the liquid exiting the 20 mm diameter tube inclined at 45° and rotating at 6550 rpm, for a 0.2 mL/min flow rate. This processing results in at least a 9.3-fold increase in phase demixing efficiency, 1.18-fold increase in C-PC purity, and 22% increase in yield compared to conventional ATPS methods. Multistage counter current distribution (CCD) using VFD-ATPS followed by removal of PEG and salt increased C-PC purity by 6-fold compared to the crude extract, with triple TOF mass spectrometry showing more than 95% sequence coverage for both subunits. This work establishes the utility of using VFD-intensified ATPS processing for protein purification and its potential as an effective new tool for rapid processing of biologically active and intact proteins.

Keywords: Vortex fluidics device, C-Phycocyanin, microalgae, aqueous two phase system, phase demixing

6.2 Introduction

C-Phycocyanin (C-PC) is a stable fluorescent pigment protein with promising bioactivities.[1] Several methods have been developed for the extraction and purification of this phycobiliprotein.[2-8] However, most of them involve the use of chromatographic techniques,[9] and such methods can suffer from high cost, low efficiency, low recovery rates, and difficulties in scaling up.[10] In recent years, the use of aqueous two phase systems (ATPS) has attracted considerable attention in attempting to overcome some of these disadvantages. Employing differential partitioning of ATPS results in C-PC being preferentially taken up in the polymer-rich top phase, as identified by a major absorption peak maximum at 620 nm, whereas other contaminants partition to the salt-rich bottom phase.[10] One of the main contaminant proteins is allophycocyanin (APC), which also belongs to the phycobiliprotein family, having an absorption maximum at 650 nm. The fractionation of these two biliproteins is based on the higher affinity of C-PC to the PEG-rich phase than that of APC.[11]

Most ATPS-related research on C-PC purification focuses on process optimization involving varying the pH, volume ratio, and molecular weight of PEG,[12] with limited research exploring the demixing efficiency. ATPS involves two unit operations, namely, mixing components and phase separation through droplet−droplet collision and coalescence.[13] Thorough mixing can be achieved by stirring for half an hour to an hour for a 10−20 g system[12,14] or by vortex mixing.[8,15] The most common methods for phase separation of C-PC are gravity and centrifugation.[16] One of the obstacles to the application of ATPS is the slow demixing rate for the phase separation due to small difference in the densities between the two phases, high viscosity of individual phases, low interfacial tension, and longer time required for droplet−droplet collisions.[13] Although there is little data on the effect of gravity-associated phase separation for C-PC, overnight phase separation is possible for this protein.[17] Apart from high speed centrifugation, demixing efficiency can be improved using external electric, magnetic, acoustic, and microwave fields.[18,19] However, a heating free, energy efficient, and technically simplified method for protein recovery from ATPS is required. To this end, we have explored the use of the vortex fluidic device (VFD) to intensify ATPS for C-PC purification, and the results are reported herein. The VFD is a recently developed microfluidic processing platform operating under either the confined mode, as a batch type process for finite volumes, typically 1−2 mL, or the continuous flow mode where scalability of the processing is addressed.[20] We note that the VFD is effective in room temperature transesterification of vegetable oil with spontaneous separation of three phases post-processing.[20] Thus, the mechanoenergy induced in the dynamic thins films in the VFD and the intense micromixing of two otherwise immiscible liquids are likely to facilitate the processing of C-PC.

In this study, two immiscible fluids are intensively mixed in a rapidly rotating tube in a VFD (Figure 6.1 a), under continuous flow conditions. A glass tube with an internal diameter of 17.7 mm was used, for convenience as a borosilicate nuclear magnetic resonance (NMR) tube. It was inclined at 45° relative to the horizontal position, which corresponds to the optimum angle for many applications of the VFD with jet feeds used to deliver liquids to the hemispherical bottom of the tube.[20-22] Different from the Y-shape microchannel-processing platform introduced by Šalić *et al*.[23] for polyphenol extraction using ATPS, processing in the VFD tracks toward turbulent flow with high Reynolds number >2000, which further overcomes the normal mass transfer boundary and diffusion control in a liquid−liquid processing. The aim of the present study is to establish an efficient, simple, and viable downstream process to efficiently recover C-PC from the dry *Spirulina maxima* powder, using a PEG_{4000}/potassium phosphate system.[12,16] Effects of flow rate and rotational speed on the partition behavior were studied and optimized, and compared to conventional batch processing. The separated phases post-VFD processing were tested for the presence of C-PC and APC.

6.3 Materials and methods

PEG with molecular weight of 4000 (PEG_{4000}) was purchased from Sigma (CAS 25322-68-3). Potassium dihydrogen phosphate (KH_2PO_4) and dipotassium hydrogen phosphate (K_2HPO_4) were from Univar, Ajax Chemicals (Sydney, Australia). *Spirulina maxima* was purchased from Oxymin (KRPAN Enterprises, Australia). All the chemicals used were of analytical grade. Commercial C-PC was obtained from Fuqing King Dnarmsa Spirulina Co., Ltd. (Fujian, China). Crude extract was prepared by mixing the Spirulina maxima biomass with Milli-Q water in a ratio of 1:20 (w:v), for releasing the phycobiliproteins. The slurry was then subjected to a freezing and thawing procedure which was repeated twice with 24 h intervals, followed by centrifugation (Beckman, J2-MC) at 10000g for about 15 min at 19 °C to remove the biomass residue. Crude extracts (the supernatants) were stored at 4 °C for further experiments. ATPS extraction was set up at room temperature based on predetermined quantities of PEG_{4000} and potassium phosphate from the previously reported binodal curve.[24] Milli-Q water was added to the crude extracts [10% (w/w)], and the pH of all the systems was maintained at 6.83 using a 1.82:1 ratio of K_2HPO_4 to KH_2PO_4.[7,24] Every system was mixed for 30 min in a 15 mL graduated centrifuge tubes on a rotary plate at room temperature. After that, the phases were separated by centrifugation or by gravity. The volume of the top and bottom phase of each system was measured and analyzed. The reference systems for each trial were prepared without addition of crude extract. For VFD-processing, the glass tube was rotated at a tilt angle θ of 45° relative to the horizontal position. The reagents were separately added through jet feeds via the use of two automated syringe pumps (Dual NE-1000X, Adelab Scientific, Australia) (Figure 6.1). Intense micromixing from the viscous drag and the Stewartson/ Ekman layers at various speeds as the liquids whirl up the glass tube rapidly reduced the mixing lengths. The VFD was equipped with one outlet for sample collection. The aqueous PEG_{4000} solution (6.4%, w/w) in the crude extract (10%, w/w) was fed from one inflow jet feed, and potassium phosphate (13.5%, w/w) was fed from another inflow jet feed for single ATPS and multistage counter current distribution (CCD). This was conducted by mixing the top PEG_{4000} phase from the previous extraction and the fresh bottom phase. Multiple ATPS were conducted on a larger scale of 20 g. PEG_{4000} and phosphate salt were separated from C-PC using Amicon Ultra-15 30 kDa cutoff centrifugal filters (Merck Millipore Ltd., Ireland) at 5000g for 1 h.

Phycobiliproteins purified by VFD-ATPS was analyzed by sodium sulfate-polyacrylamide gel (SDS-PAGE). This was performed using 4−20% Mini-PROTEAN TGX Stain-Free Protein Gels (BioRad 4568095). The molecular weight of the sample was determined by running Precision Plus Protein Standards, BioRad (Cat 161-0374). A 20 μg portion of proteins was dissolved in 15 μL of distilled water with 5 μL loading sample buffer, which was made up of 50% (v/v) 0.5 M Tris-HCl at pH 6.8, 40% (v/v) glycerol, 8% (w/v) SDS, 6.2% (w/v) DTT, and 0.04% (w/v) bromophenol blue. Electrophoresis was run at 300 V, 400 mA for 30 min. Images were captured using a Bio-Rad Gel Doc EZ system and Image Lab software. Carestream Molecular Imaging software was used to quantify net band intensities (mean pixel intensity by number of pixels). The percentage of C-PC in each lane of the gel was quantified by comparison to the overall protein amount in that specific lane. Total protein concentrations were tested using DC Protein Assay (Cat# 5000111), which gives comparable results to the Kjeldahl nitrogen method on this protein sample. The gel was placed in fixative solution with 20% (v/v) methanol and 7.5% (v/v) acetic acid, and was visualized by staining with colloidal Coomasie blue. The bands of interest were excised and digested in gel with trypsin as reported by Shevchenko *et al*.[25] A 10 μL portion of digested peptide was separated using Eksigent Ekspert nanoLC 415 (AB Sciex, CA) before entering the Triple TOF 5600+ quadrupole time-of-flight mass spectrometer (AB Sciex), in ESI positive mode with a Nano Spray III source. The .mgf file was converted using MSConvert (ProteoWizard 3.0.5759) and was searched against the *Spirulina* (strain NIE-391 IAMM-135) from UniProt database, and then analyzed by ProteinPilot software 4.5 1656 (AB Sciex) using search algorithm Paragon 4.5.0.0, 1654 (AB Sciex). The absorption spectra from 240 to 800 nm was measured using a UV−vis spectrophotometer (Varian Cary 50). The concentration of C-PC was determined as described by Bennett and Bogorad[26] using eq 1 and the purity by Boussiba and Richmond[27] using eq 2.

$$\mathrm{CPC(mg/mL)} = \frac{\mathrm{A620} - 0.474 \times \mathrm{A650}}{5.34} \quad (1)$$

$$\mathrm{Purity} = \frac{\mathrm{A620}}{\mathrm{A280}} \quad (2)$$

The fluorescence spectra of purified C-PC were measured using a fluorescence spectrometer (Cary Eclipse, Agilent). The secondary structure of C-PC was analyzed using Fourier transform infrared spectroscopy (FT-IR) (PerkinElmer, Frontier, Australia) and circular dichroism (CD) using a spectropolarimeter (Jasco Model J-720). Freeze-dried C-PC samples were dissolved in 10 mM potassium phosphate buffer, pH 6.9, for a final protein concentration of 0.2 mg/mL. Far-UV CD spectra were acquired between 195 and 260 nm with a resolution of 0.1 nm, bandwidth of 1.0 nm, signal averaging time of 1 s, and a path length of 1 mm. Three accumulations were recorded at a scan speed of 20 nm/min, and each spectrum was corrected for baseline by the subtraction of the buffer blank. The raw data in millidegrees was converted to mean residue ellipticity $[\theta]_{\mathrm{MRE}}$ (deg cm^2 dmol^{-1}) using a mean residue weight of 115 as described in Patil *et al*.[17] Experiments were carried out in triplicate with the average values of three independent experiments reported as mean ± SEM. Statistical analysis for protein purity and recovery were performed by One-Way ANOVA, followed by Duncan's test considering a significant difference at $p < 0.05$. The rest were conducted by Tukey's HSD post hox test/Dunnett's T3 post hoc test for equal and unequal variances as appropriate. These tests were performed using SPSS 20 (SPSS, Chicago, IBM).

6.4 Results and discussion

Different extraction buffers and extraction methods were investigated before further experiments (Figures S1, S2, and S3a). Extraction was conducted using repeated freezing and thawing using Milli-Q water (Figure S3b) in this study. To determine the optimum phase composition, ATPS was carried out at five different tile line length (TLL) with the same volume ratio at 1 and left overnight for phase demixing as in Patil *et al*.[17] (Tables S1 and S2). Considering the optimized yield and purity of both C-PC and APC, the TLL of 18.64% and the volume ratio of 0.3 were applied for subsequent experiments. Conventional phase demixing methods, gravity, and centrifugation were conducted as controls. Gravity-facilitated phase separation was a time- dependent process and plateaued after 1 h residence time at 0.96 with 84% recovery rate. The highest average purity of 0.99 and 1.3 was recovered from 33 h residence time with gravity and 20 min centrifugation at 1400g, respectively, with 77% recovery rate in both conditions (Figure S4) ($p < 0.05$).

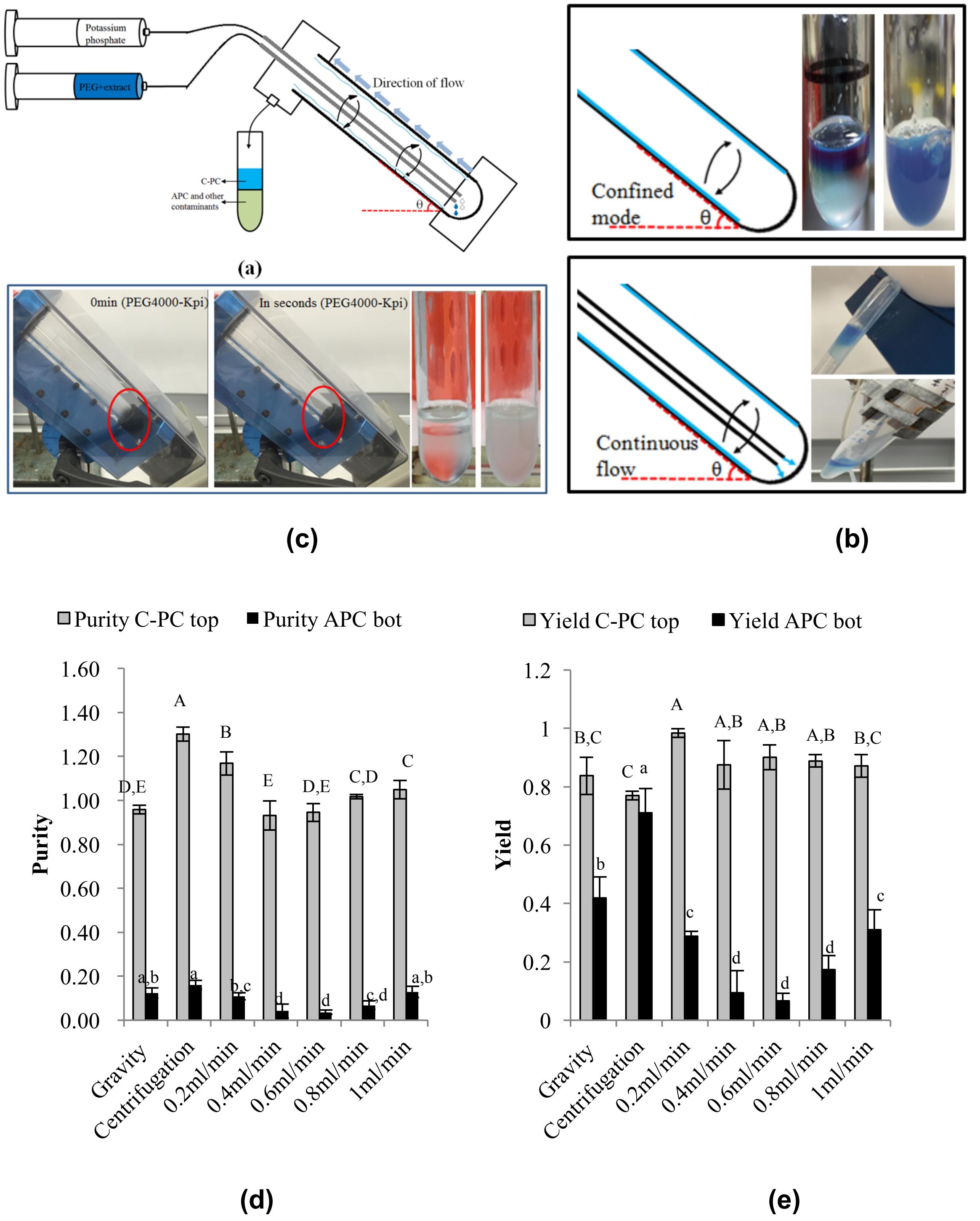

Figure 6.1 *Purification of C-PC using an aqueous two phase system (ATPS) of PEG$_{4000}$ and potassium phosphate: (a) Schematic of the VFD and experimental setup for continuous flow mode with jet feeds at different flow rates delivering solutions to the base of the rapidly rotating tube. (b) Experimental setup for ATPS for confined (insets from left to right showing spontaneous phase separation post-VFD and post-benchtop-vortexing) and continuous flow modes of operation of the VFD (insets showing spontaneous phase separation post-VFD for the liquids exiting the VFD*

through the Teflon unit). (c) Left to right: PEG_{4000} and potassium phosphate (no protein) 0 s spinning and a few seconds spinning at 6550 rpm, spontaneous phase separation post-VFD processing, and no phase separation postbenchtop vortexing. (d) Purity of C-PC and APC post-VFD processing. (e) Yield of C-PC and APC post-VFD processing. Results are shown as mean ± SD. Different uppercase (C-PC) and lowercase (APC) letters indicate significant differences ($p < 0.05$).

In contrast, spontaneous phase separation was observed using the confined mode of operation of the VFD for 2 mL of liquid, with the tube spun at 6550 rpm for 30 min. Continuous flow processing in the VFD also resulted in spontaneous phase separation, for the liquid exiting from the Teflon unit (Figure 6.1 b). Delivering the liquids to the base of the tube in the VFD without it rotating during mixing did not show any change on C-PC purity (Figure S5). At 0.2 mL/min flow rate, the mixing time or residence time was 5.35 min, as the time for a drop of liquid hitting the hemispherical base of the tube to exit from the Teflon unit. In contrast, both conventional methods require 30 min of mixing followed by a residence time of about 1 h and 20 min for gravity and centrifugation, respectively. Thus, spontaneous phase separation post-VFD resulted in at least a 9.3-fold (50 min/5.35 min) increase in phase demixing efficiency relative to centrifugation. With mixing PEG_{4000} and potassium phosphate in the VFD in the confined mode for a few seconds, in the absence of protein, the two liquids become miscible under visual observation (Figure 6.1 c). This might be explained by the shear force in the dynamic thin film in the VFD intensely mixing the two immiscible liquids down to nanosize structures, or at the molecular level. There was no further droplet coalescence between the two phases visually observed on stopping the rotation of the tube, whereas the control group (no VFD confined mode processing) took 6.5 min for the droplets to collide in the dispersion for coalescence.

Demixing behavior depends on the droplet size of the dispersed phase.[28] The Hadamard−Rybzcynski equation (Figure S6) derived from Stoke's law indicates that the change of demixing rate is proportional to the square of the droplet diameter. Breaking the droplets down to nanometer dimension under shear in the VFD may significantly reduce the phase demixing time. Moreover, according to Xue *et al.*,[29] the surface tension (the specific excess free energy) of microdroplets or nano-droplets decreases with decreasing droplet size, which will favor rapid phase separation. It is logical to deduce that, post-VFD processing, interactions between high surface energy nanosize droplets result in the spontaneous phase separation. For continuous flow processing, shear stresses were generated as the two liquids strike the hemispherical base of the tube and are accelerated rapidly with intense micromixing in the thin film. This mode imparts additional shear relative to the confined mode (for tilt angles $\theta > 0°$) which arises from the viscous drag of the liquid against the glass surface as it whirls along the tube.[30,31] Some phase demixing studies using the equation from Mistry *et al.*[32] (Figure S6) correlate the phase separation with more physical properties of the system, including density differences. However, density was not significantly changed for VFD-processing compared with the gravity method (Table S3).

The flow rates of PEG_{4000} containing crude extract and the potassium phosphate solution were optimized first. Here spontaneous phase separation was only observed when the two liquids were delivered at the same rates to the base of the rapidly rotating tube. Therefore, further optimization followed with finer control of the flow rates of those two liquids. Increases in purity and yield were observed at a flow rate of 0.2 mL/min, which were 18% and 14% higher than the optimum control process using gravity ($p < 0.05$) (Figure 6.1 d,e). Compared to centrifugation, the yield was 22% higher for VFD separation ($p < 0.05$) (Figure 6.1 e). In contrast, the separation of APC using VFD processing was less promising than the controls. At a flow rate between 0.2 and 1 mL/min, the recovery of APC fluctuated ($p < 0.05$). The decrease in recovery rate was associated with a migration of APC to the PEG_{4000}-rich phase as evidenced by an increase in K (partition coefficient) of APC at 0.6 mL/min ($p < 0.05$) (Figure S7). As mentioned, the separation of C-PC and APC using ATPS can be attributed to the higher affinity of C-PC to the PEG_{4000}-rich phase compared to that of APC.[11] Therefore, the change of affinity of APC to PEG_{4000} during VFD mixing depends on the duration of mixing. Dynamic light scattering showed that the partitioning of APC to the PEG_{4000}-rich phase was not caused by particle size modification of the polymers under the shear (Figure S8). Therefore, the recovery of C-PC using VFD is flow-rate dependent with better separation of the two proteins at certain flow rates relative to others. However, the increased purity of C-PC in VFD is not only related to APC separation but also other contaminants as evidenced by the similar APC recovery but different C-PC recovery ($p < 0.05$) between 0.2 mL/min for VFD processing and the gravity control. Therefore, VFD processing improved the separation via partitioning of C-PC to the PEG_{4000}-rich phase and most contaminant proteins to the bottom phase. In addition, the improved C-PC recovery using VFD processing may also relate to the spontaneous phase separation and the changes of surface area when the liquid droplets are broken down under shear. Such nanodroplets carry a much larger surface area, collision frequency, and liquid−liquid interfacial area, all of which reduce the diffusion distance, enhance the mass transfer rate, and finally facilitate the recovery process.[33] Minimal residence time for phase demixing again minimized the loss of protein between the interface area.

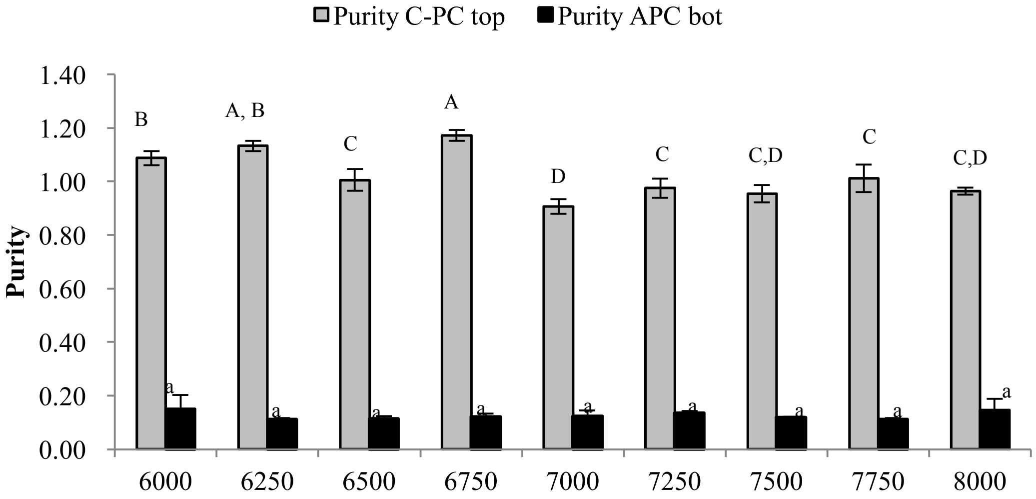

(a)

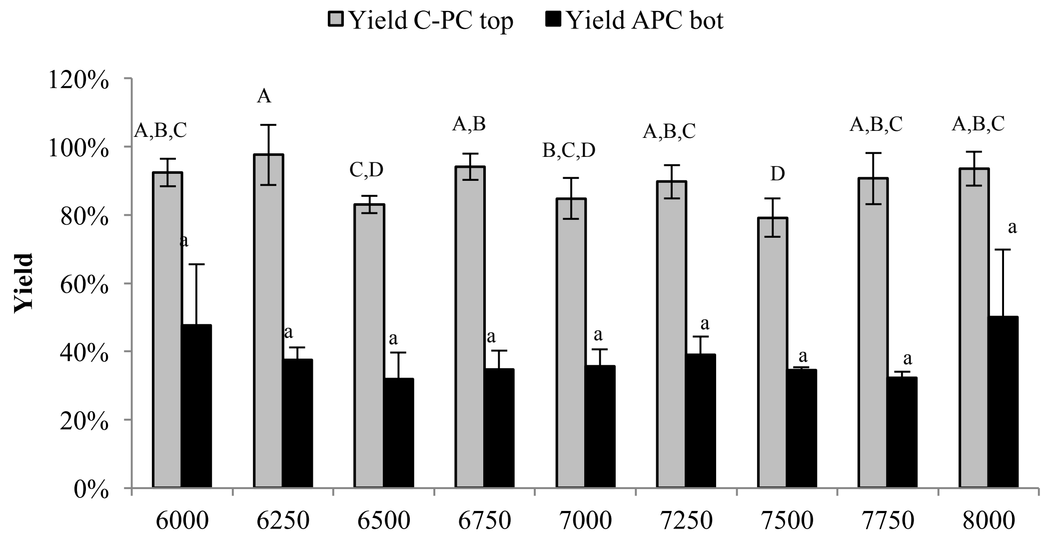

(b)

Figure 6.2 *(a) Purity (A620/A280) of CPC and APC recovered by VFD-ATPS for solutions processed at different rotational speeds (rpm). (b) Yield of CPC and APC recovered by VFD-ATPS for solutions processed at different rotational speeds (rpm). Different uppercase (C-PC) and lowercase (APC) letters indicate significant differences (p < 0.05).*

The highest recovery of C-PC was obtained at a flow rate of 0.2 mL/min ($p < 0.05$). Accordingly, this condition was utilized for further optimization of the rotational speeds of VFD. Speeds were varied from 6000 to 8000 rpm in 250 rpm increments under continuous flow (Figure 6.2). Purity and recovery of C-PC fluctuated slightly with the optimum condition at 6750 rpm, $p < 0.05$ (Figure 6.2). As the equivalent purity (1.17) and recovery (98%) could also be achieved at 6550 rpm, the rotational speed of 6550 rpm with a flow rate of 0.2 mL/min is considered to be optimum. Compared to Liu *et al.*,[7] the purity of C-PC increased from 0.5 to 0.82 in a single ATPS using centrifugation, with the yield <60%. The changes in purity and recovery of APC at different rotational speeds using the VFD are not significantly different. Therefore, the change of affinity of APC to the PEG_{4000}-rich phase is considered rotational-speed-independent. To confirm that the reduced recovery of APC from the bottom phase is caused by the affinity change of APC to the PEG_{4000}-rich phase and not by loss of protein activity under the shear of VFD, the top phase obtained from 0.2 mL/min at 6550 rpm was subjected to centrifugation at 1400g for 20 min. The purity of APC increased to 0.26 with the overall yield increased to 69%, indicating that the difference is caused by the change of the affinity of APC to PEG_{4000}.

Multiple ATPS treatments using VFD processing further increased the purity of C-PC. Centrifugation was conducted once after the first purification using ATPS-VFD for further removal of APC from the top phase. After purification four times by introducing fresh bottom phase (aqueous potassium phosphate), the purity of C-PC increased from 1.3 to 2.3 with a reduction of recovery from 93% to 78% (Table S4). However, the purity of APC remained constant around 0.15. By removing the PEG_{4000} and salt, the purity of top and bottom phases increased the purity of C-PC to 2.92 compared to commercial C-PC purity of 3.04, and the purity of APC to 0.58 due to the permeation of contaminants through the membrane along with the PEG_{4000} and the salt, which is consistent with the findings reported by Patil *et al*.[11] ATPS using two VFD processes increases the K of C-PC by 6.9-fold, and the K becomes infinite the third time. Therefore, VFD processing also reduces the number of cycles required for the multistage CCD.

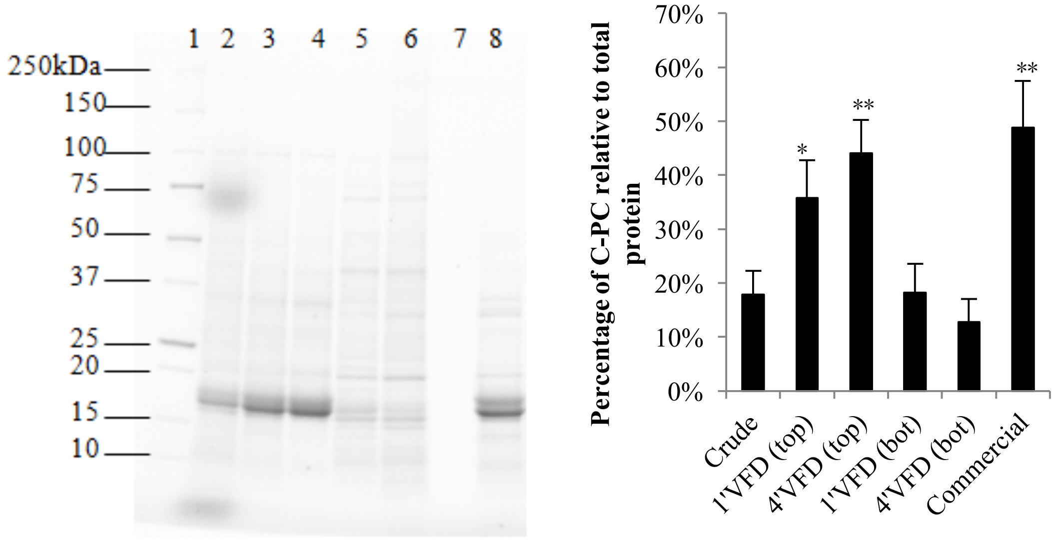

(a) **(b)**

Figure 6.3 *(a) SDS-PAGE gel, lane 1: molecular weight markers. Lane 2: crude extract. Lane 3: single ATPS-VFD (1'VFD) purified (top phase). Lane 4: multiple ATPS-VFD (4 times or 4'VFD) purified (top phase). Lane 5: 1'VFD (bottom phase). Lane 6: 4'VFD purified (bottom phase). Lane 7: water control. Lane 8: commercial C-PC. A 20 µg* *portion of overall proteins was loaded in each lane. PEG_{4000} was removed from all samples before running the gel. (b) Percentage of C- PC relative to all proteins in each lane in Figure 6.3 a. Statistical significance is indicated by single ($p < 0.05$) and double ($p < 0.01$) asterisks.*

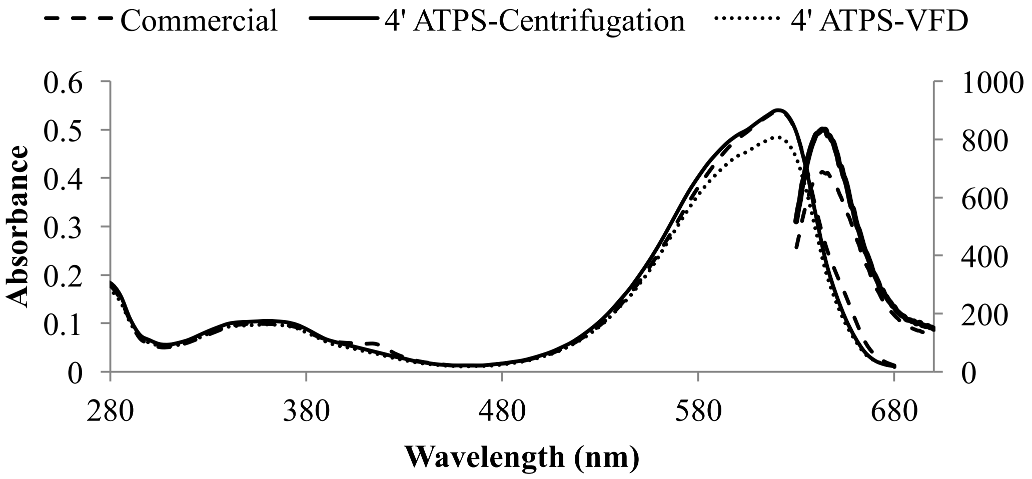

(a)

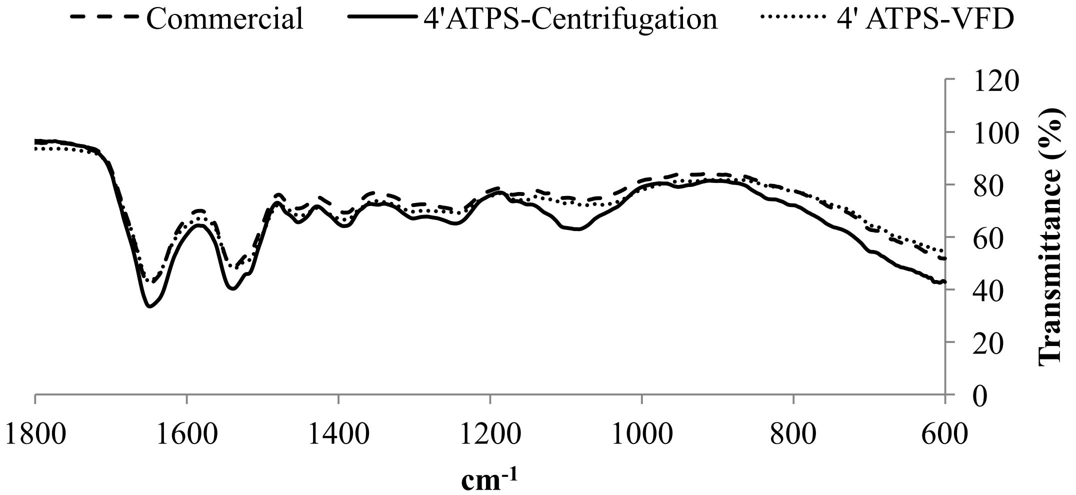

(b)

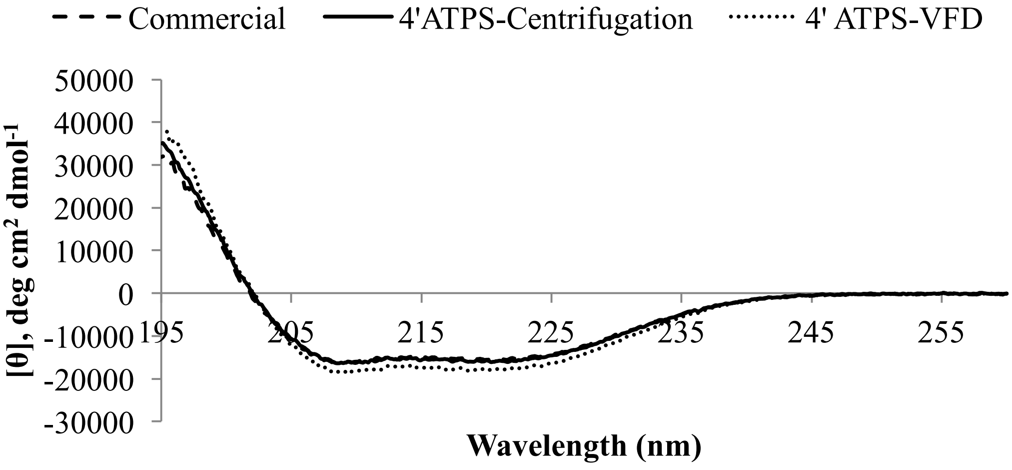

(c)

Figure 6.4 *Spectroscopic characterization of C-phycocyanin. (a) Absorption and fluorescence spectra of commercial C-PC, 4'ATPS- centrifugation, and 4'ATPS-VFD C-PC. UV−vis/absorbance was conducted at a total protein concentration of 0.5 mg/mL. Fluorescence was conducted at 12.5 μg/mL. (b) FT-IR spectrum of C-PC samples. (c) Circular dichroism spectra of C-PC samples (far- UV) at protein concentration of 0.2 mg/mL.*

The purified C-PC showed an intensive band around 17 kDa (Figure 6.3), which is in good agreement with the reported molecular weight of α (17.4 kDa) and β (17.8 kDa) subunits of C-PC from Spirulina maxima.[34] Quantitative analysis of the band intensity using Carestream showed a significant enrichment of α and β subunits from 36% to 44% after multiple purifications using ATPS-VFD ($p < 0.01$). The distribution of proteins in lanes 5 and 6 (samples from bottom phases) and the similarity of lane 4 (samples from top phases) and lane 8 (commercial C-PC) also indicated a successful removal of contaminant proteins using this purification method. The VFD purified proteins were further characterized using fluorescence. The absorption maximum occurred at 615 nm, and when excited at 620 nm, the purified C-PC gave a fluorescence emission at 643 nm (Figure 6.4 a). Compared to the commercial C-PC, VFD-ATPS purified C-PC showed similar FT-IR spectra (Figure 6.4 b) with a protein specific amide I peak around 1650 cm^{-1} from C=O stretching vibration and an amide II peak around 1539 cm^{-1} arising from the in-plane NH bending and CN stretching vibration.[35,36] The sharp 1650 cm^{-1} peak for the purified protein using the VFD is consistent with the presence of α-helices as the major element of its secondary structure,[30] which is well-maintained after the processing, as evidenced by the similar amide I band observed in the controls. Circular dichroism spectra also confirmed maintaining the integrity of their structure after VFD-processing (Figure 6.4 c). The far-UV spectra showed negative bands at 222 and 208 nm and a positive band at 195 nm, which is in accord with α helix secondary structure.[37]

Proteins identification from the excised band are listed in Table S5, and confirm the purified protein as C-phycocyanin (Figure S9). For the α and β subunits, the sequencing encompassed 2894 peptides which covers the entire amino acid sequence for both subunits. Sequence coverages for α and β subunits are 96% and 97% (both with >95% confidence), respectively. The small amounts of peptide sequences identified with lower confidence are most likely caused by the tryptic cleavage rule by cutting after arginine or lysine, which generated extremely small peptide sequences that are beyond analysis. None of the peptides show any indication of protein oxidative destruction. Cysteine-containing peptides were all detected in a carbamidomethylated form, using iodoacetamide which transforms cysteine to the stable *S*-carboxyamidome-thylcysteine thereby preventing the free sulfhydryls from reforming disulfide bonds. Because this alkylation reaction was performed after the gel staining, it infers that no cysteine oxidation to cysteic acid or desulfurization took place during the VFD-processing. Methionine-containing peptides were found in native and oxidized forms, which have been reported in polyacrylamide gel isolated proteins.[38] However, it is possible that some of the oxidation reactions with methionine and proline might occur during VFD-processing. Such processing may also trigger the deamidation reaction of asparagine (Asn) and glutamine (Gln) within the protein.[39] Nonenzymatic deamidation of Asn and Gln residues could occur in vitro and generate different aspartic acid (Asp) and isoaspartic acid (isoAsp), for Asn[40] and glutamic acid (*α*-Glu), and isoglutamic acid (*γ*-Glu) for Gln. In some peptide sequences with both Asn and Glu, the deamidation has been observed only on Glu but not Asn. Deamidation rate of Asn should be much faster than that of Glu except when Glu is located at the N-terminus.[41] In the present case, it is likely that the dynamic thin films in the VFD may facilitate the deamidation reaction toward Glu which is not located at the N-terminus.

6.5 Conclusion

This study established a novel processing methodology of VFD-intensified ATPS for enhancing the phase demixing of ATPS and increasing the recovery of biologically active and intact C-PC with higher purity from blue-green microalga *Spirulina maxima*. Although the demixing concept in the VFD has so far been investigated without much reference to the specific hydrodynamics involved, this present study demonstrates the potential of the VFD as a new phase demixing microfluidic platform for application in protein purification. Future research will focus on investigating the fluid dynamics involved in phase demixing during and post-VFD processing, along with extending the application of the methodology to other proteins and possibly protein modification.

6.6 Acknowledgements

The authors gratefully acknowledge financial support from the Australian Research Council and the Government of SA, Australian Postgraduate Award to X.L., and Flinders University−Tianjiu Group Joint Laboratory. The authors thank Prof. Gregory A. Weiss and Dr. Tim Chataway for discussion on protein characterization and Dr. Emma Parkinson-Lawrence in the Biophysical Characterization Facility, University of South Australia, for discussions on the circular dichroism characterization. The authors acknowledge the kind supply of commercial C-PC by Fuqing King Dnarmsa Spirulina Co., Ltd. (Fujian, China).

6.7 References

(1) Ge, B.; Qin, S.; Han, L.; Lin, F.; Ren, Y. Antioxidant properties of recombinant allophycocyanin expressed in Escherichia coli. J. Photo- chem. Photobiol., B 2006, 84 (3), 175−180.

(2) Yin, L.; Xu, L.; Yu, K.; Zhen, Y.; Han, X.; Xu, Y.; Qi, Y.; Peng, J.; Tan, A. Orthogonal test design for optimization of suitable conditions to separate C-phycocyanin from Spirulina platensis by high-speed counter-current chromatography using reverse micelle solvent system. J. Sep. Sci. 2011, 34 (11), 1253−1260.

(3) Moraes, C. C.; Sala, L.; Ores, J. d. C.; Braga, A. R. C.; Costa, J. A. V.; Kalil, S. J. Expanded and fixed bed ion exchange chromatography for the recovery of C-phycocyanin in a single step by using lysed cells. Can. J. Chem. Eng. 2015, 93 (1), 111−115.

(4) Moraes, C. C.; Mazutti, M. A.; Maugeri, F.; Kalil, S. J. Modeling of ion exchange expanded-bed chromatography for the purification of C-phycocyanin. J. Chromatogr. A 2013, 1281 (0), 73−78.

(5) Yan, S.-G.; Zhu, L.-P.; Su, H.-N.; Zhang, X.-Y.; Chen, X.-L.; Zhou, B.-C.; Zhang, Y.-Z. Single-step chromatography for simulta- neous purification of C-phycocyanin and allophycocyanin with high purity and recovery from Spirulina (Arthrospira) platensis. J. Appl. Phycol. 2011, 23 (1), 1−6.

(6) Liao, X.; Zhang, B.; Wang, X.; Yan, H.; Zhang, X. Purification of C-phycocyanin from Spirulina platensis by single-step ion-exchange chromatography. Chromatographia 2011, 73 (3−4), 291−296.

(7) Liu, Y.; Feng, Y.; Lun, J. Aqueous two-phase countercurrent distribution for the separation of c-phycocyanin and allophycocyanin from Spirulina platensis. Food Bioprod. Process. 2012, 90 (2), 111−117.

(8) Antelo, F. S.; Anschau, A.; Costa, J. A. V.; Kalil, S. J. Extraction and purification of C-phycocyanin from Spirulina platensis in conventional and integrated aqueous two-phase systems. J. Braz. Chem. Soc. 2010, 21 (5), 921−926.

(9) Chen, T.; Wong, Y. S.; Zheng, W. Purification and character- ization of selenium-containing phycocyanin from selenium-enriched Spirulina platensis. Phytochemistry 2006, 67 (22), 2424−2430.

(10) Zhao, L.; Peng, Y.; Gao, J.; Cai, W. Bioprocess intensification: an aqueous two-phase process for the purification of C-phycocyanin from dry Spirulina platensis. Eur. Food Res. Technol. 2014, 238 (3), 451−457.

(11) Patil, G.; Chethana, S.; Madhusudhan, M. C.; Raghavarao, K. S. M. S. Fractionation and purification of the phycobiliproteins from Spirulina platensis. Bioresour. Technol. 2008, 99 (15), 7393−7396.

(12) Patil, G.; Raghavarao, K. S. M. S. Aqueous two phase extraction for purification of C-phycocyanin. Biochem. Eng. J. 2007, 34 (2), 156− 164.

(13) Hatti-Kaul, R. Aqueous Two-Phase Systems: Methods and Protocols; Humana Press, 2000.

(14) Narayan, A.; Raghavarao, K. Extraction and purification of C- phycocyanin from Spirulina platensis employing aqueous two phase systems. Int. J. Food Eng. 2007, 3 (4), 1−17.

(15) Antelo, F. S.; Costa, J. A. V.; Kalil, S. J. Purification of C- phycocyanin from Spirulina platensis in aqueous two-phase systems using an experimental design. Braz. Arch. Biol. Technol. 2015, 58 (1), 1−11.

(16) Chethana, S.; Nayak, C.; Madhusudhan, M. C.; Raghavarao, K. S. M. S. Single step aqueous two-phase extraction for downstream processing of C-phycocyanin from Spirulina platensis. J. Food Sci. Technol. 2015, 52 (4), 2415−2421.

(17) Patil, G.; Chethana, S.; Sridevi, A. S.; Raghavarao, K. S. M. S. Method to obtain C-phycocyanin of high purity. J. Chromatogr. A 2006, 1127 (1−2), 76−81.

(18) Raghavarao, K. S. M. S.; Todd, P. W. Method and apparatus for acoustically demixing aqueous solutions. US Patent 6,090,295, July 18, 2000.

(19) Flygare, S.; Wikström, P.; Johansson, G.; Larsson, P. O. Magnetic aqueous two-phase separation in preparative applications. Enzyme Microb. Technol. 1990, 12 (2), 95−103.

(20) Britton, J.; Raston, C. L. Continuous flow vortex fluidic production of biodiesel. RSC Adv. 2014, 4 (91), 49850−49854.

(21) Vimalanathan, K.; Chen, X.; Raston, C. L. Shear induced fabrication of intertwined single walled carbon nanotube rings. Chem. Commun. 2014, 50 (77), 11295−11298.

(22) Yuan, T. Z.; Ormonde, C. F. G.; Kudlacek, S. T.; Kunche, S.; Smith, J. N.; Brown, W. A.; Pugliese, K. M.; Olsen, T. J.; Iftikhar, M.; Raston, C. L.; Weiss, G. A. Shear-stress-mediated refolding of proteins from aggregates and inclusion bodies. ChemBioChem 2015, 16 (3), 393−396.

(23)Šalic,́A.;Tusěk,A.;Fabek,D.;Rukavina,I.;Zelic,́B.Aqueous two-phase extraction of polyphenols using a microchannel system− process optimization and intensification. Food Technol.Biotechnol. 2011, 49 (4), 495−501.

(24) Albertsson, P. A. Partition of Cell Particles and Macromolecules; Wiley-Interscience, 1986.

(25) Shevchenko, A.; Tomas, H.; Havlis, J.; Olsen, J. V.; Mann, M. In-gel digestion for mass spectrometric characterization of proteins and proteomes. Nat. Protoc. 2007, 1 (6), 2856−2860.

(26) Bennett, A.; Bogorad, L. Complementary chromatic adaptation in a filamentous blue-green alga. J. Cell Biol. 1973, 58 (2), 419−435. (27) Boussiba, S.; Richmond, A. E. Isolation and characterization of

phycocyanins from the blue-green alga Spirulina platensis. Arch. Microbiol. 1979, 120 (2), 155−159.

(28) Srinivas, N. D.; Barhate, R. S.; Raghavarao, K. S. M. S.; Todd, P. Acoustic field assisted enhanced demixing of aqueous two-phase systems. Biochim. Biophys. Acta, Gen. Subj. 2000, 1524 (1), 38−44.

(29) Xue, Y.; Yang, X.; Cui, Z.; Lai, W. The effect of microdroplet size on the surface tension and tolman length. J. Phys. Chem. B 2011, 115 (1), 109−112.

(30) Vimalanathan, K.; Gascooke, J. R.; Suarez-Martinez, I.; Marks, N. A.; Kumari, H.; Garvey, C. J.; Atwood, J. L.; Lawrance, W. D.; Raston, C. L. Fluid dynamic lateral slicing of high tensile strength carbon nanotubes. Sci. Rep. 2016, 6, 22865.

(31) Britton, J.; Dalziel, S. B.; Raston, C. L. The synthesis of di- carboxylate esters using continuous flow vortex fluidics. Green Chem. 2016, 18, 2193.

(32) Mistry, S. L.; Kaul, A.; Merchuk, J. C.; Asenjo, J. A. Mathematical modelling and computer simulation of aqueous two- phase continuous protein extraction. J. Chromatogr. A 1996, 741 (2), 151−163.

(33) Okubo, Y.; Mae, K. Process intensification using a two-phase system and micromixing for consecutive and reversible reactions. AIChE J. 2009, 55 (6), 1505−1513.

(34)Fernańdez-Rojas,B.;Hernańdez-Juaŕez,J.;Pedraza-Chaverri,J. Nutraceutical properties of phycocyanin. J. Funct. Foods 2014, 11, 375−392.

(35) Patel, A.; Mishra, S.; Pawar, R.; Ghosh, P. K. Purification and characterization of C-Phycocyanin from cyanobacterial species of marine and freshwater habitat. Protein Expression Purif. 2005, 40 (2), 248−255.

(36) Kong, J.; Yu, S. Fourier transform infrared spectroscopic analysis of protein secondary structures. Acta Biochim. Biophys. Sin. 2007, 39 (8), 549−559.

(37) Greenfield, N. J. Using circular dichroism spectra to estimate protein secondary structure. Nat. protoc. 2007, 1 (6), 2876−2890.

(38) Shevchenko, A.; Wilm, M.; Vorm, O.; Mann, M. Mass spectrometric sequencing of proteins from silver-stained polyacryla- mide gels. Anal. Chem. 1996, 68 (5), 850−858.

(39) Li, X.; Lin, C.; O'Connor, P. B. Glutamine deamidation: differentiation of Glutamic acid and γ-Glutamic acid in peptides by electron capture dissociation. Anal. Chem. 2010, 82 (9), 3606−3615.

(40) Yang, H.; Zubarev, R. A. Mass spectrometric analysis of asparagine deamidation and aspartate isomerization in polypeptides. Electrophoresis 2010, 31 (11), 1764−1772.

(41) Tonie Wright, H.; Urry, D. W. Nonenzymatic deamidation of asparaginyl and glutaminyl residues in protein. Crit. Rev. Biochem. Mol. Biol. 1991, 26 (1), 1−52.

Appendix: the first page of published article and the first page of published supporting information

ACS Sustainable Chemistry & Engineering
Research Article
pubs.acs.org/journal/ascecg

Vortex Fluidic Device-Intensified Aqueous Two Phase Extraction of C-Phycocyanin from *Spirulina maxima*

X. Luo,[†,‡,§] P. Smith,[∥] C. L. Raston,[*,†,§] and W. Zhang[*,†,‡]

[†] Centre for Marine Bioproducts Development, Flinders University, Adelaide, South Australia 5042, Australia
[‡] Department of Medical Biotechnology, School of Medicine, Flinders University, Adelaide, South Australia 5042, Australia
[§] Centre for NanoScale Science and Technology, School of Chemistry and Physical Sciences, Flinders University, Adelaide, South Australia 5042, Australia
[∥] The Australian Wine Research Institute, Hartley Grove, Urrbrae, South Australia 5064, Australia

Ⓢ *Supporting Information*

ABSTRACT: A vortex fluidic device (VFD) is effective for downstream processing of C-phycocyanin (C-PC) from blue-green microalga *Spirulina maxima* using an aqueous two phase system (ATPS): polyethylene glycol (PEG) and aqueous potassium phosphate. The VFD-intensified ATPS continuous flow processing (VFD-ATPS) has spontaneous phase separation of the liquid exiting the 20 mm diameter tube inclined at 45° and rotating at 6550 rpm, for a 0.2 mL/min flow rate. This processing results in at least a 9.3-fold increase in phase demixing efficiency, 1.18-fold increase in C-PC purity, and 22% increase in yield compared to conventional ATPS methods. Multistage counter current distribution (CCD) using VFD-ATPS followed by removal of PEG and salt increased C-PC purity by 6-fold compared to the crude extract, with triple TOF mass spectrometry showing more than 95% sequence coverage for both subunits. This work establishes the utility of using VFD-intensified ATPS processing for protein purification and its potential as an effective new tool for rapid processing of biologically active and intact proteins.

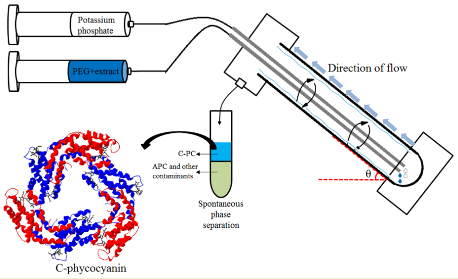

KEYWORDS: *Vortex fluidics device, C-Phycocyanin, Microalgae, Aqueous two phase system, Phase demixing*

■ INTRODUCTION

C-Phycocyanin (C-PC) is a stable fluorescent pigment protein with promising bioactivities.[1] Several methods have been developed for the extraction and purification of this phycobiliprotein.[2−8] However, most of them involve the use of chromatographic techniques,[9] and such methods can suffer from high cost, low efficiency, low recovery rates, and difficulties in scaling up.[10] In recent years, the use of aqueous two phase systems (ATPS) has attracted considerable attention in attempting to overcome some of these disadvantages. Employing differential partitioning of ATPS results in C-PC being preferentially taken up in the polymer-rich top phase, as identified by a major absorption peak maximum at 620 nm, whereas other contaminants partition to the salt-rich bottom phase.[10] One of the main contaminant proteins is allophycocyanin (APC), which also belongs to the phycobiliprotein family, having an absorption maximum at 650 nm. The fractionation of these two biliproteins is based on the higher affinity of C-PC to the PEG-rich phase than that of APC.[11]

Most ATPS-related research on C-PC purification focuses on process optimization involving varying the pH, volume ratio, and molecular weight of PEG,[12] with limited research exploring the demixing efficiency. ATPS involves two unit operations, namely, mixing components and phase separation through droplet−droplet collision and coalescence.[13] Thorough mixing can be achieved by stirring for half an hour to an hour for a 10−20 g system[12,14] or by vortex mixing.[8,15] The most common methods for phase separation of C-PC are gravity and centrifugation.[16] One of the obstacles to the application of ATPS is the slow demixing rate for the phase separation due to small difference in the densities between the two phases, high viscosity of individual phases, low interfacial tension, and longer time required for droplet−droplet collisions.[13] Although there is little data on the effect of gravity-associated phase separation for C-PC, overnight phase separation is possible for this protein.[17] Apart from high speed centrifugation, demixing efficiency can be improved using external electric, magnetic, acoustic, and microwave fields.[18,19] However, a heating free, energy efficient, and technically simplified method for protein recovery from ATPS is required. To this end, we have explored the use of the vortex fluidic device (VFD) to intensify ATPS for C-PC purification, and the results are reported herein. The

Received: April 13, 2016
Revised: May 20, 2016
Published: May 23, 2016

© 2016 American Chemical Society

DOI: 10.1021/acssuschemeng.6b00756
ACS Sustainable Chem. Eng. 2016, 4, 3905−3911

Supplementary Information

Vortex fluidic device-intensified aqueous two phase extraction of C-phycocyanin from *Spirulina maxima*

X. Luo [1,2,3], *P. Smith* [4], *C. L. Raston* [3*], *W. Zhang* [1,2*]

[1] *Centre for Marine Bioproducts Development, Registry Road, Flinders University, Adelaide, SA 5042, Australia;* [2] *Department of Medical Biotechnology, School of Medicine, Flinders University, Adelaide, SA 5042, Australia;*[3] *Centre for NanoScale Science and Technology, School of Chemistry and Physical Sciences, Flinders University, Adelaide, SA 5042, Australia;* [4] *The Australian Wine Research Institute, Hartley Grove, Urrbrae, SA 5064, Australia*

Corresponding Authors

*W. Zhang. Tel.: +61 8 72218557. Fax: +61 8 72218555. E-mail: wei.zhang@flinders.edu.au

*C. Raston. Tel.: +61 8 82017958. Fax: +61 8 8201290. E-mail: colin.raston@flinders.edu.au

7 CONCLUSIONS AND FUTURE DIRECTIONS

7.1 Summary of key findings

Microfluidic technology provides alternative advanced strategies for the synthesis of various materials with precise control over size, shapes and homogeneity. There is growing recognition that the thin film microfluidics within the VFD has established a paradigm shift and has a variety of potentials applications in various material processing.[1,2] Despite the extensive exploration in the field of organic synthesis and material science, VFD has rarely been explored for fabricating high valued materials for biomedical applications in the fileds of biomedicine, biosensors, cell imaging, protein purification and targeted theranostics.[3] Although most of the published methods are significant innovations in science, the main limitations are yet to be addressed including the generation of polydispersed materials and waste and high energy usage. Materials prepared from these published techniques easily agglomerate, oxidize, and lack of precise control of mixing, nucleation, and growth in large scale synthesis. As a result, homogeneity and reproducibility of the final product varies from batch to batch.[4,5] Purification or multi-step processing is often needed, however this limits the scope for scaling up the process. In the present study these issues have been addressed, up front at the inception of the science. It presents a significant advance in exploring potential application of VFD in generating high-valued biomedical materials in a more benign way in filling this gap of research.

A detailed literature review was conducted, which highlighted the growing interest of conducting reactions in micrometer dimensions where the fluid mechanics change significantly compared to that in macroscales, resulting in efficient micromixing and better control of synthesis parameters. It revealed that the process intensification among next generation MDs such as VFD, as an alternative route to other microfluidic techniques, has resulted in significant advancement in a broad range of studies in fabricating different high-valued materials and their derivatives. The VFD allows the development of a more environmentally friendly method of processing various materials, driven by shear stress generated within the thin dynamic film (>200 µm thick), with scalability and controlled processing addressed in a continuous flow manner.

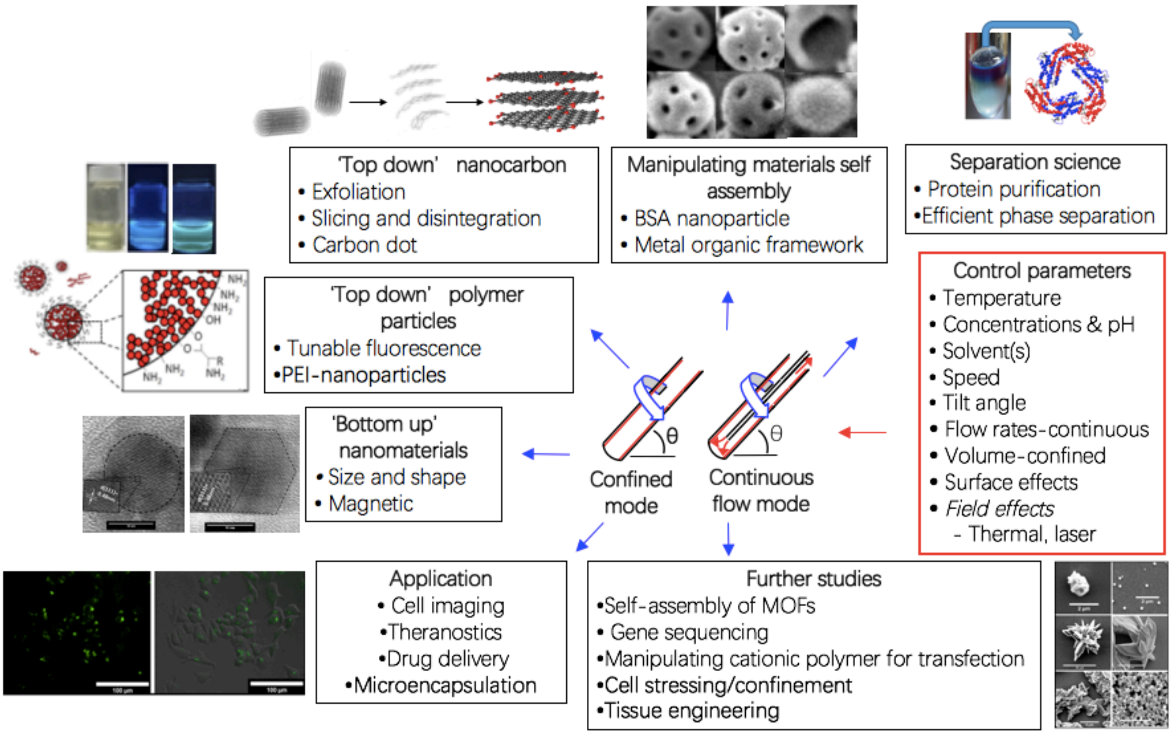

***Figure 7.1** Summary of various materials fabricated using VFD and future directions*

To summarise the findings, the first study focused on the fabrication of carbon-based material. Most of the reported methods for fabricating carbon nanodots involve tedious purification processes, the use of harsh chemicals, difficulties in scaling up and sample inhomogeneity. The vortex fluidic-mediated synthesis of CDs overcomes the clogging issue in conventional microfluidics, as well as enhancing the prospect of product homogeneity under plug flow and uniform irradiation and shear stress. CDs produced using this method have a relatively narrow size distribution, between 3 to 13 nm, and have high colloidal stability and are non-toxic up to 200 µg/mL, as established from a skin fibroblast CRL2076 cytotoxicity study. The CDs exhibit excitation wavelength independent PL behaviour with two distinctive emission peaks around 420 and 460 nm, being an integration of at least three emissive sites originating from the aromatic core, defects and functional groups. These carbon dots have potential application in imaging, and in security material, for example in bank notes.

Fabrication of magnetite nanoparticles has also been achieved in a single step of VFD processing. Pulsed laser ablation, which can be a simple and surfactant and counter-ion free technique, has been used to prepare magnetic nanoparticles with a narrow size distribution. However, selectively forming only one iron oxide phase, precisely controlling the collapse of plume and scaling up are major challenges for conventional laser processing techniques. Laser ablation of an iron target in the gas-phase can circumvent some of the above drawbacks for liquid ablation processing, using air as the oxidant. We have established that the VFD is effective in forming superparamagnetic magnetite nanoparticles of spheroidal or hexagonal shapes with a narrow size distribution, as a one-step continuous flow process at ambient pressure, using i*n situ* laser ablation from a pulsed laser operating in the NIR. The process uses water as solvent which minimizes the generation of waste by avoiding the need for any chemicals/surfactants, and avoids time consuming purification steps by reducing any negative impact of the processing on the environment.

VFD processing has been efficiently applied in making polymer nanoparticles, with tunable fluorescence. Polyethylenimine-based nanoparticles *ca.* 10 nm in diameter, devoid of auxiliary structures, and with tunable fluorescence are generated in air under high shear at high temperature and different flow rates in VFD. The processing carried out under shear stress and high temperature facilitates oxidation, both of which trigger polymer degradation, chain scission and entangling of sliced polymers into self-passivated nanoparticles, and this is independent of sample molecular weight of the starting material. Nanoparticles with low toxicity and good photostability were rapidly prepared. The optimum quantum yield is higher than that of most published PEI-based nanoparticles devoid of auxiliary moieties. Chemical-adoption of amide functional groups triggers enhanced fluorescence intensity and auto-fluorescence over a wide excitation range, and the resulting nanoparticles showed significantly reduced cytotoxicity against MCF-7 cell line compared to as received materials. The biocompatibility of these fluorescent nanoparticles can facilitate their application in imaging live cells, with the overall study contributing to an understanding of fluorescence arising from amino-containing materials and the development of new functional fluorescent nanoparticles.

Nanoparticles derived from bovine serum albumin (BNPs) are biodegradable, biocompatible, and have advantages over synthetic polymers in medical applications. Biocompatible BNPs have potential in drug delivery applications with a capacity for incorporating drugs within the particle matrix for their enhanced endocytic uptake. However, most of the cross-linking processes applied in the desolvation of BNPs have long processing times and none of those reported particles appear to be devoid of pores connecting the outer surface with the core of the particles. The shear stress in the VFD can mediate the fabrication of BNPs with tuneable size, shape and inbuilt porosity, while at the same time controlling the crosslinking chemistry. Macroporous BNPs are readily generated in high homogeneity, and remarkable as spheroidal particles with randomly localised pores on their surface. These BNPs particles have a strong intrinsic fluorescence emission at 555 nm when excited at 532 nm, and have high absorption efficiency of Rhodamine B compared to non-optimised particles with smooth surfaces devoid of any pores. Further reduction of the size of BNPs is effective by incorporating c-phycocyanin protein into the system during processing in the VFD, as well as controlling their shape, from nanospheres to pockets.

Finally, efficient protein purification in aqueous two phase systems (ATPS) has been demonstrated in the microfluidic-based VFD platform. One of the obstacles to the application of ATPS is slow demixing rates for the phase separation. Apart from gravity and centrifugation-facilitated phase separation, demixing efficiency can be improved using external electric, magnetic, acoustic and microwave fields. However, a heating free, energy efficient and technically simplified method for protein recovery from ATPS is required. To this end, we have developed the use of VFD to intensify ATPS for C-PC purification. We show that efficient purification of C-phycocyanin derived from microalgae *Spirulina maxima* by VFD-intensified ATPS as an example with spontaneous demixing and phase separation post-VFD-ATPS extraction, demonstrated the potential of the VFD as a new phase demixing technology in protein purification. This novel process results in a 1.18 fold increase in purity of C-PC with a

22% increase in yield compared to conventional ATPS methods. Multi-stage counter current distribution (CCD) using VFD-ATPS followed by a removal of PEG and salt led to a 6 fold increase in C-PC purity compared to crude extract, from 0.5 to 3.0.

In conclusion, this work establishes the utility of using a novel VFD-intensified process for preparing various high-valued functional materials. VFD as an effective and scalable new tool for rapid processing showed great potential in biochemical applications particularly for cell imaging and drug delivery. As one of the next generation microreactors, VFD starts to become more application-directed and will further develop towards more integrated, automated, modular, and multistage microsystems, incorporating real time, and in time processing.

7.2 Current research interests and future directions

The key findings from this study indicate that there is huge potential for further exploration of VFD-fabricated nanoparticles for different biomedical applications. For example, as we mentioned in Chapter 1, microfluidic devices have also been widely applied in biologics delivery and controlled release and theranostics. Our preliminary studies in 7.2.1 and 7.2.2 show promising results in these aspects. In regards to material processing, we have investigated carbon, metallic, polymer and protein based nanoparticles in this study, however, future research should not be limited within these materials, many other environmentally-friendly and nontoxic candidates are also worth to be investigated such as liposome, DNA or MOF (7.3.3).

7.2.1 Manipulating cationic polymers under microfluidics for effective gene delivery

Gene therapy has been pursued as a promising technique for the treatment of several diseases.[6] Deoxyribonucleic acid (DNA)-based gene therapy or nonviral gene-delivery technique rely upon the insertion of a functional plasmid DNA (pDNA) into the nucleus of cells, which in turn enables the expression of therapeutic proteins, which is named transfection.[7] For gene delivery to be effective, the pDNA requires appropriate protection from DNAase enzymes due to its poor cellular internalisation and fast enzymatic degradation. The use of cationic gene delivery system such as polyethylenimine (PEI) to condense pDNA through electrostatic interactions between the negatively charged phosphate group of DNA and the positively charged amine groups of PEI into cationic nanosized particles,[8] namely polyplexes for nonviral gene delivery, has received considerable attention.[9,10] Problems with current gene delivery systems include the lack of safe and efficient delivery systems, small plasmid loading capacity, unwanted immunogenicity, limited DNA cargo capacity and large-scale production of the delivery system.[11] PEI-based carriers have been suggested to trigger endosomal escape of polyplexes[12] and minimise the problems associated with unwanted immunogenicity and lysosomal degradation but its therapeutic application was largely hampered by its cellular systemic toxicity[13] and nondegradable nature.[11] It is understood that PEI-medicated toxicity depends on its molecular weight and structure.[14]

In Chapter 4, we have demonstrated the possibility of using controllable shear stress of VFD to modify PEIs with low or high MW and assemble the formation of *ca*. 10 nm PEI-based nanoparticles with significant reduction on cytotoxic effects.[15] Relatively small variation in the polycation ionisation state can result in dramatic changes in degradability and its behaviour upon interaction with DNA.[10] For example, transfection efficiency could be improved by cross-linking LMW PEI to form degradable HMW, decorating with other polymers[12] or small degradable cross-linkers such as citric acid.[16] Modification of PEI (1.8 kDa) showed improved efficiency in condensing pDNA into coplexes of sizes about 100 nm, whereas unmodified PEI/DNA coplexes display large particle sizes of 2 μm.[12] On the other hand, the current method of preparing coplexes is a bulk mixing process which involves the mixing of the two solutions followed by brief vortexing (as opposed to VFD process). This results in spontaneous self-assembly into nanostructures. N/P ratio is critical for a promising transfection outcome. Koh *et al.* showed that by using microfluidic hydrodynamic focusing (MF) device, better complexation/condensation of pDNA by PEI could be achieved, relative to conventional bulk mixing (BM).[8] More compact and ordered condensates are formed by MF (494 nm, +11.4 mV) relative to BM (898 nm, +24.8 mV) because of enhanced diffusional mass-transfer between the species in the two fluids.[8] However, this process still require a brief vortexing post the MF to make more ordered structures.

Further studies with VFD could investigate into **(i)** a simple fabrication process in modifying PEIs with high DNA binding capacity and transfection efficiency but low cytotoxicity (Figure 7.2a) **(ii)** manipulating self-assembly process of polyplexes with controlled sizes under the shear stress of VFD *in situ* for enhanced transfection efficiency (Figure 7.2b). Herein, our preliminary results indicated a simple and one-step scalable process using VFD for efficient modification of PEI in generating better alternatives for improved *in vitro* gene transfection efficiency. Cellular transfection revealed overall improvement on the expression of pGFP relative to as-received material (Figure 7.2c). When solutions of DNA and PEI are mixed, the complexation by electrostatic interactions condense the PEI/DNA conjugates into spherical, globular or rodlike nanostructures.[17] VFD processed PEI/pGFP mixture revealed a uniform distribution of pGFP molecules on mica surface with self-assembled neuron-like structures (Figure 7.3b), which has not been reported in previous literatures. The vortex mixed sample showed significant bundling and agglomeration between DNA molecules (Figure 7.3a). Controlled coplexes sizes with high monodipsersity occur at nitrogen/phosphate ratio of 6.7 at a speed of 5000 rpm for 10 min using VFD (Figure 7.3c).

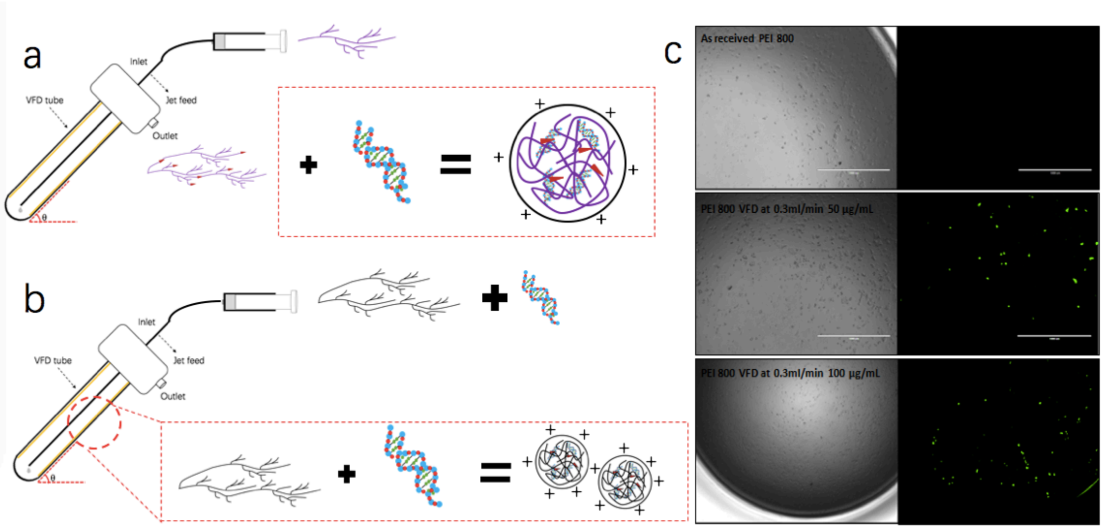

Figure 7.2 *(a) In situ modification of PEI with VFD (b) In situ self-assemly of PEI/DNA coplexes (c) Transfection of MCF-7 cell line with VFD-modified PEI (800Da)/pGFP coplexes compared to the ones form from non-modified PEI (800Da). MCF-7 cells were seeded onto 96 well plate and incubated for 24 h before transfection. PEIs/pGFP coplexes at 15 and 30 w/w ratio pre-incubated for 15 min were added and observed using inverted fluorescence microscope (EVOS® FL) after 24 h. The effect on DNA topology was evaluated using the circular, supercoiled and linearised forms of plasmid GFP (pGFP), which is 5.2kb on average which is equivalent to 1.716 µm in length.*

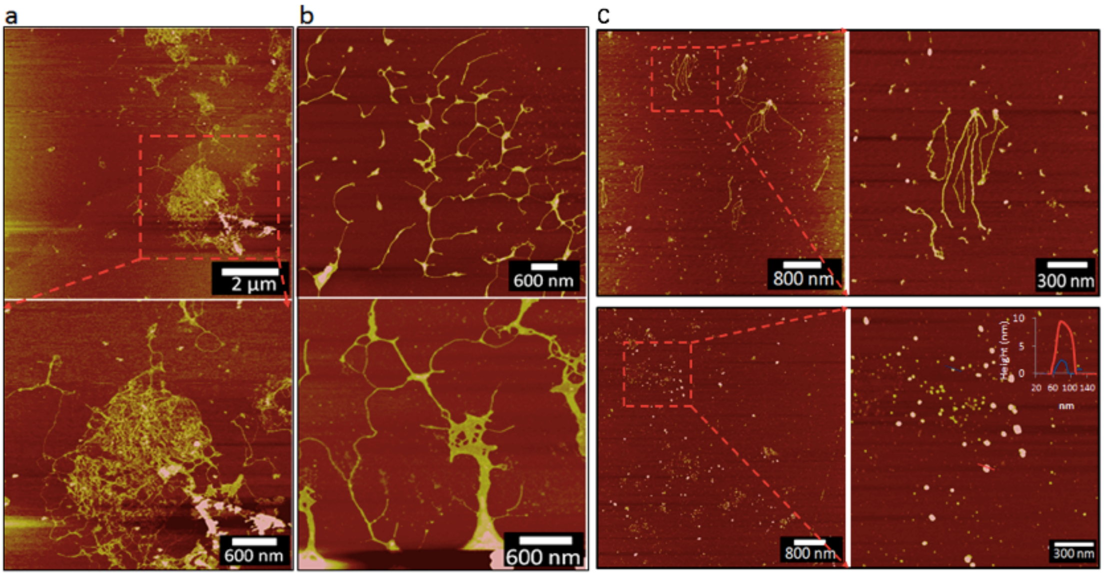

Figure 7.3 *Processing of pGFP with PEI (MW=25kDa) for 10min using* ***(a)*** *Benchtop vortex* ***(b)*** *VFD at 7500 rpm under confined mode. The concentration of pGFP is 11.2 µg/mL* ***(c)*** *Processing of pGFP with PEI (MW=25kDa) using VFD at 5000 rpm for 10 min under confined mode. The concentration of pGFP is 1.12µg/mL. The topographic line profile of two randomly chosen nanoparticles showing a sample height between 2 to 10 nm.*

7.2.2 Lateral slicing of DNAs under the shear stress of VFD for high quality sequencing

The preparation of high quality sequencing library plays an important role in next-generation sequencing (NGS) technology. The crucial step in preparing nucleic acid or template libraries for NGS is the random fragmentation of high molecular weight DNA samples.[18] Few main methods to shorten the long DNA molecules include mechanical methods (nebulisation,[18] hydrodynamic shearing, acoustic shearing and sonication),[19] microwave-irradiation,[19] enzymatic digestion and chemical methods. Disadvantages for some of these platforms include aerosolisation of genomic material, which may result in the cross-contamination and biohazards; the difficulty in multiplexing and the potential in sequence biases.[19] Thermal heating and microwave irradiation caused several reduction in PCR amplification efficiency, unsuccessful emulsion PCR and low sequence yield.[19] Enzymatic fragmentation showed highest consistency but performed slightly worse than sonication and nebulisation in the aspects of insertions or deletions in the raw sequence reads.[18] Keeping a uniform sequence length is important if long-range PCR fragments are used, otherwise, subsequent coverage drastically drops.[18] For NGS library preparation, several techniques are currently available with variable success on different platforms. Illumina genome analyser and ion read lengths are currently under 600 bases. Roche 454 genome sequencer outputs reads at less than 1kb and PacBio less than 9kb in length. Acoustic shearing with Covaris adaptive focus acoustic system was applied to generate fragments of tunable size ranges (100bp-3kb).[19] Aquatic mechanical force shearing with HydroShear to generate large fragments (1.5-8kb) for jumping library preparation.[19] In the last few years, NGS have fundamentally changed genomic research and have dominated many genomic discovery research[20] and novel diagnostic applications, however, key issues such as the simplification and multiplexing of fragmentation method need to be solved.

In this proof-of-concept study, we investigate the vortex fluidic device (VFD) as a simple, unbiased and easy-to-multiplex way to controllable fragmentation of DNA molecules for overcoming some of the limitations of existing DNA fragmentation methods and improved sequence coverage and read qualities. The effect on DNA topology was evaluated using the circular, supercoiled and linearised forms of pGFP, which is 5.2kb on average which is equivalent to 1.716 μm in length. One nucleotide unit is 0.33 nm long. Figure 7.4 indicated that processing using VFD at 7500 rpm for 10 min can linearise and fragment the pDNA (1.716 μm for as received). There is a great potential to generate DNA size ranges suitable for NGS by optimising the processing conditions. Further studies will investigate the possibility of fragmenting the genomic DNAs and electrophoresing the processed samples on an agarose gel to determine the DNA size distribution.

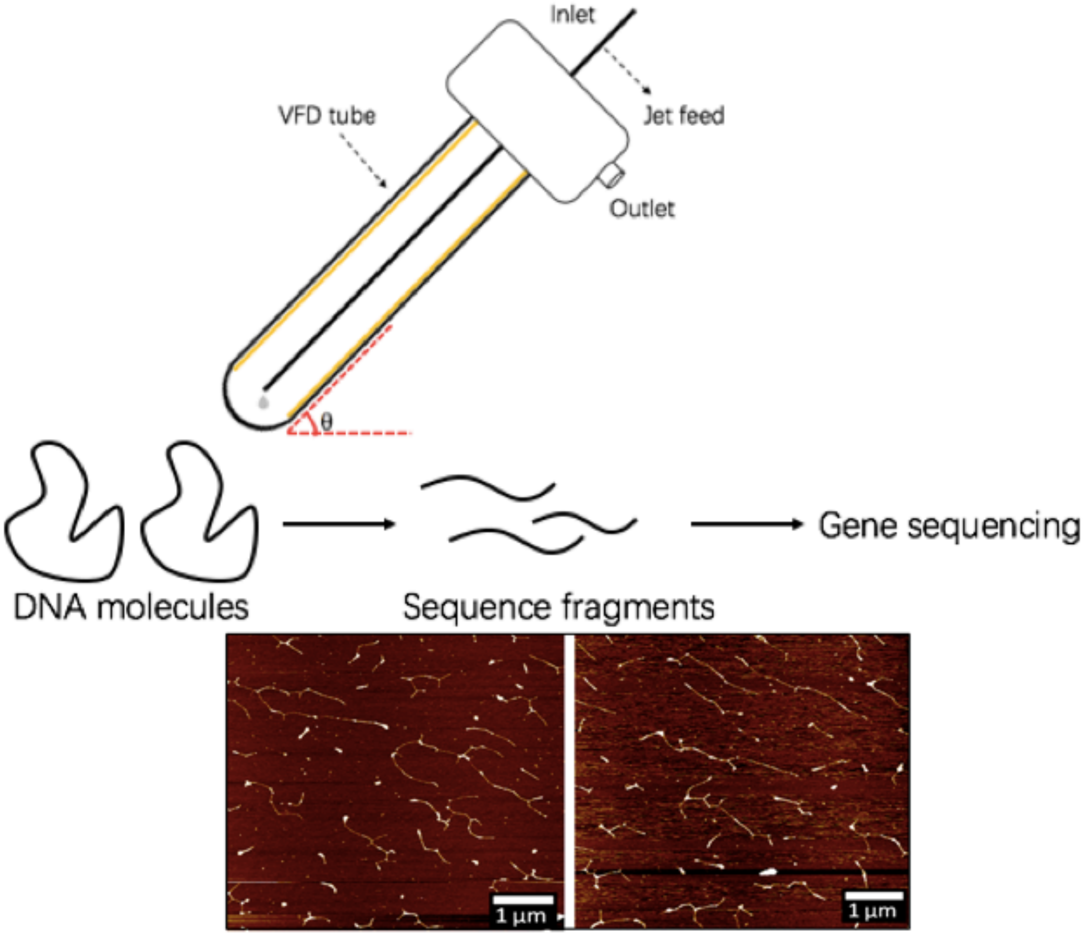

Figure 7.4 *Slicing of pGFP in the presence of PEI using VFD at 7500 rpm for 10 min.*

7.2.3 Manipulating the self-assembly process of metal organic framework (MOF) and their application in microencapsulation

The metal organic framework (MOF) can compose of metal ions coordinated to organic ligands to assemble one, two or three dimensional structures. Over the last decades, MOF started to attracts research and industry attention in biomedical areas. The unique nanoporous characteristics of MOFs make them promising candidates for drug storage and delivery, microencapsulation, imaging and sensing due to their high drug loading capacity and biodegradability.[21] Few MOF models have been investigated previously in the area of biomedical applications, such as MIL-100 (25 Å pore size), MIL-101 (29 Å),[22] MIL-53 (8.6 Å), MIL-88A (6 Å), UiO-66-N$_3$,[23] ZIF-8[24] and many more. The drug loading capacity varies based on these pore sizes.[21] To the best of our knowledge, there is no existing method in precisely controlling the size and morphology of MOFs, but which could be critical in theranostic platform. Significant outcome has been achieved in controlling the self-assembly process of C_{60} under the shear of VFD (unpublished data). Our preliminary data showed the possibility of **(i)** varying the size and morphology of two MOF systems, ZIF-8 and MOF-5 (Figure 7.5), under the shear stress of VFD **(ii)** encapsulating bioactive compounds inside the MOF nanostructures (Figure 7.6).

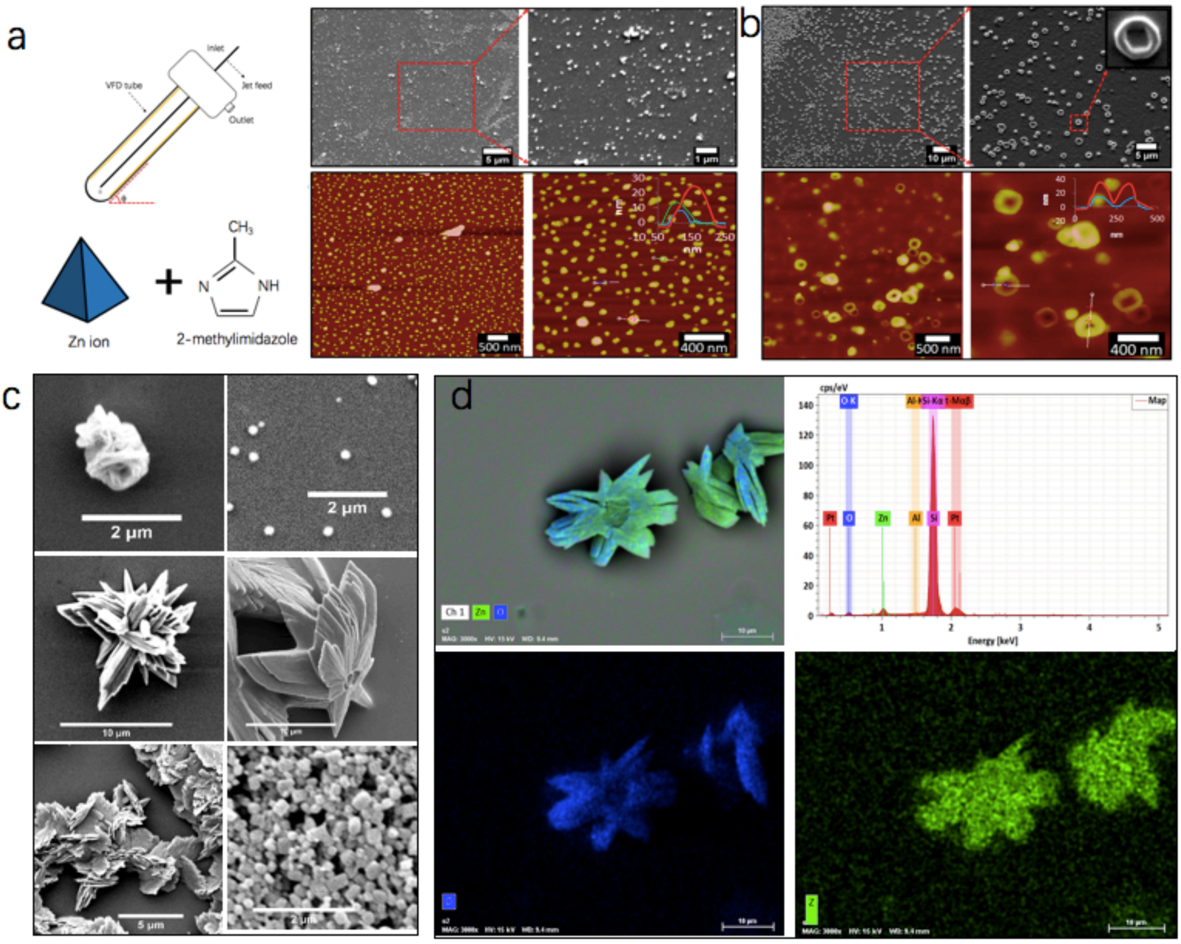

Figure 7.5 *(a) ZIF-8 prepared by VFD under confine mode at 7500 rpm for 30 min (b) ZIF-8 with BSA by VFD under confined mode at 7500 rpm for 30 min (c) Manipulating the morphology of MOF-5 at different speeds of VFD (d) SEM/EDX mapping of MOF-5 flower (at accelerating voltage of 10 kV).*

ZIF-8 prepared by VFD processing showed a size distribution between 10-30 nm (Figure 7.5a). The addition of BSA into the system led to the formation of donut-like structures (Figure 7.5b). By varying the processing conditions, structures of ZIF-8 could be tuned to special shape with sizes going up to a few microns. Different morphologies of MOF-5 could also be generated at different rotational speeds of VFD, varying from spheres, cubes, flakes to flowers (Figure 7.5c and d). Raman and FTIR spectra confirmed the typical spectrum for ZIF-8 and indicated the corporation of BSA into the ZIF-8 structures (Figure 7.6a). To further confirm that the protein is allocated inside center of the ZIF-8. We performed the experiment on a fluorescent protein, C-phycocyanin (ex. 620, em. 652 nm). The confocal mapping demonstrated successful encapsulation of this fluorescent protein inside the centre core of the ZIF-8 shell (Figure 7.6).

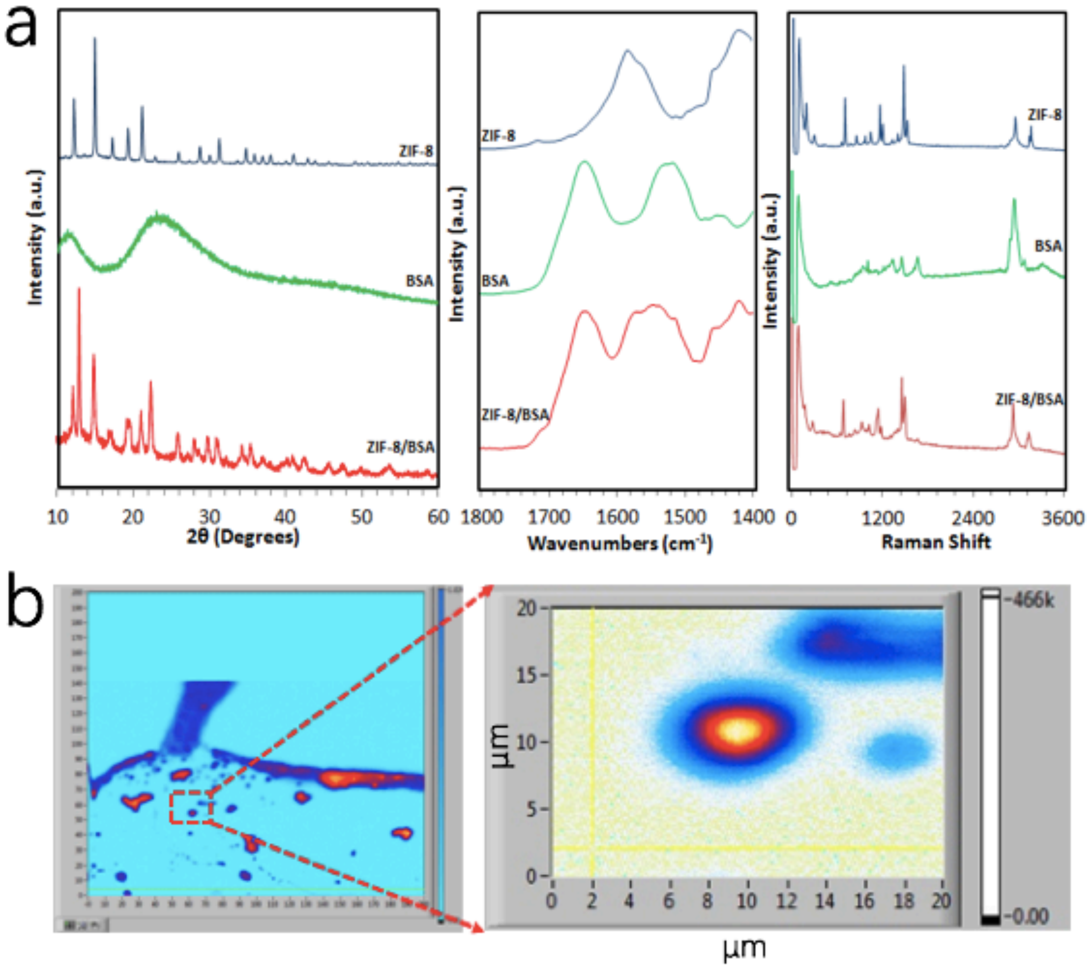

Figure 7.6 *(a) XRD, FTIR and Raman, respectively (b) Encapsulation of C-phycocyanin with ZIF-8 under VFD at 7500 rpm for 20 min. The sample was excited at 532 nm with highest fluorescence intensity presented as the red colour located inside the core part of the nanostructure.*

The advancement of VFD mediated material processing so far is still the ‘tip of the iceberg’. This project has opened huge possibilities not only in the field of various material processing but also applying these materials and the technology into varies biomedical applications, for example, advanced drug delivery, tissue engineering, cell manipulation and diagnostic monitoring.

7.3 Acknowledgement

The author gratefully acknowledges Dr. Martin Cole from NewSpec Pty Ltd for conducting the SEM/EDS experiment (Hitachi High-Technologies (Japan), TM4000Plus Tabletop Scanning Electron Microscope. Equipped with Bruker Quantax 75 Energy Dispersive X-ray Spectrometer) on the zinc flowers.

7.4 References

1. Britton, J.; Stubbs, K. A.; Weiss, G. A.; Raston, C. L., Vortex Fluidic Chemical Transformations. *Chemistry – A European Journal* **2017,** *23* (54), 13270-13278.
2. Vimalanathan, K.; Raston, C. L., Dynamic Thin Films in Controlling the Fabrication of Nanocarbon and Its Composites. **2017**, doi.org/10.1002/admt.201600298.
3. Hao, N.; Nie, Y.; Zhang, J. X. J., Microfluidic synthesis of functional inorganic micro-/nanoparticles and applications in biomedical engineering. *International Materials Reviews* **2018**, *63* (8), 461-487.
4. Abalde-Cela, S.; Taladriz-Blanco, P.; de Oliveira, M. G.; Abell, C., Droplet microfluidics for the highly controlled synthesis of branched gold nanoparticles. *Sci Rep* **2018,** *8* (1), 2440-2440.
5. Visaveliya, N.; Köhler, J. M., Single-Step Microfluidic Synthesis of Various Nonspherical Polymer Nanoparticles via in Situ Assembling: Dominating Role of Polyelectrolytes Molecules. *ACS Applied Materials & Interfaces* **2014,** *6* (14), 11254-11264.
6. Balbino, T. A.; Serafin, J. M.; Malfatti-Gasperini, A. A.; de Oliveira, C. L. P.; Cavalcanti, L. P.; de Jesus, M. B.; de La Torre, L. G., Microfluidic assembly of pDNA/cationic liposome lipoplexes with high pDNA loading for gene delivery. *Langmuir* **2016,** *32* (7), 1799-1807.
7. Boussif, O.; Lezoualc'h, F.; Zanta, M. A.; Mergny, M. D.; Scherman, D.; Demeneix, B.; Behr, J. P., A versatile vector for gene and oligonucleotide transfer into cells in culture and in vivo: polyethylenimine. *Proceedings of the National Academy of Sciences* **1995,** *92* (16), 7297-7301.
8. Koh, C. G.; Kang, X.; Xie, Y.; Fei, Z.; Guan, J.; Yu, B.; Zhang, X.; Lee, L. J., Delivery of polyethylenimine/DNA complexes assembled in a microfluidics device.

Molecular Pharmaceutics **2009,** *6* (5), 1333-1342.

9. Rungsardthong, U.; Ehtezazi, T.; Bailey, L.; Armes, S. P.; Garnett, M. C.; Stolnik, S., Effect of polymer ionization on the interaction with DNA in nonviral gene delivery systems. *Biomacromolecules* **2003,** *4* (3), 683-690.
10. Bronich, T. K.; Nguyen, H. K.; Eisenberg, A.; Kabanov, A. V., Recognition of DNA topology in reactions between plasmid DNA and cationic copolymers. *Journal of the American Chemical Society* **2000,** *122* (35), 8339-8343.
11. Cho, C.-S., Design and development of degradable polyethylenimines for delivery of DNA and small interfering RNA: an updated review. *ISRN Materials Science* **2012,** *2012*, 24.
12. Teo, P. Y.; Yang, C.; Hedrick, J. L.; Engler, A. C.; Coady, D. J.; Ghaem-Maghami, S.; George, A. J. T.; Yang, Y. Y., Hydrophobic modification of low molecular weight polyethylenimine for improved gene transfection. *Biomaterials* **2013,** *34* (32), 7971-7979.
13. Fischer, D.; Bieber, T.; Li, Y.; Elsässer, H.-P.; Kissel, T., A novel non-viral vector for DNA delivery based on low molecular weight, branched polyethylenimine: effect of molecular weight on transfection efficiency and cytotoxicity. *Pharmaceutical Research* **1999,** *16* (8), 1273-1279.
14. Jere, D.; Jiang, H. L.; Arote, R.; Kim, Y. K.; Choi, Y. J.; Cho, M. H.; Akaike, T.; Cho, C. S., Degradable polyethylenimines as DNA and small interfering RNA carriers. *Expert Opinion on Drug Delivery* **2009,** *6* (8), 827-834.
15. Luo, X.; Al-Antaki, A. H. M.; Pye, S.; Meech, R.; Zhang, W.; Raston, C. L., High shear imparted tunable fluorescence in polyethylenimines. *ChemPhotoChem* **2017**, *2* (4), 343-348.
16. Giron-Gonzalez, M. D.; Salto-Gonzalez, R.; Lopez-Jaramillo, F. J.; Salinas-Castillo, A.; Jodar-Reyes, A. B.; Ortega-Muñoz, M.; Hernandez-Mateo, F.; Santoyo-Gonzalez, F., Polyelectrolyte complexes of low molecular weight PEI and citric acid as efficient and nontoxic vectors for *in vitro* and *in vivo* gene delivery. *Bioconjugate Chemistry* **2016,** *27* (3), 549-561.
17. Dunlap, D. D.; Maggi, A.; Soria, M. R.; Monaco, L., Nanoscopic structure of DNA condensed for gene delivery. *Nucleic Acids Research* **1997,** *25* (15), 3095-3101.
18. Knierim, E.; Lucke, B.; Schwarz, J. M.; Schuelke, M.; Seelow, D., Systematic comparison of three methods for fragmentation of long-range PCR products for next generation sequencing. *PLOS ONE* **2011,** *6* (11), e28240.
19. Yang, Y.; Hang, J., Fragmentation of genomic DNA using microwave irradiation. *Journal of Biomolecular Techniques : JBT* **2013,** *24* (2), 98-103.
20. Loman, N. J.; Misra, R. V.; Dallman, T. J.; Constantinidou, C.; Gharbia, S. E.; Wain, J.; Pallen, M. J., Performance comparison of benchtop high-throughput sequencing platforms. *Nature Biotechnology* **2012,** *30* (5), 434-439.
21. Keskin, S.; Kızılel, S., Biomedical applications of metal organic frameworks. *Industrial & Engineering Chemistry Research* **2011,** *50* (4), 1799-1812.
22. Férey, G.; Mellot-Draznieks, C.; Serre, C.; Millange, F.; Dutour, J.; Surblé, S.; Margiolaki, I., A chromium terephthalate-based solid with unusually large pore

volumes and surface area. *Science* **2005,** *309* (5743), 2040-2042.

23. Morris, W.; Briley, W. E.; Auyeung, E.; Cabezas, M. D.; Mirkin, C. A., Nucleic acid–metal organic framework (MOF) nanoparticle conjugates. *Journal of the American Chemical Society* **2014,** *136* (20), 7261-7264.
24. Zhuang, J.; Kuo, C.-H.; Chou, L.-Y.; Liu, D.-Y.; Weerapana, E.; Tsung, C.-K., Optimized metal-organic-framework nanospheres for drug delivery: evaluation of small-molecule encapsulation. *ACS Nano* **2014,** *8* (3), 2812-2819.